Particle Transport by Rapid Vaporization of Superheated Liquid

Thesis by

Ichiro Sugioka

In Partial Fulfillment

of the Requirements for the Degree of

Doctor of Philosophy

California Institute of Technology

Pasadena, California

1991

(Submitted January 4, 1991)

To Elise, my love.

Abstract

Superheated liquid vaporizing explosively in a particle bed inside a cylindrical test cell has been studied using a rapid depressurization apparatus. The experiments provide insights into the explosive vaporization phenomenon and the multiphase flow which is generated by the rapid production of vapor.

Inside the sealed test cell, spherical glass particles are immersed in a volatile liquid, Refrigerant 12 or 114 at 300K. When the diaphragm at the upper end of the test cell is ruptured, the liquid pressure is reduced to a predetermined pressure within milliseconds. Since the liquid temperature is higher than the boiling temperature at reduced pressure, the liquid achieves a superheated state and nucleate boiling begins among the particles. The particle-liquid-vapor flow produced by the rapid release of vapor has been found to differ depending on whether the pressure is reduced below a critical level, which is 55% of the vapor pressure in the experiments conducted. When the final pressure is greater than critical, vapor pockets continue to grow throughout the particle bed and displace a liquid-particles mixture out from the test cell. When the final pressure is below critical, the particles are dispersed by a wave-like phenomenon (*disruption front*) where explosive vaporization appears to be localized in a narrow region. A disruption front in R12 travels at about 380 cm/s, and at about 200 cm/s in R114.

Experiments have been performed at various conditions to study the vaporization and transport process. High-speed cinematography and fast-response pressure gauges have provided data on the particle acceleration process. The inertial effect on particle acceleration has been studied by conducting similar experiments in a centrifuge. Using this data, the transport process associated with the disruption front has been examined in detail. An empirical relationship between the particle weight and viscous drag is presented for this particular case. This study concludes with discussions based on analytical models of the disruption front to approximate flows properties which are intractable experimentally. It is suggested that a disruption front is an expansion process which maximizes vaporization and entropy.

Table of Contents

List of Figures

List of Tables

List of Symbols

A	Cross-sectional area
a	Sound speed
a	Acceleration
C_D	Drag coefficient
c	Speed of the disruption front in the laboratory frame
c	Specific heat
c_p	Specific heat at constant pressure
D	Pressure drop due to particle acceleration; drag
d	Particle diameter
F	Froude number; force
G	Galileo number
G*	Modified Galileo number
g	Gravitational acceleration on earth; 980 cm s^{-2}
h	depth
h_0	Depth of the test cell cavity; maximum possibel particle depth
h_1	Particle depth at the beginning of the experiment
h_2	Particle depth at the end of the experiment
h	Enthalpy
J	Mass flux
Ja	Jakob number
KE	Kinetic energy per unit mass
l	Thickness or length
M	Mach number
N	Acceleration divided by 980 cm s^{-2}
P	Pressure
R	Gas constant

Re	Reynolds number
T	Temperature
t	Time
u	Flow velocity
V	Volume
v	Specific volume
v	Individual particle velocity
x	Mass fraction; distance
W	Weight
Y	Correlation factor for the sound speed
Z	Compressibility
α	Volumetric fraction of vapor in the liquid-vapor system
α_T	Thermal diffusivity
β	Volumetric fraction of particles
γ	Ratio of specific heats
Δ	Change in a quantity
μ	Absolute viscosity
ν	Kinematic viscosity
ρ	Density
τ	Characteristic time

Subscripts

$( )_0$	Condition upstream of the disruption front
$( )_1$	Condition immediately downstream of the disruption front
$( )_2$	Condition downstream of the acceleration region
$( )_B$	Quantity associated with a glass particle
$( )_{mix}$	Quantity associated with a droplet-vapor mixture

$( )_S$ Quantity associated with a sphere

$( )_L$ Quantity associated with the liquid

$( )_V$ Quantity associated with the vapor

Superscripts

$( )^*$ Equilibrium condition far downstream; characteristic accleration quantity

$( )'$ Hypothetical condition with no particle-liquid heat transfer

Acknowledgement

This thesis is the product of volcanological research initiated by Professor Bradford Sturtevant and Dr. Susan Werner Kieffer.

During my studies I benefitted from the support I received from many people at Caltech. I thank Professor Sturtevant for spending countless hours and resources for making my graduate studies possible. Dr. Marcus Bursik should get the credit for guiding me on the geological ideas expressed in this thesis. Various faculty members, in particular Professors Brennen, Hornung, Knauss, Marble, Scott, Stevenson, and Zukoski have supported me in many ways over the years. My colleague, Dr. Larry Hill provided me with technical assistance in the experimental work including an apparatus which provided some invaluable data for the thesis. Professor Scott and Dr. Agnes Allard provided me with the assistance necessary to perform the experiments in the Caltech Geotechnical Centrifuge.

There are many other people who aided me over the last six years at Caltech but I will not attempt to list their names since I will forget to mention somebody. However, I do not think I could have survived without the support I received from the staff and the students in Aeronautics, Geology, and the Graduate Office.

This thesis is dedicated to my wife, Elise, who somehow managed to put up with me while I was 'married' to my graduate studies.

Finally, I want to remember four Caltech friends who passed on since my undergraduate years: Professor Charles Babcock, Professor David Welch, Dr. Paul Schatzle, and Mr. James Drake. I miss them.

Chapter 1

Introduction

Certain volcanic eruptions, such as the May 18, 1980, eruption of Mt. St. Helens, and some geothermal explosions, occur when pressure is suddenly released from a confined volume of hot material. In these explosive eruptions, the eruptive material can be described as consisting of two components, volatile and nonvolatile. During the moments following depressurization, bubbles of vapor will nucleate on the surfaces of nonvolatile material. In volcanic eruptions, the growth of vapor bubbles is thought to fragment the magma into juvenile pyroclasts which are then lofted by the vapor released during the disruption of the bubbles. In geothermal systems, explosive expansion of water vapor occurring in a superheated aquifer is responsible for the eruption of a geyser. Explosions at the Kawerau geothermal field in New Zealand have been attributed to reduction of fluid pressure leading to the vaporization of hot subsurface water (Nairn & Wiradiradja, 1980).

Other examples of hazards due to explosive vaporization can be found in industry. For example, hot water in the cooling lines of nuclear power plants is kept from flashing by the high pressure. If one of these cooling lines ruptures, the pressure drops below the vapor pressure, and rapid vaporization of water results. This often leads to a loss-of-coolant accident (LOCA), because the expansion of vapor forces water out of the cooling lines through the break. Under certain conditions, such as high water temperature or an abundance of nucleation sites, the situation is even more hazardous, because the vaporization is sufficiently rapid to be considered *explosive*. This process has been observed in *blowdown experiments* which have been used to simulate LOCA incidents (Winters and Merte, 1979).

On the other hand, controlled rapid vaporization can be a useful industrial process. Aerosol production is an interesting characteristic of many rapid vaporization processes. A

technique called *spray drying* produces powder (e.g., powdered milk) from a mixture of ingredients in volatile liquid. In this process, the mixture is heated and forced through a nozzle into a region of lower pressure. The volatile liquid begins to vaporize in the nozzle and a spray of fine particulates is produced (Marshall, 1954).

The processes which transform hot material into particle-laden gas during rapid vaporization are not well understood. The conditions in which the process occurs, especially in the volcanological cases, are not amenable to direct observations. The thermodynamic and fluid dynamic behavior of complicated fluids undergoing expansion involves the transport of mass, momentum, and energy by mechanisms which are closely coupled and non-linear (Sturtevant and Kieffer, 1982). In volcanic eruptions, vaporization and particulate drag are two important features which affect the expansion of material upon depressurization. Examinations of these complex processes under controlled conditions should lead to the identification of parameters important to rapid vaporization.

1.1 Background

1.1.1 Fluid Mechanical Studies of Volcanic Eruptions. The gasdynamics approach to high-speed flow problems in geology, employed in this work, was first introduced to the study of geysers and volcanic blasts by Kieffer (1977, 1981). In these works, Kieffer demonstrates the importance of compressibility in volcanic eruptions involving high mass flux. Prior to this, Wilson (1976) postulated that supersonic velocities are produced by energetic (Plinian) eruptions, as indicated by the distribution of large pyroclastics deposited near the vents. However, the validity of his assumptions, particularly those concerning the bulk density of the transporting medium, are not well established (Woods and Bursik, 1990).

The multiphase nature of volcanic flows, both within the conduit and in the atmosphere, has also been recognized. The flow of bubble-rich magma within the conduit is treated as a homogeneous two-phase flow by Sparks (1978a). Sparks proposes a

mechanism for the fragmentation of gas-rich, viscous magma[1] which produces particulates which are transported by the released vapor. Sparks' model for the transition from bubbly two-phase flow to dispersed two-phase flow which occurs in a Plinian eruption involves a narrow fragmentation region in which the bubbles are fragmented. The fragmentation of the magma produces a high-speed flow of particulates and vapor which is characteristic of Plinian eruptions. High-speed flow of this type is analyzed by treating the particle-laden gas as a pseudo-gas by Kieffer (1978, 1981). However, not all eruptions produce a high-speed flow of particulates. Vergniolle and Jaupart (1986) apply the concept of separated two-phase flow to eruptions involving low viscosity, basaltic magma.[2] Coalescence of gas bubbles in basaltic magma produces slugs of gas moving relative to the molten material, so a homogeneous flow model cannot be applied, and the two phases must be treated separately.

The experimental studies of eruption-related fluid mechanics are somewhat limited. Sheridan and Wohletz (1983) conducted experiments simulating hydro-magmatic interactions which are believed to be responsible for shallow volcanic craters called maars. These craters are formed when hot magma interacts with a substantial reservoir of subsurface groundwater or a surface body of water. The explosive phenomenon being modeled in these experiments is similar to industrial *vapor explosions* (Reid, 1983) which occur when extremely hot material is suddenly brought into contact with water. Another phenomenon in volcanic eruptions also associated with industrial application is fluidization of particulates. Wilson (1984) conducted fluidization experiments to understand the behavior of *pyroclastic flows*, a gravity driven flow of volcanic particulates. McTaggart (1960), Sparks (1976, 1978b), Sheriden (1979), and Wilson (1985) describe features of pyroclastic flows which are consistent with the behavior of partially fluidized beds

---

[1] Andesitic magma responsible for many stratovolcanoes is a material of this type.

[2] This type of magma is responsible for *shield volcanoes* such as Mauna Loa and Mauna Kea in Hawaii.

observed in the experiments. Fluidization has also been used to explain the transport of material in *explosive breccia pipes* (Reynolds, 1954). (Breccia pipes are vertical pipe-like features with evidences of explosive upheaval which are filled with fragmented material, or breccia.) However, the concept of transient fluidization occurring in the breccia pipe during its formation is disputed by Wolfe (1980).

1.1.2 Applications in Engineering Sciences. Gasdynamic phenomena involving phase transition have been studied since condensation shocks were first observed in early supersonic wind tunnels. Recently, several investigators have studied high-speed adiabatic phenomena involving evaporation. Evaporation waves produced by the rapid depressurization of liquid are studied by Grolmes and Fauske (1974), Chaves (1981, 1984), and Hill (1990). Chaves' experiments, conducted with liquid heated close to its critical point, are part of a larger program by Thompson *et al.* (1986, 1987). In Thompson's work, depressurization of fluids with high specific heat near the critical point was studied to investigate the possible formation of rarefaction shock waves.[3]

Flow discontinuities involving vaporization are thermodynamically equivalent to exothermic discontinuities, such as those involving combustion, because internal energy is converted into kinetic energy. However, cooling occurs in evaporation, while the release of chemical energy in combustion causes heating. In combustion, the exothermic discontinuity may be a fast-moving detonation or a slow deflagration. A detonation wave, which increases the pressure, propagates at supersonic speed through the combustible medium. A deflagration wave propagates at subsonic speed and decreases the pressure. Since a vaporization process produces a state which is lower in temperature and density, an evaporation wave is similar to a deflagration wave.

---

[3] A rarefaction shock will generally violate the second law of thermodynamics.

The speed of a deflagration wave, especially that of a *laminar premixed flame*, is determined by the rate of mass and heat transfer needed to combine and ignite the chemical species. A similar *rate relation* is believed to determine the speed of the evaporation wave (Hill, 1990). However, latent heat is transferred downstream in evaporation while the heat is transferred upstream from the flame to ignite the fuel-air mixture. Fluid mechanical instabilities, such as the Taylor-Markstein instability caused by local acceleration of the fluid, produce unsteadiness which often leads to a rate relation which is much more complex than the one-dimensional diffusion model (Hill, 1990). In the case of rapid vaporization, the surface tension at the interface will have an effect on the unsteady process which has been observed.[4] The presence of solid particles in the superheated liquid will affect such mechanisms by providing nucleation surfaces. In addition, due to the gravitational packing of negatively buoyant particles, the liquid is partitioned into small volumes which may have an effect on the unsteady processes.

High-speed transport of multiphase material is an important subject in industry. The flow of material produced by the vaporization of superheated liquid is an extreme example of a multiphase flow. For example, the flows produced by the experiments conducted for this study involve three phases of material. In the past, studies of multiphase flows have been conducted mainly on two-phase flows (Wallis, 1969). Only the special case of the fluidized bed has received a significant amount of attention as a three-phase flow (Ostergaad, 1971; Darton, 1985). In cases such as the volcanic eruption, where a particle-laden flow is accelerated, the interaction between the particles and gas, as described by Marble (1963, 1970), is also important.

1.1.3 Closely Related Works. The present work is part of an experimental effort to explore gasdynamics in multiphase media. Two previous studies are directly related to the

[4] Hill (1990) hypothesizes that "bursts" are necessary for the propagation of the evaporation wave.

present work. Anilkumar (1989) studies the behavior of macroscopic particles when gas within an initially packed bed of particles is expanded by rapid depressurization. This study shows that an isotropic *dense dusty gas*, i.e., a homogeneous dispersion of particles, cannot be produced by this method. The breakup of the particle bed by expanding interstitial gas invariably produces horizontal fractures instead of a homogeneous dispersion of particles. These fractures were observed to develop into gas bubbles bound by streams of particles. Anilkumar's work has received attention for its relevance to the flow of fine pyroclastic material deposited by a volcanic eruption. Hill (1990) studies vaporization occurring in a column of pure liquid which has been superheated by rapid depressurization. In Hill's experiments, unlike previous blowdown experiments, careful preparation of the test cell eliminates the nucleation of vapor bubbles on the test cell walls. In the absence of nucleate boiling, the bulk of the superheated liquid remains in the metastable state, and vaporization occurs at the top of the liquid column. The liquid-vapor interface is transformed by vaporization into an *evaporation wave* which travels at subsonic speed down the liquid column. A high-speed two-phase flow produced by the evaporation wave, which is not necessarily choked, carries mass out of the test cell. Thermodynamically, the process is analogous to a deflagration wave propagating in a combustible mixture. Hill proposes that the mechanism for driving an evaporation wave depends on fragmenting the thermally depleted liquid adjacent to the interface. Explosive bursts of vaporization associated with the evaporation wave are suggested as the mechanism responsible for the fragmentation process which exposes fresh superheated liquid to vaporization at the interface. Suppression of the burst by increasing the backpressure is shown to shutdown the production of high-speed two-phase flow by this process.

1.2 Basis for the Present Work

"*1.2.1 The experiment.* The experiments conducted for the present work combines aspects of Anilkumar's particulate flow experiments and Hill's rapid vaporization

experiments. In the new experiments, a packed bed of glass particles immersed in a volatile liquid is disrupted by the vaporization when the liquid is superheated by depressurization. Rapid vaporization provides a practical method for achieving the high vapor flux in a laboratory experiment necessary for simulating the transport of crystals and glassy pyroclasts by the rapid vapor release in a volcanic eruption. Although vaporization is a heat transfer dependent process and exsolution of magmatic gas is a mass diffusion process, the transport process in the experiment will be relevant to volcanic eruptions if it is controlled by the vapor flux. In the experiment, particles in the mixture promote the production of vapor by providing nucleation sites for gas bubbles. However, nonvolatile material, such as the particles or unvaporized liquid droplets, impedes the release of vapor by contributing to the pressure drop in the test cell. The interaction between the nonvolatile material and the flow of vapor is thought to be important to the transport of these materials in the test cell. In this respect, the results of the experiments should further our understanding of volcanic eruptions.

1.2.2 Scaling Considerations. The scale of the physical system involved in a volcanic eruption is far greater than what can be practically simulated in the laboratory. Even the smallest geological eruptions of interest, those of geysers, involve systems which extend on the order of 10 to 100 meters underground (Reinhart, 1980). As a consequence of the large vertical scale, gravitational effects are extremely important in geological eruptions. In experiments simulating the eruptions, it is desirable to reproduce the relative importance of inertia and gravity. This requires the ratio of inertial force to gravitational force, or the Froude number (Fr), of the experiment to have a value in the same range as that of the eruption.

$$Fr = \frac{u^2}{g\,l} \tag{1.1}$$

where u is the characteristic velocity, l is the characteristic length, and g is the acceleration of gravity. Since a process which transports material against gravity is being modeled, the

characteristic velocity and the length scale in the vertical direction are important. Although the characteristic length of the experiment is far less than that of the eruption, the velocity cannot be reduced to keep the Froude number constant because a high-speed flow is produced by an explosive eruption. The relative importance of viscosity and compressibility in a high-speed flow can only be modeled in an experiment which also involves a high-speed flow.

The gravitational force can be scaled to compensate for the reduced scale by conducting the experiment in a centrifuge. This approach has been used in reduced scale geotechnical experiments (Scott, 1983), and the effect of the centrifugal acceleration on dynamic processes is described by Ortiz *et al.* (1983). For dynamic processes occurring in the new experiments, the centrifugal acceleration replaces the gravitational acceleration in the Froude number expressed by Equation (1). Since the product of the characteristic length and the acceleration is in the denominator, the same Froude number can be obtained if the acceleration is scaled inversely proportional to the length. Then, the effect of gravity on a 50 meter deep geological system may be modeled by a half meter long apparatus if the experiment is conducted at 100g.[5] Caltech's geotechnical centrifuge, rated for use at 175g, has been used in this work to study the role of gravity in eruptions driven by the rapid release of vapor.

The relative importance of the viscosity is given by the ratio of inertial forces to viscous forces, the Reynolds number (Re).

$$\mathrm{Re} = \frac{\rho u l}{\mu} \tag{1.2}$$

where the characteristic density is ρ and the viscosity is μ. For a typical flow of particle-laden gas produced by a volcanic eruption, the estimates of Reynolds number for the

[5] "100g" should be read as "100 times earth's gravitational acceleration" or 980 m/s^2.

visibly turbulent flow exceeds 10^6; therefore the the effect of viscosity is negligible. If the Reynolds number of the experiment is sufficiently high to make the flow *fully turbulent*, then the effect of viscosity will also be negligible.

A dispersed particulate flow, such as those occurring in some volcanic eruptions, can be analyzed as a pseudo-gas (Kieffer, 1981). The compressibility of such a flow is described by the Mach number (M), a ratio of the flow speed to the sound speed (a), where the sound speed will be lower than that in pure gas (Kieffer, 1977).

$$M = \frac{u}{a} \tag{1.3}$$

In volcanic eruptions as well as in industrial accidents, the pressures involved are sufficient to produce gasdynamic choking of the flow, which means that the characteristic velocity is the sonic velocity of the medium. Sonic velocity of particle laden gas, such as in the Mt. St. Helens blast, is on the order of 100 m/s (Kieffer, 1981). The relatively high velocity and pressure necessary in the experiment for properly scaling the Reynolds and Mach number are produced by the rapid vaporization of superheated liquid.

The high-speed flow essential for modeling a geological eruption requires a rapid production of vapor. In the experiments, the vapor is produced by rapidly vaporizing a liquid using the excess enthalpy or superheat which results from depressurizing the liquid. The amount of vapor produced by depressurization is determined by the Jakob number (Ja), a ratio between the excess liquid enthalpy and the heat of vaporization. This ratio is equal to the mass fraction of superheated liquid which can be vaporized by the depressurization of liquid in an adiabatic system.

$$\mathrm{Ja}\,(P_a, P_b) = \frac{h_{liq}(P_a) - h_{liq}(P_b)}{h_{vap}(P_b) - h_{liq}(P_b)} \tag{1.4}$$

where $h_{liq}(P)$ and $h_{vap}(P)$ are enthalpies of saturated liquid and saturated vapor respectively at some pressure P; P_a is the vapor pressures of the liquid before and P_b is the vapor

pressure after the depressurization. (The time scale of explosive vaporization is usually too short for significant heat transfer, making the process essentially adiabatic. However, if additional source of latent heat exists in the system, the additional enthalpy must be added to the numerator of the expression.) Higher Jakob numbers, thus greater vapor release, can be obtained by decreasing the final pressure, P_b, relative to the initial vapor pressure, P_a. This means that experiments involving the same material and initial conditions can be used to study how the vapor production determines the behavior of an eruption by just changing the pressure downstream of the test cell. The effect of vapor production can also be studied by using test fluids of different volatility, but such results may only reflect the differences in the fluids.

1.3 Outline of the Present Work

This work discusses the results of a series of experiments which were performed to study the disruption of a particle matrix and subsequent particle transport due to the rapid vaporization of liquid within the matrix. The results of these experiments provide information regarding the parameters which are important to the dispersion and transport of particles. A series of experiments was also conducted in a centrifuge to increase the effect of gravitational force on the small-scale experiments to simulate the phenomena which occur in a large system under normal gravitational conditions.

The techniques and materials used in this work are described in Chapter 2. In Chapter 3, the results of the the flow visualization experiments are used to describe qualitative differences in the behaviors observed. The quantitative results of the experiments are discussed in Chapter 4. A hypothesis which attempts to explain behavior which is observed in the experimental data is presented in Chapter 5. Finally, Chapter 6 concludes the present work with a discussion of the implication of these results in the study of volcanic eruptions.

Chapter 2
Experimental Methods and Materials

A rapid depressurization apparatus is used to produce an explosive vaporization which simulates the rapid release of gases in a volcanic eruption. One such apparatus has been constructed for experiments in the Caltech geotechnical centrifuge at Froude numbers consistent with that of geologic phenomena. These experiments are complemented with experiments conducted under normal gravitational conditions using a similar apparatus. In all of these experiments, the crystal-rich magma responsible for the eruption is simulated by glass particles in a volatile liquid. The high-speed phenomena which occur in these experiments are examined using high-speed photography and fast response pressure instrumentation.

2.1 Apparatus Design

The apparatus is designed to rapidly vent the test cell, a small cylindrical pressure vessel, by opening its upper end to a region of low pressure. The basic apparatus is composed of two main parts: a test cell with a diaphragm sealing the top and a mechanism for cutting the diaphragm. These parts are shown in Figure 2.1, a schematic drawing of the equipment necessary for conducting the experiments. Two apparatus configurations have been used in this study. The *1g Apparatus* (Figure 2.2) has been used to conduct experiments at normal gravitational conditions. The *Hi-g Apparatus* (Figure 2.3) is a separate apparatus designed for use in the Caltech geotechnical centrifuge; it is capable of operating at 200g. The test cells for these configurations are identical, making components such as the Pyrex pipe sections and the endwalls interchangeable. By using the same test cell, geometrically similar 1g and Hi-g experiments can be conducted.

2.1.1 Test Cell Design. The test cells used in the present work are identical to those used by Hill (1990) except for the overall length. The test cell is composed of three main parts (Figure 2.4). The central part of the test cell is a Pyrex pipe section, 2.5 cm I.D.,

which allows photography of the phenomena inside. Pyrex pipe sections are available in various lengths at 15 cm increments; the test cell length depends on the experiment being conducted. These sections feature flanges for joining them to other components at either end.[1] The upper flange joins the pipe to a *service assembly*,[2] and a solid *endwall* is attached to the lower flange. The complete assembly forms a 2.5 cm diameter cavity formed by the Pyrex pipe that extends through a 1.3 cm long cylindrical hole in the service assembly. Destaco clamps attached to the service assembly are used to seal the open end of the test cell with a metal diaphragm. The service assembly also features a port for introducing fluids into the test cell after the diaphragm is in place. Two Bourdon-tube pressure gauges (one for 0 to 1 bar and another for 0 to 20 bar measurements) connected to this port are used to measure the pressure in the test cell prior to the experiment.

The diaphragms for most experiments are 0.1 mm thick disks of 1100-C aluminum alloy.[3] An arrangement of clamps holds the diaphragm against O-ring seals. Because it is resistant to the fluorocarbon liquids used in the experiments, Neoprene is used for sealing the test cell. A 3 mm Neoprene sheet is used for the gasket sealing the junctions between the Pyrex pipe section and other parts of the test cell. The 22 bar hydrotest which has been conducted to qualify the test cell as a pressure vessel also demonstrates the effectiveness of these seals.[4]

The endwall at the bottom of the test cell houses a PCB piezoelectric pressure transducer. Since temperature affects its performance, the transducer is isolated from evaporative cooling with a layer of glass particles immersed in Refrigerant 113 (R113).[5]

---

1 Corning Conical System.

2 This part is called the *Reservoir/Test Cell Interface Assembly* in Hill (1990).

3 Thinner diaphragms are used if the test cell pressure is less than 4.5 bars above the reservoir pressure.

4 This hydrotest is used to qualify the test cell to a safety factor of 2.5. The test cell is designed to withstand a pressure which is the sum of vapor pressure and the hydrostatic pressure exerted by a 50 cm column of R12 at 200g.

5 This technique was developed in 1988 after early efforts to produce an evaporation wave in the centrifuge was hampered by the gelatin-layer-method which was then used to suppress nucleate boiling in pure

R113 has a low vapor pressure which keeps it from being vaporized like the test fluid by depressurization.[6] In addition, R113 is denser (1.57 g/cc) than the test fluids used in the experiments (R12 is 1.31 g/cc and R114 is 1.46 g/cc), and thus settles under the volatile liquid, isolating the pressure transducer. Consistent pressure data cannot be obtained without this layer. Comparative tests show that the R113 layer has a negligible effect on the response of the pressure transducer (see 2.1.5).

In addition to the endwall pressure transducer, a pressure transducer is mounted in the service assembly, 0.6 cm from the diaphragm. This transducer is flush mounted to measure the static pressure of the flow at the exit. The sensitive surface of the transducer, a stainless steel diaphragm, can be insulated from evaporative cooling with a Neoprene plug (Hill 1990). However, the plug has been found to eliminate signals produced by particle impacts which provide useful information on the speed of the particles (Figure 2.5). For this reason, the Neoprene plug is not used in the experiment except where low frequency pressure measurement is sufficient. Without the plug, the exit transducer will drift slowly as the transducer is cooled by evaporation without obscuring its response to rapid changes in pressure and particle impacts.

2.1.2 1g Apparatus. The apparatus used to conduct experiments at normal gravitational condition has been used previously to study evaporation waves. A detailed description of this apparatus and the study of evaporation waves can be found in Hill (1990). Figure 2.2 illustrates the general arrangement of the apparatus. The test cell is positioned below a 270 liter pressure reservoir, which sets the downstream condition of the experiment, while the diaphragm cutting mechanism is mounted inside. Since the reservoir is 125 cm off the floor, this apparatus can be used with test cells having up to a 91 cm

---

liquid. Hill (1990) eventually adopted the R113 method for experiments where the final pressure is higher than 0.5 bar. Subsequently, it was found that glass particles do not hamper the effectiveness of this technique.

[6] This technique requires the final pressure following depressurization to be greater than 0.5 bars, the vapor pressure of R113 at room temperature.

Pyrex pipe section.[7] The pressure reservoir can be set to any pressure between vacuum and 3.1 bar by means of a vacuum pump and a compressed gas supply. The Heise pressure gauges used to monitor the pressure inside the test cell can be connected to the reservoir through a three-way ball valve.

2.1.3 Hi-g Apparatus. The apparatus used to conduct experiments in the geotechnical centrifuge is essentially a reinforced version of the 1g Apparatus. As shown in Figure 2.3, the test cell is supported by two 3.8 cm thick walls of 6061 aluminum. These walls are bolted to a cradle on the centrifuge rotor (Figure 2.6), while counterweights are attached to another cradle at the opposite end. The test cell is suspended from the service assembly between the walls and extends through a circular hole in the cradle. The test cell is supported against the centrifugal force by four 0.8 cm diameter steel rods which extend from the service assembly to the endwall.

Due to space restrictions, there is no pressure reservoir attached to the test cell, which limits the downstream condition to atmospheric pressure. Therefore, all experiments in the centrifuge have been conducted by venting the test cell to atmospheric pressure. In addition, the test cell length is limited to 47 cm. Unlike the 1g Apparatus, the apparatus has been designed with an umbilical system, which supplies the volatile liquid under pressure and monitors pressure inside the test cell. Before the centrifuge enclosure is closed for a run, the test cell is sealed with a plug valve and the umbilical cord is disconnected. This approach guarantees that only the minimum of equipment is subjected to high centrifugal loads.

2.1.4 Diaphragm cutting mechanism. The test cell is vented by mechanically piercing a thin aluminum diaphragm at the top of the test cell. This high speed depressurization method is necessary to produce superheated liquid necessary for explosive

[7] Since the test cell is lowered to change the diaphragm, a longer test cell cannot be used in the apparatus.

vaporization. Upon actuation, crossed knife blades cut the diaphragm into four petals which are blown back by an initial burst of vapor escaping from the cavity above the test liquid. The actuation method is apparatus dependent. The knife blades in the 1g Apparatus are driven directly by a pneumatic cylinder. However, because the space required by a pneumatic cylinder above the apparatus is not available in the centrifuge, it could not be used on the Hi-g Apparatus. Therefore, in the Hi-g Apparatus, the knife blades are mounted midway on a 30 cm arm with the actuation mechanism at the end of the arm, on the side of the apparatus. A small pneumatic cylinder is used to release a catch, which then allows the arm to swing the knife blades a short distance into the diaphragm. O-rings mounted at the end of the arm, where they have a 2-to-1 mechanical advantage, are tensioned to apply approximately 200 newtons of force on the knife blades. The blockage ratio of the exit by the knife blades, based on the horizontal cross section of the knife blades and the orifice, is about 3.5% (Figure 2.7).

2.1.5 Fast response pressure instrumentation. The pressure instrumentation depends on the series of experiments for which they are used. Experiments conducted in the centrifuge during June 1989 with the Hi-g Apparatus are instrumented with a PCB 112A21 (voltage-mode) transducer at the exit and a PCB 113A02 (charge-mode) at the endwall. The 1g experiments are instrumented with a PCB 112A02 due to difficulties in obtaining reliable performance from the PCB 113A02 (charge-mode) in the 1g experiments.[8] The PCB 112A21 also instruments the exit of the 1g Apparatus, although in experiments where lower sensitivity can be tolerated, the PCB 113A26 (voltage-mode), a transducer with longer discharge time, is used.

Charge-mode transducers (PCB 112A02 or 113A02) are used to measure the pressure at the endwall, or base pressure, because the R113 layer protects the highly sensitive gauge

[8] Unlike the Hi-g Apparatus, the pressure reservoir of the 1g apparatus requires the removal of the test cell from the apparatus for replenishing the glass particles. The particular *Micro-Dot* connector on the PCB 113A02 is somehow sensitive to the movement in the cable and the connection may fail unexpectedly.

from temperature changes. A PCB 462A charge amplifier converts the piezoelectric charge generated by the transducer to output voltage. The amplifier is used in the *long-time-constant* setting which gives a discharge time of over 500 seconds.[9] This is much greater than the duration of an experiment, which is always less than a second, so the base pressure data are equivalent to measurements by a static pressure gauge. Voltage-mode transducers used at the exit are powered by either a PCB 482A power supply or an H-Tech RCVR/XMTR-01 low noise amplifier. The typical discharge times for the dynamic, voltage-mode pressure transducers are 1 second for PCB 112A21 and 25 seconds for PCB 113A26.

The pressure transducers are calibrated before each series of experiments. These calibrations are based on the change in output voltage caused by a measured change in pressure, since the linearity of transducer response is shown to be better than 1% full scale in an earlier test; the calibration factor, in *bars per volt,* is obtained by dividing the change in pressure by the change in voltage. In the calibration trials, the test cell pressure is changed by venting nitrogen to the atmosphere. A Bourdon-tube pressure gauge is used to measure the test cell pressure to better than 0.04 bars, and a mercury barometer is used to measure the atmospheric pressure to about 0.001 bar. The results of two calibration trials conducted on February 27, 1990, are shown in Figure 2.8. The first trial is conducted without any R113 and particles covering the base transducer, while a 3 cm layer is used in the second calibration trial. The calibration factors calculated from similar trials are shown in Figure 2.9. These calibration factors can be checked if the pressure is known at two or more points in an experiment. Such data indicates that the transducer calibration varies negligibly (within 2%) between experiments.

2.1.6 Geotechnical centrifuge. The facility used for the experiments at high centrifugal acceleration is operated by Caltech for civil engineering research. This facility is

---

[9] Ref. PCB literature.

equipped with a Genisco Model A1030 centrifuge (Figure 2.6). This machine has a nominal rotor radius of 1 meter and is rated to 175g. For the present study, experiments have been conducted at 7g to 100g, with experiments being repeated at 10g and 100g. Electrical sliprings built into the centrifuge driveshaft allow remote control of the experiment and collection of data while the centrifuge is in motion. Rotary couplings for two pneumatic lines are also available. One pneumatic line is used to release the diaphragm cutter, while the other is used to measure the ambient pressure outside the test cell. (The method used to conduct high-speed photography in the centrifuge is described later in this chapter.)

2.2 Description of Materials in the Experiments

2.2.1 Volatile component (Test fluid). The fluids which serve as the vapor source in the experiments are chlorinated fluorocarbons which have been developed as nontoxic, nonflammable refrigerants. Refrigerants with room temperature vapor pressure above one bar but below the apparatus design limit are used; they are Dichlorodifluoromethane (CCl_2F_2), commonly known as Refrigerant 12 (R12), and dichlorotetrafluoroethane ($C_2Cl_2F_4$), commonly known as Refrigerant 114 (R114). The experiments are conducted with fluids manufactured for use in refrigeration equipment, which are filtered using a Nupro 0.5 μm sintered 316 stainless steel filter. The reference properties of these fluids (saturation condition at 300K) are listed in Table 2.1.

Table 2.1: Properties of saturated refrigerants at 300K.

Refrigerant	R12 (CCl_2F_2)	R114 ($C_2Cl_2F_4$)
Vapor Pressure (P_v)	6.85 bars	2.23 bars
Density (Liquid, ρ_L)	1.31 g/cc	1.456 g/cc
(Vapor, ρ_v)	0.0391 g/cc	0.0167 g/cc
Viscosity (Liquid, μ_L)	0.214 cp	0.36 cp
(Vapor, μ_v)	0.0123 cp	0.0112 cp
Surface Tension (σ)	9 dynes/cm	12 dynes/cm

2.2.2 Non-volatile component (Glass particles). The monodisperse glass spheres[10] used in the experiments are the same as those used by Anilkumar (1989). Relatively large particles (0.5 mm nominal diameter) compensate for the low resolution of 16 mm high-speed films. However, the effects due to the finite test cell diameter is not considered to be significant because the particle diameter is only 2% of the diameter.

Table 2.2: Properties of spherical glass particles used in the experiments.*

Material	Dragonite (Leaded Glass)
Density, ρ_B	2.95 g/cc
Diameter (Sieved)	0.5 mm (nominal) 0.425 - 0.500 mm (5.9%wt) 0.500 - 0.589 mm (93.6%wt) 0.589 - 0.701 mm (0.5%wt)

*Note: This data does not apply to experiments JUL26-2, JUN27-1, and MAR4-3/4/5.[11]

The particles selected for this study are negatively buoyant in the volatile liquid and remain packed at the bottom after the test cell is filled with liquid. The void fraction of the packed particles is between 0.35 and 0.40.[12] This value is consistent with the value, 0.32, which can be calculated for monodisperse spheres in body-centered cubic arrangement. In addition, the value of 0.4 is often used for packed spherical particles. Since the test cell has a constant internal diameter, the particle number can be specified by the depth of packed particles in the test cell. The particle depth before and after the experiment, h_1 and h_2 respectively, are recorded in every experiment. The length of the test cell cavity (h_0)[13] is

[10] This means that the diameter of the glass spheres are distributed around one nominal diameter.

[11] JUL26-2, JUL27-1, and MAR4-3 are experiments conducted with 1 mm monodisperse spheres of the same material. MAR4-4 uses 50% of each diameter, i.e., bidisperse glass spheres. MAR4-5 is conducted with beach sand.

[12] The data obtained by recording the displacement of R113 by glass particles in a 2.5 cm I.D. graduated cylinder.

[13] This is equivalent to the maximum possible particle depth.

determined by subtracting the depth of the R113 layer used to insulate the endwall pressure transducer[14] from the length of the test cell.

Particle depths are measured using a device consisting of a 1.25 cm diameter, 92 cm long wooden rod (dowel stick) with a 2.5 cm cardboard disk at one end. This device is inserted down the open end of the test cell to remove any particles clinging to its walls while packing the particles against the bottom. With the device resting inside the test cell, the point on the rod which is level with the upper end of the test cell is marked. The distance between the lower surface of the cardboard disk and the mark on the rod is measured with a ruler to the nearest 0.5 mm. The particle depth is obtained by subtracting this distance from h_0. The standard deviation of repeated measurements is less than 1 mm, and the maximum deviation from the mean rounded to the nearest 0.5 mm does not exceed 1 mm.

2.3 Typical Experimental Procedures

Before an experiment is carried out, the pressure transducers are calibrated with the R113 layer in the test cell. The particles, which have been sorted by sieves of 0.425 mm and 0.701 mm, are then poured into the open test cell. After the test cell is sealed with the diaphragm, it is pressurized by opening the connection to the test fluid reservoir. (Purging the test cell with the test fluid has been found to produce no noticeable difference, and the practice has been discontinued.[15]) The flow of liquid is carefully metered to minimize mixing with the R113, and the liquid is added until the surface is about 1 cm above the particles. One to two minutes after the liquid supply line has been closed, the vapor pressure of the liquid in the test cell is measured using a pressure gauge opened to the test

---

[14] The depth is typically less than 3 cm but must be greater than 2 cm. The interface between the clear test fluid and the dyed R113 must be visible while filling the test cell with the former in order to check for mixing and contamination of the test fluid by R113. About 2 cm of the Pyrex section at both ends is blocked from view by the flanges.

[15] Air cannot be purged effectively from the particle bed. Evacuation of the test cell to remove this air produces undesirable evaporation and cooling of R113.

cell. Since the vapor pressure varies with temperature, it is used to indicate whether the test fluid has remained near room temperature during the filling process. Any pockets of vapor which are not displaced out of the particle bed by the liquid are then eliminated by pressurizing the test cell with nitrogen. During the pressurization process, the liquid level first decreases as bubbles collapse. The liquid level then increases as vapor above the liquid condenses due to the increase in pressure. It is necessary to have sufficient amount of liquid covering the particles before pressurization so the condensed liquid, being warmer, will remain above the room temperature liquid and remain isolated from the particles. The experiment is performed immediately to minimize the amount of heat transfer across the stratified liquid layer above the particles.

Pressurizing the test cell to a level above the test fluid vapor pressure improves the experimental repeatability in two ways. First, the procedure provides a control over the amplitude of the rarefaction wave generated by diaphragm rupture. Since the amplitude is determined by the pressure difference across the diaphragm before the rupture, the test cell pressure is set to a level higher than the vapor pressure and the diaphragm is ruptured by the means independent of pressure. Secondly, the procedure eliminates random vapor pockets in the particle matrix trapped by the liquid. In the absence of vapor, the *liquid fraction* of the particle bed is known from the particle packing geometry. It is clear that nucleation-sites in the particle bed are not entirely eliminated by pressurization since high-speed photographs show bubbles forming immediately after depressurization. Whether the pressurization eliminates *any* nucleation sites for vapor bubbles is not known.

The experiment is initiated by electrically activating a solenoid valve in the pneumatic system which operates the diaphragm cutter. The electricity to the solenoid may be manually switched on if there are no critical timing requirements. As discussed previously, the pneumatic system drives the knife blades in the 1g Apparatus and releases the cutting arm in the Hi-g Apparatus. Upon diaphragm rupture, the drop in exit pressure produces a

drop in transducer output voltage which triggers the oscilloscope. Therefore, timing is not essential for experiments instrumented only by an oscilloscope connected to the pressure transducers. A Nicolet 4094 oscilloscope is used to record 16 kilobytes of data from the exit and base transducers at 5 kHz sampling rate.[16] By using the *pretrigger mode*, the oscilloscope records data which begin 200 ms before the drop in exit pressure. The voltage level corresponding to the test cell pressure before depressurization is used as a baseline.

2.4 High-Speed Photography

High-speed photography has been conducted to study the details of several representative experiments. The procedures for these experiments differ from others in that the cameras must be brought to speed before the test cell is depressurized. The configuration of the equipment and the procedures used to conduct photography of the experiments are described below.

2.4.1 Illumination of the test cell. The side views of experiments by Hill (1990) are backlit to reduce the illumination required to produce a high contrast image of the phenomenon. Unfortunately, glass particles scatter almost as much light as the aerosol particles produced by the explosive vaporization of liquid. Therefore, backlighting does not produce significant contrast between glass particles and the aerosol particles. For this reason, the test cell has been illuminated from the front to rely on reflectivity to distinguish features inside the test cell. The contrast of the images on the film is increased, with slight loss in resolution, by pushing it one stop. Since glass and aerosol particles are reflective, a dark backdrop has been used. Therefore, dark areas in the photographs are regions with only vapor or undisturbed liquid.

2.4.2 Wide-angle photography of 1g experiments. The high-speed photography of experiments FEB15-2, FEB20-2, FEB20-4, FEB22-3, and FEB23-3 focuses on the

[16] At this setting, each record covers approximately 1.5 seconds. A faster sampling rate by the Nicolet reduces the length of the record to less than 0.8 second, which is less than optimum for the experiments.

difference in behavior caused by reservoir pressure. The motion pictures of these experiments are filmed with a Redlake Hycam II 16 mm, rotating prism camera. In these experiments, the camera is positioned 60 cm from the test cell in order to photograph about 35 cm of the 44 cm test cell using a Pailard-Bolex Switar 50 mm lens. Two Berkeley Colortran 104-051 photoflood fixtures, each with a Sylvania FCM-type 1000 watt tungsten halogen lamp, are mounted at 45 degrees above and below the camera axis to alleviate the glare of direct reflection by the test cell (Figure 2.10). The illumination is sufficient to film at 4000 frames per second, with the lens aperture at f/8, using Eastman 7222 film pushed to 400 ASA.

In experiments involving the Hycam camera, the experiment is initiated by starting up the camera. When the proper film speed has been achieved, the Hycam camera triggers the solenoid valve, activating the diaphragm cutting mechanism. In order to film the experiment at 4000 frames per second, the camera is set to trigger the mechanism after 36 feet of film has been exposed. Unlike the Fastax camera used in the centrifuge experiments, the Hycam camera maintains nearly constant film speed after accelerating to the desired film speed. At 4000 frames per second, about 700 ms can be filmed with a 100 foot roll of film; this is sufficient for filming a complete experiment.[17]

The high-speed motion picture and the oscilloscope record of the experiment are correlated by a timing mark exposed on the film by the Hycam camera when the Nicolet oscilloscope is triggered. Additional marks are exposed at 1 millisecond intervals by a flashing LED inside the camera. These millisecond timing marks, instead of the nominal framing rate, are used when correlating the motion picture images to changes in pressure recorded by the oscilloscope.

---

[17] The pressure recordings of earlier experiments are used to approximate the duration of the filming..

The wide-angle motion pictures are complemented by 35 mm still photographs shot at 1/4000 second shutter speed. A Nikon FE camera with MD-12 motor drive attachment is used to obtain photographs at 0.3 second intervals. By incorporating a mirror in the optical path of the Nikon camera, the full test cell length has been photographed along nearly the same line of sight as the Hycam camera. A Nikon 50 mm f/1.2 lens with the aperture set at f/5.6 exposes Kodak T-Max 400 B/W negative film. Timing for these photographs is controlled by a solid state time delay relay. This device starts the Nikon motor drive 0.9 seconds after the Hycam camera, about 0.1 second before the test cell is depressurized. Due to the delay in the motor drive, first image recorded by the Nikon occurs about 0.2 seconds after depressurization of the test cell. At this point in the experiment, the activity in the test cell has slowed sufficiently for the photographs to be essentially free of blurs.

Only the 35 mm still photography have been conducted for experiments FEB20-3X, FEB21-1, FEB23-4, FEB23-5, and MAR4-2. Since the low framing rate of the Nikon camera could produce uncertainties regarding the processes being photographed, a shuttered video camera is used when interpreting the photographs from these experiments. These video footages are compared to footages of the wide-angle high-speed motion picture experiments due to the poor resolution of the images. Otherwise, the videotapes have not been used for scientific purposes in this study.

2.4.3 Close-up photography of 1g experiments. Experiments FEB27-3, FEB28-2, and FEB28-3 have been conducted to produce close-up motion pictures of the processes observed in the Series 1 experiments. Close-up photography is achieved by placing the Hycam camera 0.5 meter from the test cell, and the image is magnified with a Nikon 85 mm f/2 lens mounted on a 4 cm extension tube.[18] This arrangement produces a field of view which covers a 5 cm section of the test cell and 0.1 mm features can be resolved. The light sources are arranged closer to the test cell to concentrate the light in a smaller area

[18] This extension is obtained using a 1 cm extension tube and a F-C lens mount adapter.

(Figure 2.11). The illumination is sufficient for exposing Eastman 7222 film, pushed to 400 ASA, at 5000 frames per second. Due to the higher film speed, 48 feet of the film is expended during acceleration, and 400 ms of the experiment can be filmed with a 100 foot roll of film.

The test cell used in the close-up photography is equipped with a flat glass panel to reduce glare and refraction. The sealed space between a flat panel and the Pyrex pipe is filled with glycerol, which has an index of refraction close to glass, in order to eliminate internal reflections. Since the flat panel is fitted to a 15 cm long pipe section, another 15 cm pipe section is added between it and the service assembly. This arrangement maintains the distance between the particles and the test cell exit found in the wide-angle photography experiments. In order to film a complete experiment, the duration of the experiment is shortened by reducing the initial depth of particles (h_1) to 9 cm from 21.5 cm used in the earlier motion picture experiments.

2.4.4 High-speed photography in the centrifuge. Experiments JUL7-5 and JUL7-7 are experiments involving the rapid vaporization of R12 at 100g and 10g, respectively, using a 47 cm test cell. High-speed motion pictures of these experiments have been filmed with a Fastax 16 mm, rotating prism camera with a 25 mm lens. The particular camera has been modified to alleviate problems with the Coriolis force acting on the film. As shown in Figure 2.12, the camera is mounted near the centrifuge axis to minimize the effects of rotation. A flat mirror is used to reflect the image of the test cell to the camera via a periscope adjacent to the camera. The camera is powered by 65 VAC using a variable step-down transformer. The camera is allowed to accelerate for 1 second before compressed air is supplied to the pneumatic cylinder which releases the diaphragm cutter.[19] Total time between powering up the camera and the test cell depressurization is approximately 1.25 seconds. This delay allows acceleration of the framing rate to over 1000 per second. Since

[19] A solid state time delay relay in the camera electrical supply actuates a solenoid valve.

the film speed is not regulated by the camera, a 1 kHz LED blinker inside the camera is used to mark the film at 1 ms intervals.

The test cell is illuminated by a single 1000 watt tungsten halogen lamp mounted in a Berkeley Colortran 104-051 fixture. Since the illumination axis and the photographic axis are close together, the light reaches the test cell through the same flat mirror used to reflect the image toward the camera. The periscope is used to offset the axis of the illumination as much as possible from the optical axis of the camera within the confines of the centrifuge; this minimizes direct reflection of the light by the glass sides of the test cell. The illumination requires the lens aperture to be set at f/2.8 for exposing Eastman 7222 B/W negative film, pushed to 400 ASA during processing.

2.5 Summary

The test conditions and the instrumentation used in the experiments conducted for this study are summarized in Table 2.3 below. *Run No.* designates an experiment by its date and order. The particle diameter is given in millimeters in the next column. *RPM* is the rotational speed of the centrifuge in revolutions per minute; zero is the normal gravitational condition, 291 is approximately 100g, and 101 is approximately 10g. Reservoir pressure is *P-Res*, and the vapor pressure of the test fluid is *P-Vap*. h_0 is the depth of the test cell cavity, h_1 is the initial depth of the particles, and h_2 is the final depth of the particles. *Cat* refers to the experiment category used in a later discussion. *Press. Data* is the pressure data recorded by the oscilloscope; B is the base pressure and E is the exit pressure. *Photo* refers to the type of photography conducted in the experiment: 16 mm motion picture, 35 mm still photography, or both.

Table 2.3: Experimental conditions and instrumentation.

	Run No.	Test Fluid	RPM	P-Res.	P-Vap.	h0	h1	h2	Cat.	Press.	Photo.	Comments
	Particle Dia			(bar)	(bar)	(cm)	(cm)	(cm)		Data		
	1989 Experiments:											
1	JUN2-9	R12, 0.5	214.0	1.0	6.53	28.5	2.0	1.2		B/E		Nicolet: Low sampling rate.
2	JUN4-11	R12, 0.5	160.0	1.0	7.94	47.0	14.6	3.5	4	B/E		Premature diaphragm rupture.
3	JUN5-2	R12, 0.5	187.0	1.0	6.81	47.0	13.5	4.7	4	B/E		Premature diaphragm rupture.
4	JUN5-3	R12, 0.5	292.0	1.0	6.72	47.0	13.5	6.8	4	B/E		OK (Evaluation run)
5	JUN5-4	R12, 0.5	160.0	1.0	6.74	47.0	13.5	4.5	4	B/E		Premature diaphragm rupture.
6	JUN5-5	R12, 0.5	0.0	1.0	6.81	47.0	13.6	0.1		B/E		Centrifuge off.
7	JUN5-10	R12, 0.5	293.8	1.0	7.25	30.7	6.7	3.7	4	B/E		OK (Evaluation run)
8	JUN5-11	R12, 0.5	289.7	1.0	7.27	44.7	12.1	6.6	4	B/E		OK (Evaluation run)
9	JUN7-2x	R12, 0.5	101.0	1.0	7.17	44.7	21.4	2.2	4	B/E		Repeated run (glitch in scope)
10	JUN7-3	R12, 0.5	290.8	1.0	7.44	44.7	21.3	6.5	4	B/E		OK
11	JUN7-4	R12, 0.5	291.7	1.0	7.10	44.7	21.5	6.5	4	B/E		OK
12	JUN7-5	R12, 0.5	291.0	1.0	7.26	44.7	21.4	6.6	4	B/E	16 mm	OK
13	JUN7-6	R12, 0.5	101.0	1.0	7.22	44.7	21.4	2.1	4			Scope did not trigger
14	JUN7-6x	R12, 0.5	101.8	1.0	7.18	44.7	21.3	2.2	4	B/E		OK
15	JUN7-7	R12, 0.5	102.0	1.0	7.33	44.7	21.3	2.2	4	B/E	16 mm	OK
16	JUN8-2	R12, 0.5	290.2	1.0	7.33	44.7	40.4	6.3	4	B/E		OK
17	JUN8-3	R12, 0.5	289.2	1.0	7.33	44.7	30.0	5.8	4	B/E		Premature diaphragm rupture.
18	JUN8-4	R12, 0.5	292.0	1.0	7.31	44.7	6.7	4.7		B/E		OK
19	JUN8-5	R12, 0.5	102.5	1.0	7.29	44.7	40.4	2.1	4	B/E		OK
20	JUN8-6	R12, 0.5	61.0	1.0	7.25	44.7	30.2	0.9	4	B/E		Premature diaphragm rupture.
21	JUN8-7	R12, 0.5	292.0	1.0	7.22	44.7	3.2	2.8		B/E		Scope: 50 kHz sampling rate
22	JUN8-8	R12, 0.5	102.0	1.0	7.08	44.7	3.2	1.1		B/E		OK
23	JUN9-2	R114, 0.5	290.8	1.0	2.21	47.0	13.5	12.2		B/E		No R113 (Evaluation run)
24	JUN9-3	R114, 0.5	102.2	1.0	2.22	47.0	13.6	2.8		B/E		No R113 (Evaluation run)
25	JUN9-4	R114, 0.5	0.0	1.0	2.22	47.0	14.7	8.5		B/E		Bad diaphragm (50% open)
26	JUN9-5	R114, 0.5	0.0	1.0	2.22	47.0	13.5	9.8		B/E		Bad diaphragm (50% open)
27	JUN9-6	R114, 0.5	101.6	1.0	2.22	47.0	9.8	6.5	1	B/E		OK
28	JUN9-7	R114, 0.5	0.0	1.0	2.22	47.0	6.5	3.9	1	B/E		OK
29	JUN9-8	R114, 0.5	0.0	1.0	2.43	44.7	3.9	1.4	1	B/E		OK
30	JUN9-9	R114, 0.5	290.3	1.0	2.01	44.7	21.4	21.1		B/E		Chilled liquid remained.
31	JUN9-10	R114, 0.5	0.0	1.0	2.15	44.7	21.3	2.6	1	B/E		OK
32	JUN9-11x	R114, 0.5	101.4	1.0	2.22	44.7	21.3	5.0		B/E		Repeated run (bad diaphragm)
33	JUN9-12	R114, 0.5	101.8	1.0	2.22	44.7	21.3	5.5	1	B/E		Scope: 10 kHz sampling rate
34	JUN9-13	R114, 0.5	101.7	1.0	2.22	44.7	30.0	8.1		B/E		Bad diaphragm (50% open)
35	JUN9-14	R114, 0.5	101.3	1.0	2.22	44.7	30.0	8.4		B/E		Bad diaphragm (50% open)
36	JUN9-15	R114, 0.5	101.3	1.0	2.22	44.7	30.0	12.3		B/E		Bad diaphragm (25% open)
37	JUN9-17	R114, 0.5	0.0	1.0	2.22	44.7	21.3	1.8	1	B/E		Bad diaphragm (leaks)
38	JUN9-18	R114, 0.5	289.3	1.0	2.22	44.7	24.6	23.9		B/E		Chilled liquid remained.
39	JUL26-1	R114, 0.5	0.0	1.0	2.43	45.0	21.8	1.1	1			OK; Confirmation of results
40	JUL26-2	R114, 1.0	0.0	1.0	2.43	47.2	22.4	3.3	3			Bad diaphragm (50% open)
41	JUL27-1	R114, 1.0	0.0	1.0	2.43	44.0	38.7	3.4	3			1 mm particle result

	Run No.	Test Fluid	RPM	P-Res.	P-Vap.	h0	h1	h2	Cat.	Press.	Photo.	Comments
	Particle Dia			(bar)	(bar)	(cm)	(cm)	(cm)		Data		
	1990 Experiments:											
42	JAN17-5	R114, 0.5	0.0	1.0	2.00	43.9	22.1	2.2	2			Inadvertent diaphragm rupture.
43	JAN17-5x	R114, 0.5	0.0	1.0	2.07	43.9	22.1	2.2	2	B/E		OK (Evaluation run)
44	JAN17-6	R114, 0.5	0.0	1.0	2.43	43.9	22.1	2.4	2	B/E		OK (Evaluation run)
45	JAN17-7	R114, 0.5	0.0	1.0	2.43	43.9	22.1	2.3	2	B/E		OK (Evaluation run)
46	JAN18-2	R114, 0.5	0.0	1.0	2.42	43.9	22.1	2.4	2	B/E		OK (Evaluation run)
47	JAN18-3	R114, 0.5	0.0	1.0	2.43	43.9	22.1	2.3	2	B/E		OK (Evaluation run)
48	JAN18-4	R114, 0.5	0.0	1.0	2.43	43.9	22.1	1.1	2	B/E		OK (Evaluation run)
49	JAN18-5	R114, 0.5	0.0	0.6	2.43	43.9	22.1	1.9	2	B/E		OK (Evaluation run)
50	JAN19-2	R114, 0.5	0.0	0.6	2.22	43.9	22.1	3.2	2			Bad diaphragm (50% open)
51	JAN19-2x	R114, 0.5	0.0	0.6	2.11	43.9	22.1	2.1	2	B/E		Bad diaphragm (25% open)
52	JAN19-3	R114, 0.5	0.0	0.6	2.43	43.9	22.1	1.6	2			Scope did not trigger
53	JAN19-3x	R114, 0.5	0.0	0.6	2.26	43.9	22.1	1.5	2	B/E		OK (Evaluation run)
54	JAN22-1	R114, 0.5	0.0	1.0	2.43	47.0	15.5	1.9	2	B/E		No R113 (Evaluation run)
55	JAN22-2	R114, 0.5	0.0	0.6	2.13	47.0	15.5	1.7	2	B/E		No R113 (Evaluation run)
56	JAN22-3	R114, 0.5	0.0	0.0	2.47	47.0	15.5	1.4		E		No R113 (Evaluation run)
57	JAN22-4	R114, 0.5	0.0	1.5	2.60	47.0	22.1	20.0		B/E		No R113 (Evaluation run)
58	JAN25-3	R114, 0.5	0.0	1.4	2.64	43.9	31.8	6.1		B/E		OK
59	JAN25-4	R114, 0.5	0.0	1.7	2.40	43.5	17.7	18.3		B/E		OK
60	JAN25-5	R114, 0.5	0.0	1.5	2.68	43.9	15.6	11.9				Inadvertent diaphragm rupture.
61	JAN25-7	R114, 0.5	0.0	1.7	2.45	43.9	22.1	20.2		B/E		OK
62	JAN25-8	R114, 0.5	0.0	1.9	2.68	43.9	22.1	22.7		B/E		OK
63	JAN25-9	R114, 0.5	0.0	1.5	2.64	43.9	22.1	5.6		B/E		OK
64	JAN25-10	R114, 0.5	0.0	2.1	2.44	43.9	22.0	22.0		B/E		OK
65	FEB15-2	R114, 0.5	0.0	1.6	2.43	43.5	21.5	21.5		B/E	Both	OK; wide-angle photography
66	FEB20-2	R114, 0.5	0.0	1.4	2.65	44.0	21.5	6.6		B/E	Both	OK; wide-angle photography
67	FEB20-3	R114, 0.5	0.0	1.5	2.64	44.0	21.5	19.9				Premature diaphragm rupture.
68	FEB20-3x	R114, 0.5	0.0	1.5	2.68	44.0	21.5	15.2		B/E	35 mm	16 mm film destroyed.
69	FEB20-4	R114, 0.5	0.0	0.6	2.51	44.0	21.5	1.9	2	B/E	Both	OK; wide-angle photography
70	FEB21-1	R114, 0.5	0.0	2.1	2.49	44.0	21.5	21.5		B/E	35 mm	OK; videotaped
71	FEB22-2	R12, 0.5	0.0	0.6	6.13	44.0	21.5	1.1	5	B/E		OK; new test fluid
72	FEB22-3	R12, 0.5	0.0	1.0	6.77	44.0	21.5	1.4	5	B/E	Both	OK; wide-angle photography
73	FEB22-4	R12, 0.5	0.0	1.4	6.60	44.0	21.5	1.1	5	B/E		OK
74	FEB23-2	R12, 0.5	0.0	2.8	6.72	44.0	21.5	2.0		B/E		OK; videotaped
75	FEB23-3	R12, 0.5	0.0	3.1	6.76	44.0	21.5	2.4		B/E	Both	OK; wide-angle photography
76	FEB23-4	R12, 0.5	0.0	2.1	6.53	44.0	21.8	1.3	5	B/E	35 mm	OK
77	FEB23-5	R12, 0.5	0.0	1.0	6.76	44.0	21.5	0.9	5	B/E	35 mm	OK; videotaped
78	FEB23-6	R12, 0.5	0.0	1.0	6.53	44.0	5.1	0.5		B/E		OK
79	FEB23-7	R12, 0.5	0.0	1.0	6.71	25.9	17.6	0.9	5	E		OK; short test cell.
80	FEB27-3	R12, 0.5	0.0	1.0	6.65	29.6	8.9	0.8	5	B/E	16 mm	OK; close-up photography
81	FEB28-2	R114, 0.5	0.0	1.6	2.79	30.1	9.0	2.8		B/E	16 mm	OK; close-up photography
82	FEB28-3	R114, 0.5	0.0	0.6	2.67	30.1	9.0	1.1	2	B/E	16 mm	OK; close-up photography
83	MAR4-2	R114, 0.5	0.0	1.6	2.64	44.0	40.0	8.4		B/E	35 mm	OK; wide-angle photography
84	MAR4-3	R114, 1.0	0.0	1.6	2.71	44.0	40.0	11.5		B/E		OK; larger particles
85	MAR4-4	R114, Mix	0.0	1.6	2.64	44.0	40.0	7.9		B/E		OK; bidisperse particles
86	MAR4-5	R114, Sand	0.0	1.6	2.64	44.0	40.0	11.4		B/E		Sand not saturated w/liquid.
87	MAR20-3	R114, 0.5	0.0	1.0	2.53	44.0	35.7	1.1	2	B/E		OK
88	MAR20-4	R114, 0.5	0.0	1.0	2.70	44.0	26.4	1.9	2	B/E		OK
89	MAR20-5	R114, 0.5	0.0	1.0	2.63	44.0	8.6	1.3	2	B/E		OK
90	MAR20-6	R12, 0.5	0.0	1.0	6.59	44.0	40.0	1.1	5	B/E		OK
91	MAR20-7	R12, 0.5	0.0	1.0	6.76	44.0	30.0	0.9	5	B/E		OK
92	MAR20-8	R12, 0.5	0.0	1.0	6.76	44.0	20.4	0.9	5	B/E		OK

	Run No.	Test Fluid	RPM	P-Res.	P-Vap.	h0	h1	h2	Cat.	Press.	Photo.	Comments
	Particle Dia			(bar)	(bar)	(cm)	(cm)	(cm)		Data		
	1990 Experiments (cont'd):											
93	MAR20-9	R12, 0.5	0.0	1.0	6.76	44.0	10.0	0.6		B/E		OK
94	MAR20-10	R12, 0.5	0.0	0.0	6.76	44.0	7.5	0.3				Inadvertent diaphragm rupture.
95	MAR20-11	R12, 0.5	0.0	1.0	6.56	44.0	5.0	0.3		B/E		OK
96	MAR20-12	R12, 0.5	0.0	1.0	6.69	44.0	2.5	0.1		B/E		OK(?); R113 and R12 mixed?
97	APR5-1	R12, 0.5	0.0	1.0	6.31	89.6	21.6	1.8	5	B/E		OK; longest test cell.
98	APR5-3	R12, 0.5	0.0	1.0	6.63	89.6	21.5	1.9	5	B/E		OK; longest test cell.
99	APR5-5	R12, 0.5	0.0	1.0	6.68	59.2	21.8	1.3	5	B/E		OK; long test cell.
100	APR5-6	R12, 0.5	0.0	1.0	6.69	59.2	21.5	1.0	5	B/E		OK; long test cell.
101	APR5-7	R12, 0.5	0.0	1.0	6.63	24.0	21.4	0.7	5	E		Ok; short test cell.
102	JUN7'-3	R12, 0.5	0.0	1.0	6.7	13.2	7.4	-		E		OK; 500 kHz sampling rate
103	JUN7'-4	R12, 0.5	0.0	1.0	6.7	13.2	7.8	-		E		OK; 1 MHz sampling rate
104	JUN7'-5	R12, 0.5	0.0	1.0	6.7	13.2	9.3	-		E		OK; 2 MHz w/o insulation
105	JUN11-5	R12, 0.5	0.0	1.0	6.7	13.2	9.2	-		E		OK; insulated exit transducer
106	JUN11-7	R12, 0.5	0.0	1.0	6.7	13.2	9.3	-		B/E		OK; insulated exit transducer
107	JUN11-8	R12, 0.5	0.0	1.0	6.7	13.2	9.0	-		B/E		OK; insulated exit transducer
108	JUN26-2	R12, 0.5	0.0	1.0	6.76	13.2	8.0	0.7		B/E		OK; insulated exit transducer
109	JUN26-3	R12, 0.5	0.0	1.0	6.75	13.2	8.5	-		E		OK; insulated exit transducer
110	JUN26-4	R12, 0.5	0.0	1.0	6.69	13.2	9.0	0.5		B/E		OK; insulated exit transducer
111	JUN26-5	R114, 0.5	0.0	1.0	2.62	13.2	9.0	-		B/E		OK; insulated exit transducer
112	JUN26-6	R114, 0.5	0.0	1.0	2.6	13.2	10.0	-		B/E		OK; insulated exit transducer
113	JUN29-1	R114, 0.5	0.0	0.6	2.6	13.2	9.0	-		B/E		OK; insulated exit transducer

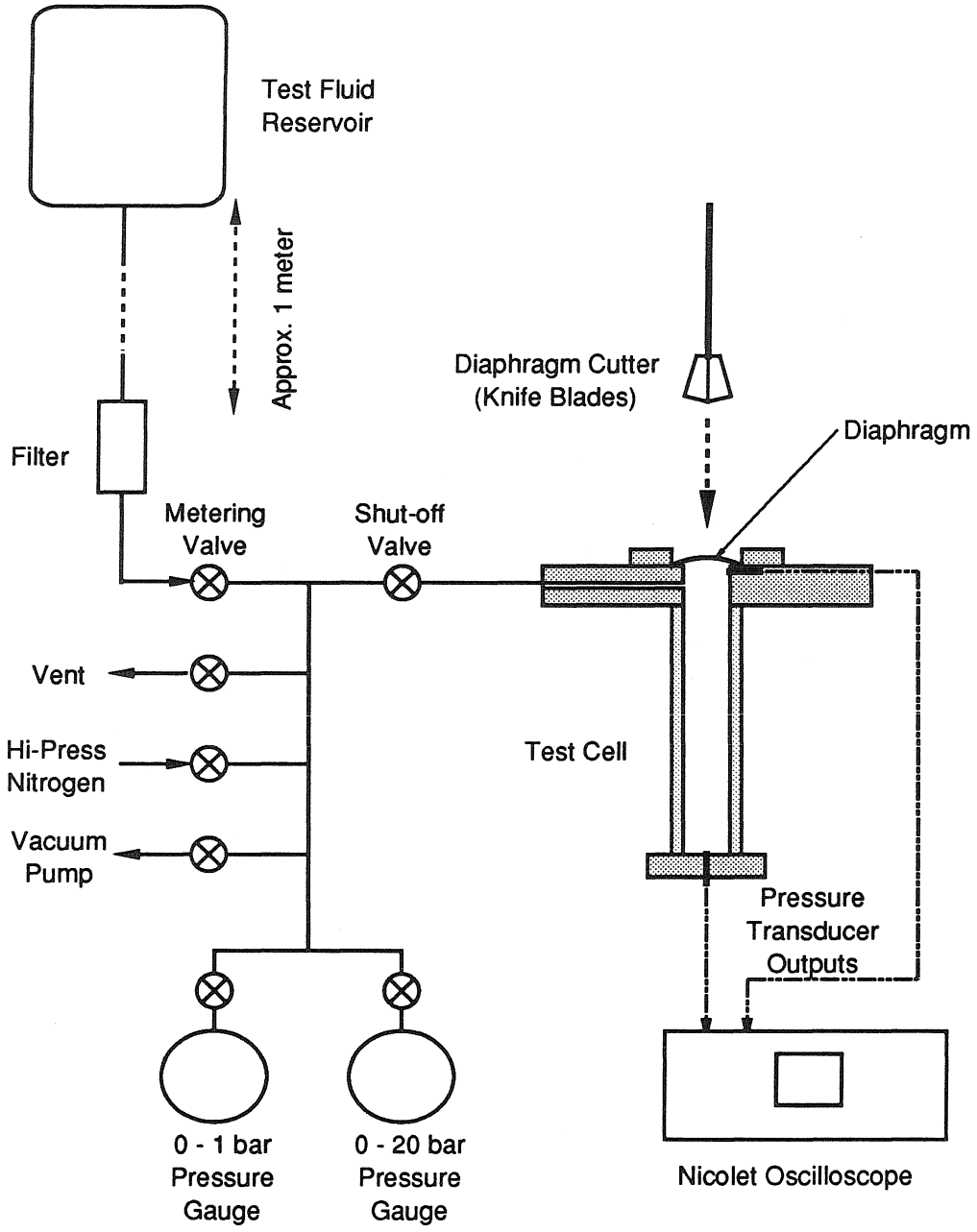

Figure 2.1 Schematic drawing of the basic rapid vaporization apparatus. The equipment used to handle the test fluid, shown to the left of the test cell, is essentially the same for the two appartuses used in the study; the test fluid flows into the test cell by gravity.

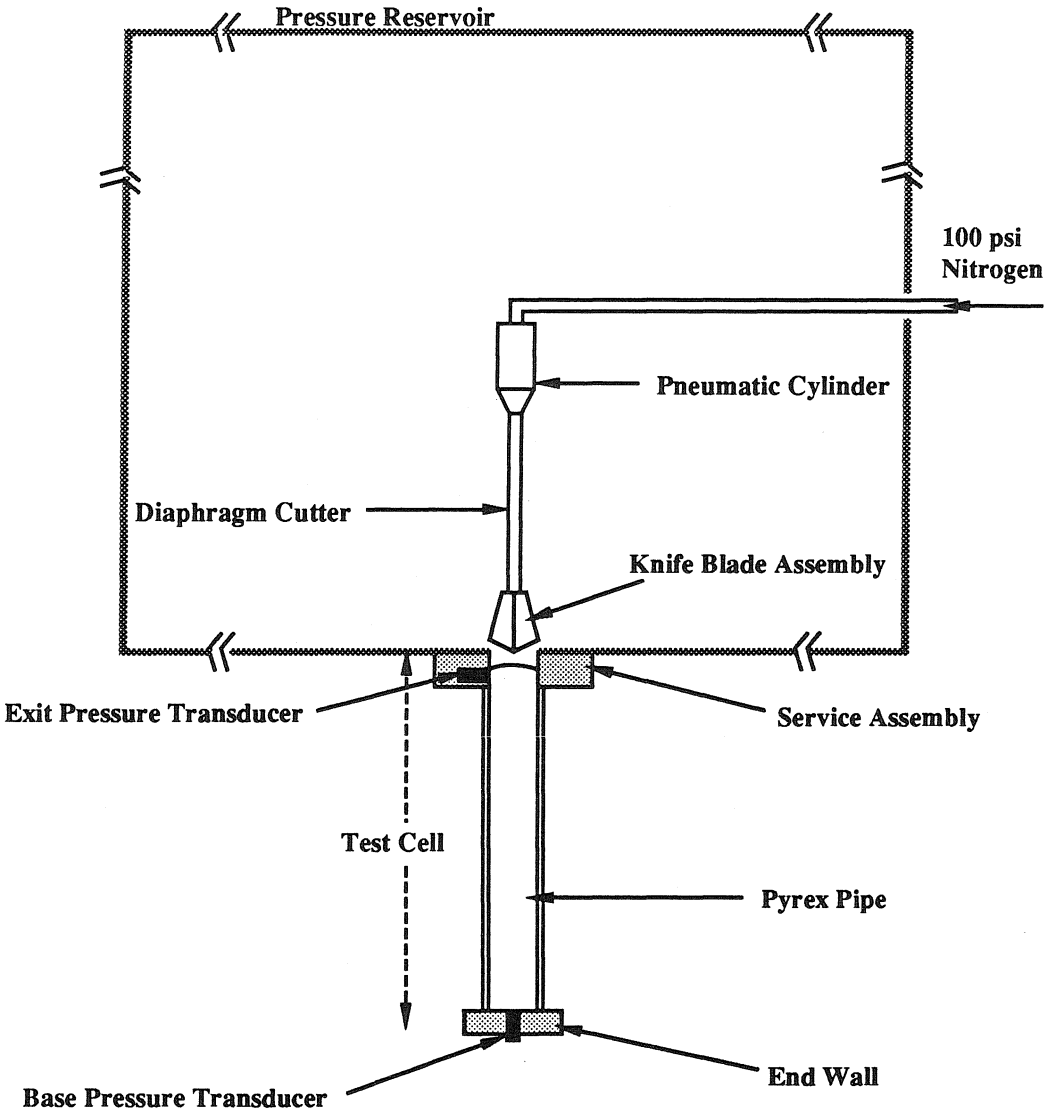

Figure 2.2 Basic layout of the 1g Apparatus. This apparatus was constructed by Hill (1990) for the study of evaporation waves. It is used in the present work to perform experiments at normal gravitational conditions. The pressure downstream of the test cell can be varied with this apparatus. See Figure 2.4 for a detailed drawing of the test cell.

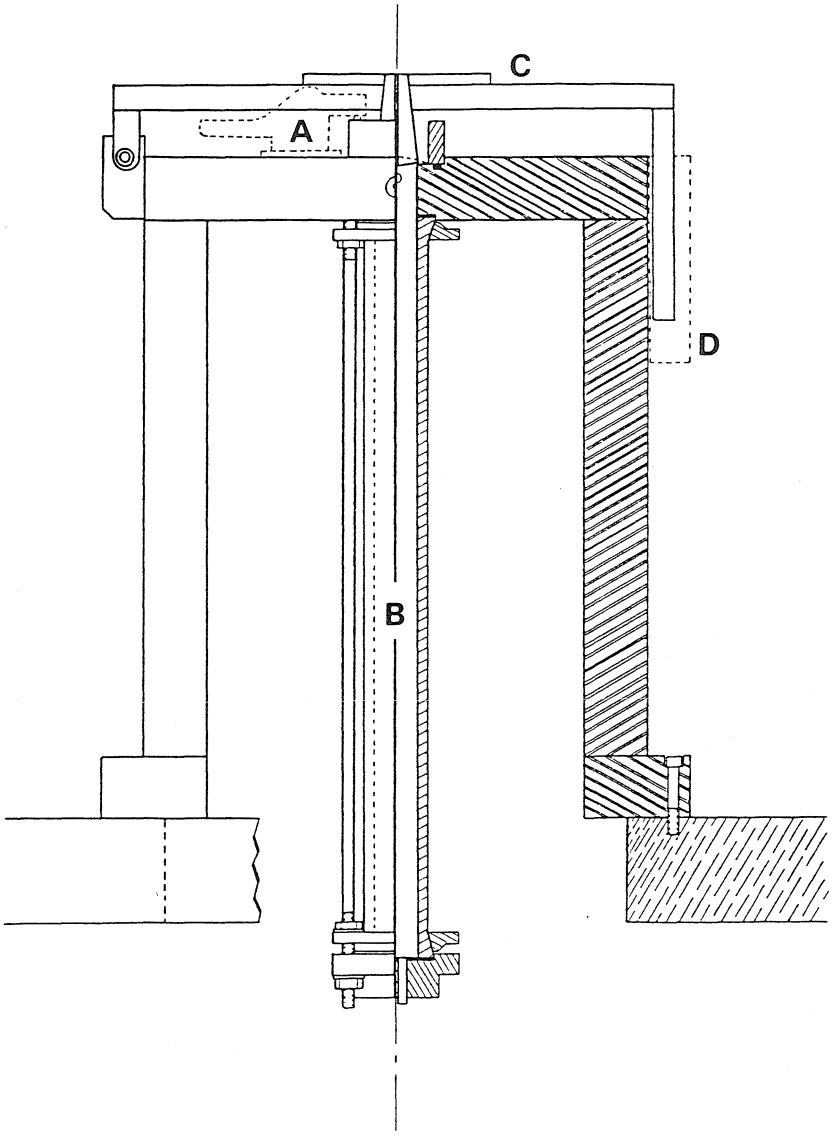

Figure 2.3 Partial cross-section of the Hi-g Apparatus. "A" is the outline of one of two Destaco clamps used to hold the diaphragm sealing the test cell (B). "C" is the arm of the diaphragm cutter which pivots about a bearing on the left end. "D" is the outline of the diaphragm cutter release mechanism. The interior geometry of the test cell is identical to that used by Hill (1990).

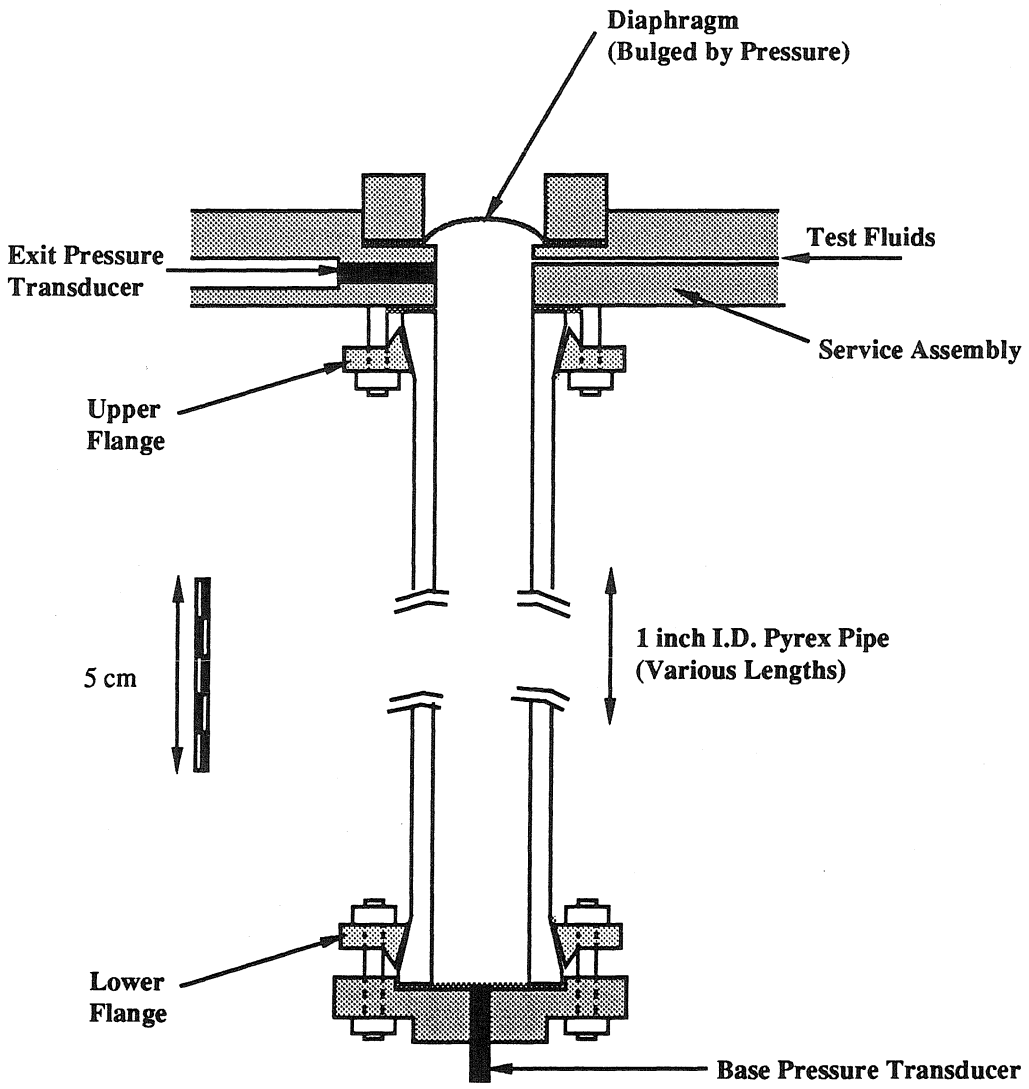

Figure 2.4 Cross-section of the test cell used in the rapid vaporization experiments. The transparent walls of the Pyrex pipe facilitate photography of the phenomena occurring inside.

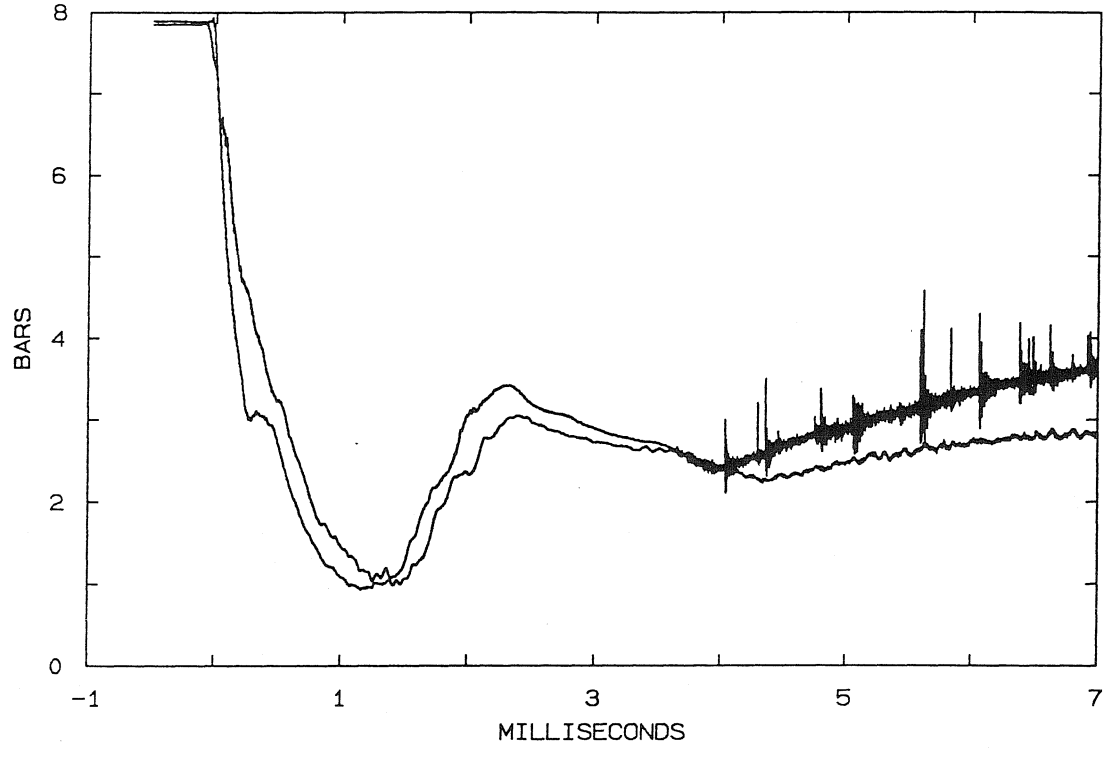

Figure 2.5 Examples of exit pressure measurements. The time span shown in these plots are much shorter than typical experiment duration; data sampling rate is 2 MHz. In one trace, that of experiment JUN7(90)-5, the transient responses to particle impacts is recorded after 4 ms. The other trace, that of JUN11(90)-5, is the signal for an identical experiment obtained from a transducer with Neoprene insulation. Insulation damps out the particle impacts, and it may also be responsible for the 0.2 ms delay in the signal.

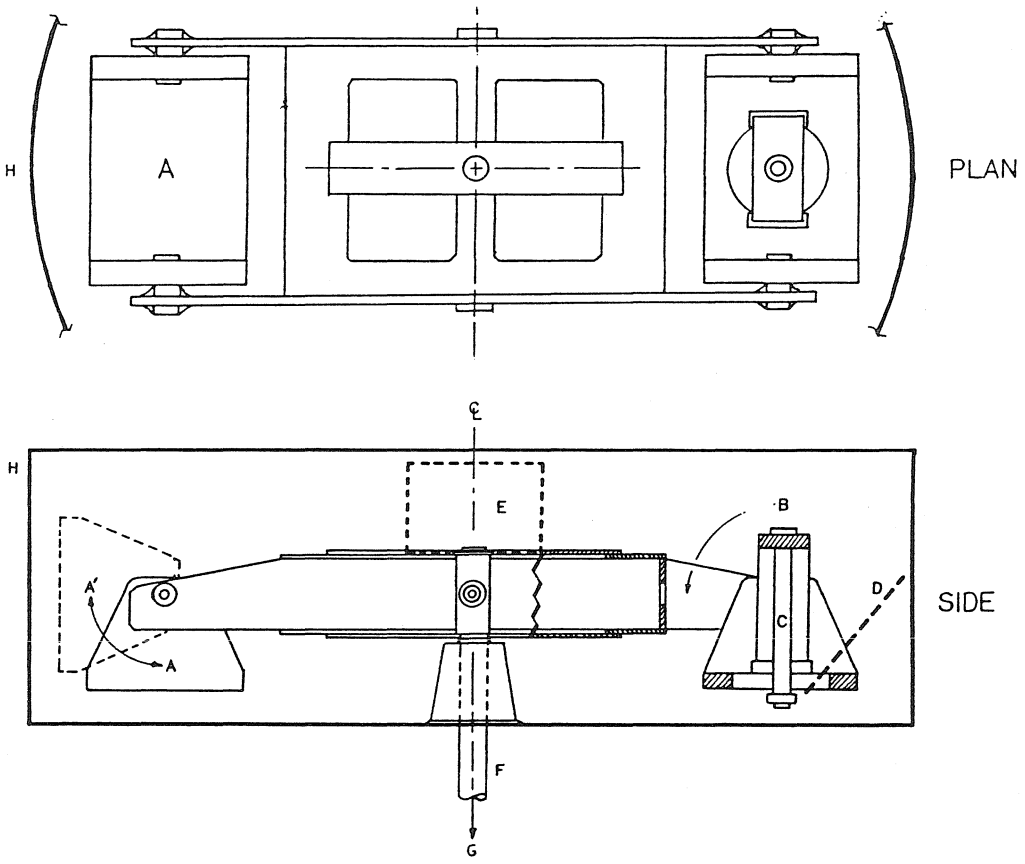

Figure 2.6 Arrangement of equipment in the Genisco centrifuge. Venting mechanism (B) and the test cell (C) are mounted on a swinging cradle (A) at the end of the rotor. During operation, the cradle swings out to position A'. In this position, the mirror (outlined at D) allows photography by cameras at E (see Figure 2.12 for details). The hollow driveshaft (F) houses electrical connections to the sliprings (G). The moving components are completely enclosed by a housing (H).

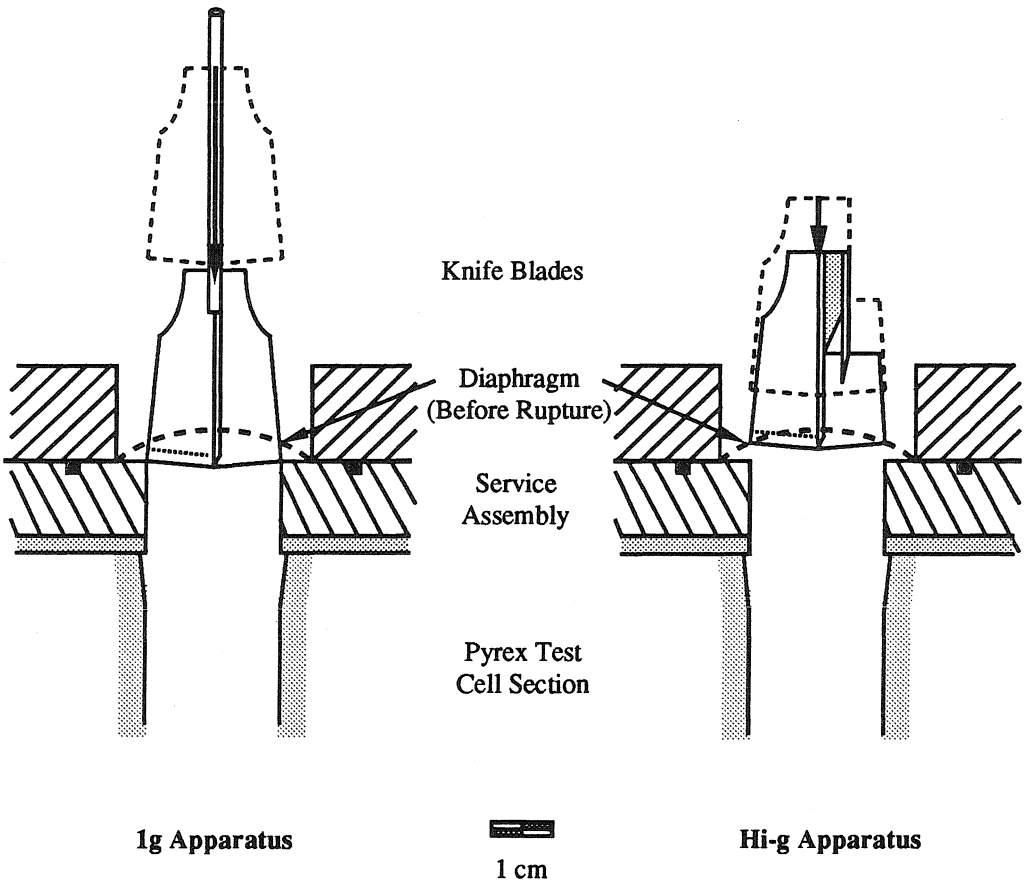

Figure 2.7 Positions of the knife blades used to rupture the diaphragm. Solid lines show the knife blades in the position after they are driven into the diaphragm; light dashed lines outline their original positions. The downward arrows show the movement of the knife blades. Heavy dashed line outlines the diaphragm sealing a pressurized test cell.

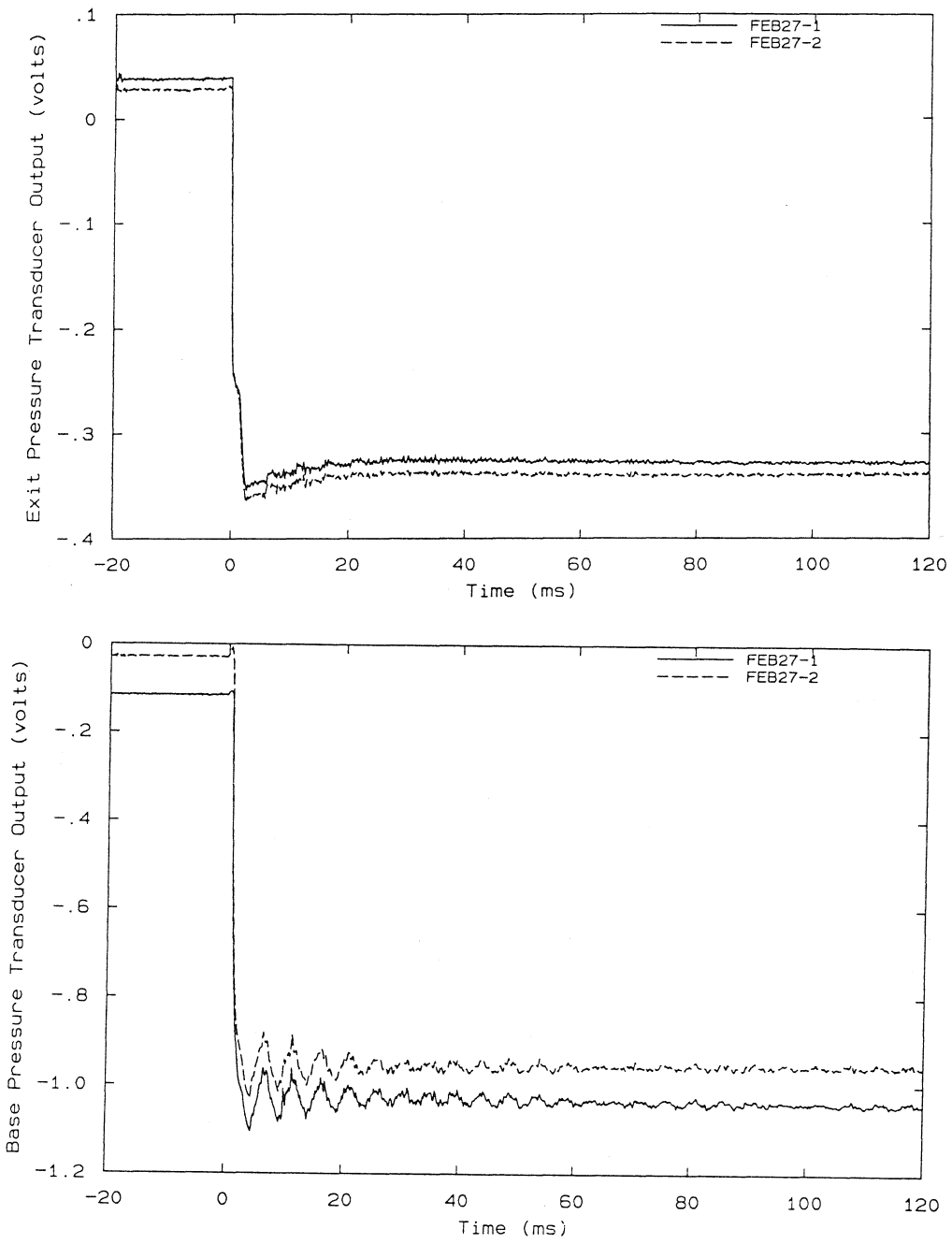

Figure 2.8 Examples of signals used to calibrate the pressure transducers. Nitrogen at 100 psig is rapidly vented into the atmosphere; the responses of the exit transducer is shown above the responses of the transducer at the bottom of the test cell. Dashed lines show the responses obtained with a 3 cm layer of R113 and particles in the test cell. The small step in the pressure drop at the exit is due to choked flow. Test cell cavity is 32.6 cm long when empty. (Calibration trials FEB27-1 and FEB27-2).

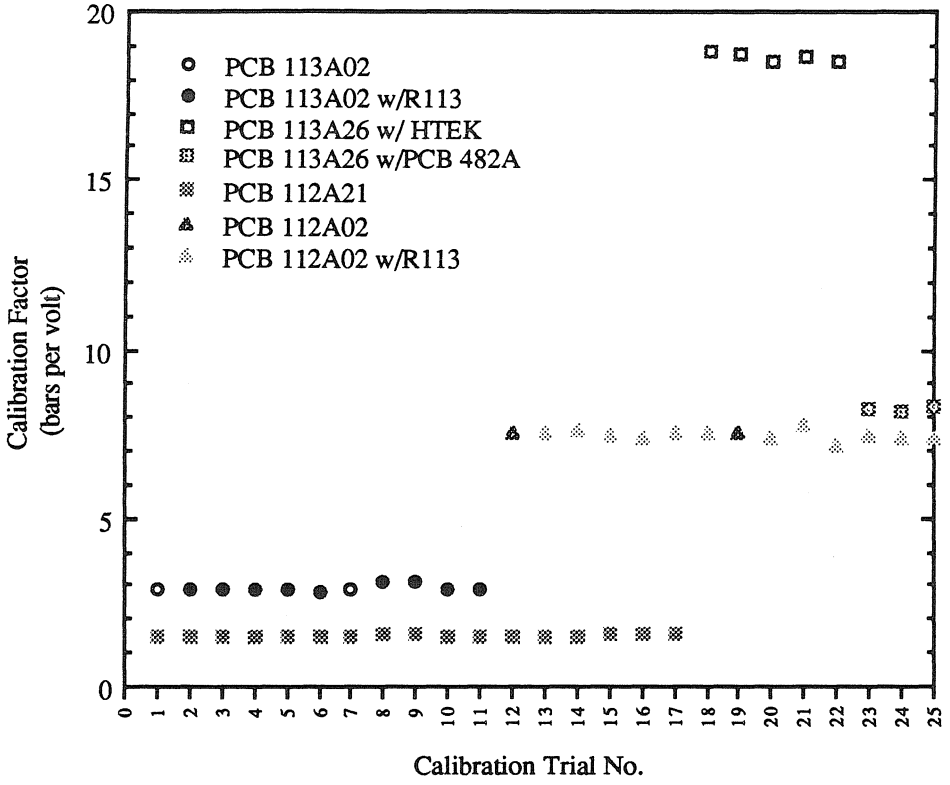

Figure 2.9 Pressure transducer calibrations. Calibration factors are determined before each series of experiments using signals produced by the rapid depressurization of nitrogen (see Figure 2.8). Legend for the trial numbers are given below with the drop in N_2 pressure used for calibration.

Trial No.	1	2	3	4	5	6	7
Run No.	JUN2-2	JUN2-3	JUN2-4	JUN2-5	JUN2-7	JUN2-8	JUN4-7
N_2 Press.	5.7 bar	5.5 bar	5.4 bar	5.4 bar	5.4 bar	5.3 bar	5.5 bar

Trial No.	8	9	10	11	12	13	14
Run no.	JUN5-7	JUN5-8	JUN7-1	JUN8-1	JAN25-1	JAN25-2	JAN25-6
N_2 Press.	5.5 bar	5.5 bar	5.4 bar	5.5 bar	6.9 bar	6.9 bar	5.9 bar

Trial No.	15	16	17	18	19	20	21
Run No.	FEB15-1	FEB20-1	FEB22-1	FEB23-1	FEB27-1	FEB27-2	FEB28-1
N_2 Press.	5.9 bar	6.9 bar	6.9 bar	6.9 bar	6.9 bar	6.9 bar	6.9 bar

Trial No.	22	23	24	25
Run No.	MAR4-1	MAR20-1	MAR20-2	APR5-2
N_2 Press.	6.9 bar	3.8 bar	4.1 bar	6.9 bar

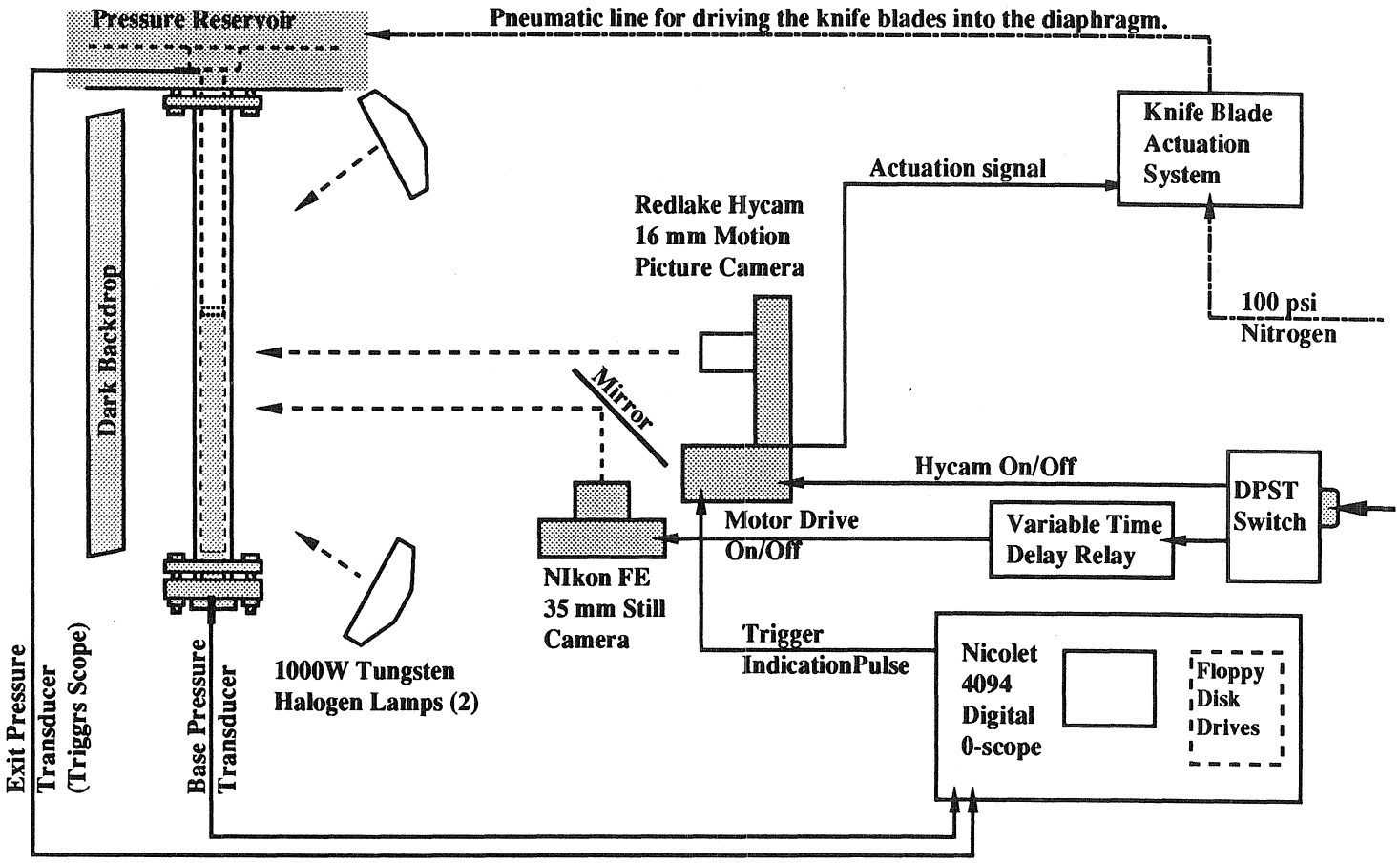

Figure 2.10 Equipment used for wide-angle filming (experiments FEB15-2, FEB20-2, FEB20-4, FEB22-3 and FEB23-3). The DPST switch to the right begins the photographic sequence necessary to achieve proper camera speed before depressurizing the test cell. The variable time dealy relay determines when the first 35 mm photograph is taken.

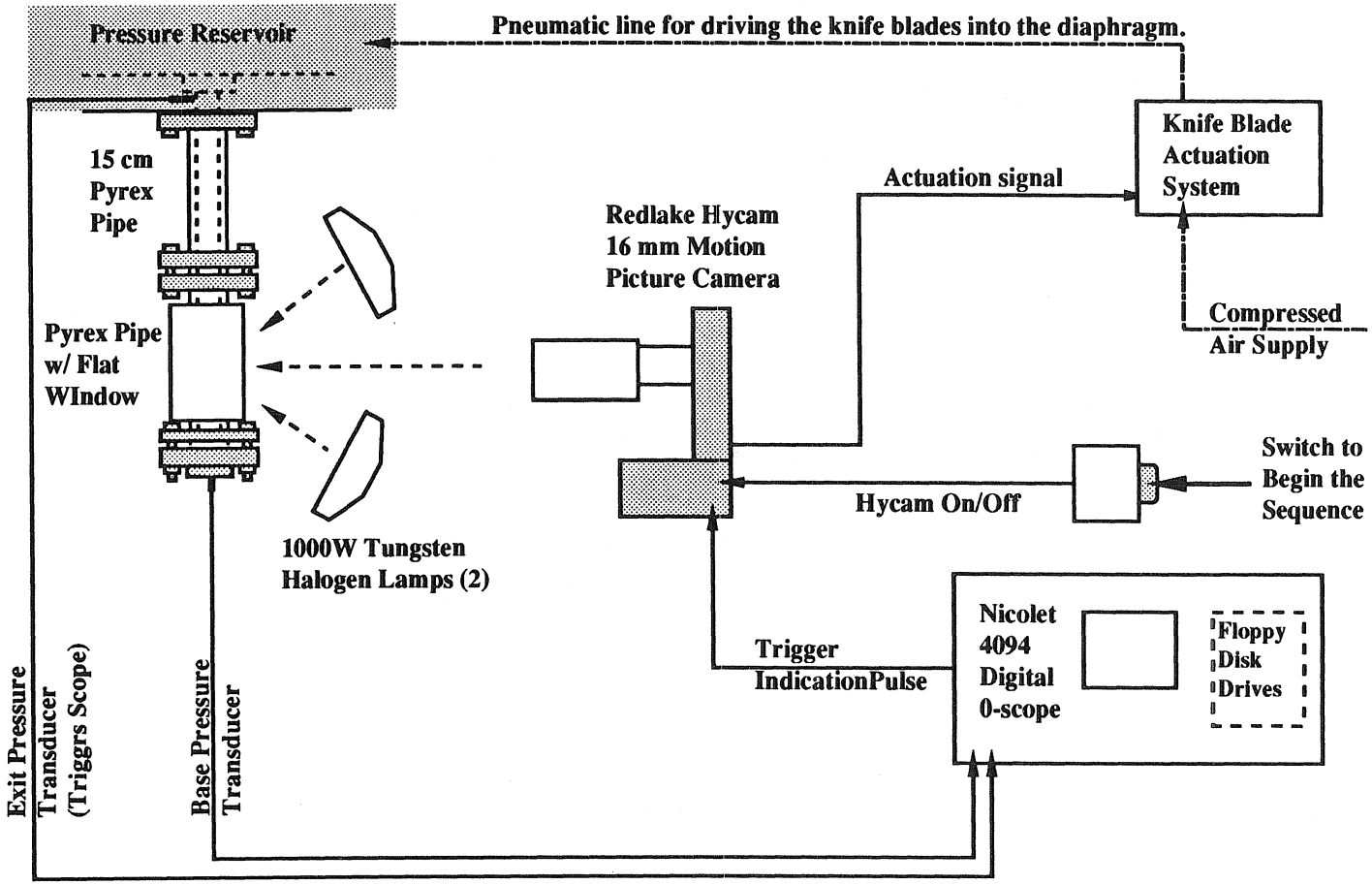

Figure 2.11 Equipment used for close-up photography (experiments FEB27-3, FEB28-2, and FEB28-3). The switch to the right begins the photographic sequence which delays the depressurization of the test cell until the proper film speed has been achieved. The rectangular enclosure on the test cell incorporates a flat glass panel and a dark backdrop.

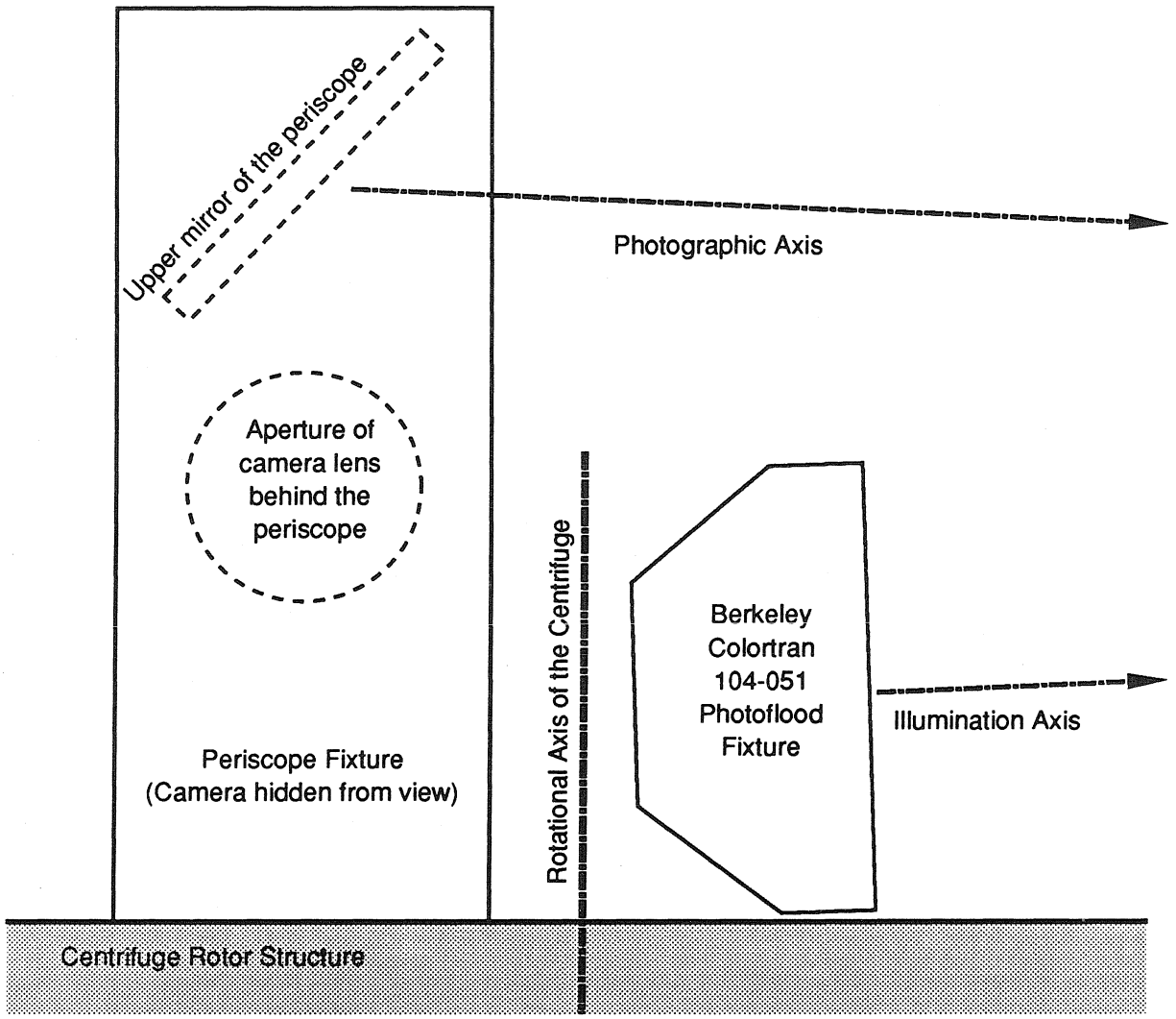

Figure 2.12 Equipment used for filming experiments in the centrifuge. This figure represents "E" in Figure 2.6. A two-mirror periscope is used so the camera and the light source can be bolted directly to the rotor. The photographic and illumination axes intersect at the test cell when the cradle is rotated into position by the centrifugal force.

Chapter 3
Experimental Results

The results of rapid vaporization experiments described in Chapter 2 are presented in this chapter. An initial overview of the experiment divides it into three phases: the process of initiating particle transport (start-up), particle expulsion, and process termination (Figure 3.1). The quantity of particles expelled from the test cell during an experiment is largely determined by the type of particle transport produced by the vaporization process, and it is determined by independent variables of the experiment.

3.1 Overview of the Phases of an Experiment

3.1.1 Start-up. The start-up phase occurs immediately after the test cell is vented; it begins when the diaphragm ruptures and ends when the first particle is expelled. Figure 3.2 shows the start-up period of experiment FEB22-3 and is typical for experiments conducted with R12. The pressure trace of the start-up period is presented as Figure 3.3. Upon diaphragm rupture, the test cell is depressurized by a rarefaction wave which propagates into the test cell. The wave amplitude is limited by choking at the exit; this is indicated by a short plateau in the exit pressure. Condensation of vapor by the sudden reduction in pressure is also visible in some of the photographs. When the head of the initial rarefaction wave reaches the liquid surface above the particles, waves are transmitted and reflected by the surface. The transmitted rarefaction wave depressurizes the liquid and particles. Since the acoustic impedance of the liquid is 130 times that of the vapor, a rarefaction wave is reflected back towards the exit. The subsequent arrival of the wave at the exit causes the flow to become unchoked, which causes the exit pressure to drop from the plateau level.

The transmitted rarefaction wave lowers the pressure on the test fluid below its vapor pressure, causing the liquid to become superheated[1] (Figure 3.2, t = 1 ms). Since the

[1] Rapid drop in pressure is necessary for heat transfer to be negligible, allowing the process to be modelled as an adiabatic process (see Chapter 4).

liquid and the particles are virtually incompressible, the material below the liquid surface is depressurized very rapidly by the transmitted rarefaction wave.[2] The formation of vapor bubbles can be observed (Figure 3.2, t = 2 ms), especially at the top of the particle bed. The bubbles appear white in the photograph since they increase the vapor-liquid interface, thus increasing the amount of reflected light. Discrete nucleation of bubbles is visible lower in the bed; bubbles appear as small reflective patches (Figure 3.2, t = 4 ms). The expansion of vapor released from the bubbles produces an upward multiphase flow of liquid droplets and particles; the contact surface between this multiphase flow and the vapor is visible (Figure 3.2, t = 3 to 4 ms).

A one-dimensional model of the start-up is summarized by an x-t plot which qualitatively shows the development of the particle transport process (Figure 3.4). A small drop in the exit pressure (B in Figure 3.3) coincides with the extrapolated arrival of the upward flow front visible in Figure 3.2 at t = 3 ms. The initial part of this flow consists of droplets, not lofted particles; this is indicated by the appearance of transient signals caused by particle impacts 6.5 ms after the extrapolated arrival of the front (C in Figure 3.3). At the beginning of the flow, the pressure at the bottom of the test cell increases (A in Figure 3.3) as a result of explosive vaporization by the superheated liquid. Thus, the time required by the uppermost particles to travel from the bed to the exit, or the time of flight, is given by the interval between points A and C in Figure 3.3. The time of flight data for experiments conducted with R12 (Figure 3.5) varies approximately linearly with the distance traveled by the uppermost particle, which is equal to the length of the test cell minus the depth of the particles.[3] Table 3.1 gives the mean acceleration and the final speed calculated from the data in Figure 3.5 using the uniform acceleration model presented in Appendix A.

---

[2] The rarefaction wave propagates through the liquid and glass particles at the acoustic velocity which is greater than 500 m/s.

[3] Particle impacts in experiments conducted with R114 do not produce distinct signals necessary for the arrival time of the first particles to be measured.

Table 3.1 Mean acceleration and final speed calculated from Figure 3.5.[4]

"Gravity"[5]	Mean Acceleration	Final Speed
1g	540g	3870 cm/s
80-100g	450g	3070 cm/s

3.1.2 Particle expulsion. Two distinct types of particle transport are observed depending on the reservoir pressure. At low reservoir pressures, explosive vaporization of superheated liquid is limited to the upper layers of the particle bed; this process is called Type 1. At higher reservoir pressures, nucleation and growth of bubbles distributed throughout the particle bed results in a large-scale break-up; this process is called Type 2.

Experiment FEB20-4 shows the characteristics of Type 1 behavior (Figure 3.6). The test fluid is R114 and the test cell is vented to 0.6 bar. Although reflective spots of discrete bubbles can be observed throughout the particle bed, these spots remain in place until they are obscured by a vaporization front. During the experiment, the base pressure is elevated by the expansion of vaporized test fluid which is responsible for the expulsion of particles. The plateau in base pressure above the reservoir level, indicating a sustained momentum flux, shows that the effect of vaporization is sustained for a period during the experiment.

Experiment FEB15-2 shows the break-up of the particle bed associated with Type 2 behavior. In this case, R114 is the test fluid and the test cell is vented to 1.6 bars. In the photographs (Figure 3.7), the reflective bubbles among the particles grow into dark voids spanning the test cell (photographs C and D in Figure 3.7). In this experiment, the base pressure does not rise above the reservoir level; this indicates that the vaporization process lacks the momentum flux observed in FEB20-4 (Figure 3.6). The lack of momentum flux

---

[4] See Appendix 3 for details of the calculations.

[5] The resultant of normal gravitational acceleration and centrifugal acceleration calculated in the test cell. Since the data in Figure 3.5 are obtained with a variety of particle depths, the radial position of the uppermost particle and the centrifugal acceleration on the particle may vary from 80g to 100g.

is apparently related to negligible expulsion of particles which is indicated by the fact that the initial and final particle depths being equal.

The differences in the transport processes are shown by identically filled test cells after they are vented to different pressures. In these experiments, a 45 cm test cell is initially filled to about 50% capacity with particles and test fluid. Experimental results obtained with different test fluids, R12 and R114, are compared by normalizing the reservoir pressure with the vapor pressure of the test fluid. In Figure 3.8, the quantity of particles expelled from the test cell is represented by the decrease in particle depth relative to the initial depth; the plot shows the amount of particles expelled during the experiment being significantly less when the reservoir pressure is greater than a critical level; the critical pressure is about 0.55 times the vapor pressure. The base pressure traces of experiments have the characteristics of a Type 1 process when the reservoir pressure is below the critical level and Type 2 characteristics at higher pressures (Figure 3.9a). Figure 3.9b is a plot of the maximum base pressure following depressurization, normalized by the vapor pressure, corresponding to the experimental data in Figure 3.8. The break in the data profile corresponds to a change in the particle transport process determined by the reservoir pressure. The distance above the unit slope line in Figure 3.9b, which is proportional to the difference between reservoir pressure and the base pressure, is indicative of the pressure drop in the flow out of the test cell. The break in the profile which takes the data closer to the reservoir pressure shows that the pressure drop, or the momentum flux of the flow, is characteristically lower in the Type 2 process than in the Type 1 process.

3.1.3 Process termination. The terminal phase of the experiment begins when the supply of fresh superheated liquid is exhausted and the production of vapor is reduced. The supply of fresh liquid is exhausted when the vaporization process reaches the test cell bottom; at this point, the base pressure begins its decay to the reservoir level. An example of particle motion during the terminal phase is shown in Figure 3.10. Although the base

pressure is elevated for about 50 ms, particles in the test cell begin descending about 120 ms later. The particles observed descending in the test cell are only those which never traveled beyond the test cell; the probability of any particle traveling out of the test cell and returning is small. For this reason, the number of particles found in the test cell after the experiment indicates the number of particles in the test cell when the particle descent begins. In cases where the particles are transported by a Type 2 process, the terminal phase begins immediately after the initial rise in base pressure due to vaporization.

3.2 Types of Transport Processes

3.2.1 Type 1 process. The Type 1 process observed in experiment FEB20-4 (see *3.1.2*) has been reproduced for close-up photography in experiment FEB28-3 (Figure 3.11). The rapid vaporization disrupting the particle matrix (the white area in the photograph) does not have a planar boundary. A rapid change in luminosity occurs over a depth of about 2.5 cm or one test cell diameter.[6] Movements of darkened particles in the motion picture (Figure 3.11b) show the actual disruption of the particle matrix. The data in Figure 3.11b when numerically differentiated, show sequential acceleration of particles by the disruption front (Figure 3.11c). Initiation of particle acceleration at different depths of the particle bed has been used to track the disruption front in order to calculate the mean front speed. The speed of the disruption front obtained by this and other techniques is summarized in Table 3.2.

Table 3.2 Speed of the disruption front in two experiments using R114.*

Measurement	Distance (cm)	Time (ms)	Speed (cm/s)
Interpretation of photographs (Fig 3.6)	4.5 ± 0.3	20	225 ± 15
Duration of sustained pressure (FEB20-4)	21.5	120 ± 10	180 ± 15

* Particles: 0.5 mm Dragonite spheres. Reservoir pressure: 0.6 bar. No centrifugal acceleration.

[6] This interpretation recalls the Plinian eruption model by Sparks (1986) which features a narrow region separating the bubbly magma and the fragmented magma in the volcanic conduit during a Plinian eruption.

Table 3.2 Continued

Measurement	Distance (cm)	Time (ms)	Speed (cm/s)
Duration of sustained pressure (FEB28-3)	9.0	45 ± 5	200 ± 25
Time between the acceleration	1.2 ± 0.05	7 ± 0.5	170 ± 23
of particles (Fig 3.11)	0.8 ± 0.05	5 ± 1.0	160 ± 55

Hill (1990) describes the propagation of an evaporation wave which is essentially a disruption front occurring in nucleate-free superheated liquid. A photograph of this phenomenon (Figure 3.12a) shows a high-speed flow of liquid droplets driven by the rapid vaporization of superheated liquid. The momentum flux generated by this process is responsible for elevating the base pressure (Figure 3.12b). Using high-speed motion pictures of the experiment, Hill showed that the base pressure is sustained at an elevated level during the wave propagation. The end of the sustained pressure occurs when the wave arrives at the bottom of the test cell. Due to the similarities in the pressure profile, Hill's analysis of the evaporation wave has been used as a basis for the present analysis of the disruption front associated with the Type 1 process. However, the speed of the evaporation wave in R114 measured by Hill (c = 21 to 32 cm/s) is significantly lower than the speed of the disruption front (c = 200 cm/s) approximated from the results in Table 3.2. Since the R114 liquid density is 1.46 g/cc and that of the particle bed immersed in R114 is 2.35 g/cc,[7] the difference in mass flux ($\rho_0 c$) is quite significant: 31 to 47 g cm^{-2} s^{-1} for the evaporation wave and 470 g cm^{-2} s^{-1} for the disruption front.

3.2.2 Type 2 process. Conditions identical to that for experiment FEB15-2 (described earlier in *3.1.2*) are used in the close-up photography experiment FEB28-2 (Figure 3.13a). Expansion of material occurring below the field of view is indicated by the upward displacement of particles prior to the disruption of the particle matrix (photographs A and B). Plots of particle position and velocity reveal simultaneous acceleration of particles

[7] Details are discussed in Chapter 4.

located at different levels in the bed (Figures 3.13b,c); the sequential particle acceleration of Type 1 process is not observed.

The oscillations in FEB28-2 base pressure occur at the acoustic reverberation frequency of the test cell filled with R114 vapor.[8] Therefore, the oscillations are believed to indicate the formation of a vapor channel extending the length of the test cell. Such a channel, though it cannot be discerned in the photographs, is believed to be responsible for decreasing the amount of particles expelled by the vapor flow. The oscillation is absent in the pressure trace of experiment FEB15-2. Therefore a vapor channel did not extend to the bottom of the test cell where the pressure transducer is located.

The bubble growth low in the particle bed and the vapor channel development are similar to the break-up of a particle bed caused by gas expanding in the particle matrix (Anilkumar, 1989). As illustrated in Figure 3.14, the phenomenon studied by Anilkumar begins with horizontal fractures forming in the particle bed. As this flow develops, fractures begin to divide into bubble-like structures which grow and deform into elongated regions relatively void of particles, and they are outlined by thin streams of particles. The elongated voids observed by Anilkumar are believed to be analogous to the channels allowing the vapor to escape in a Type 2 process.

3.2.3 Extreme example of Type 2 behavior. In Hill's experiments, the speed of the evaporation wave decreases with increasing reservoir pressure[9]; the speeds measured by Hill converge to null at the *absolute threshold.* When nucleation-free liquid is vented to a pressure between the absolute threshold and the vapor pressure of the test fluid, the resulting vaporization is not explosive and an evaporation wave is not observed. In these

---

[8] Test cell length or the depth of an open cavity, h_0, is 30.1 cm. Sound speed in R114, a, is 117 m/s. Therefore, the frequency of acoustic reverberation in the test cell, $2h_0/a$, should equal 194 Hz. The oscillations in the FEB28-2 are roughly 190 Hz.

[9] Highest wave speeds are observed when the test cell is vented into an evacuated reservoir. For R12, the maximum wave speed is about 0.6 m/s.

experiments, the vaporization of superheated liquid is limited by convective transfer of latent heat.

A situation similar to Hill's non-explosive vaporization of superheated liquid has been observed in the present work when R114 is vented to 0.85 times the vapor pressure. In contrast, the absolute threshold measured by Hill for the same test fluid (R114) is about 0.28 times the vapor pressure. Although depressurization causes bubble nucleation throughout the particle-liquid mixture, the particles remain largely undisturbed (Figure 3.15a). On the videotape and in still photographs, bubbles of vapor are observed moving upward through the particle matrix. The base pressure trace shows acoustic reverberation in the vapor above the particles (Figure 3.15b).

3.2.4 Test fluid volatility and the transport process. Experiments have been conducted with R12, a fluid with a vapor pressure higher than R114, to determine the effect of increased fluid volatility[10]. As shown by Figures 3.16 and 3.17, the characteristics of Type 1 process are observed in experiments with R12 at higher reservoir pressure than R114 experiments discussed earlier. The momentum flux higher than that of R114 is indicated by the higher base pressure plateau observed in experiments with R12 . Higher flux is also indicated by the higher speed of the disruption front produced by the vaporization of R12 (Table 3.3). As expected from the higher momentum flux, the close-up motion picture of an R12 experiment (Figure 3.18) shows higher particle acceleration than that observed in an R114 experiment; the values obtained from the particle motion in the close-up motion pictures are compared in Table 3.4. The higher acceleration and higher speeds indicate that the power of vaporization process[11] increases with the volatility of the test fluid. Particle acceleration also agrees with results obtained earlier for the acceleration of particles by the initial explosive vaporization (Table 3.1).

---

[10] Other properties of these test fluids are very similar (see Table 2.1).

[11] A factor that determines the rate at which thermal energy is transformed into kinetic energy of particles.

Table 3.3 Speed of the disruption front in two experiments using R12*.

Measurement	Distance (cm)	Time (ms)	Speed (cm/s)
Interpretation of photograph (Fig 3.16)	8.3 ± 0.3	20	415 ± 15
Duration of sustained pressure (FEB22-3)	21.5	55 ± 5	390 ± 40
Duration of sustained pressure (FEB27-3)	9.0	23 ± 2	400 ± 40
Time between particle acceleration (Fig 3.18)	1.00 ± 0.05	2.7 ± 0.1	375 ± 25

* Particles: 0.5 mm Dragonite spheres. Reservoir pressure: 1.0 bar. No centrifugal acceleration.

Table 3.4 Acceleration of particles by Type 1 process at 1g.

Experiment	Test Fluid	Acceleration
FEB27-3	R12	500g
FEB28-3	R114	80g

3.2.5 Characteristic result of a Type 1 process. As shown earlier in Figure 3.8, the quantity of particles expelled from the test cell by a Type 1 process is much greater than that by a Type 2 process. Experiments have revealed that the quantity of particles expelled by a Type 1 process with a given test fluid is affected by the initial particle depth and the test cell size. The effects of these factors have been investigated by varying one while keeping the other constant.

The results in Figure 3.19 show that if the initial particle depth is greater than about 10 cm, the initial particle quantity has little effect on the quantity of particles remaining after a Type 1 process at two body force levels.[12] This is in sharp contrast to cases where the reservoir pressure exceeds 0.55 times the vapor pressure and most of the particles are not expelled (Figure 3.8). Therefore, Type 2 process differs from Type 1 in that the initial particle depth influences the final depth because almost no particles are expelled.

[12] The significance of the 10 cm particle depth in this result is yet unclear.

Figure 3.19 also shows that the final depth of particles is greater in experiments conducted at 100g than in identical experiments at 1g. The difference in the final depth reflects the difference in body force restraining the upward trajectory of the particle. As indicated by the greater final depth at 100g, the increasing force decreases the quantity of particles transported out of the test cell. The effect of the body force on particle transport is discussed in section 3.3.

The effect of test cell size on the Type 1 particle transport is shown in experiments conducted with the same initial particle depth in test cells of different lengths (Figure 3.20). The final particle depth increases approximately linearly as the test cell length is increased, thus indicating that the final depth appears to scale with the length of the test cell. Therefore, in subsequent discussions, the depth of the particles will be normalized by the test cell length.

3.2.6 Characteristic results of a Type 2 process. The test cell after a Type 2 process contains an abundance of unvaporized liquid. A mixture of unvaporized liquid and particles forms a slurry-like mixture which coats the interior of the test cell when the reservoir pressure is too high for explosive vaporization to occur (see *3.2.3*). The importance of bubble growth in Type 2 process is indicated by the bubble-like structures preserved in the slurry-like coating (Figure 3.21).

The large-scale bubble growth in the Type 2 particle transport implies that effects of surface tension (σ) and viscosity (μ) important. The effect of large bubbles on a flow is usually characterized by the Bond and the Morton numbers which involve the acceleration of gravity (g) and the densities of fluids (ρ):

$$Bo = \frac{(\rho_{slurry} - \rho_{vapor})\, g\, d_{bubble}^2}{\sigma_{slurry}} \tag{3.1a}$$

$$Mo = \frac{g\, \mu_{slurry}^4}{\rho_{slurry}\, \sigma_{slurry}^3} \tag{3.1b}$$

The Bond number is a ratio of buoyancy to viscosity and the Morton number is the ratio of viscous forces generated by the buoyancy driven motion of the bubble to the surface tension. These parameters are used in the study of two-phase flows dominated by bubbles (Vergniolle & Jaupart, 1986). Quantitative analysis of the slurry has not been conducted for this work. It will be necessary to correctly define σ and μ for the slurry for such an analysis. In addition, since vaporization causes the diameter of the bubbles to increase with time, the parameters are not constant during an experiment and time-dependent analysis will be necessary.

3.3 Factors Affecting the Particle Transport

The effect of test cell length and the initial particle depth on the expulsion of particles are described in *3.2.5*. However, the transport process resulting from the vaporization of superheated liquid is influenced by non-geometrical factors such as the reservoir pressure, the centrifugal acceleration, and the volatility of the liquid.

3.3.1 Effect of reservoir pressure on particle transport process. The reservoir pressure relative to the critical value of 0.62 times the vapor pressure determines whether the particle transport will be Type 1 or Type 2 (see Figures 3.8 and 3.9). Different types of multiphase flows associated with these processes are shown in Figure 3.22. The 35 mm still photographs of the flow are taken at about the 200 ms point in the experiment; this is before the particles begin to descend.[13] Photographs show a dispersed flow of particles at low reservoir pressure and amalgamations of particles bound by unvaporized liquid[14] as the reservoir pressure increases. Since increasing the reservoir pressure results in decreased mass fraction of vapor, the phenomenon is comparable to the transition from

---

[13] In the case of FEB21-1, this is a mute point since there is negligible lofting of the particles (see Fig. 3.15).

[14] The surface tension of the liquid is the only significant force available to bind the particles together. The production of a charge necessary for the electrostatic forces to be equally significant is considered unlikely.

annular flow to *wispy annular flow* as flux of gas in a liquid-gas flow is decreased (Blevins 1984).

In a fluidized bed, where particles are supported against gravity by upward flow, Richardson (1970) describes the deflation of such beds caused by the formation of *bubbles* void of particles. Richardson's data in Figure 3.23 shows the effect of bubble formation.[15] Since air flowing out of the bed as bubbles does not support any particles, the overall volume of the fluidized bed is unaffected by changes in airflow. As a result, given a limited supply of fluidizing gas, the formation of bubbles will quickly deplete the supply and lead to earlier collapse of the fluidized bed. Photographs and base pressure traces of a Type 2 process appear to show the vapor escaping in this manner. Since vapor escapes without interacting with the particles when bubbles form, decreased expulsion of particles is observed.

3.3.2 Effect of reservoir pressure on Type 1 particle transport. The speed of the multiphase flow associated with the Type 1 particle transport process can be sufficiently high for compressibility to be important. In certain experiments, the multiphase flow is choked. Thus, the exit pressure is determined by the sonic flow condition of the multiphase flow. When the reservoir pressure is less than the static pressure of a sonic flow, choking causes the exit pressure to be higher than the reservoir pressure. Figure 3.24 shows the pressure traces used to determine the choking conditions of the multiphase flows generated by the vaporization of the two test fluids. The exit pressure of the choked flow in these results is shown in Table 3.5. The choking pressure of the multiphase flow, measured by the exit pressure, is 0.30 to 0.35 times the vapor pressure of the test fluid; this is below the critical reservoir pressure and choking does not occur in a Type 2 process.

---

[15] The Perspex particles' slip velocity, given by the horizontal axis of Figure 3.23, is in the range of 1 cm/s which is much less than the 1 m/s range for heavier particles used in this work. However, bubbling is a phenomenon observed in all particle beds fluidized by gas. The Richardson's data have been used because it shows the values in both fluidization regimes.

Therefore, the transition from Type 1 to Type 2 process is not related to choking at the exit because unchoked flow can also be produced by a Type 1 process.

Table 3.5 Exit pressure of choked multiphase flow generated by Type 1 processes.

Test Fluid	P_{exit}	P_{vapor}	P_e/P_v
R12	2.2 bars	6.8 bars	0.32
R114	0.9 bars	2.2 bars	0.41

Since the experiments are conducted with constant diameter test cells, choking results when a sonic flow occurs at the exit. Therefore, since pressure waves cannot travel upstream against a sonic flow, the downstream pressure condition is not determined by the reservoir when choking occurs. On the other hand, if the reservoir pressure exceeds the condition necessary for choking, the downstream condition is determined by the reservoir pressure and its effect on the particle transport process can be observed. A decrease in particle expulsion is observed in Type 1 experiments as the reservoir pressure is increased above the critical pressure. Although the effect on expulsion quantity is similar regardless of the test fluid, observations indicate that the causes of these effects differ with the fluid. (The reasons for the difference are discussed in Chapter 4.)

In experiments conducted with R12, the effect is attributed to the duration of upward force acting on the particles. Figure 3.25 shows the effect of the reservoir pressure on experiments conducted with R12; the initial depths of particles in these experiments are the same. In these experiments, a Type 1 process causes the base pressure to plateau before it decreases to the reservoir level. As the reservoir pressure is increased, the base pressure remains above the reservoir level for shorter durations. The pressure decay at the end of the pressure plateau being lessened by the rising reservoir pressure is responsible for the shorter overall duration. The overall duration is important because it defines the duration of upward particle acceleration; the particles begin downward acceleration by gravity when the

base pressure decays to the reservoir level. This can be observed in the pressure trace and particle velocity data for experiment FEB27-3 (Figures 3.18a and 3.26).[16]

In experiments with the less volatile R114, the reservoir pressure appears to have a more complicated and fundamental effect on the transport process. Comparison of photographs obtained in R114 experiments FEB20-2 and FEB20-4 conducted at different reservoir pressures reveal identical Type 1 behavior early in the thrust phase (Figure 3.27). However, a multiphase flow similar to that produced by Type 2 behavior is observed in experiment FEB20-2 conducted with the reservoir pressure near the critical value (1.5 bar vs. 1.6 bar). The transition from Type 1 behavior to Type 2 behavior late in the thrust phase is apparently responsible for reducing the quantity of expelled particles. In addition, the base pressure in R114 experiments with the reservoir at 1 bar show irregular fluctuations near the end of the thrust phase (Figure 3.28). Because the final particle depths in these experiments are greater than expected from a Type 1 process, the fluctuations are believed to indicate the breakdown of Type 1 particle transport.

3.3.3 Effect of reservoir pressure on Type 2 particle transport. The Type 2 particle transport process is characterized by vapor escaping through regions of low particle concentration. The formation of these regions displaces the surrounding regions of high particle concentration, but most of the particles are not lofted by the flow of vapor. An increase in the reservoir pressure decreases the volume of vapor released in the experiment, thus reducing the displacement of particles and unvaporized liquid. As the reservoir pressure approaches the vapor pressure of the test fluid, the volume of vapor asymptotically approaches zero and the displacement of particles becomes negligible. Observations of experiments conducted with high reservoir pressure, such as experiment FEB21-1 (see *3.2.3*), reveal the importance of surface tension when the vapor production is

[16] The upward motion of particles, indicated by positive particle velocity, is the result of momentum imparted on the particle by explosive vaporization. The acceleration of the particle, indicated by the gradient in velocity is being used to indicate the magnitude of particle transport driven by vaporization.

low; nearly spherical bubbles are visible among the particles (see photograph in Figure 3.15). Bubbles below a certain size have a negligible effect on the particle matrix. The vapor produced in such experiments escapes in bubbles which rise slowly through unvaporized liquid in the particle matrix.

3.3.4 Effect of the body force on the particle transport process. The body force exerted on the particles by gravity or by centrifugal acceleration acts to oppose particle expulsion. As shown in Table 3.1, the centrifugal acceleration will directly reduce the acceleration of a particle driven by vaporization. Since the acceleration of particles caused by R114 vaporizing at 1g is about 80g (see Table 3.4), the transport process is affected significantly by 100g centrifugal acceleration. Figure 3.29 shows that the experiments at 100g, JUN9-9 and JUN9-18, differ greatly from an identical experiment performed at 10g (e.g., JUN9-12). The acoustic oscillations in the base pressure trace and the negligible particle expulsion indicate that the 100g centrifugal acceleration is responsible for producing Type 2 process under a condition known to produce a Type 1 process at 1g and 10g. In this case, Type 2 occurred because the body force exceeded the drag on the particles.

Vapor drag and body force are the two opposing forces determining the acceleration of particles. Therefore, the particle acceleration data in Table 3.4 can be used to calculate the vapor drag using the mass of the particle[17]; the results are shown in Table 3.6. Using these results, it is possible to predict the results obtained by substituting 0.5 mm spheres of different density in the experiments. Based on the drag measured in the experiments, the accelerations of 0.5 mm lead spheres (density: 11.34 g/cc) in R114 at 1g will be about 20g, compared to 80g for Dragonite spheres (density: 2.95), if other factors, such as surface tension and heat transfer, are unimportant. This also means that Type 1 behavior will not occur in experiments with lead particles if the centrifugal acceleration exceeds 20g.

[17] Particle mass: 0.193 milligrams.

Table 3.6 Drag on a 0.5 mm sphere calculated from data in Table 3.4.

Test Fluid	Drag
R12	94.6 dynes
R114	15.3 dynes

3.3.5 Effect of the body force on the transport of dispersed particles. Particles transported by a Type 1 process are dispersed throughout the test cell. The quantity of particles remaining after experiments involving the Type 1 process at various centrifugal accelerations are plotted in Figure 3.30. Since in Type 1 transport, the quantity of particles left in the test cell can be independent of the initial quantity, the following discussion focuses on the quantity remaining in the test cell (i.e., final particle depth) and not the quantity of particles expelled in the experiment. Although the data are divided into groups by their experimental categories (see Table 2.3), the centrifugal acceleration restrains the expulsion of particles to increase the quantity of particles left in the test cell.

The particles are transported against gravitational and inertial forces by vapor escaping the test cell. A commonly used parameter for describing such a process is the Galileo number, G, or the ratio of body force to viscous drag. (The acceleration due to the body force, a, will be written Ng in the following equations, where N = a/g.) It is useful for computing the terminal velocity of a sphere using similarity and it is defined as follows:

$$G = C_D \, Re_d^2 = \frac{\rho_B}{\rho_v} \frac{d^3 \, Ng}{\nu^2} \tag{3.2}$$

The Reynolds number, Re, appears in this expression because while the terminal velocity of a particle is unknown, it is a function of the Reynolds number. The Galileo number has also been used to analyze the velocity necessary to fluidize a bed of monodisperse spheres (Barnea & Mizrahi, 1973).

The data plotted in Figure 3.30 have been found to collapse when plotted with respect to a modified Galileo Number, G*:

$$G^* = \left(\frac{\rho_B}{\rho_v}\right)^2 G = \left(\frac{\rho_B}{\rho_v}\right)^2 C_D \, Re_d^2 = \left(\frac{\rho_B}{\rho_v} d\right)^3 \frac{Ng}{\nu^2} \quad . \tag{3.3}$$

Since the slope of the data in a logarithmic plot is approximately 0.5, the data have been plotted against the square root of G* (Figure 3.31). The linear regression of the data shown by the solid line gives a functional relationship between the amount of material remaining after an experiment and the parameter G*.

$$h_2 / h_0 = 0.017 + 1.8 \times 10^{-7} \sqrt{G^*} \tag{3.4}$$

The data in Figure 3.31 have been obtained at a variety of experimental conditions in which Type 1 process has been observed; the experimental conditions are divided into categories tabulated below (Table 3.7). As shown by data from various experiments, Figure 3.31 shows that Equation 3.4 holds under a variety of test conditions, particle diameter, and test fluid. The maximum deviation of the regression, neglecting those in Category 1 which follow a parallel trend (dashed line), is ± 0.02. The five Category 1 points which lie above the scatter in Figure 3.28 are from R114 experiments conducted with the reservoir at 1 bar where Type 1 process is believed to break down during the experiment. The transition to Type 2 process is thought to terminate the Type 1 transport of particles prematurely in these experiments.

Table 3.7: Experimental categories for data in Figure 3.31 (Type 1 process). Run numbers for experiments of a given categories can be found in Table 2.3.

Cat.	Particle Dia. (d)	Test Fluid	Apparatus	Reservoir Pressures	Body Force per Mass
1	0.5 mm	R114	Hi-g	1 bar	1 to 10 g
2	0.5 mm	R114	1g	0.6 to 1.0	1 g
3	1.0 mm	R114	Hi-g	1 bar	1 g
4	0.5 mm	R12	Hi-g	1 bar	1 to 100 g
5	0.5 mm	R12	1g	0.6 to 1.4	1 g

It should be noted that G* has a physically more significant functional dependence on material properties than the original parameter, G. Since the particle weight is proportional to $\rho_B\, d^3$ and the drag is proportional to $\rho_V\, d^2$:

$$G^* = f\left(\frac{\rho_B}{\rho_v}\, d\right) = f\left(\frac{\rho_B\, d^3}{\rho_v\, d^2}\right) \propto f\left(\frac{\text{Weight}}{\text{Drag}}\right) \tag{3.5}$$

A *Particle Froude number*, F_p, can be defined based of the terminal velocity, u_t, and the diameter, d, of the particle,

$$F_p(d,u_t) = \frac{u_t}{\sqrt{Ng\, d}}. \tag{3.6}$$

Dividing this parameter by the Reynolds number of the falling particle, it can be shown that

$$F_p\left(d, \frac{\nu}{d}\right) = \frac{F_p\,(d,\, u_t)}{Re(d,\, u_t)} = \frac{\nu}{\sqrt{Ng\, d^3}}$$

$$= \left(\frac{Ng\, d^3}{\nu^2}\right)^{-1/2} \propto \frac{1}{\sqrt{G^*}}. \tag{3.7}$$

Therefore, based on equation (3.3), h_2/h_0 is inversely proportional to the Particle Froude number based on the viscous velocity scale, ν/d.

3.4 Rate of Particle Transport

Measurements of mass and momentum flux generated by rapid vaporization are essential for modelling the transport process. While the momentum flux is measured directly using a pressure transducer on the solid endwall of the test cell, direct measurement of the mass flux out of the test cell has proved intractable due to the violence of the flow. Fortunately, the speed of the disruption front can be used to calculate the downstream mass flux generated by Type 1 behavior, because the density of the upstream material is relatively unaffected by depressurization.

3.4.1 Propagation speed of the disruption front. The disruption front velocity has been determined using data derived from high-speed motion pictures. In Tables 3.2 and

3.3, the results of these direct observations confirm the mean velocity calculated indirectly using the duration of sustained momentum flux. Further confirmation of the front speed is provided by a series of experiments conducted with various initial depths of particles. The base pressure traces (Figure 3.32a) reveal a regular trend in the duration of thrust phase for increasing initial depth as shown in Figure 3.32b. If the data for low initial particle depths are neglected,[18] the linear regression of the data indicates propagation speed of 380 cm/s. The consistency of this value with data in Table 3.3 indicates that the front propagation velocity is fairly constant over a distance less than 1 meter.

3.4.2 Effect of reservoir pressure. The effect of reservoir pressure on the disruption front has been studied using data from experiments involving R12 only, because breakdown of Type 1 to Type 2 behavior is observed in R114 experiments when reservoir pressure exceeds 1.0 bar (see Figure 3.28). The high-speed motion pictures of experiments FEB22-3 and FEB23-3, conducted with the reservoir at 1.0 bar and 3.1 bar respectively, show little difference in the propagation speed of the front (Figures 3.16 and 3.17). The effect of reservoir pressure on the momentum flux is indicated by the difference in the base pressure traces. Figure 3.25 shows that the reservoir pressure has only a small effect on the base pressure plateau; the maximum value of elevated pressure is plotted in Figure 3.9. In Figure 3.25, the duration of the pressure plateau appears to increase with increasing reservoir pressure. However, the end of the plateau which is the beginning of the pressure decay, cannot be defined clearly. The apparent lengthening of the plateau indicates that the speed of the disruption front decreases with increasing reservoir pressure.

3.4.3 Effect of the test cell length. The effect of increasing the test cell length by a factor of two or less is shown in base pressure traces of Figure 3.33; these are results of R12 experiments conducted with the same initial depth of particles (21.5 cm) and same

[18] Results in Figure 3.19 indicate that the Type 1 behavior is insensitive to initial particle depth only if the initial depth is significantly greater than the final depth.

reservoir pressure (1 bar). The pressure traces differ mainly in the rarefaction process after the base pressure plateau. This difference is caused by the dispersion of a rarefaction wave which propagates down the test cell at the end of the thrust phase. Since the length and the level of the pressure plateau are unaffected, this degree of change in the test cell length is shown to have negligible effect on the flux of mass and momentum.

3.4.4 Effect of the body force. Figure 3.34 shows the results of an experiment involving the rapid vaporization of R12 at 100g (JUN7-5). The disruption front motion (Figure 3.34b) indicates a decrease in the propagation speed with depth, an effect apparently related to increasing hydrostatic pressure acting on the front. The hydrostatic pressure is similar to the reservoir pressure in that the downstream pressure condition of the disruption front is affected; the increase in *back pressure* also appears to decrease the front propagation speed when it is determined by the reservoir pressure instead of the hydrostatic pressure (see *3.4.2*).

The effect of the body force can be represented by a Froude number based on the test cell length or the particle diameter, or *Conduit* and *Particle Froude numbers* respectively.

The Conduit Froude number for conduit depth (h) and centrifugal acceleration (Ng) can be defined as follows:

$$F_c = \frac{u}{\sqrt{Ng\,h}} \tag{3.8}$$

It compares the dynamic pressure to the local hydrostatic pressure.

The Particle Froude Number for particle diameter (d) and centrifugal acceleration (Ng) is defined as follows:

$$F_p = \frac{u}{\sqrt{Ng\,d}} \tag{3.9}$$

This parameter can be related to the drag and the weight of a particle.

In the experiments where the test cell length is doubled, F_c is decreased by 70% relative to F_p. This has a negligible effect on the disruption front speed. On the other

hand, F_p has been found to affect the particle transport (see *3.3.4*). Since both Froude numbers are affected by conducting experiments at various centrifugal accelerations, the effect of each parameter cannot be easily isolated.

The base pressure recorded in the experiments conducted at 100g displays the effect of decreasing hydrostatic pressure as well as effects due to changes in the momentum flux. As material is expelled during the experiment, the hydrostatic pressure acting on the base pressure decreases. The base pressure during experiments conducted with different initial particle depths are dominated by decreasing hydrostatic pressure as particles are expelled (Figure 3.35a). For this reason, the plateau in momentum flux during the propagation of the disruption front appear as a constant gradient in the base pressure trace. In experiments with initial particle depth greater than 12 cm, this portion of the signal overlaps for initial particle depths exceeding 10 cm, indicating that the momentum flux is not being affected by the initial particle depth. Although the rarefaction at the end of the thrust phase is not clearly discernable, it can be assumed to be identical since the test cell is unchanged. Therefore, the mean speed of the disruption front is measured in the manner used in *3.4.1* for 1g experiments (Figure 3.35b), and shows that gravity slows the propagation of the disruption front as indicated originally by the motion picture data.

Mass and momentum fluxes is determined from the data using techniques based on the conservation of mass and momentum. The analysis and the results are given in Chapter 4.

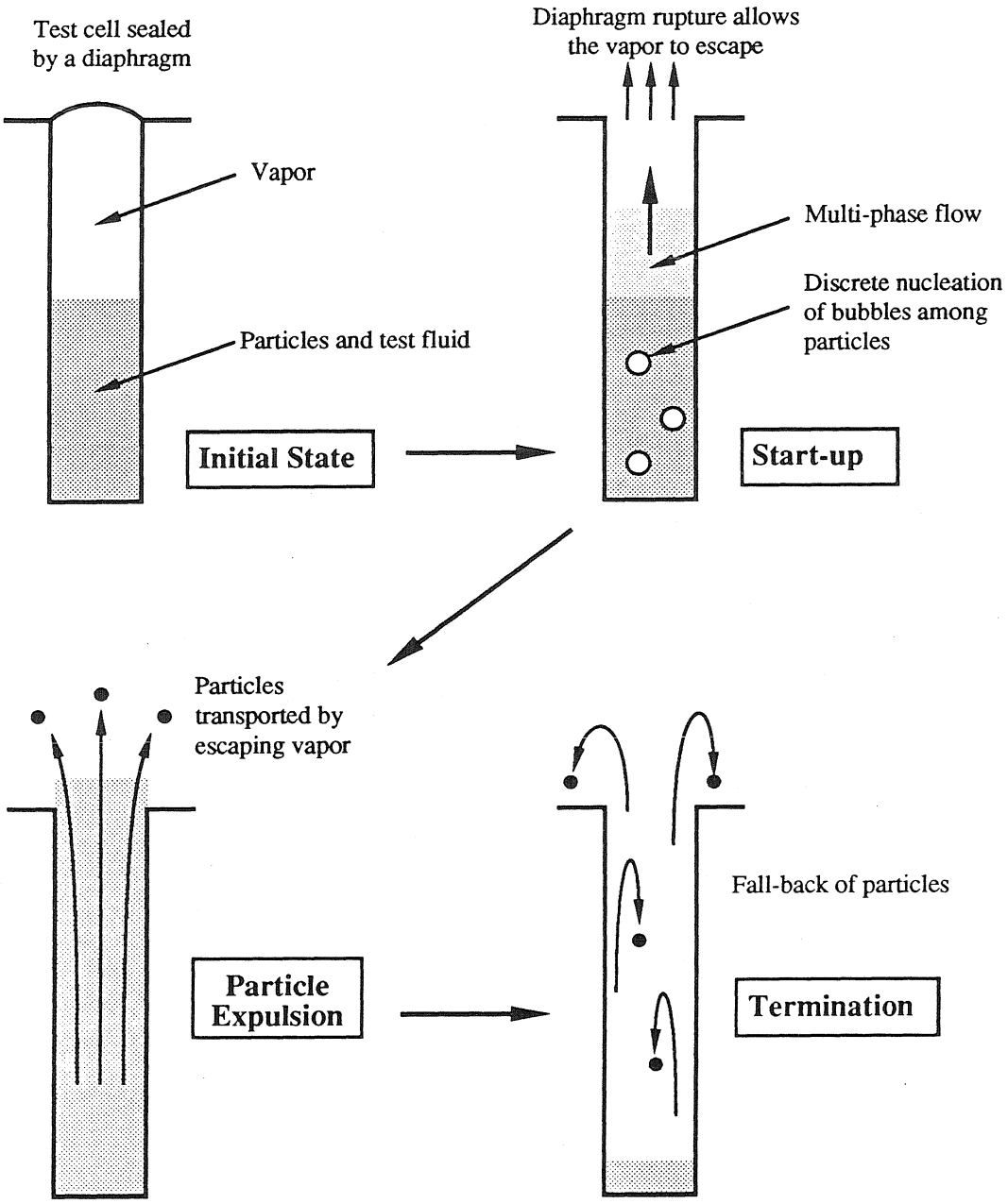

Figure 3.1 The sequence of phases in a typical experiment.

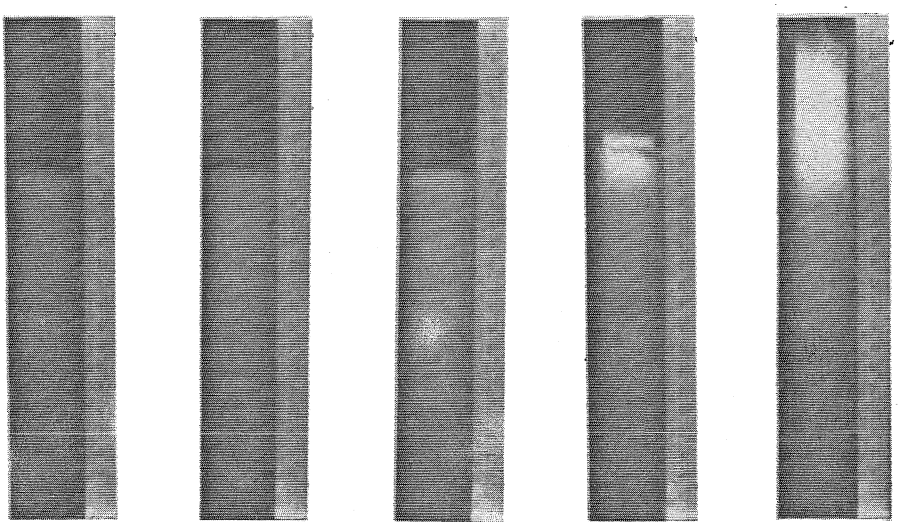

Time (t): 0 ms 1 ms 2 ms 3 ms 4 ms

Figure 3.2 Typical start-up phase of experiments at 1g with R12 as the test fluid. Wide angle photographs taken from the motion picture of experiment FEB22-3. Note the beginning of bubble nucleation at the top of the particle bed at t = 2 ms.

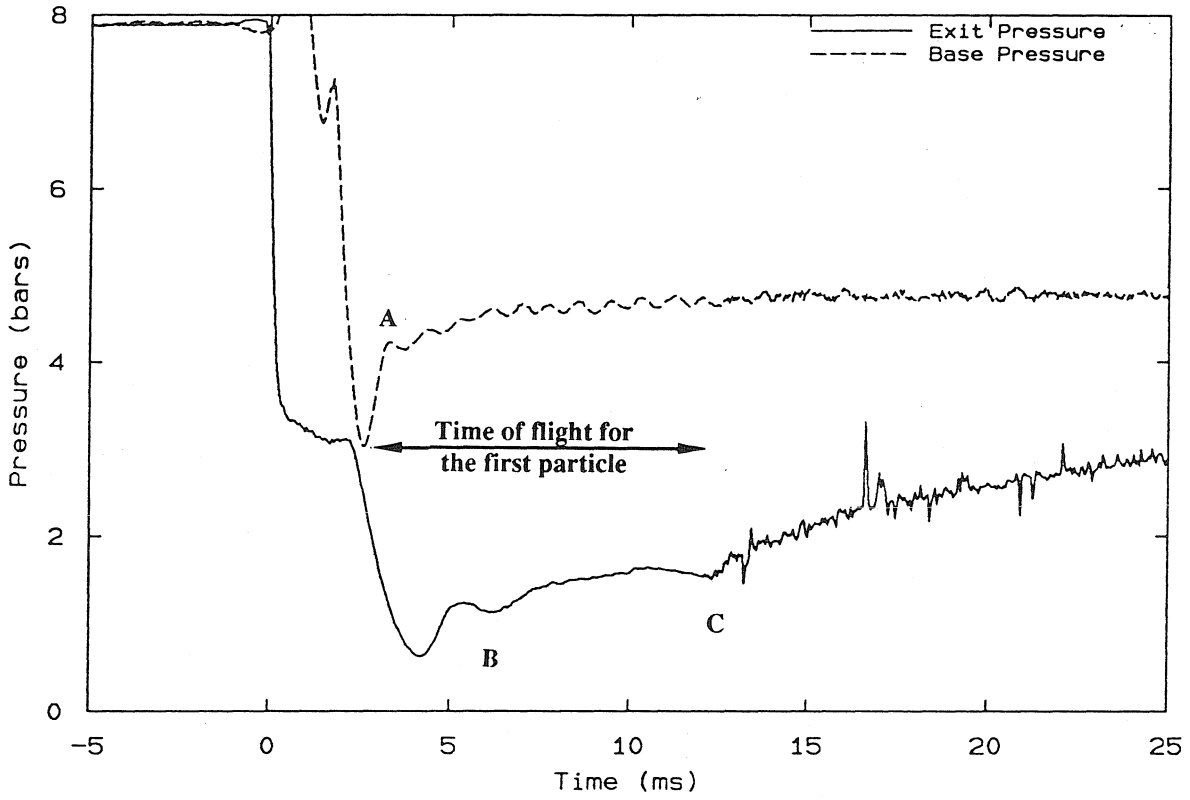

Figure 3.3 Detail of the base and exit pressure recorded during experiment FEB22-3 showing the start-up phase. A: Explosive vaporization of the superheated liquid and beginning of particle transport. B: Arrival of the spray front at the exit pressure transducer extrapolated from photographic images (Figure 3.2). C: Arrival of particles at the exit pressure transducer as indicated by particle impacts.

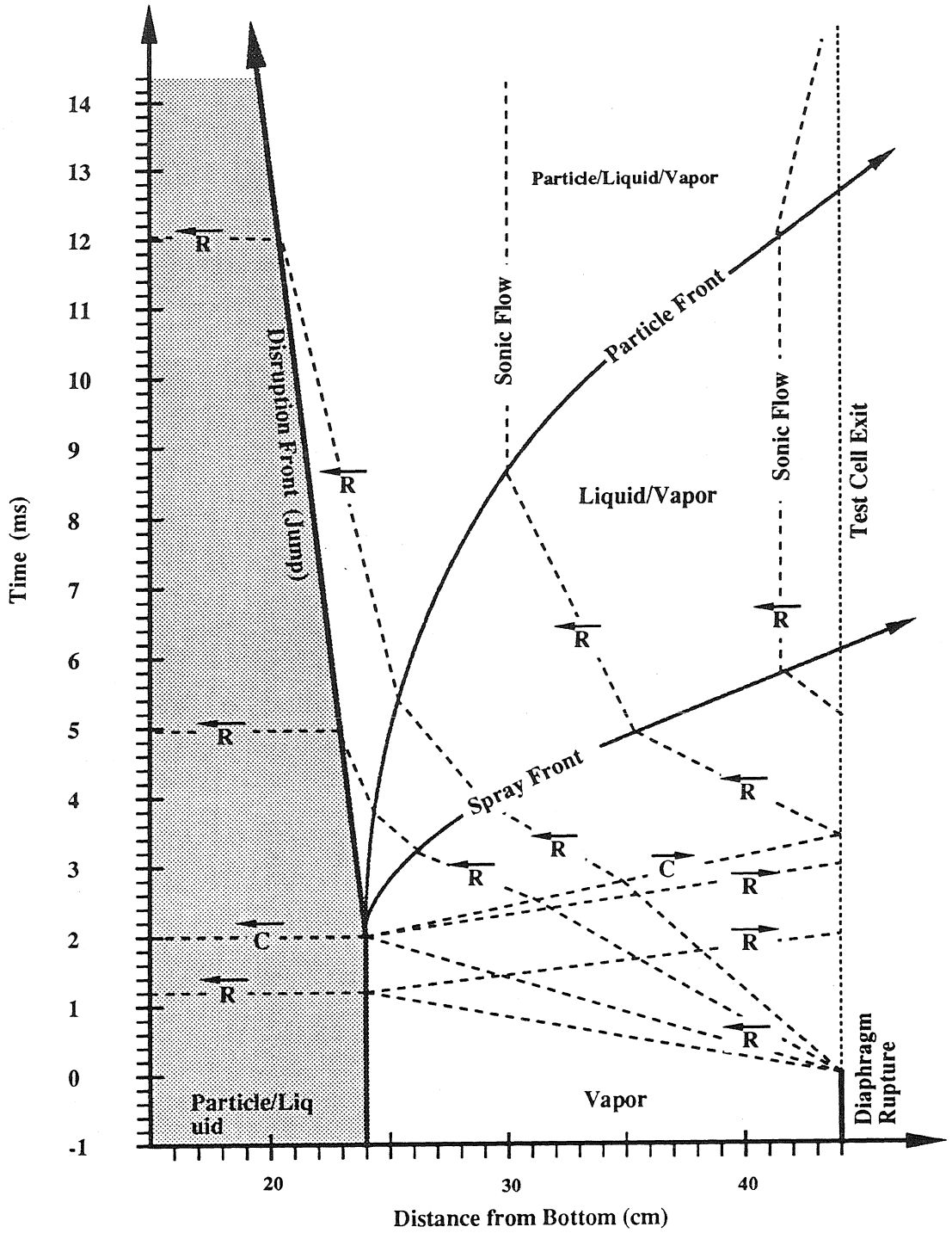

Figure 3.4 The trajectories of pressure waves inside the test cell during the startup phase of a choked Type 1 event (FEB22-3). Lines labeled "R" are rarefaction waves and "C" are compression waves. The particular experiment involved the vaporization of R12; a diagram for a R114 experiment will be similar.

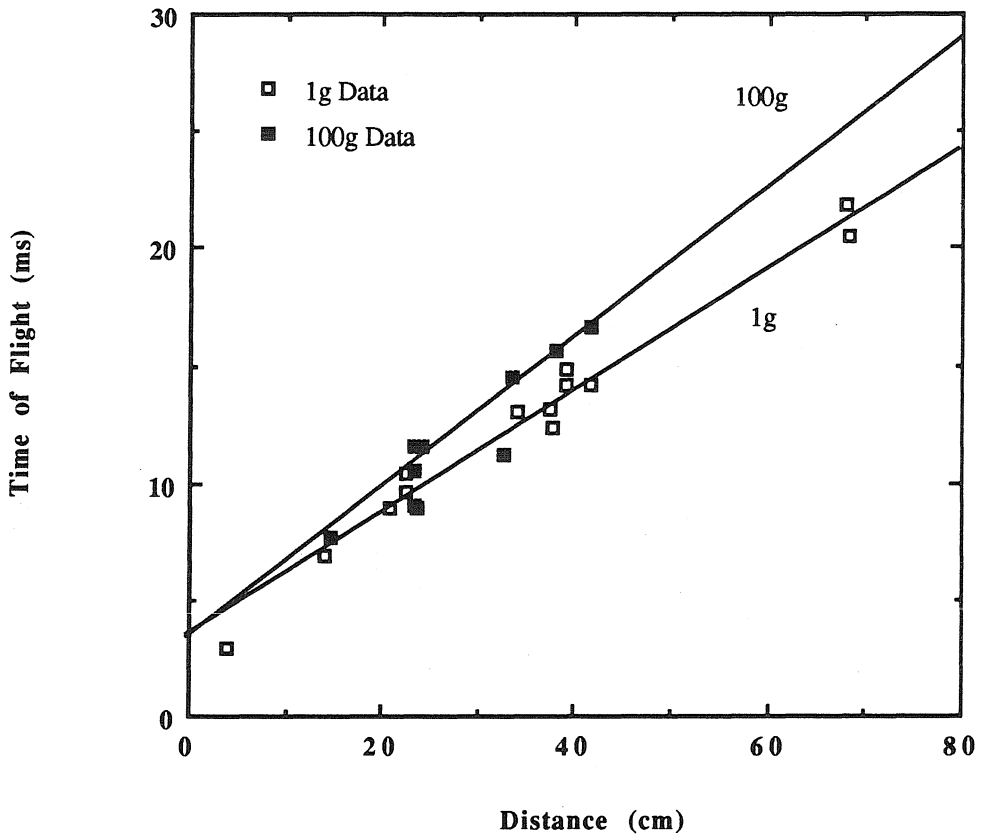

Figure 3.5 Time required by the first beads expelled in the experiments to travel from the top of the particle bed to the exit. In these experiments, the test fluid is R12 and the test cell is vented to 1 bar. The lines show that the particles are accelerated against gravity to a certain velocity; the y-intercept indicates a characteristic time of acceleration. The slope of the 1g trend is equivalent to 3870 cm/s and the y-intercept equals 3.6 ms. Similarly, the values for the 100g trend are 3000 cm/s and 3.3 ms.

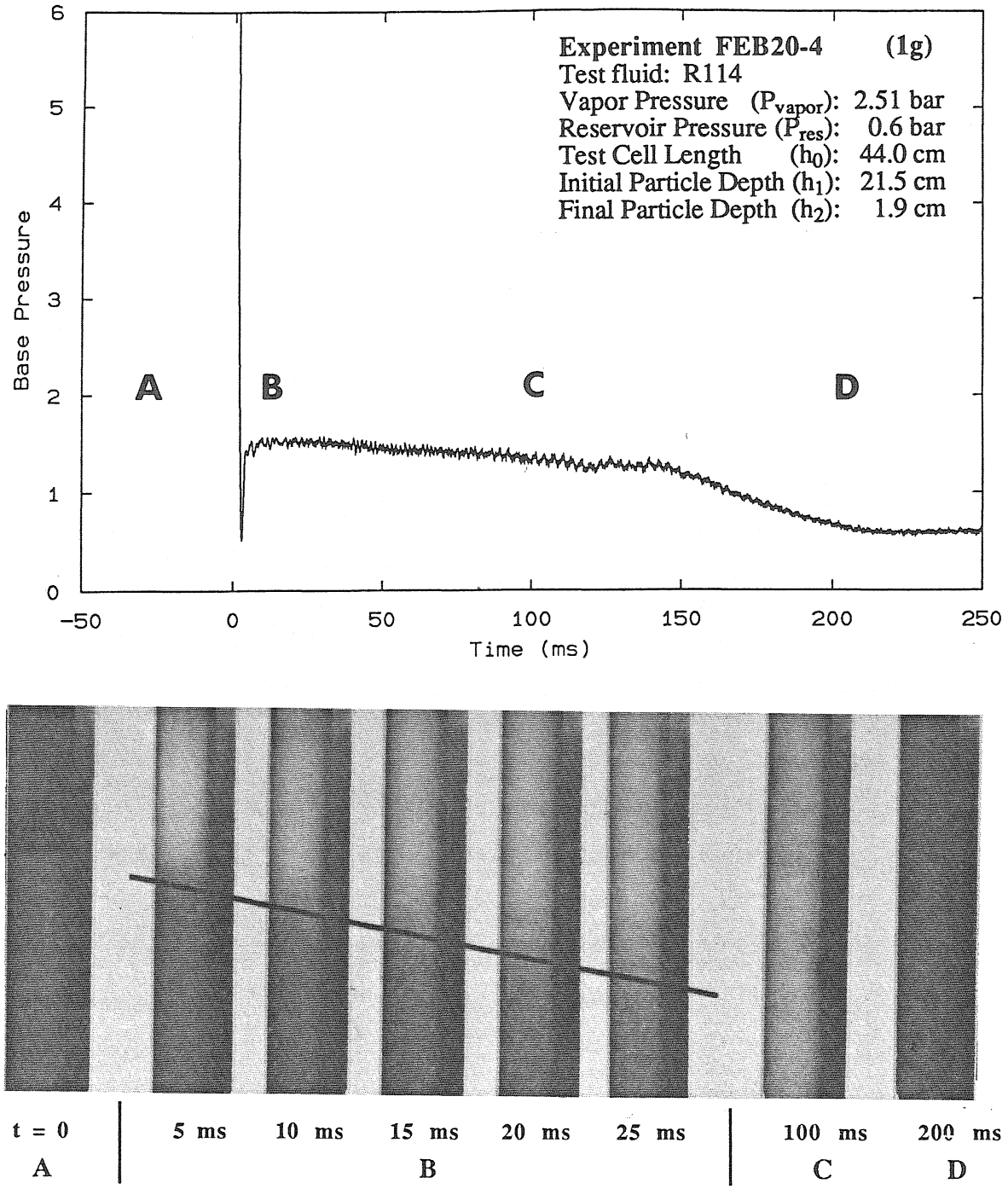

Figure 3.6 Experiments venting the test cell to lower reservoir pressures are characterized by a plateau in the base pressure. A downward moving front can be defined in the photograph sequence B. High-speed multiphase flow blurred in C slows 100 ms later to reveal a flow of dispersed particles (D). Most of the particles are expressed when dispersed in this manner.

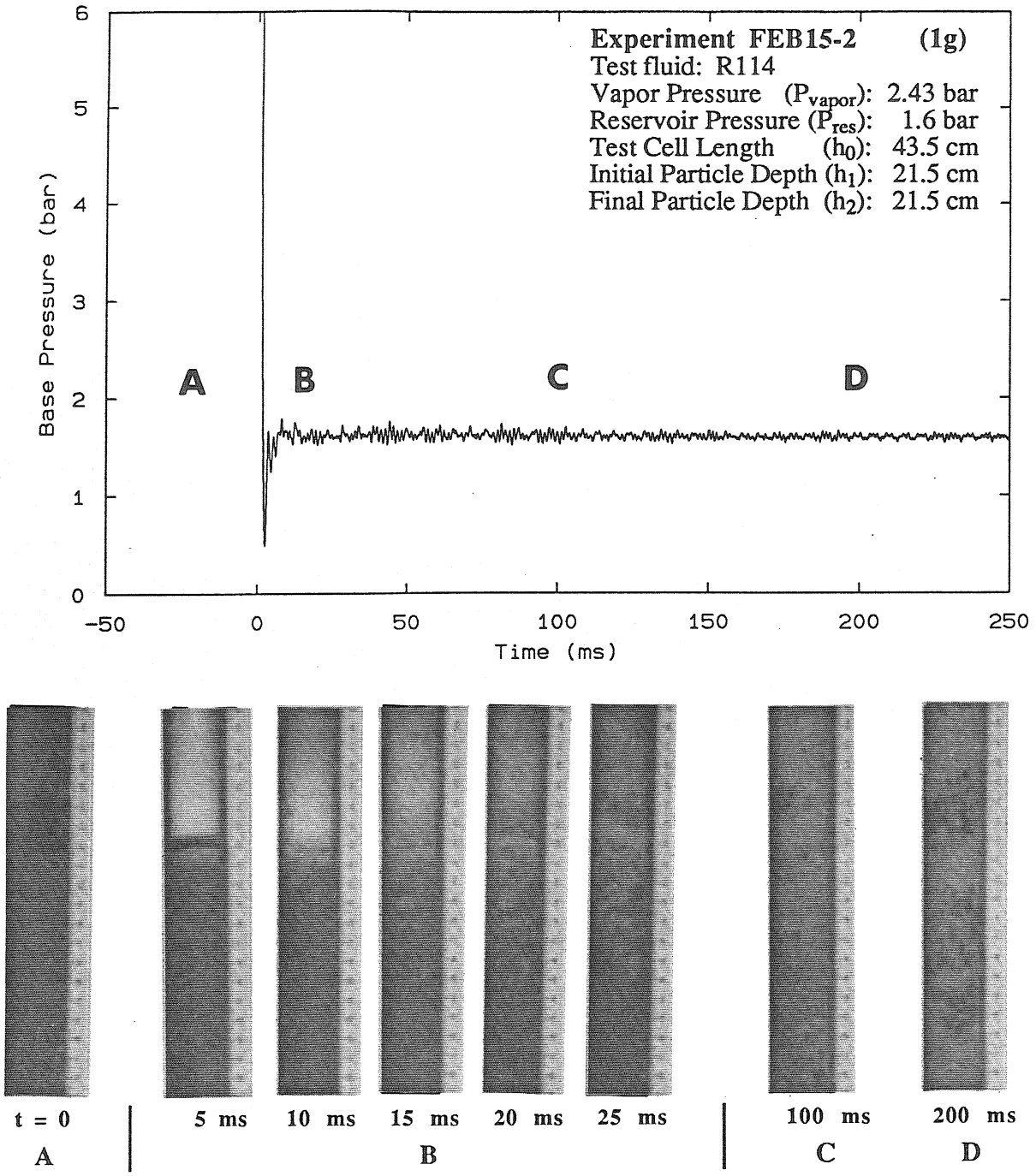

Figure 3.7 Experiments conducted at this level of depressurization are characterized by the formation and growth of vapor cavities (light colored patches in B). In this experiment, large cavities formed by the coalescence of smaller cavities are visible in D. The gradual release of vapor produces little rise in the base pressure after the initial reaction to depressurization, a sharp spike at 2 ms.

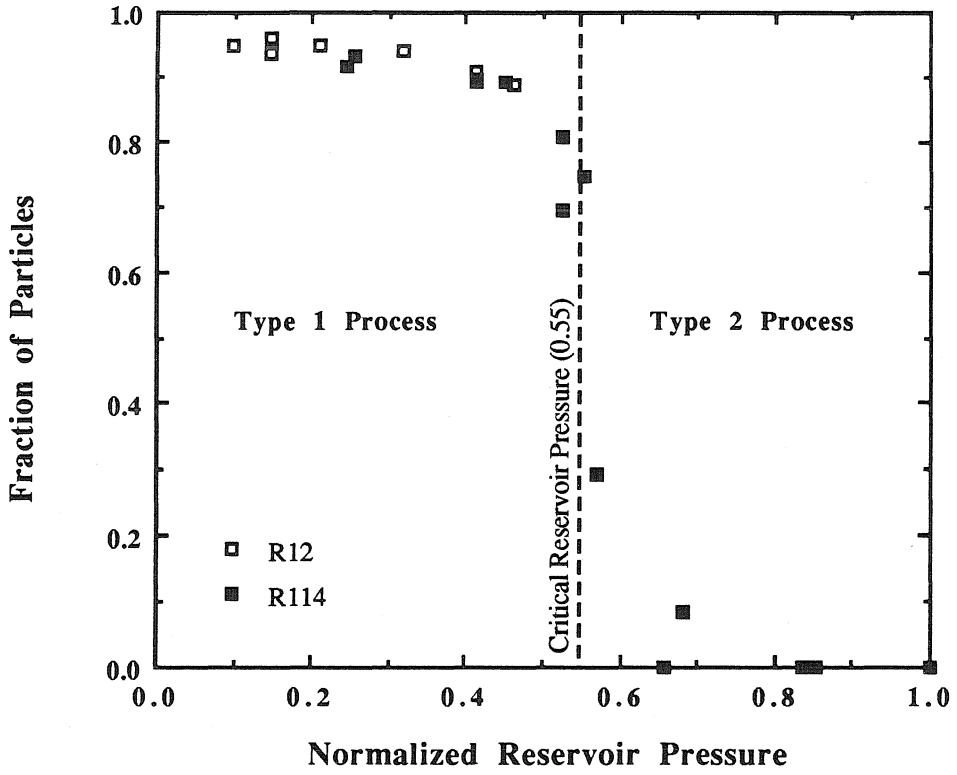

Figure 3.8 Quantity of particles expelled from the test cell; the quantity is expressed as the fraction of the initial quantity in the test cell, i.e., $y = (h_1 - h_2) / h_1$. The reservoir pressure for the experiments have been normalized by the vapor pressure of the test fluid, i.e., $x = P_{res} / P_{vap}$. The experiments were conducted with 45 cm test cell which was initially filled to the 50% mark.

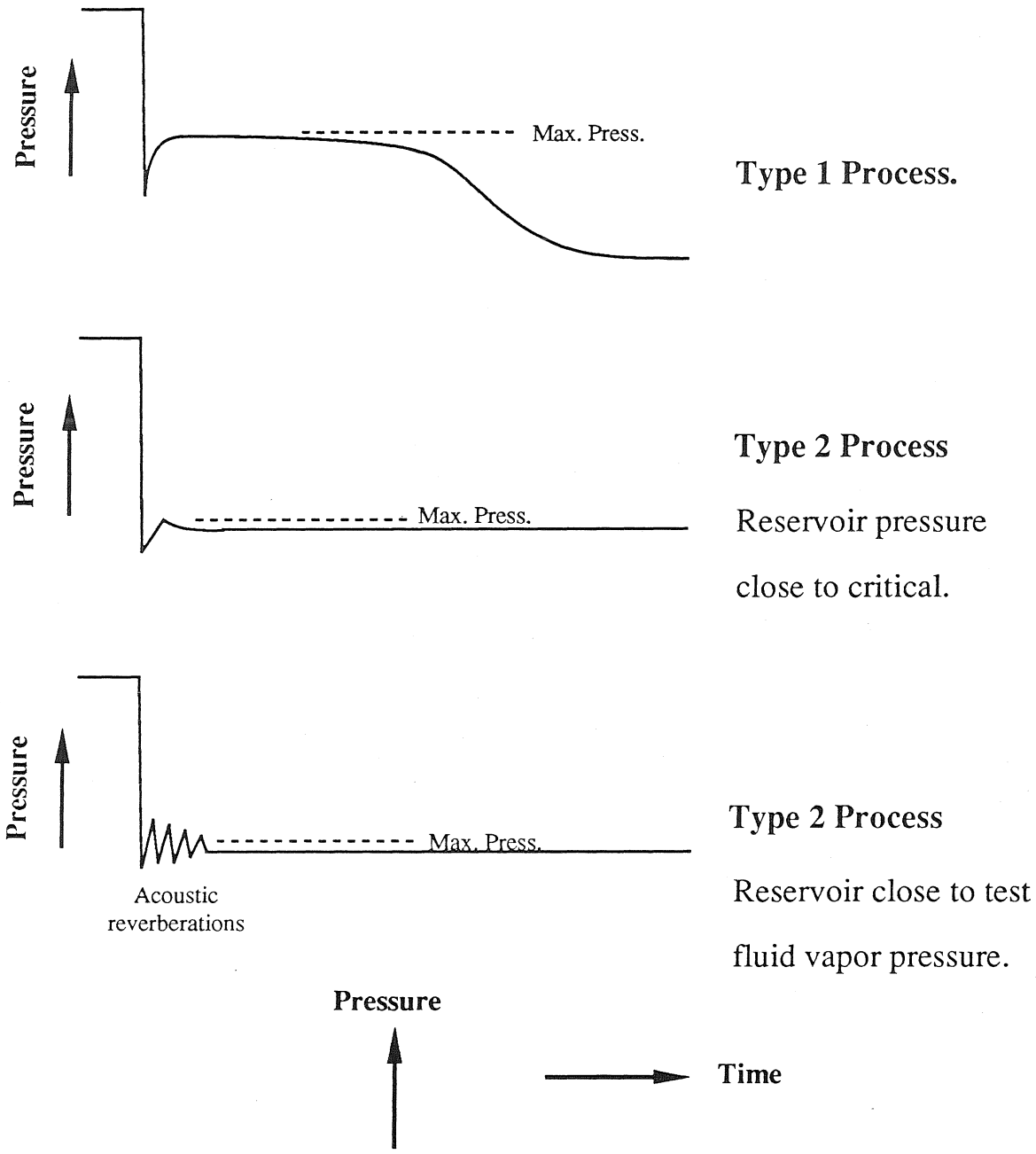

Figure 3.9 (a) Characteristic base pressure traces for particle transport processes observed in the experiments. The maximum pressure value following the depressurization used in the following diagram is defined.

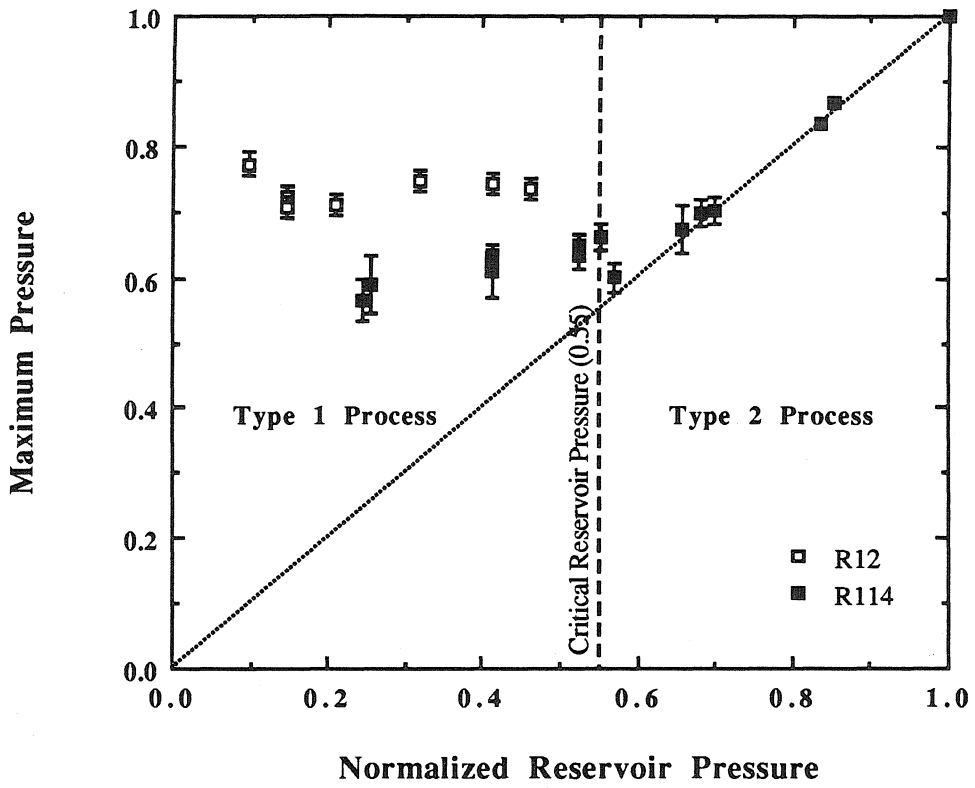

Figure 3.9 (b) Maximum pressure level at the bottom of the test cell recorded during the expulsion of particles; the maximum pressure is expressed as a fraction of the vapor pressure, i.e., $y = P_{max} / P_{vap}$. The reservoir pressure for the experiments have also been normalized by the vapor pressure of the test cell, i.e., $x = P_{res} / P_{vap}$. The experiments were conducted with a 45 cm test cell which was initially filled to the 50% mark.

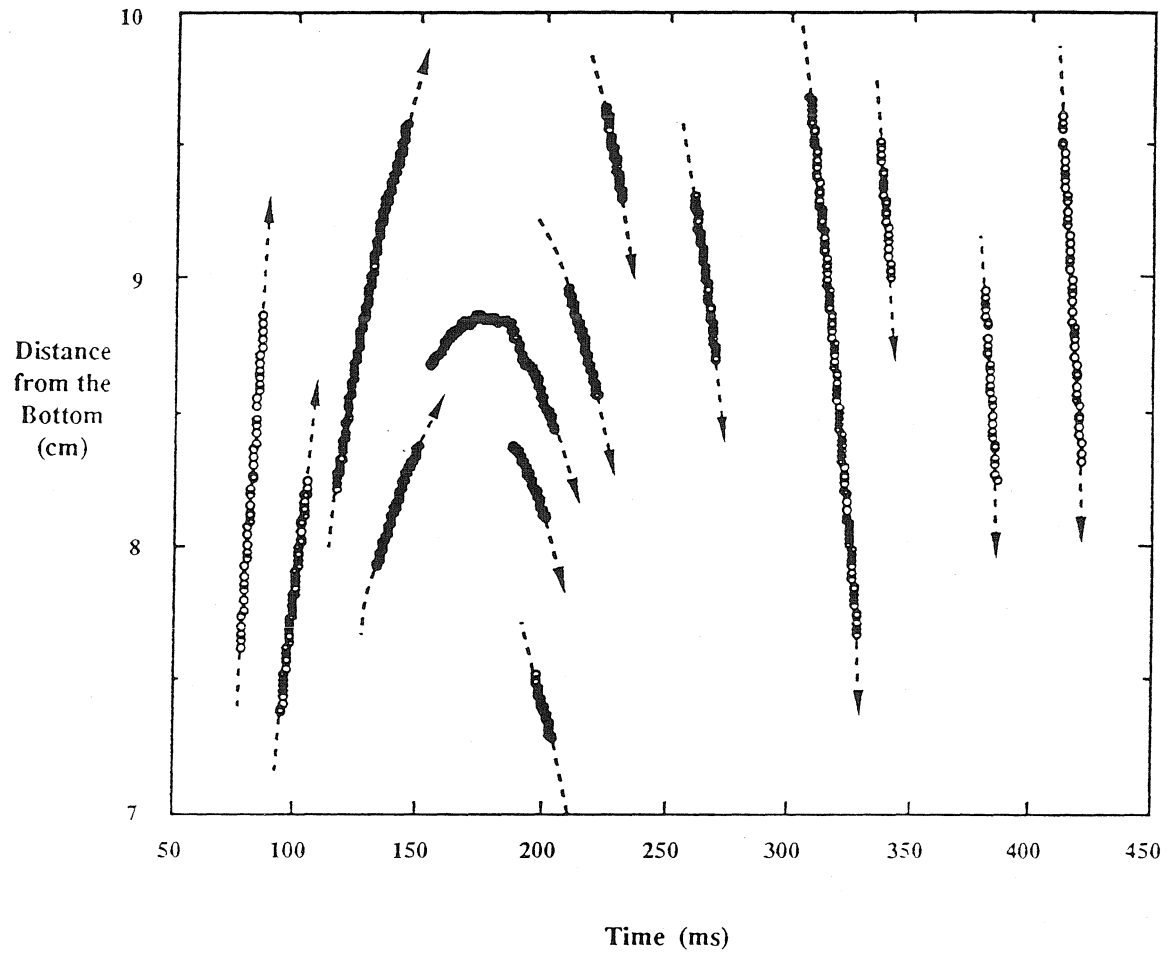

Figure 3.10 The position of the particles crossing the field of the high-speed motion picture camera after the first 70 ms following depressurization. The experiment is FEB27-3 (see Figure 3.18). The data show particle position every 0.2 ms.

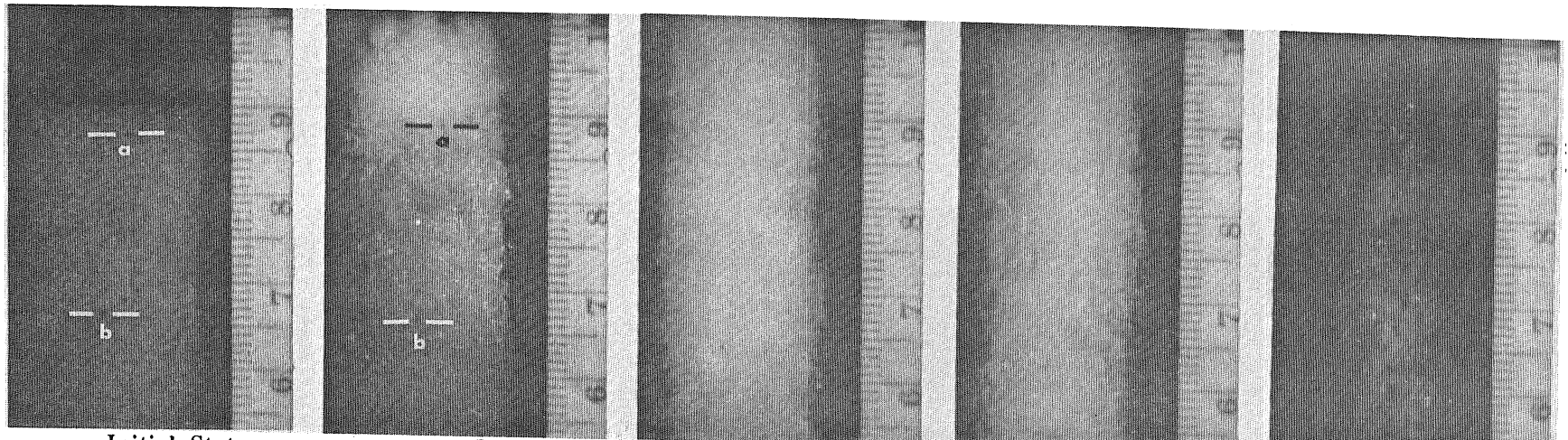

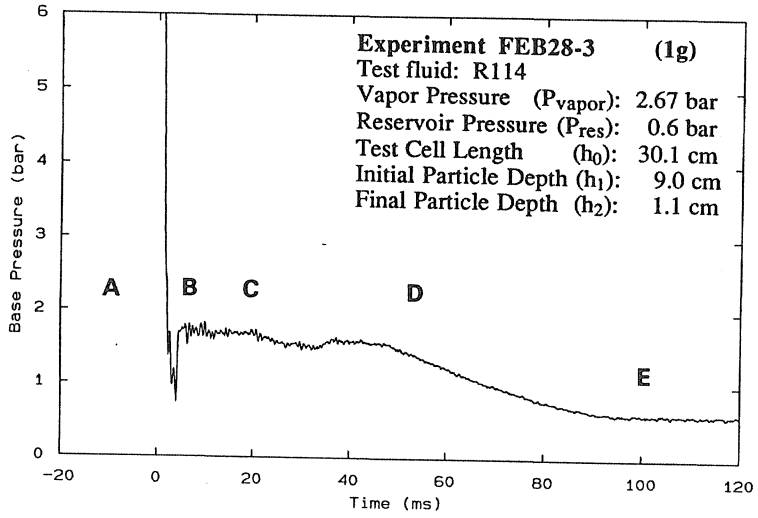

Figure 3.11 (a)

Photographs taken from the close up motion picture of a Type 1 process produced by the explosive vaporization of R114 (above). Note the motion of particle 'a' during the first 5 ms while particle 'b' is motionless.

The base pressure measured during the same experiment (left).

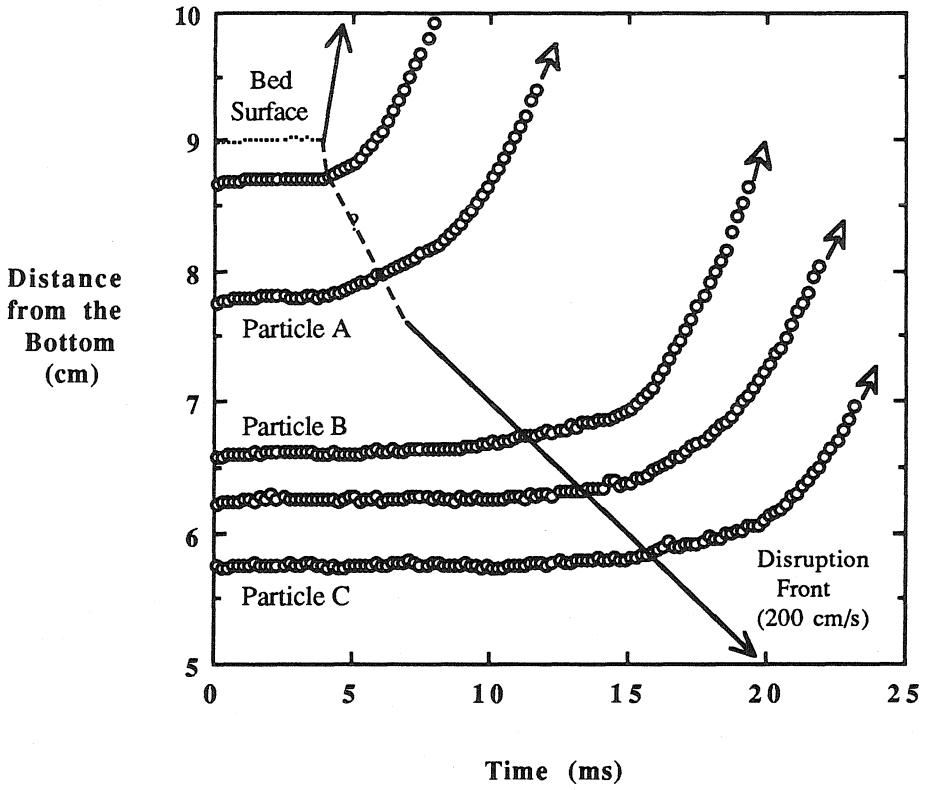

Figure 3.11 (b) The movement of darkened particles visible in the motion picture of experiment FEB28-3. The velocities of particles A, B, and C are shown in the following figure.

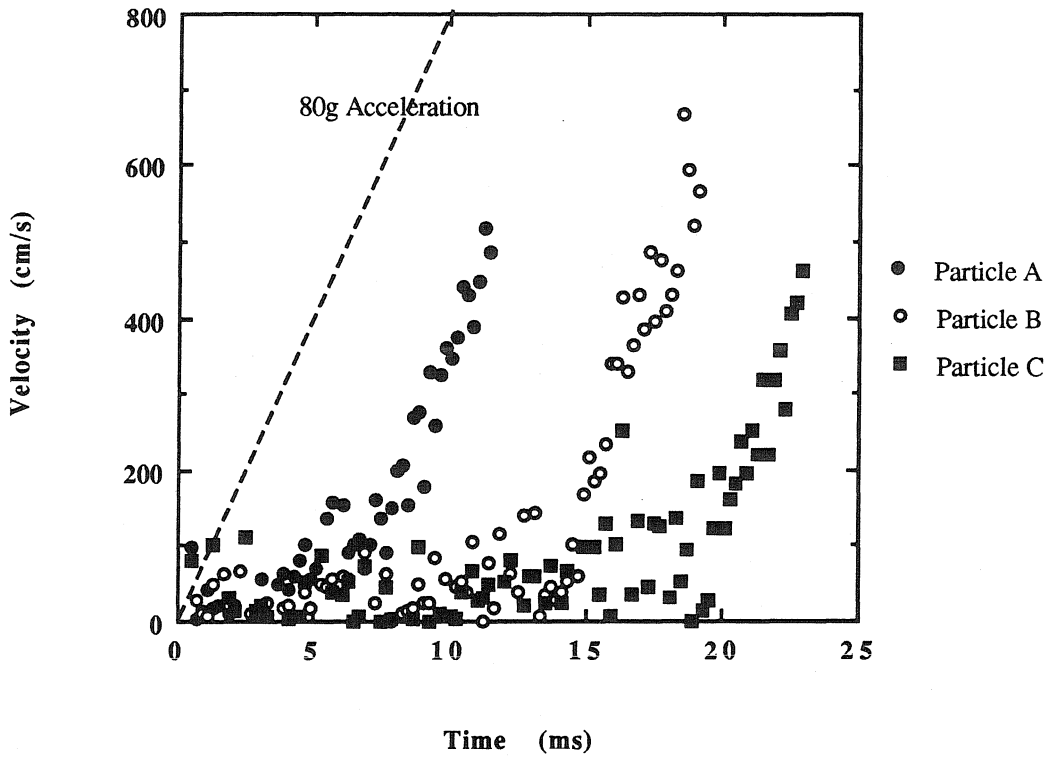

Figure 3.11 (c) The velocity of three particles visible in the motion picture of experiment FEB28-3. A line with slope equivalent to 80g acceleration is shown. This figure clearly shows the sequential acceleration of the particles in the previous figure.

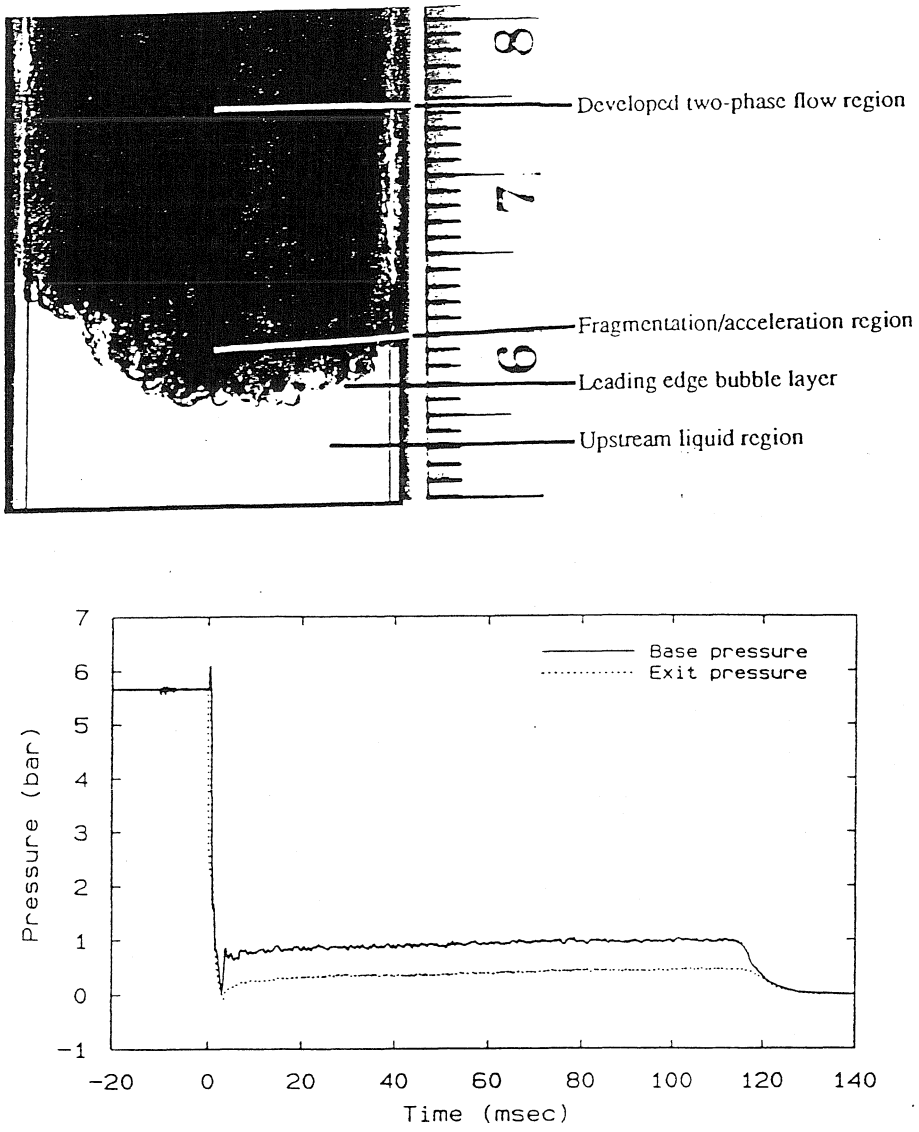

Figure 3.12 Evaporation wave in R12 (Hill 1990).

Top: high speed photograph showing the wave traveling downward. The cylindrical glass test cell is backlit so that the transparent material appears white in the photograph.

Bottom: Pressure measurements recorded during the propagation of the wave. Locations of the pressure transducers are the same as those for experiments in the present work.

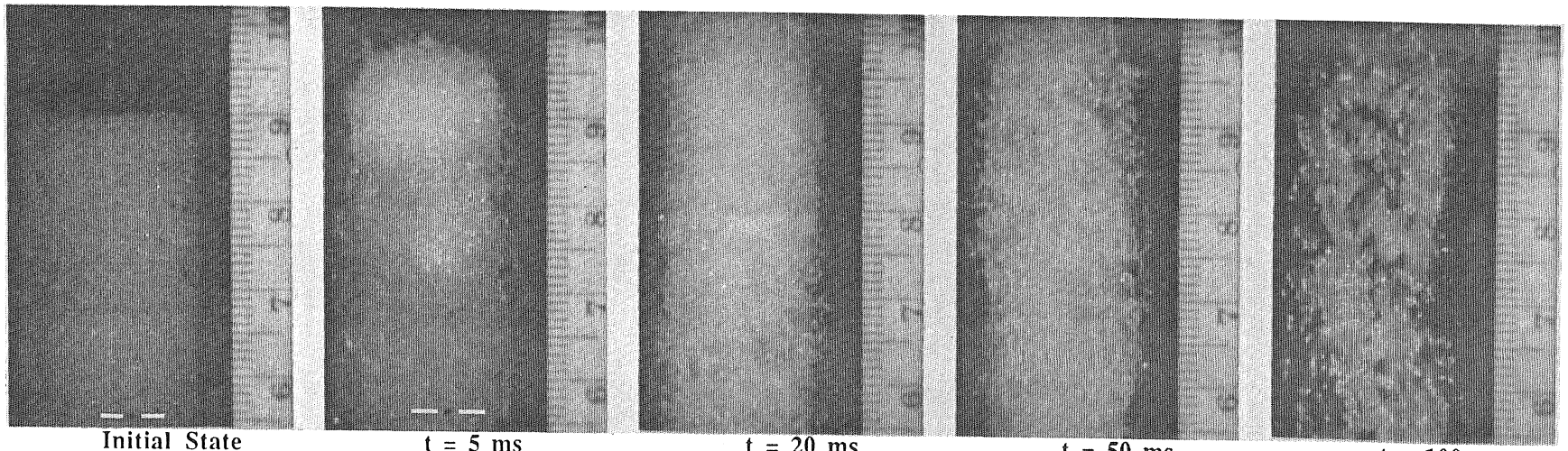

Initial State
A

t = 5 ms
B

t = 20 ms
C

t = 50 ms
D

t = 100 ms
E

t = 150 ms
F

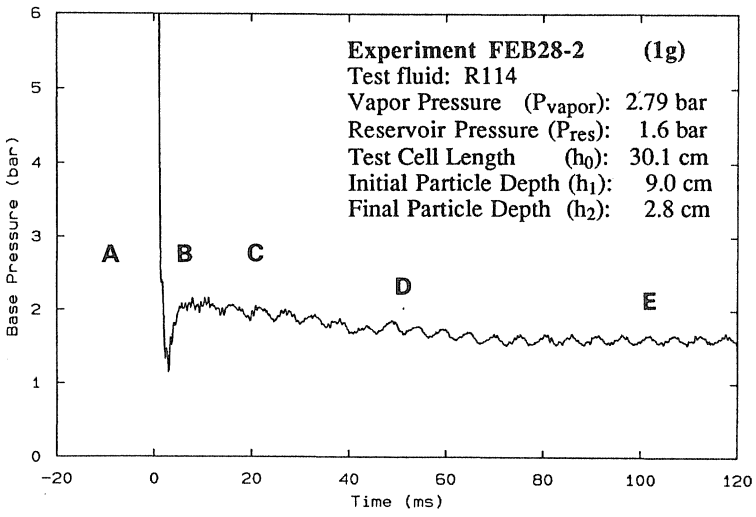

Figure 3.13 (a)

See comments on the next page.

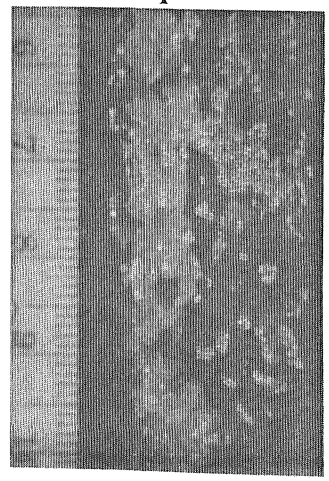

Figure 3.13 (a)

Photographs taken from the close up motion picture of a Type 2 process produced by the vaporization of R114 and the base pressure recorded during the experiment. Note the motion of a darkened particle, indicated by white bars, during the first 5 ms of the experiment; the particle motion precedes the vaporization process appearing white in the photograph. The motion of particles indicates displacement by expansion of vapor below the field of view.

The base pressure trace shows acoustic reverberations and a rise in pressure immediately after depressurization. This pressure trace combines the two profiles of a Type 2 process shown in Figure 3.9 a.

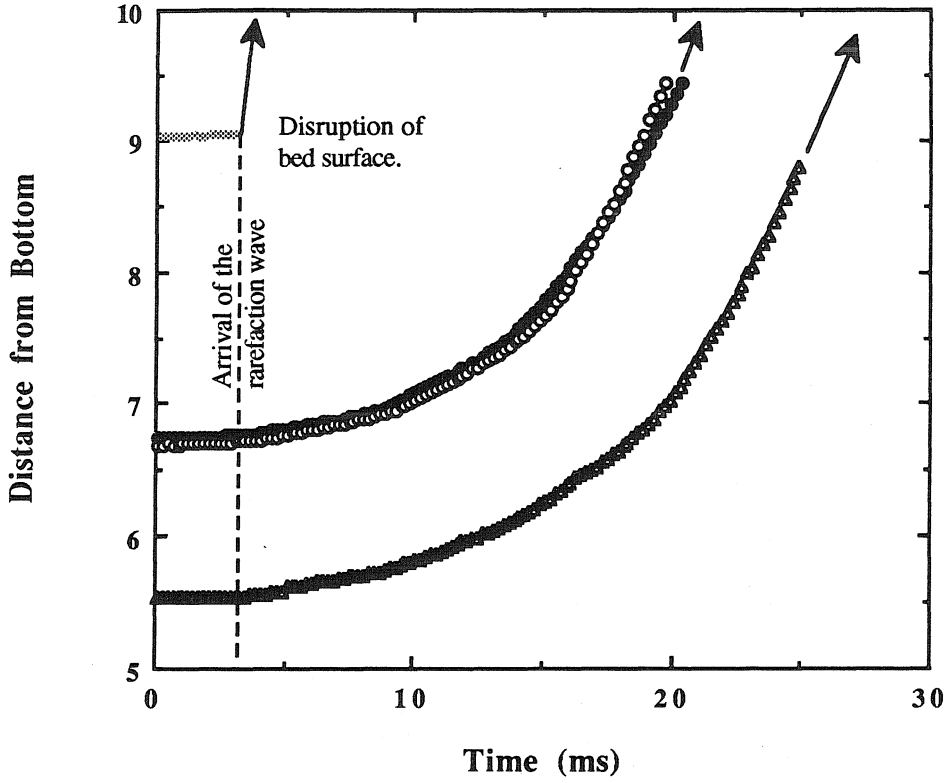

Figure 3.13 (b) Movement of three darkened particles in the motion picture of experiment FEB28-2. Note the simultaneous motion of the particles coinciding with the arrival of the rarefaction wave which is indicated by the beginning of vaporization at the bed surface. Particles are tracked until obscured by foreground material in the motion picture.

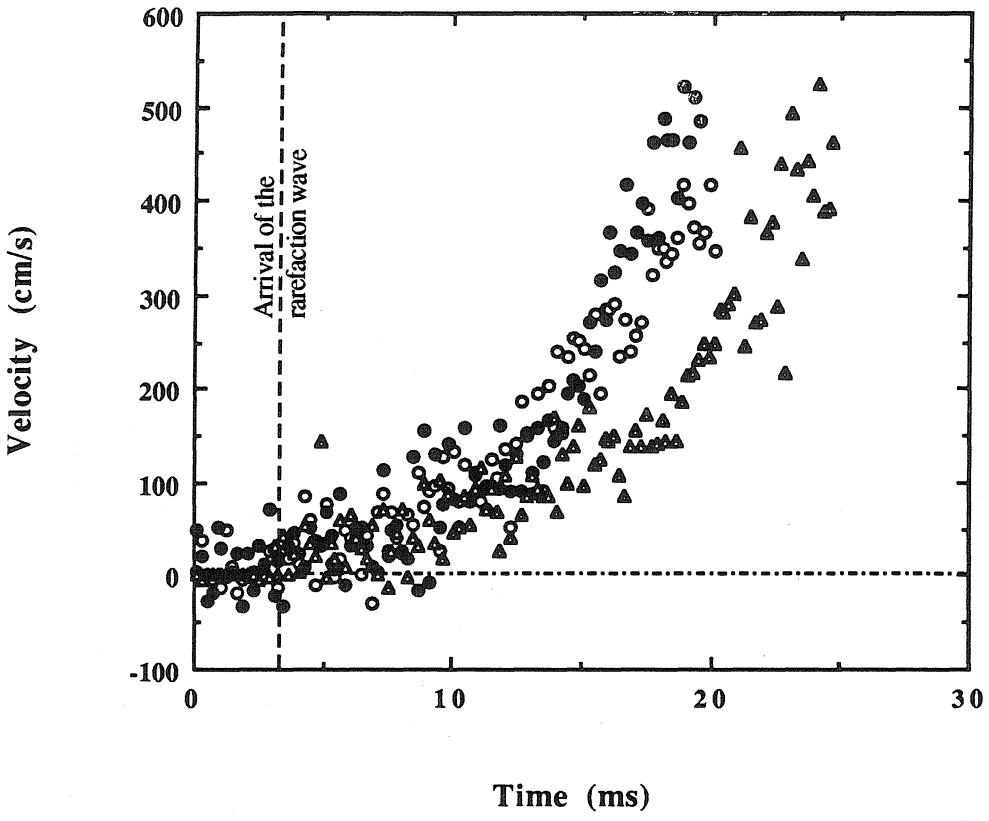

Figure 3.13 (c) Velocities calculated from the data in Figure 3.13 (b).

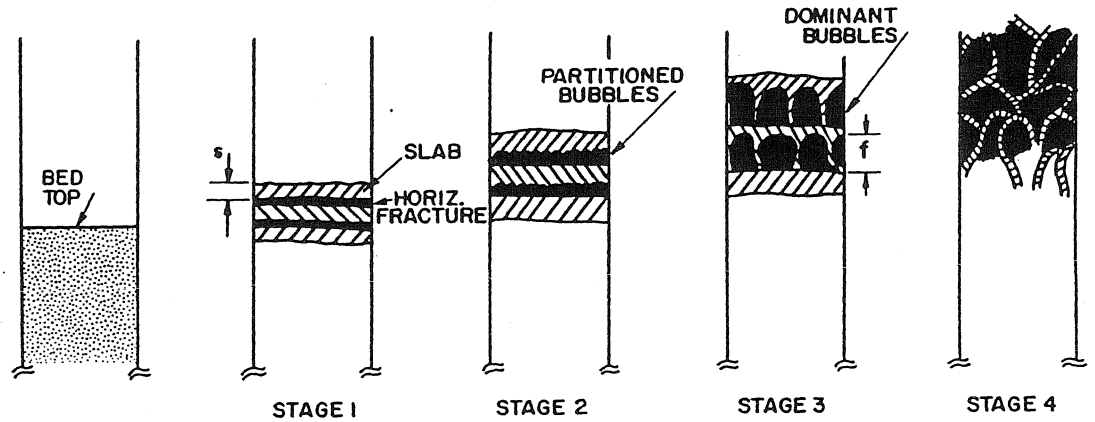

Figure 3.14 Break-up of a bed of monodisperse spheres by the expansion of gas in the particle matrix (Anilkumar 1989).

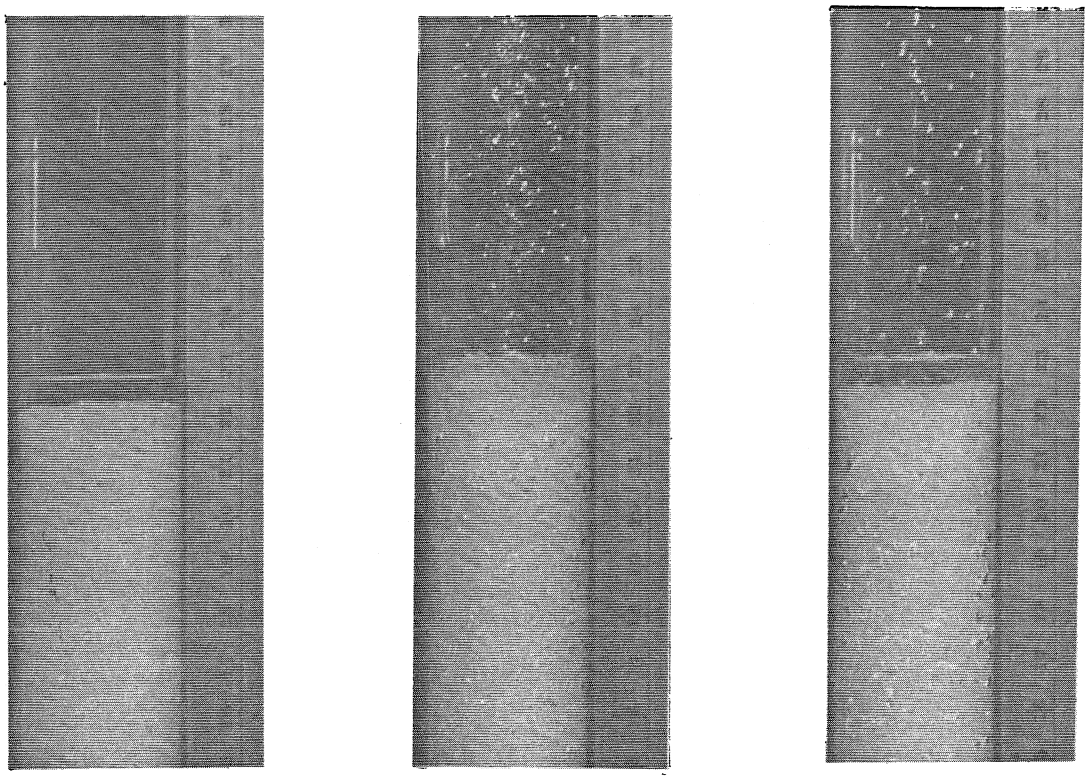

Initial State t = 0.3 sec t = 0.6 sec

Figure 3.15 (a) Sequence of photographs taken by a motor driven 35mm camera during experiment FEB21-1; the test fluid is R114 and the reservoir pressure is 2.1 bars. In the middle photograph, the displacement of liquid out of the particle matrix by the expansion of gas bubbles is visible. Some liquid droplets visible in the upper half of the photographs appear to have been ejected by the vapor production, but the particles have not been displaced.

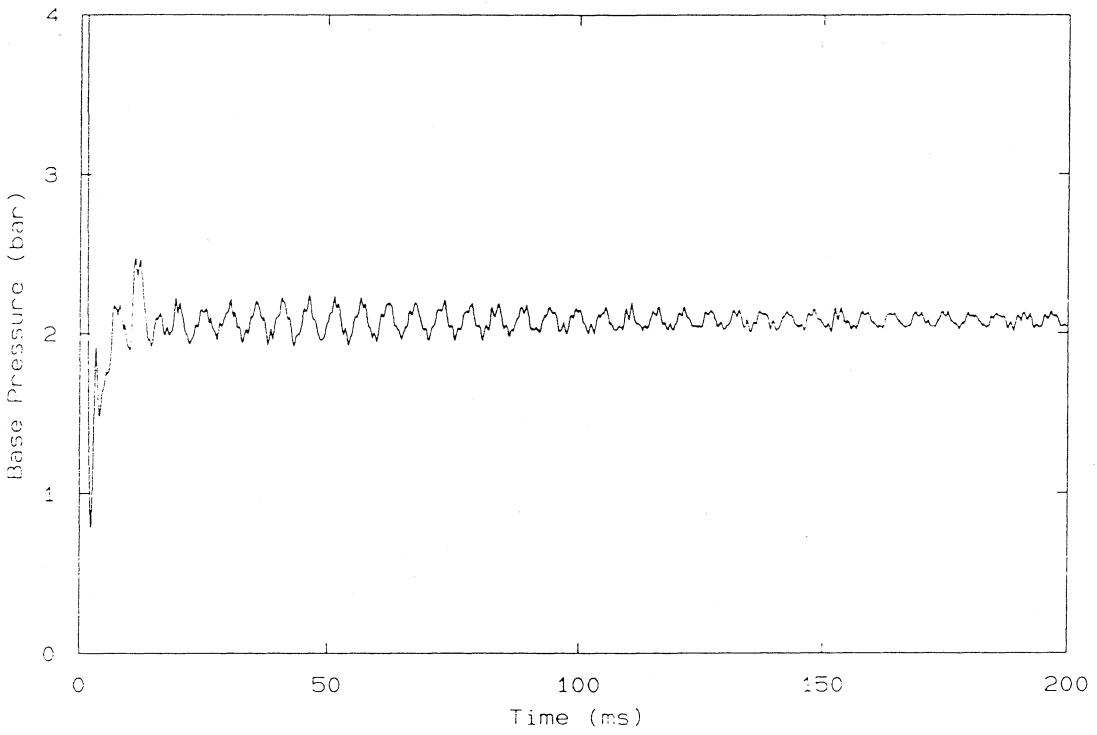

Figure 3.15 (b) Base pressure trace for experiment FEB21-1. Acoustic reverberations occur because the bed of glass particles is not disrupted by an explosive vaporization.

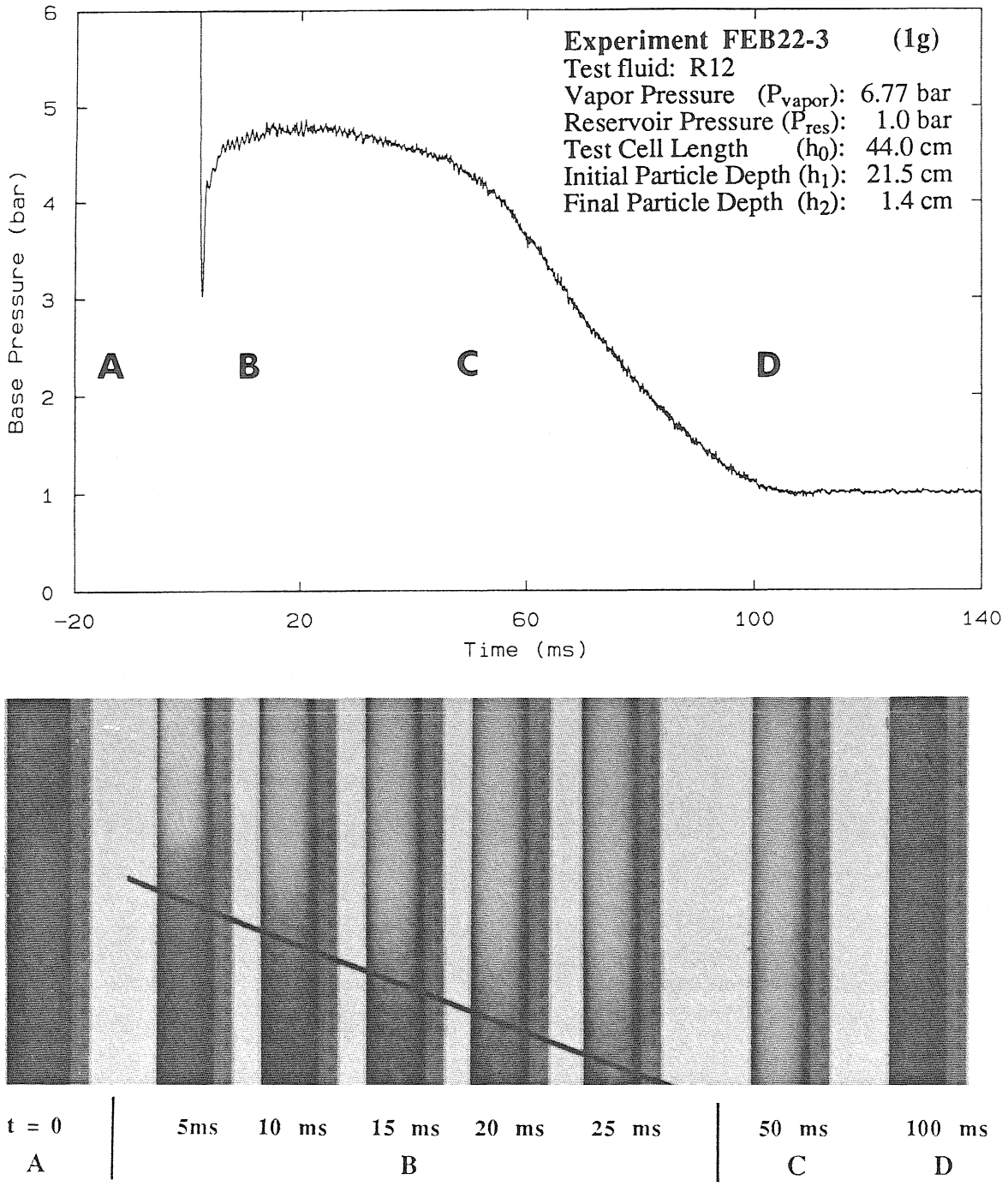

Figure 3.16 In this experiment, a more volatile refrigerant has been substituted for the test fluid used in FEB15-2 and FEB20-4. The front propagation in B is now much faster than in FEB20-4 (Figure 3.6) and the base pressure rise produced by the momentum flux is greater as a result (note vertical scale). The particles visible in D is indicative of the quantity remaining in the test cell after the experiment (h_2).

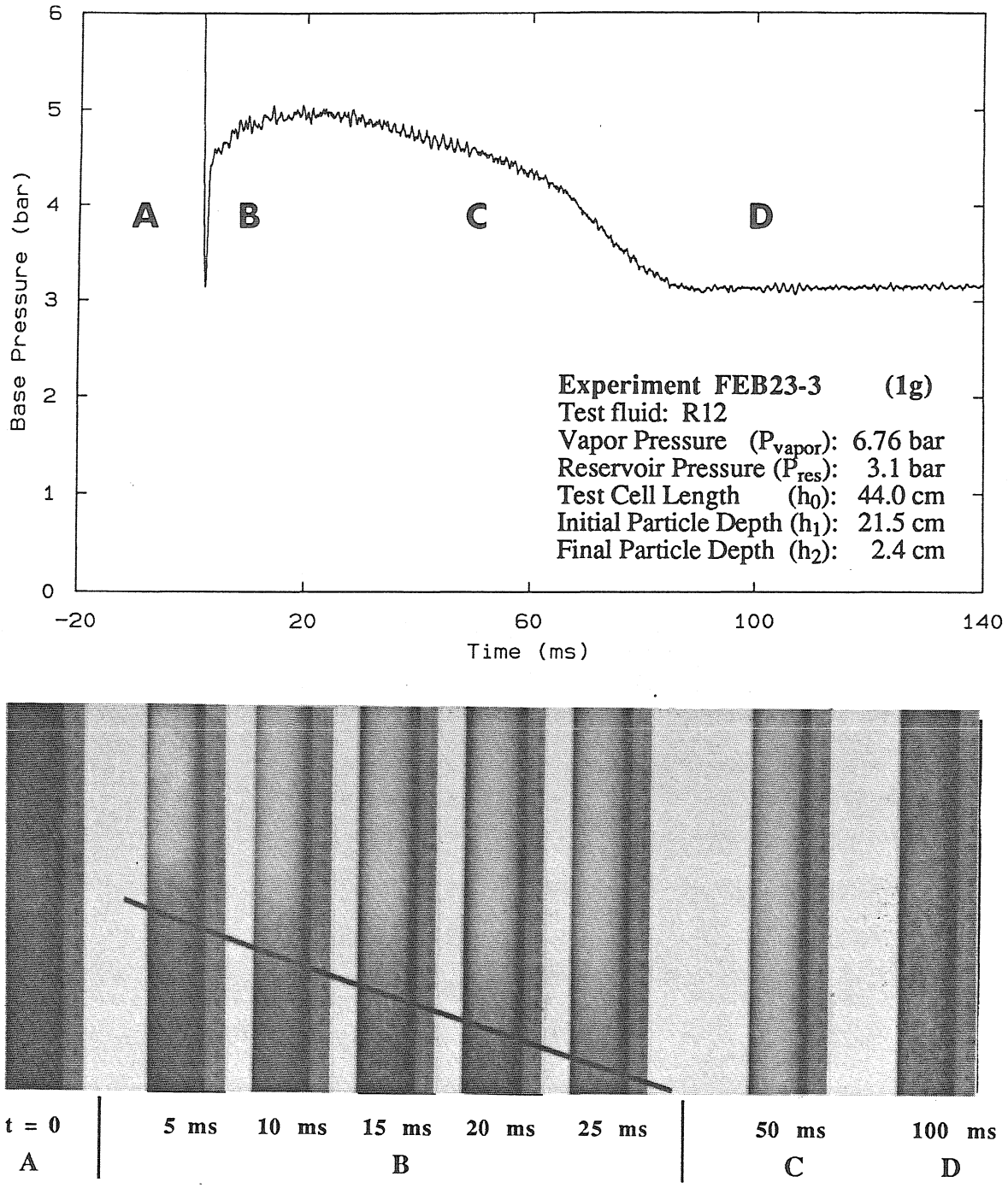

Figure 3.17 Venting the test cell to a pressure higher than FEB22-3 (Figure 3.16) produces little qualitative changes. The two experiments show that reservoir pressure has little effect on the level of the base pressure plateau. Photographic sequence B shows a in crease in the front speed during the first 10 ms (also in Figure 3.16).

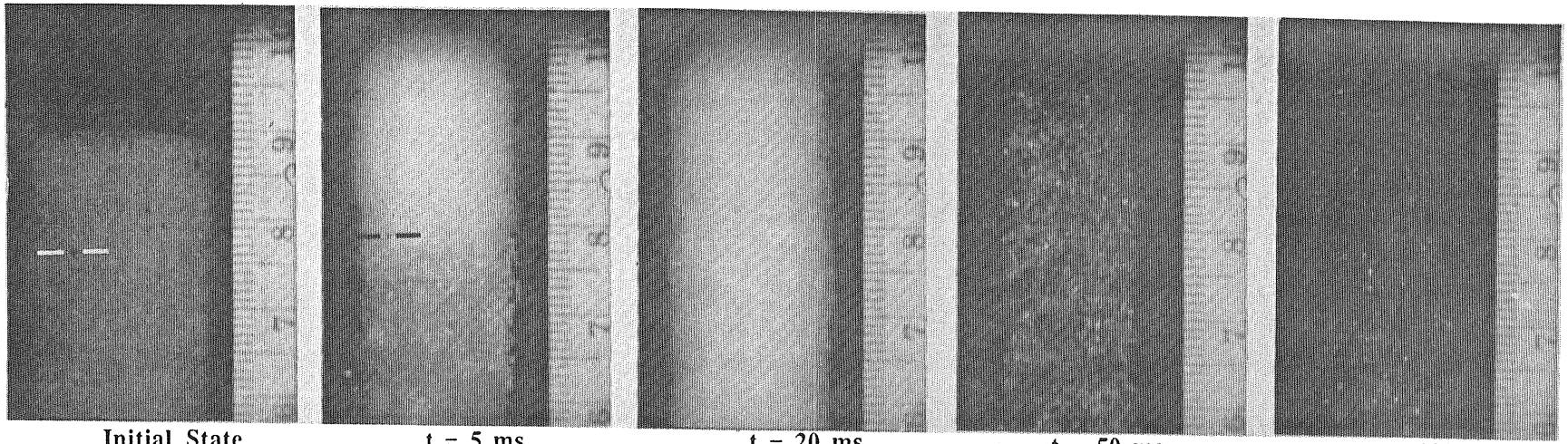

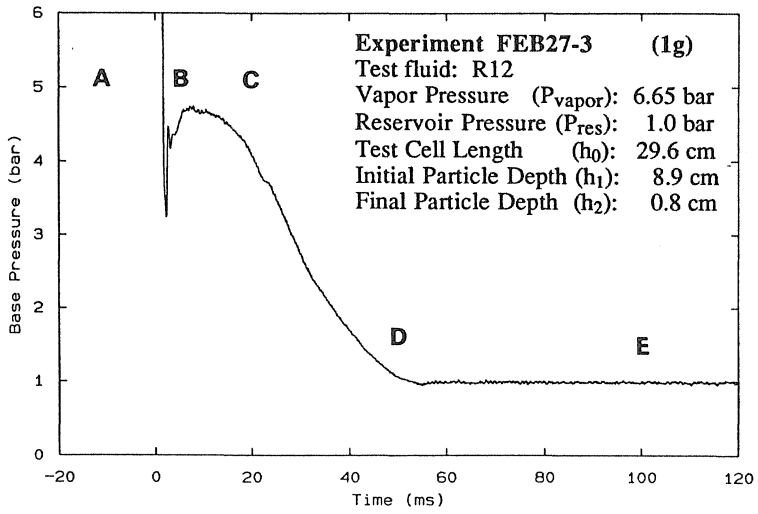

Figure 3.18 (a)

The experiment was conducted with a more volatile test fluid than one used in FEB28-2/3 (Figures 3.11/3.13). The behavior exhibited by this experiment is similar to what was observed in FEB28-3, but the time scales are shorter by afactor of about two. The darkened particle inidicated by a pair of bars shows the upward motion produced by the downward propagation of the light colored vaporization region.

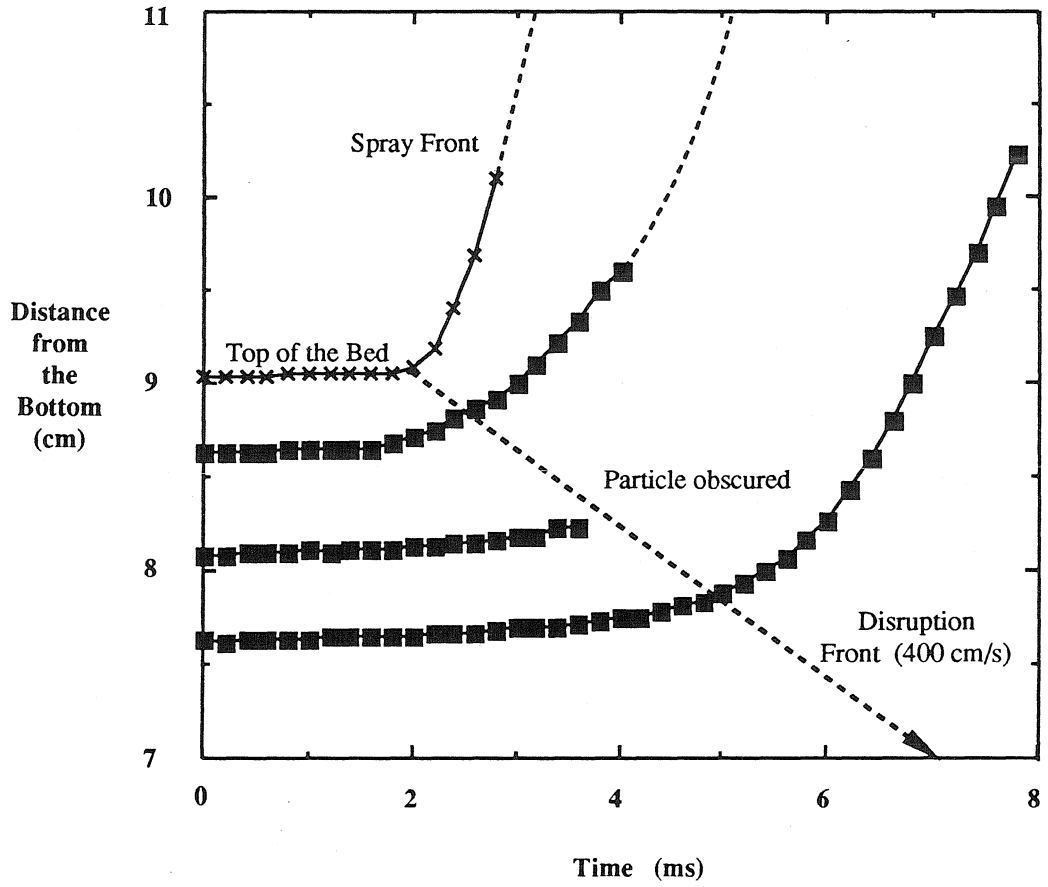

Figure 3.18 (b) Movement of darkened particles in the early stages of FEB27-3.

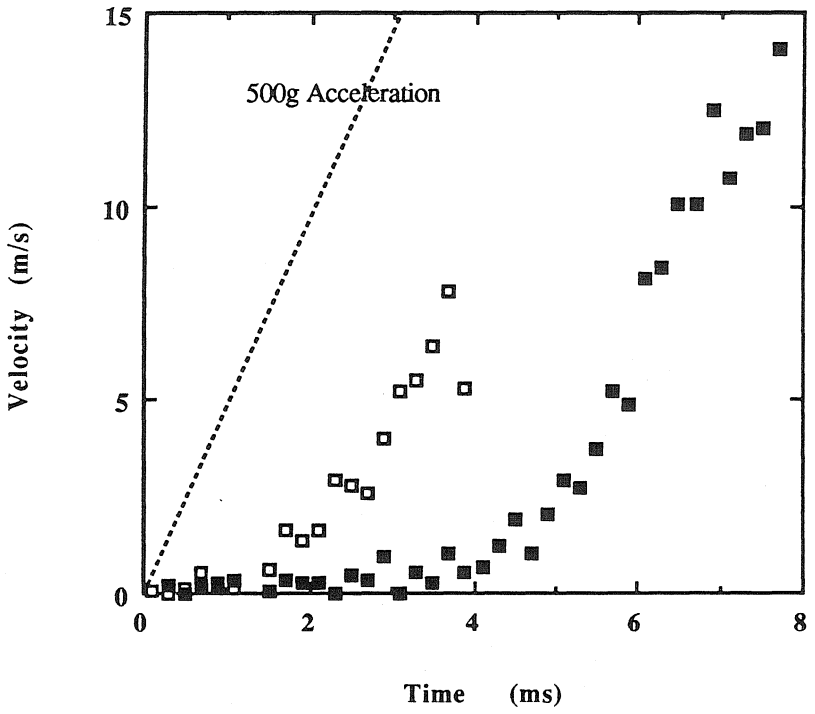

Figure 3.18 (c) The velocity of two unobscured particles visible in the motion picture of experiment FEB27-3. A line with slope equivalent to 500g acceleration is shown. The sequential acceleration of particles at different levels of the bed is indicative of a disruption front.

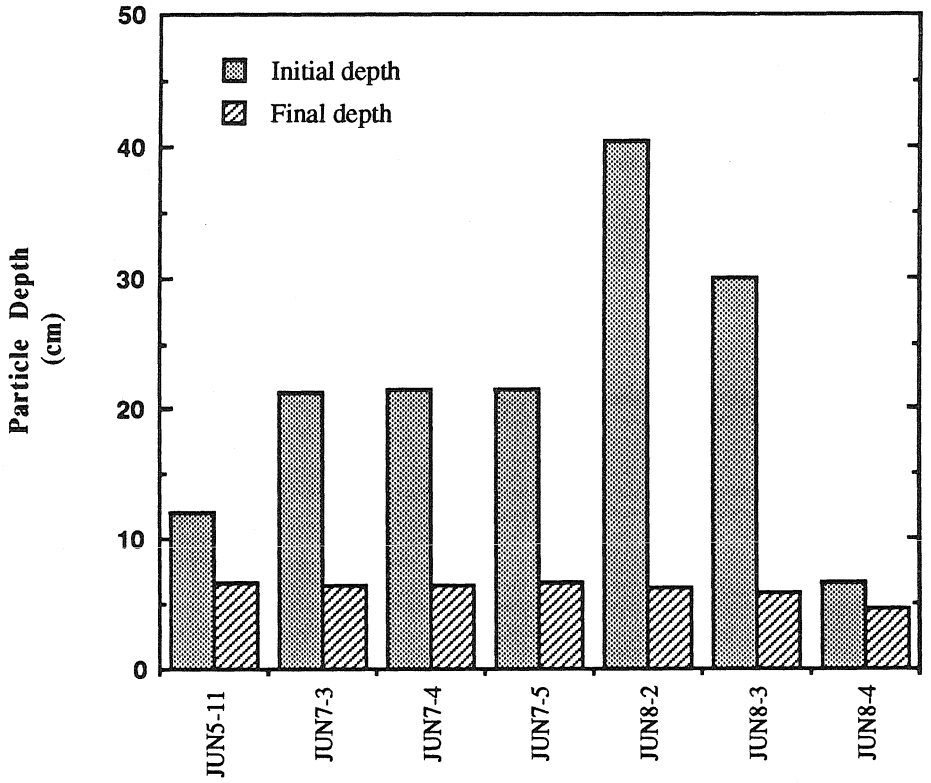

Figure 3.19 (a) Histograms showing the effect of initial particle depth on the particle depth after Type 1 particle transport process at 100g.

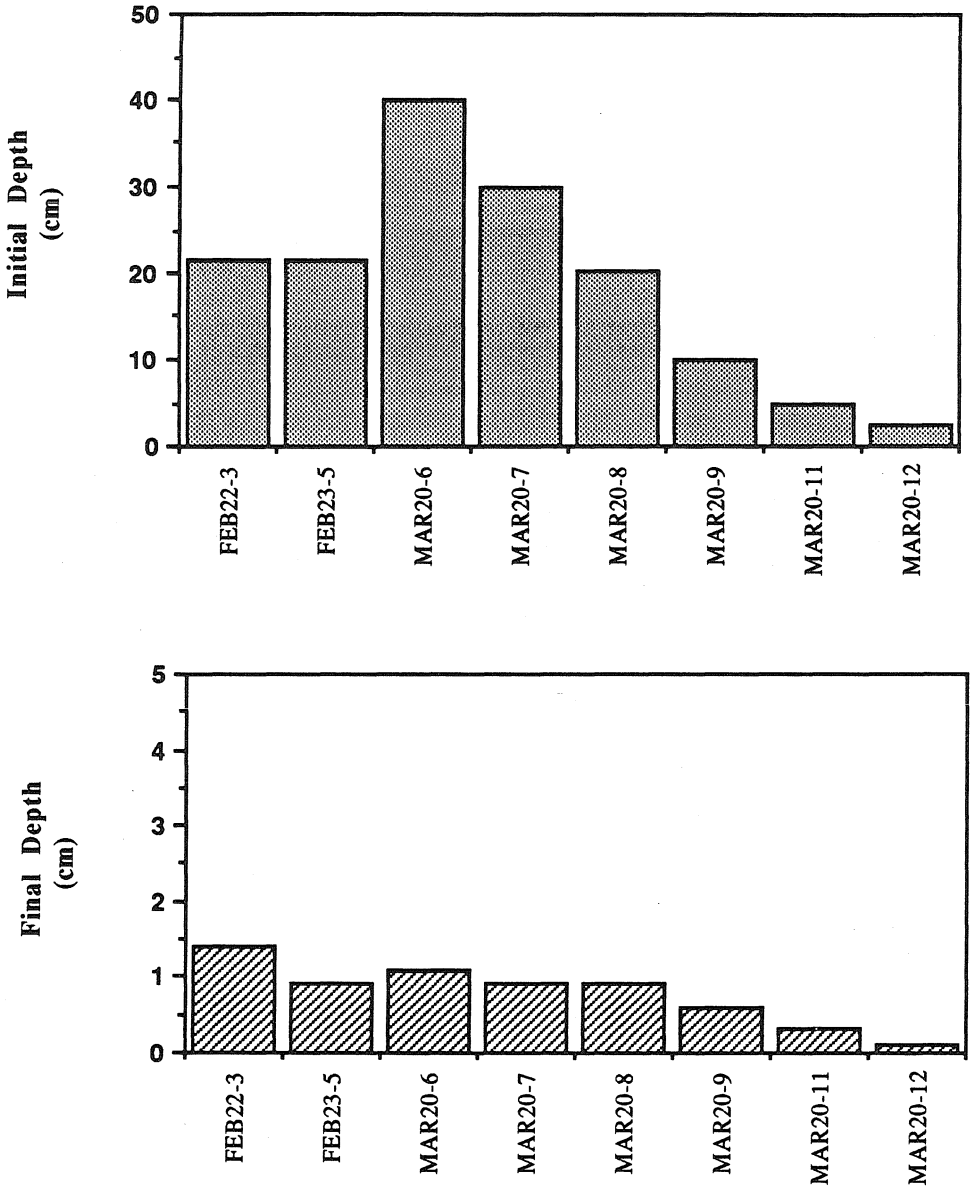

Figure 3.19 (b) Histograms showing the effect of initial particle depth on the particle depth after Type 1 particle transport process at 1g. Uncertainty in depth is less than ± 0.01 cm.

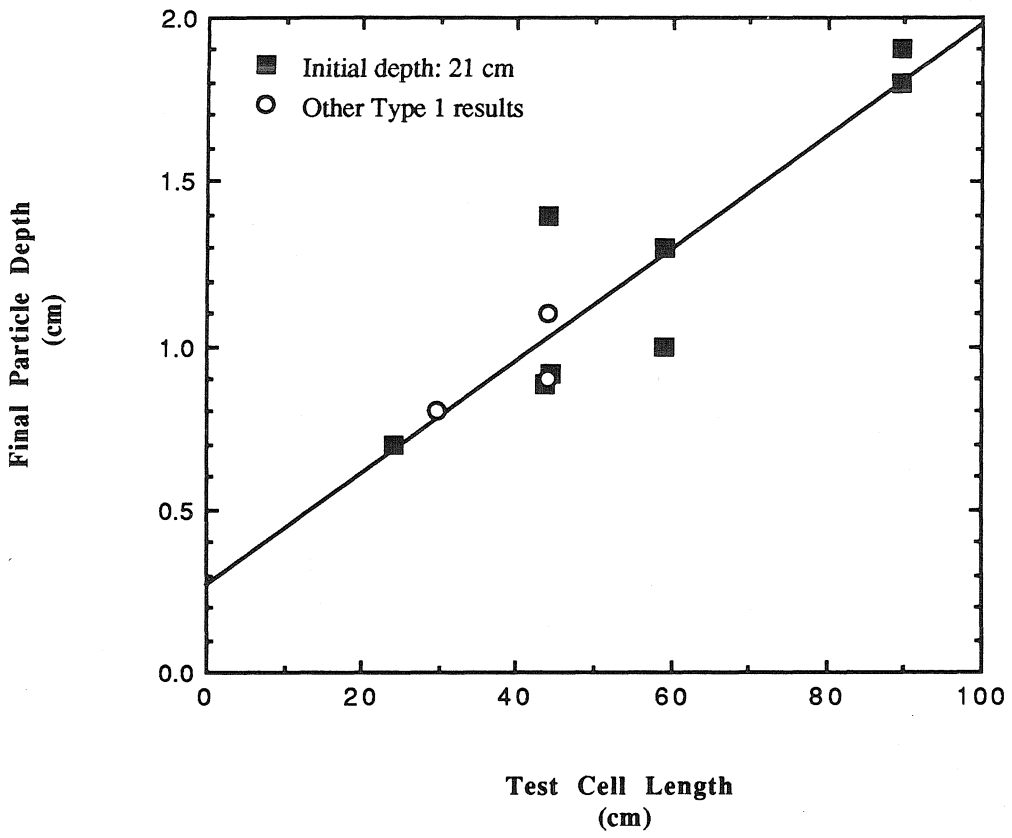

Figure 3.20 The effect of test cell length on the quantity of particles remaining after identical experiments with Type 1 transport. Test fluid is R12 and the test cell is vented to 1 bar at 1g.

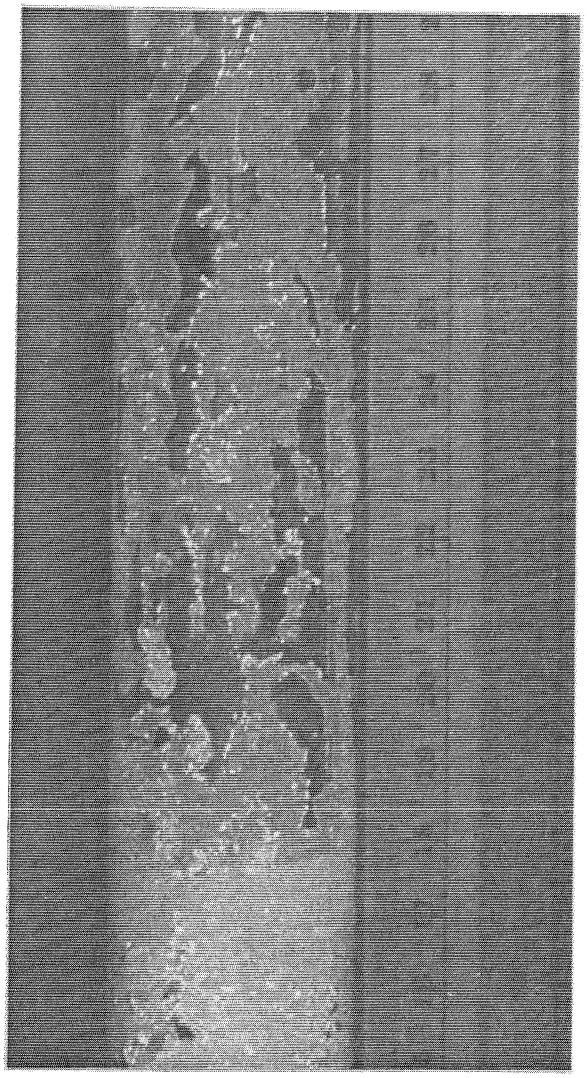

Figure 3.21 Photograph of test cell after a Type 2 process (Experiment FEB20-3).

The lower portion of the photograph shows particles which have settled at the bottom of the test cell. A slurry-like mixture of particles and unvaporized liquid clinging to the test cell sides defines bare areas which disappear with time as the slurry-like layer slides down the sides. The bare areas increase in area as reservoir pressure is decreased. These areas are believed to be remnants of low particle regions formed during the particle expulsion phase.

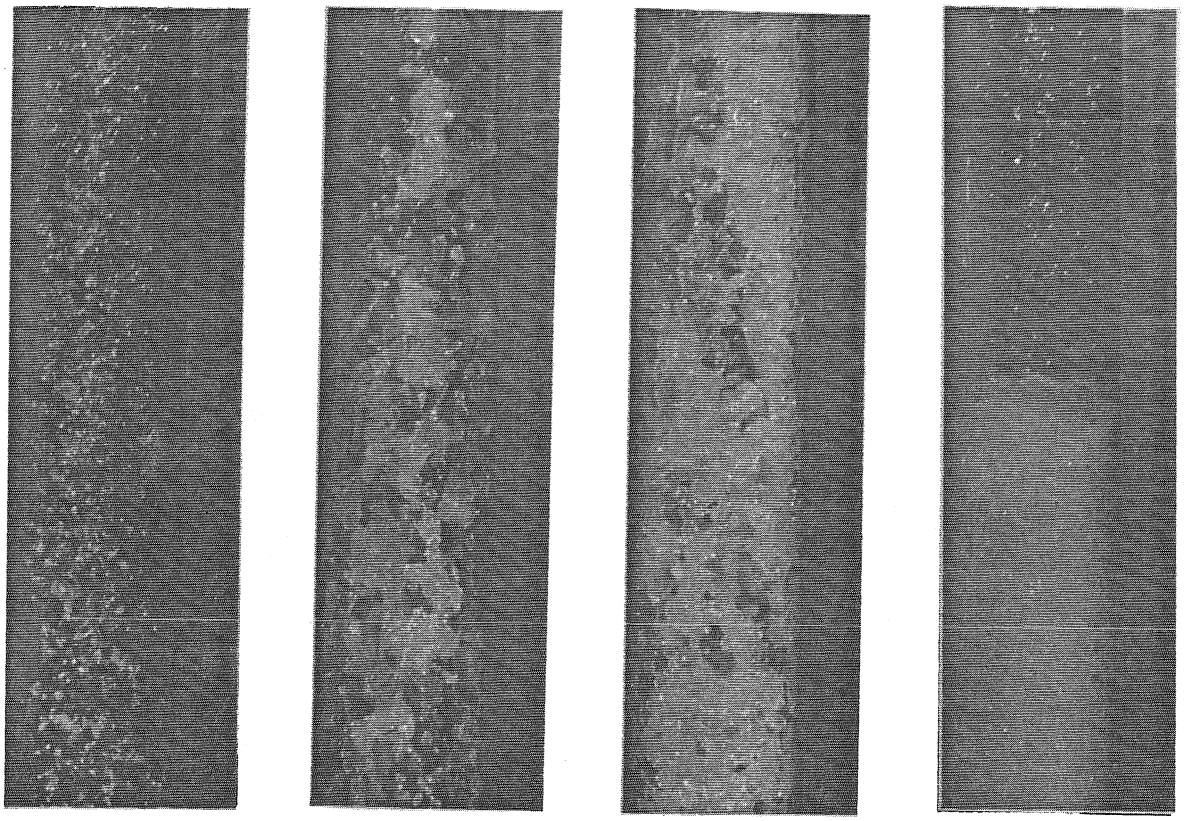

Type 1	Type 1/2	Type 2	Type 2
FEB20-4	**FEB20-2**	**FEB20-3**	**FEB21-1**
P_{res}/P_{vap} = 0.24	P_{res}/P_{vap} = 0.53	P_{res}/P_{vap} = 0.56	P_{res}/P_{vap} = 0.84
Ja = 0.27	Ja = 0.15	Ja = 0.13	Ja = 0.05
h_2/h_1 = 0.09	h_2/h_1 = 0.31	h_2/h_1 = 0.71	h_2/h_1 = 1.00
"Dispersed Annular"	"Annular"	"Churning Slug"	"Bubbly"

Figure 3.22 Photographs of material 210 ms after depressurization, before the expanded material settles down in the test cell. The vapor pressure of the test fluid R114 is: $P_{vap} = 2.58 \pm 0.1$ bars. The Jakob number (Ja) is calculated from the enthalpy of saturated fluid at the reservoir pressure (P_{res}). The ratio of particle depth before and after the experiment (h_2/h_1) indicate the quantity of particles expelled. (Initial depth: h_1 = 21.5 cm.) The multiphase flow in the photographs are categorized based on the descriptions by Wallis (1969).

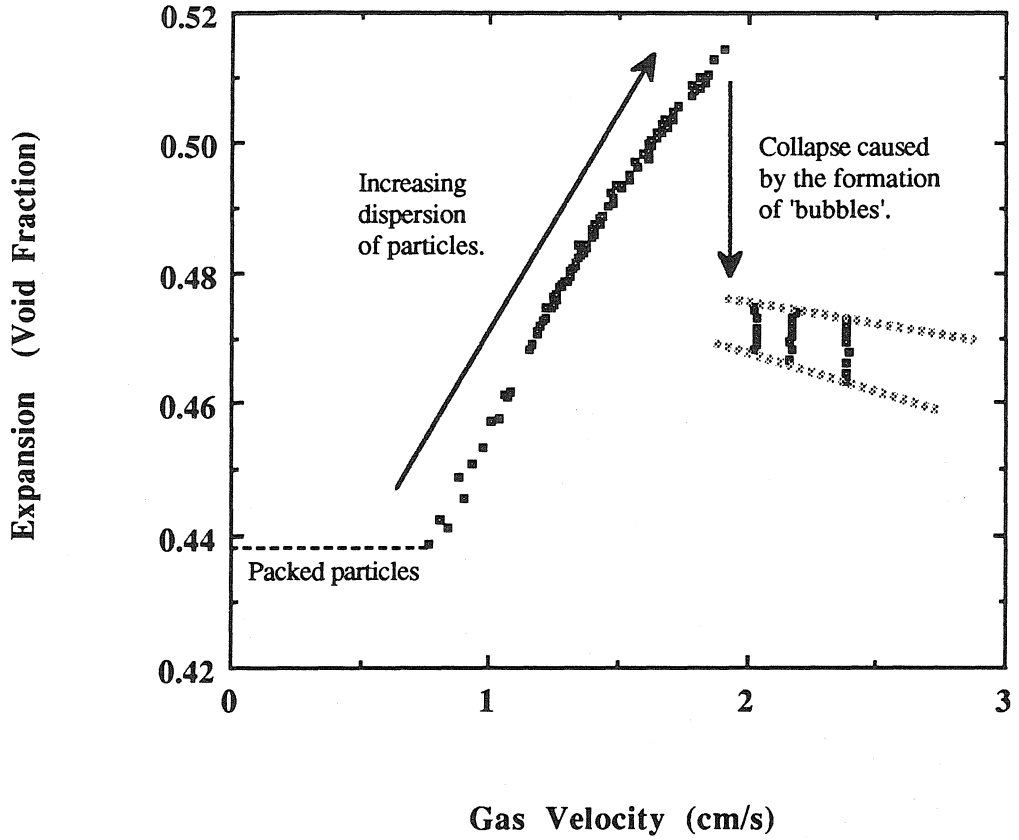

Figure 3.23 The effect of gas-particle segregation, or bubble formation, on a fluidized bed of mondisperse spheres. Data from Richardson (1971). The particles are 125 μm Perspex spheres (ρ = 1.185 g/cc) and they are supported against gravity by a flow of air. Air pressure is 1 bar. Expansion (void fraction) is the volumetric fraction of gas indicated by the volume occupied by the fluidized bed. Segregation of the components allows air to escape at higher velocities since it does not have to support any particles.

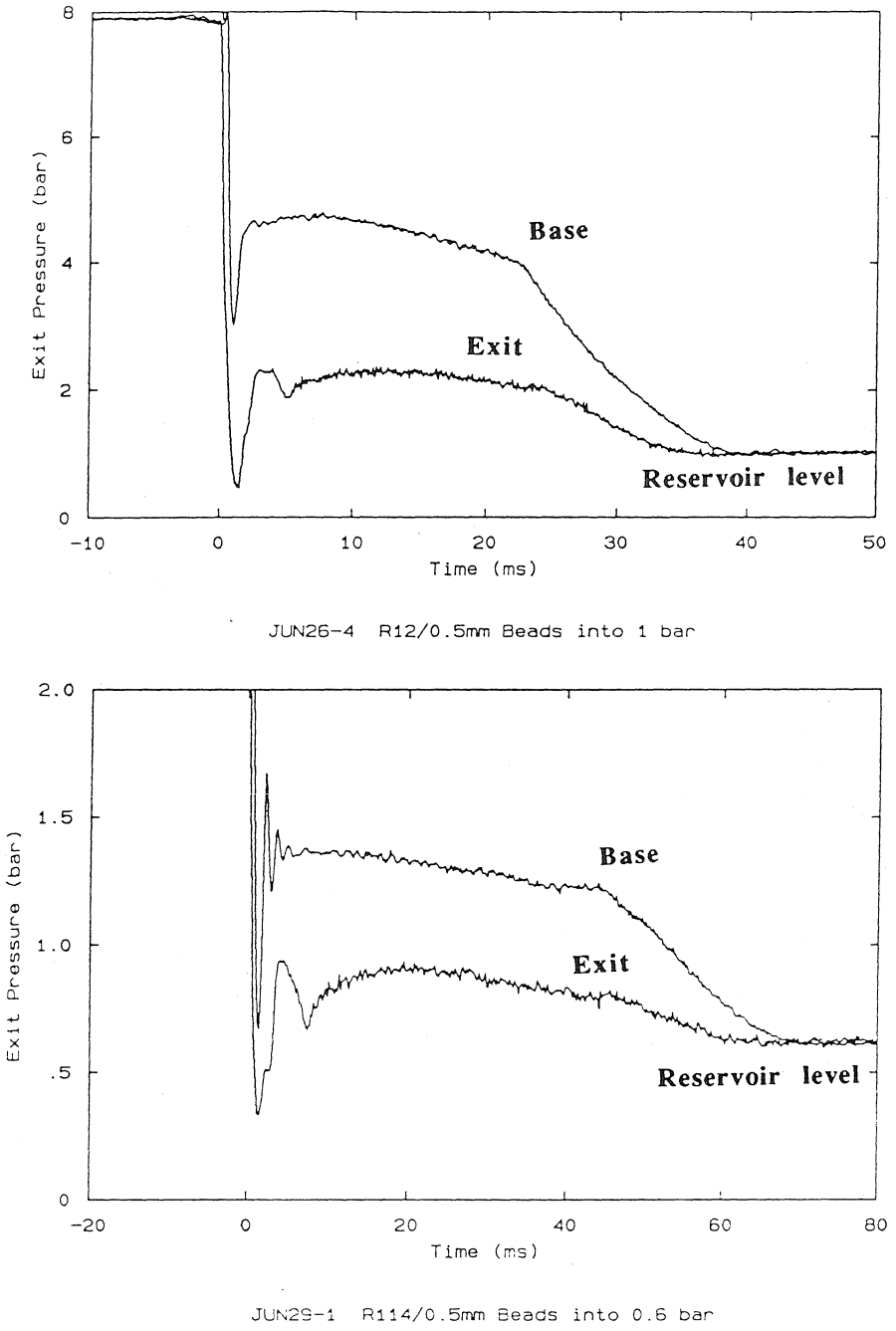

Figure 3.24 Pressure traces indicating the occurrence of gasdynamic choking at the exit of the test cell in Type 1 particle transport occurring with R12 and R114. For these measurements, the exit transducers had to be insulated from evaporative cooling; consequently, no particle impacts are registered by the transducer.

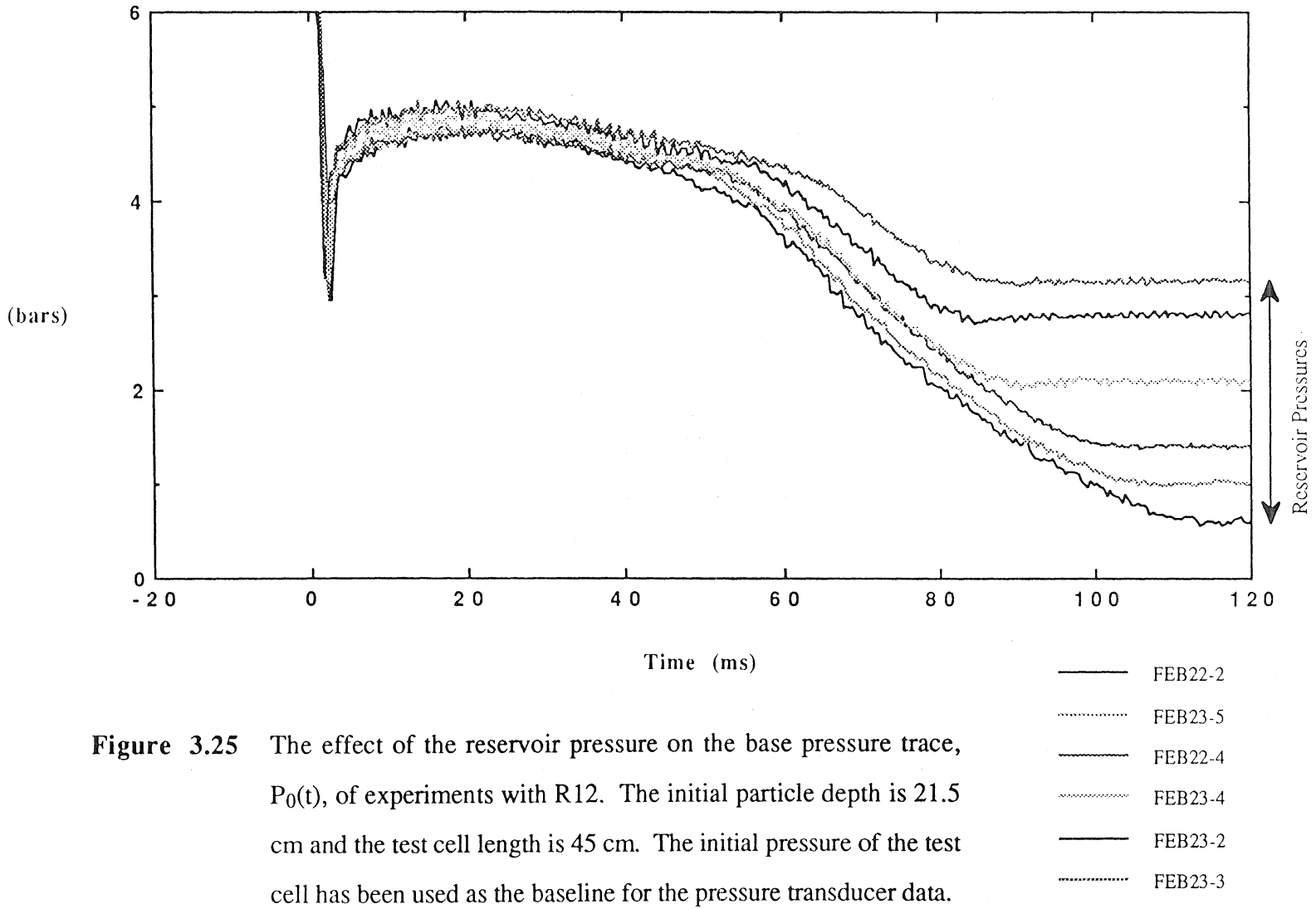

Figure 3.25 The effect of the reservoir pressure on the base pressure trace, $P_0(t)$, of experiments with R12. The initial particle depth is 21.5 cm and the test cell length is 45 cm. The initial pressure of the test cell has been used as the baseline for the pressure transducer data.

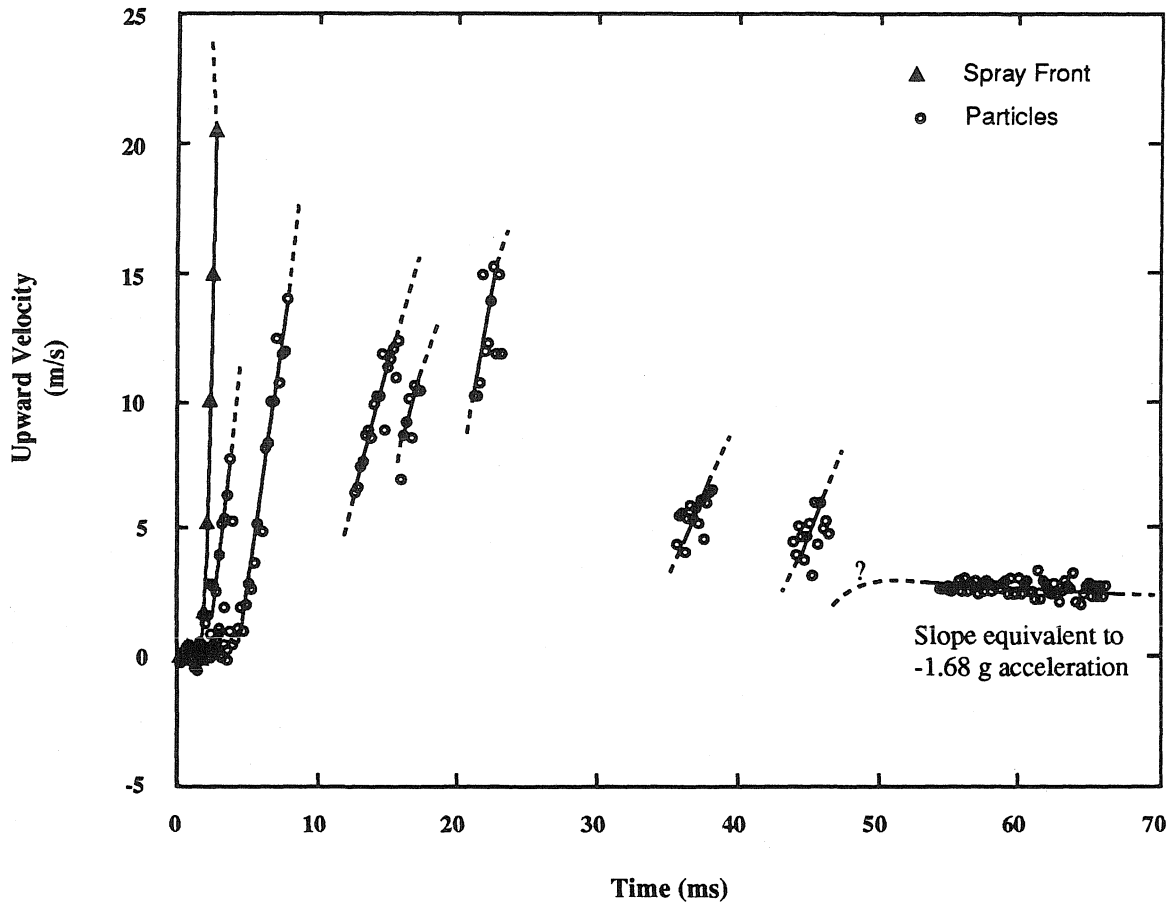

Figure 3.26 Velocity of the particles calculated from the motion picture of experiment FEB27-3 (see Figure 3.18). The slopes represented by each group of points show approximate acceleration of the beads. Note the negative slope of the rightmost group of points which indicates that the experiment begins the terminal period at about the 50 ms point; the base pressure has also decayed to the reservoir pressure by this time. Negative, or downward, acceleration greater than 1g at about the 60 ms indicates that the particular particle is decelerated by drag as well as gravity; the positive speed of the particle shows it is still moving upward. This means that the speed of the particle is greater than the speed of the vapor escaping the test cell after the 50 ms point.

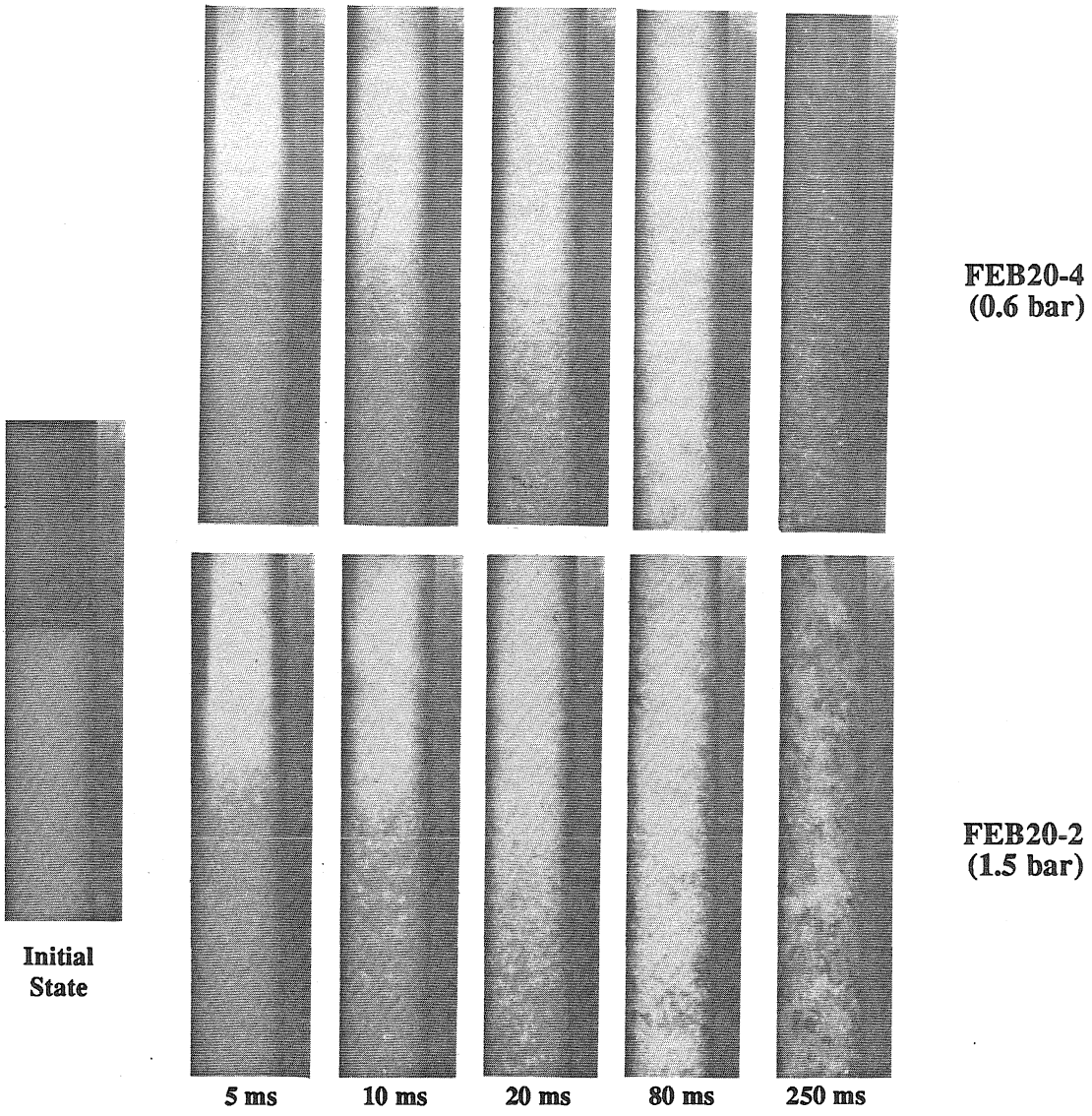

Figure 3.27 Photographic comparison of two experiments conducted at two reservoir pressures; both less than 0.55 times the vapor pressure (0.6 bar and 1.5 bar). Type 1 particle transport progress identically for at least the first 20 ms; the flow is too rapid to be resolved for about 100 ms afterwards. The abundance of particles and the bubble-like structures indicate that the higher reservoir pressure experiment made a transition to Type 2 process before the 250 ms point; the photograph of the other experiment shows a flow of dispersed particles observed in a Type 1 process.

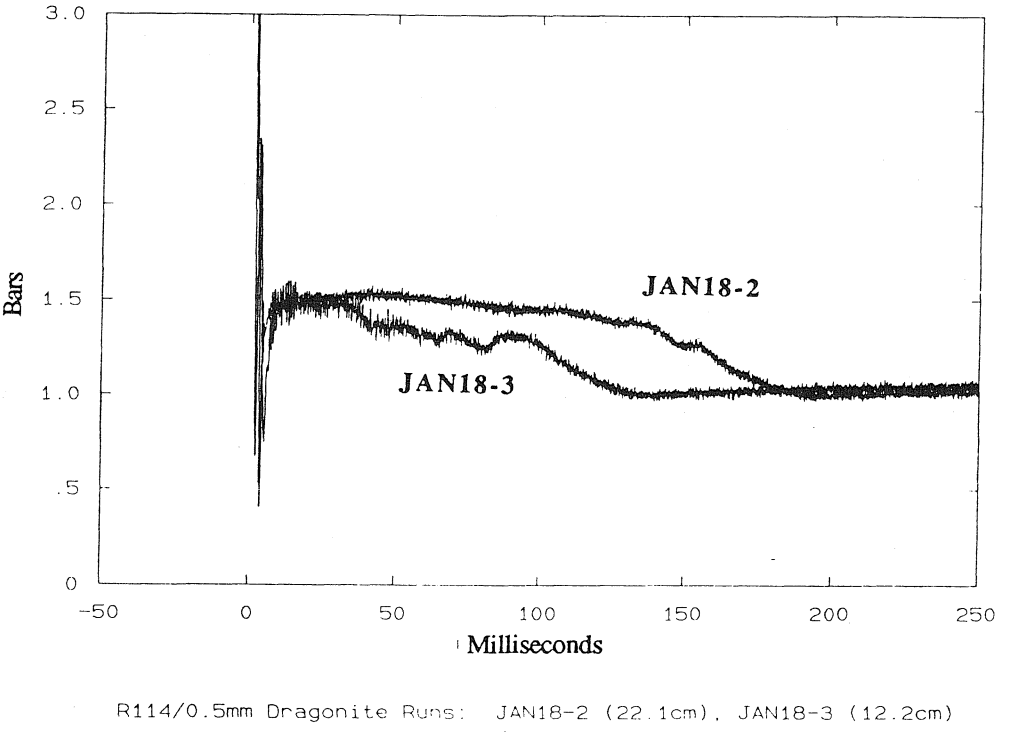

Figure 3.28 The base pressure traces of two experiments where Type 1 behavior is expected; the test fluid is R114 and the reservoir is at 1 bar. Monotonic decay of the pressure plateau is also found in similar experiments with R12, but fluctuations in the pressure traces are not. The base pressure decays to the reservoir level at a later time than expected from the speed of disruption fronts measured in other experiments. These results are believed to show the breakdown of Type 1 process.

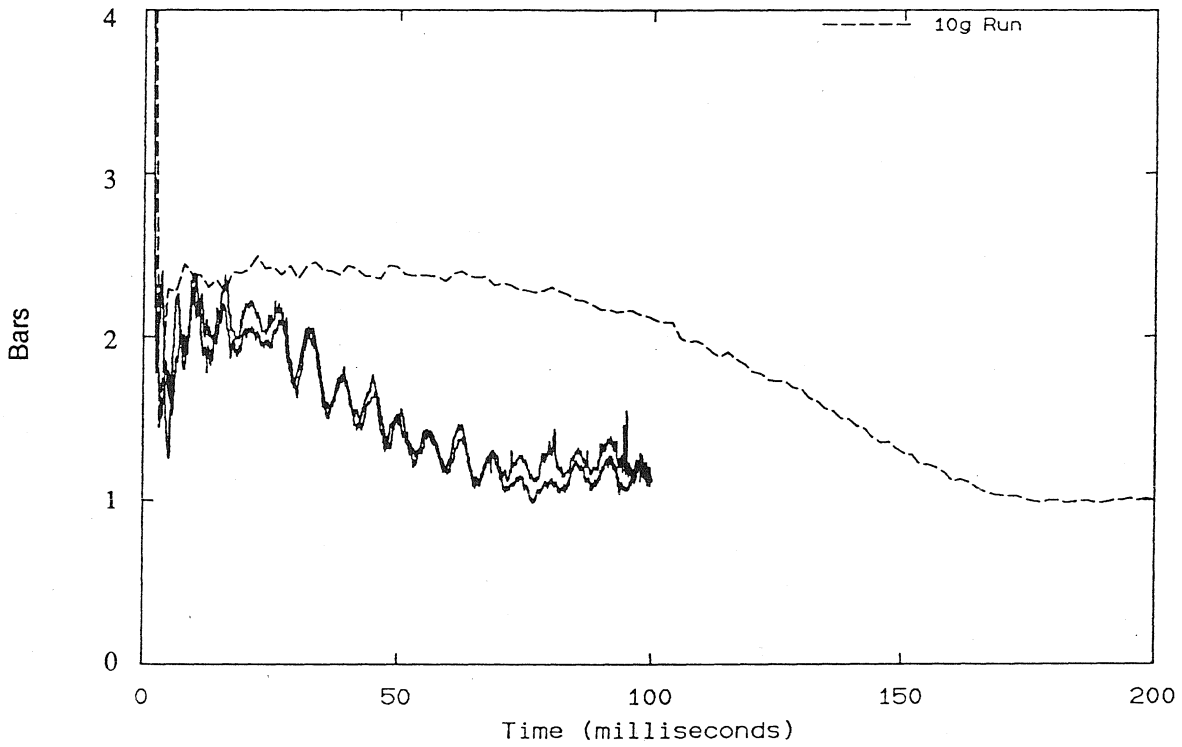

Figure 3.29 Base pressure traces of two experiments conducted at 100g with R114 as the test fluid and the test cell is vented to 1 bar: experiments JUN9-9 and JUN9-18 (overlapping solid lines). The acoustic reverberations in pressure and the rapid decay of pressure are consistent with Type 2 particle transport. An identical experiment at 10g (JUN9-12) has the base pressure profile (broken line) consistent with Type 1 particle transport.

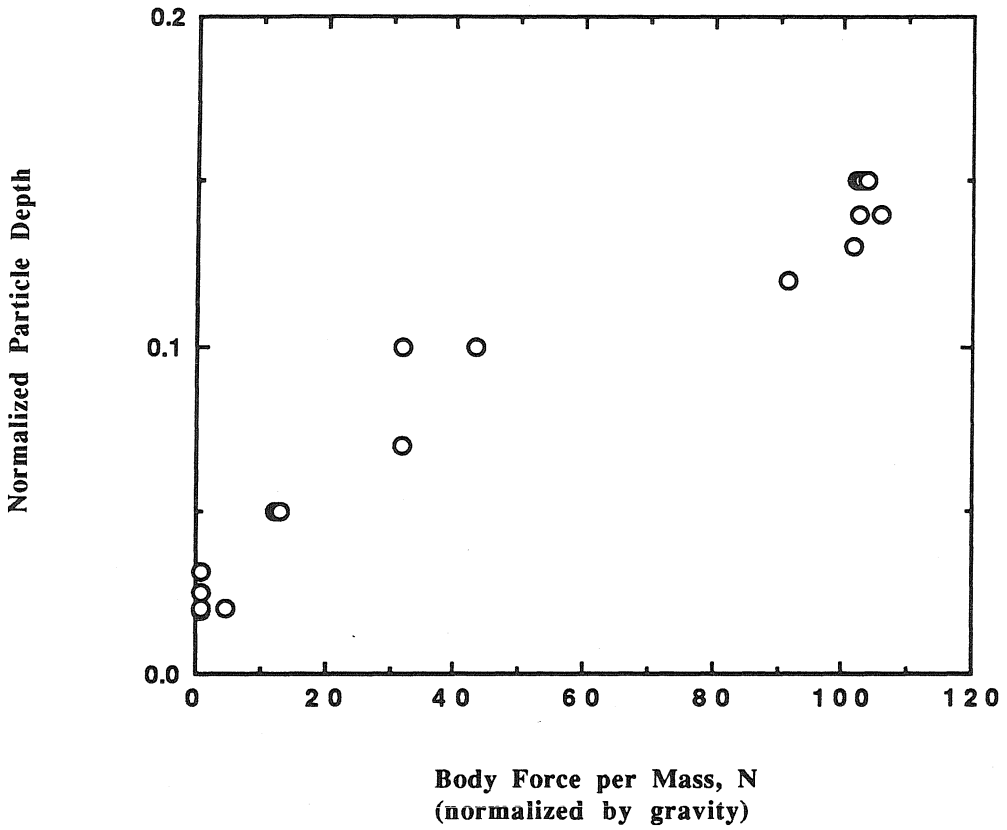

Figure 3.30 The effect of body force on the depth of particles resulting from a Type 1 process; the depth has been normalized by the test cell length. The data are for R12 experiments where a 45 cm test cell is vented to 1 bar.

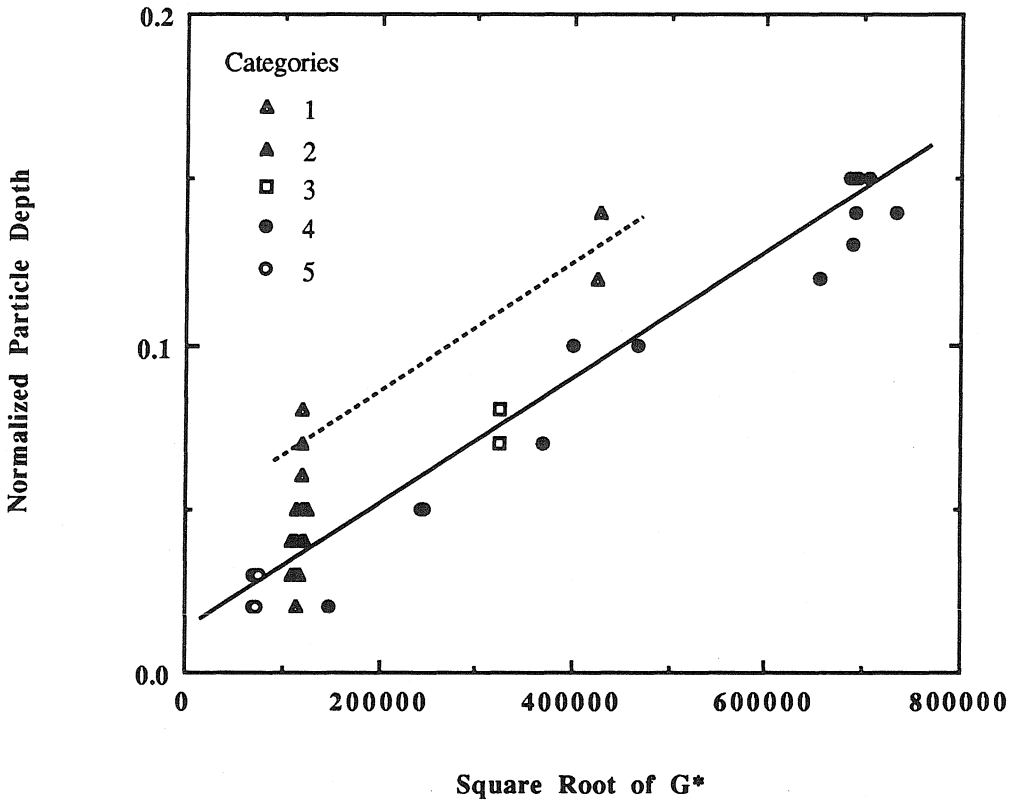

Figure 3.31 The effect of parameter G* on the final depth of particles in a Type 1 process; the depth has been normalized by the test cell length. The data are obtained from a variety of experiments producing Type 1 behavior; the experimental categories are described in Table 3.7. Note the higher but parallel trend of the Category 1 data (broken line) attributed to the premature breakdown of the Type 1 process.

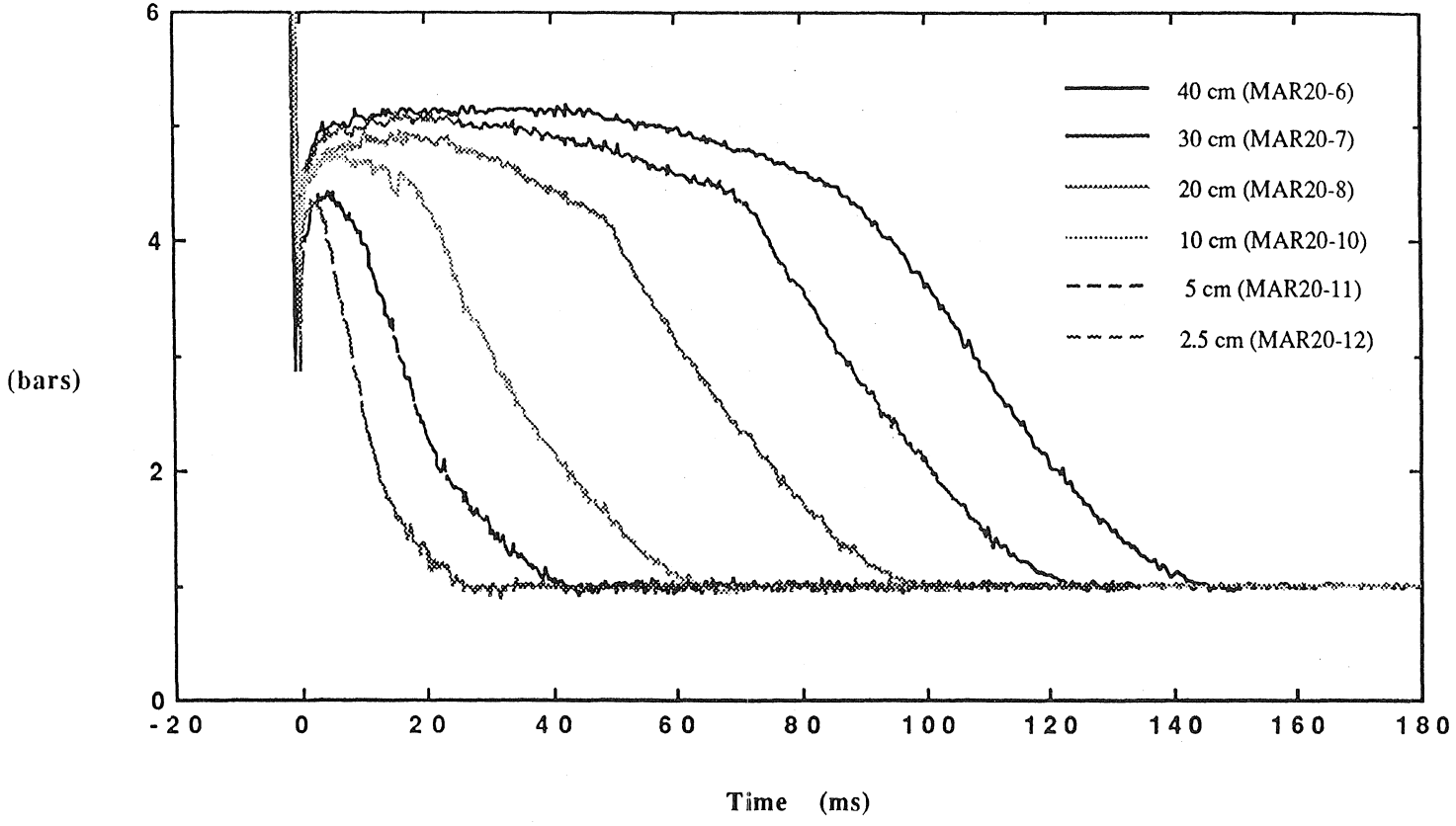

Figure 3.32 (a) The effect of initial particle depth on the base pressure trace, $P_0(t)$, of experiments using R12 as the test fluid. Experiments in which the initial particle depth is less than 10 cm do not result in final particle depths consistent with the empirical relationship with G*. The reservoir pressure (1 bar) has been used as the baseline for the pressure transducer data.

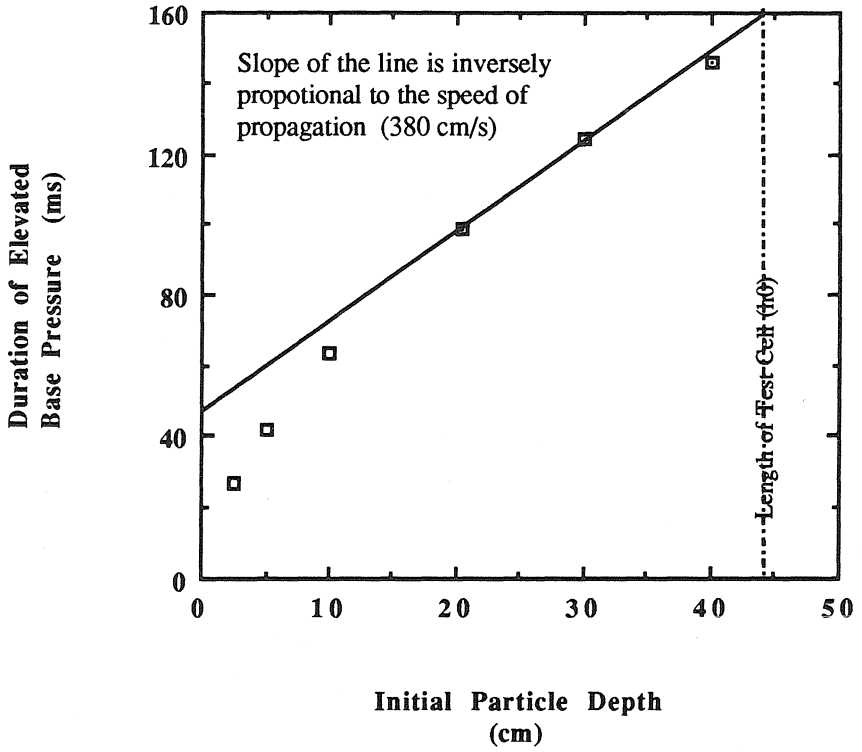

Figure 3.32 (b) The effect of initial particle depth on the time between test cell depressurization and the base pressure decaying to the reservoir level. The result shows the disruption front time necessary for the disruption front to travel a variety of distances.

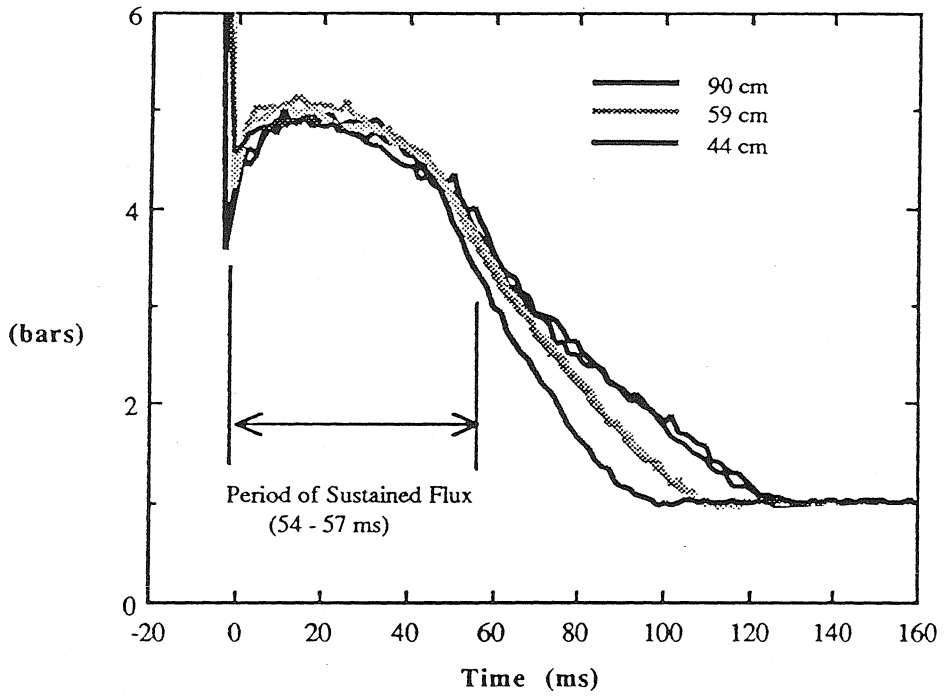

Figure 3.33 The effect of the test cell length (h_0) on the base pressure trace. Data are from experiments in which the test fluid is R12, reservoir pressure is 1 bar, and the initial particle depth is 21.5 cm. Overlap in the plateau portion of the pressure traces shows that Type 1 particle transport is not significantly affected by the test cell length.

Experiments: APR5-1 (90 cm)
APR5-3 (90 cm)
APR5-5 (59 cm)
APR5-6 (59 cm)
FEB23-5 (44 cm)

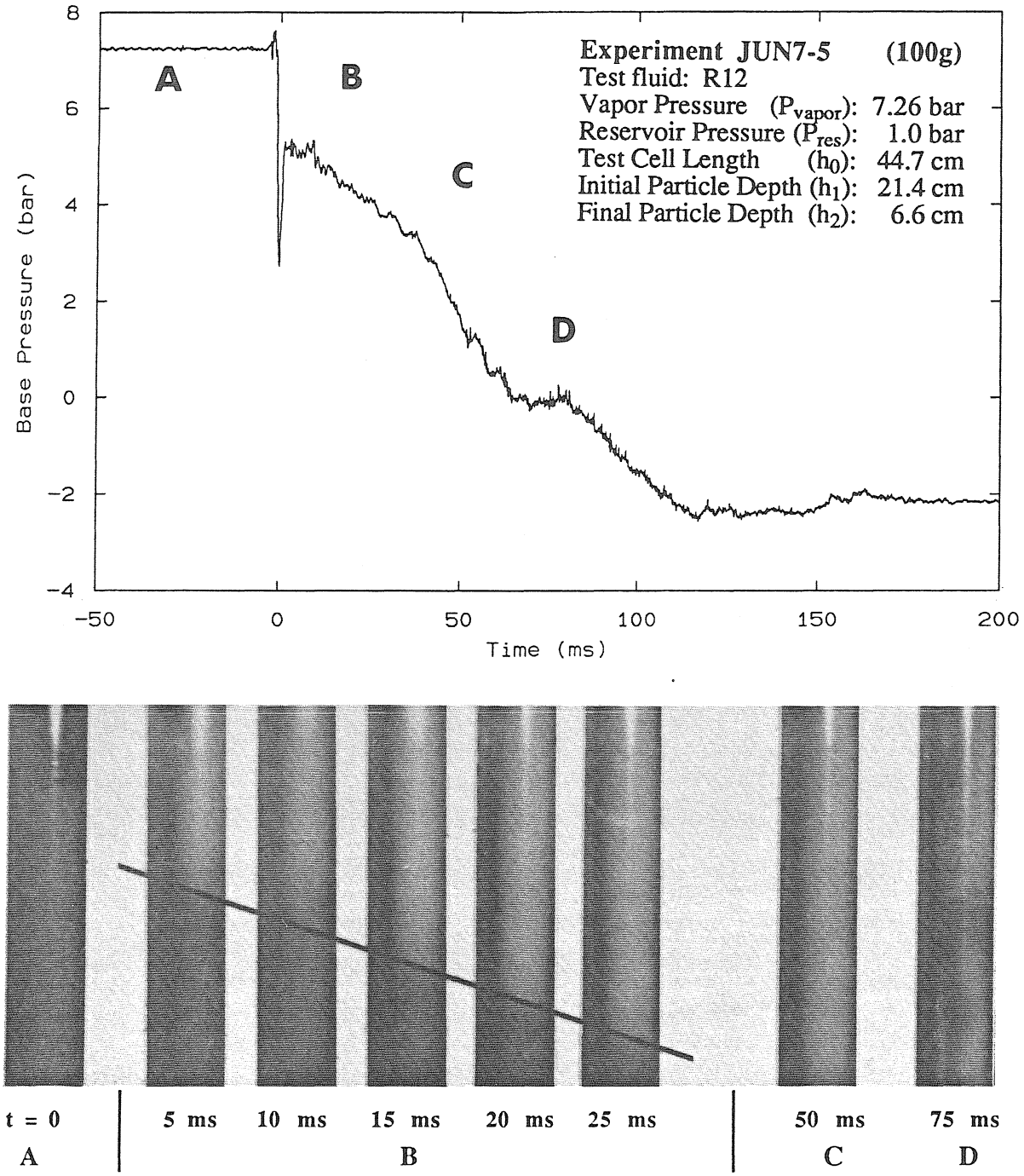

Figure 3.34 (a) This experiment conducted in the centrifuge can be compared to FEB22-3 at 1g. The increase in h_2 is produced by the centrifugal force restraining particle expulsion. The downward trend in the base pressure reflects decreasing weight of the particles in the test cell. Spurious image at 10 ms is caused by the film skipping a sprocket in the camera. The front speed in B is consistent with 1g results.

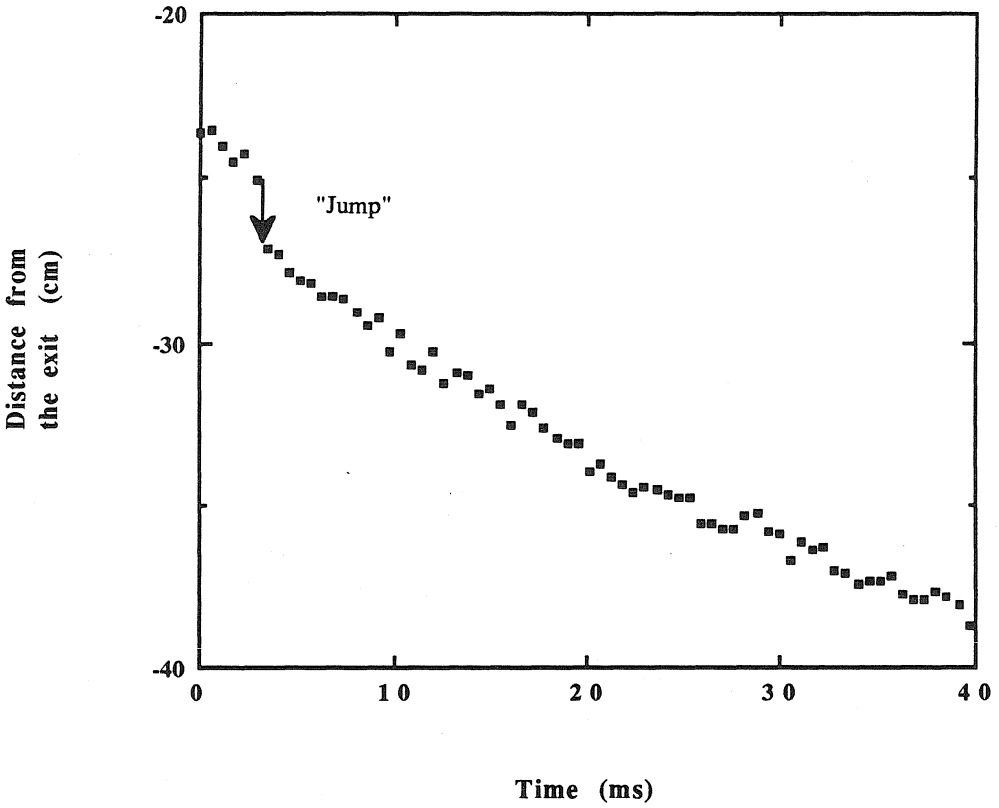

Figure 3.34 (b) Position of the disruption front filmed during Type 1 particle expulsion in the 100g experiment shown in (a). The test fluid is R12 and the test cell is vented to 1 bar. The "Jump" may have been caused by a momentary film feed problem in the camera.

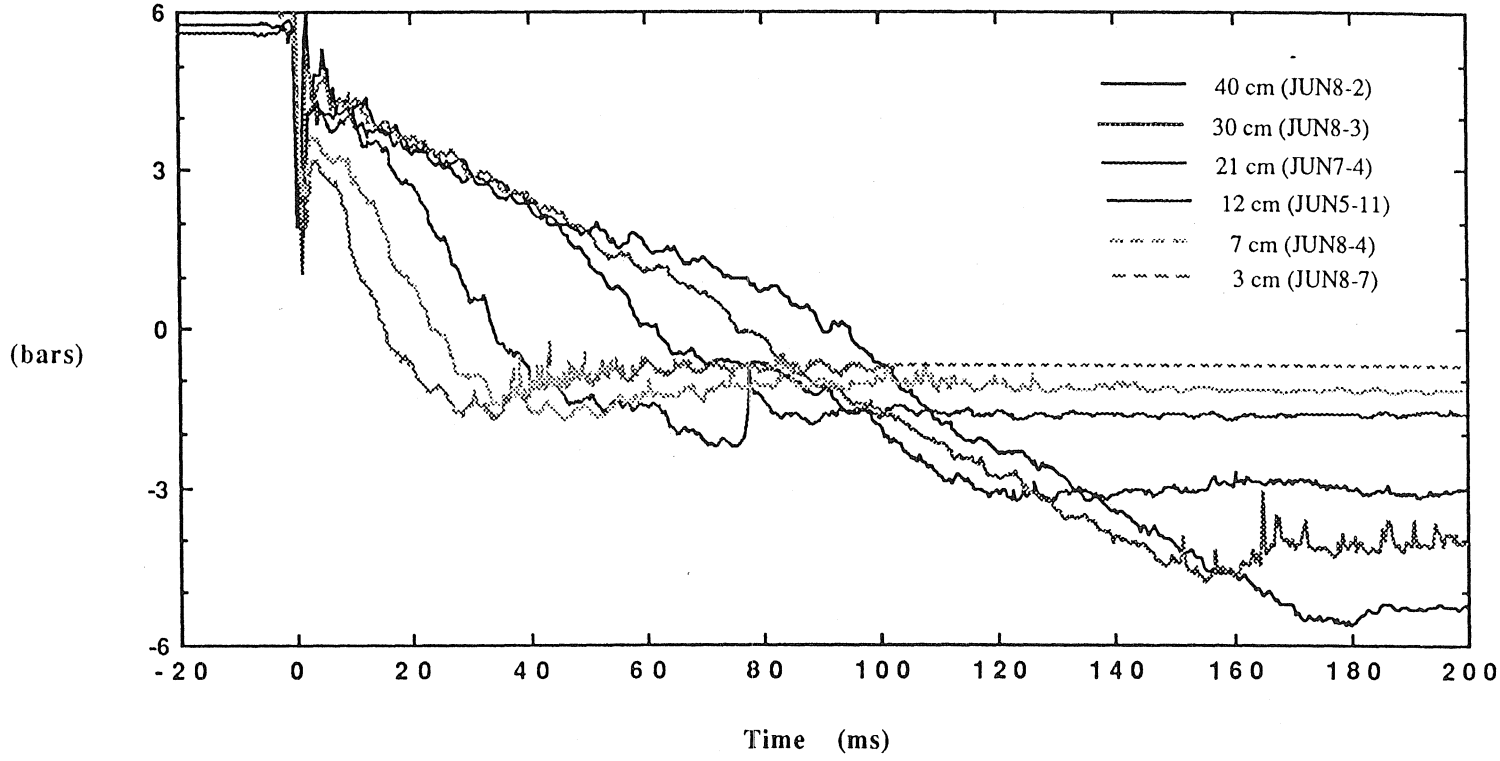

Figure 3.35 (a) The effect of initial particle depth on the base pressure trace, $P_0(t)$, of 100g experiments with R12 test fluid. Experiments in which the initial particle depth is less than 10 cm do not result in final particle depths consistent with the empirical relationship with G*. The initial pressure of the test cell has been used as the baseline for the pressure transducer data; therefore, the final presure levels reflects the change in hydrostatic pressure at the the base.

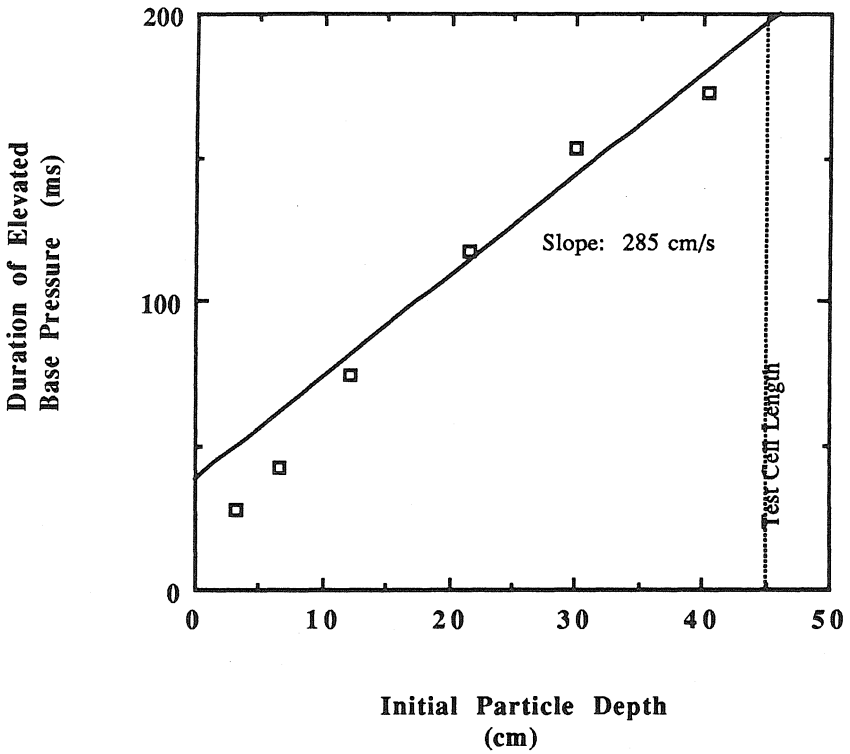

Figure 3.35 (b) The effect of initial particle depth on the time between test cell depressurization and base pressure decaying to the reservoir level for experiments in (a).

Chapter 4
Theoretical Analysis of the Experiments

The explosive vaporization of superheated liquid in the experiments (Chapter 3) results in a multiphase flow which is either Type 1 or Type 2 depending on the experimental conditions. Type 1 behavior occurs when the liquid is superheated by depressurization greater than a certain fraction of the vapor pressure. The resulting behavior is characterized by a disperse particulate flow produced by a disruption front. The analysis in this chapter exploits the quasi-steady front propagation by modeling the front as a discontinuity in steady flow by Galilean transformation. In experiments where the depressurization is insufficient for Type 1 behavior, particles and unvaporized liquid are displaced by expanding pockets of vapor. This process (Type 2) is not rigorously studied in this work.

Two analyses have been made of the Type 1 particle transport process. In *Control Volume Analysis #1,* the density and velocity at the test cell exit are derived using data from experiments with Type 1 behavior. A control volume which encloses the particle acceleration region is used in this analysis. As seen in the motion picture data, the particles accelerate at 500g in the lower portion of the acceleration region in the R12 experiment (Figure 3.18c). In Figure 3.5, it can be seen that uppermost particles in the bed accelerate at approximately the same rate for about 10 cm to a speed which is maintained to the exit. Based on these data, the following analysis assumes a particle velocity history which is shown in Figure 4.1a. This analysis is based on density, velocity, and pressure for the material upstream of the fragmentation front and pressure measured at the test cell exit. Conservation of mass and momentum are used to calculate the density and the velocity at the exit. The exit velocity in a typical experiment is found to be much greater than the velocity difference between vapor and particles necessary for vapor drag to equal the particle weight. Since particles, liquid, and vapor move at nearly the same velocity, the flow can be modeled as a homogeneous flow and the vapor fraction of the multiphase flow

in the experiments can be approximated. These results are compared with the potential for vaporization based on energy available in the superheated liquid-particle mixture.

In *Control Volume Analysis #2,* the disruption front is analyzed as an adiabatic, gasdynamic discontinuity with gasdynamic jump conditions. If the mass flux and entropy production are maximized by the disruption front, a sonic flow can be expected in liquid-vapor system.[1] Since the sound speed for nonequilibrium multiphase flow[2] at the disruption front is not known, rapid vaporization is assumed to release a vapor at sonic speed at the disruption front.[3] The analysis, based on mass and momentum conservation, suggests that sonic flow can only occur if downstream pressure is sufficiently below the upstream pressure. Type 2 behavior is believed to occur when the conditions necessary for the disruption front, thus Type 1 behavior, can not be satisfied.

4.1 Steady Flow Model

The disruption front timed over various distances suggests that the front moves at a relatively constant speed, thus the mass flux during the front propagation is quasi-steady. The quasi-steadiness is also indicated by the gradual change in mean base pressure. For example, in experiment FEB27-3,[4] the variation in the base pressure is ±5% of the average level (4.5 bars) during the 20 ms plateau; the rate of change is less than 0.025 bars per millisecond after the initial pressure rise. Based on acceleration by the uppermost particles in the bed, the characteristic acceleration time for a 0.0.5 mm glass particle by the explosive vaporization of R12 is about 3.6 ms at 1g.[5] Therefore, the change in base pressure during a particle's acceleration is about 0.09 bar, or 2% of the plateau in base pressure. (The data in Figure 3.32 suggest that the change is less for experiments with greater initial particle

---

1 This approach which assumes that the process maximizes the entropy is not new. For example, Sellens and Brzustowski (1985) used this approach to model the atomization process.

2 As opposed to a homogeneous flow defined by Wallis (1969) where the flow components have the same mean velocity.

3 Marble (1971) refers to the vapor sound speed as the *frozen sound speed* in a particle-vapor flow.

4 See Figure 3.15 for details of this experiment.

5 The acceleration time is based on Figure 3.5.

depth.) Since negligible change in base pressure occurs during the acceleration of individual particles, the Type 1 particle transport is modeled as a steady process. If the disruption front is assumed to propagate at a steady front speed (c), then the Galilean transformation can be used to model the front as a stationary discontinuity in a steady multiphase flow (Figure 4.1b).

4.2 Control Volume Analysis #1

In the first analysis, the Type 1 particle transport process is analyzed using a control volume enclosing the particle acceleration region (Figure 4.2). This control volume contains a process which transforms a mixture of particles and liquid in State (0) into a flow of particles, liquid, and vapor in State (2). The control volume cross-section is constant, and the streamwise boundaries, the test cell walls, are assumed to be adiabatic. In this analysis, the flow is modeled as a steady one-dimensional flow and quantitative results will be evaluated from experimental data. The multiphase flow is treated as a homogeneous flow characterized by spatially averaged (bulk) properties.[6]

4.2.1 Density before vaporization. The bulk density, ρ_0, of the material flowing into the control volume is calculated from the volumetric fraction of the particles (β_0) and the densities of the liquid and particles, ρ_{L0} and ρ_{B0}, respectively. The volumetric fraction of the glass spheres in a packed bed used as β_0 in this analysis is 0.6,[7] therefore the bulk density of State (0) is evaluated using the following equation:

$$\rho_0 = \beta_0 \rho_{B0} + (1 - \beta_0) \rho_{L0} = 0.6 \rho_{B0} + 0.4 \rho_{L0} \qquad (4.1)$$

---

[6] The homogeneous flow, as described by Wallis (1969), can be used to model the multiphase flow produced by the fragmentation front if the velocity of the vapor relative to the particles is negligible when compared to the bulk flow velocity. Subsequent results will demonstrate the validity of this assumption, especially for experiments conducted at 1g conditions.

[7] The volumetric fraction of the particles is obtained by measuring the displacement of liquid in a graduated cylinder with the same diameter as the test cell.

Table 4.1 Density of the components and the bulk density of State (0).

Material	Density	Bulk Density w/ Particles
R12 (liquid)	1.31 g/cc	2.29 g/cc
R114 (liquid)	1.46 g/cc	2.35 g/cc
Particles	2.95 g/cc	----------

4.2.2 Choked flow case. If the flow chokes at the exit, the process inside the test cell is isolated from the downstream conditions in the reservoir since pressure waves are unable to travel upstream from the reservoir due to sonic flow at the exit. As a result, the pressure at the exit, P_2, remains higher than the reservoir pressure until there is a change in the upstream conditions (see *3.3.2*). In subsequent analyses, the maximum base pressure in experiments with choked flow is used for the upstream pressure, P_0. The flow speed in State (0) in the steady flow system is the disruption front speed, c, in the laboratory reference frame. These three properties have been measured in the experiments and they are summarized in Table 4.2; these quantities are used in the subsequent analysis of the Type 1 particle transport.

Table 4.2 Measured properties of choked flow produced by Type 1 transport of spherical 0.5 mm Dragonite particles at 1g.

Fluid	Speed (c)	Base (P_0)	Exit (P_2)[8]
R12	380 cm/s	4.7 bar	2.2 bar
R114	200 cm/s	1.45 bar	0.9 bar

Properties not measurable in the experiments must be derived by analysis. Conservation of mass and momentum between States (0) and (2) are expressed by the following equations.

$$\rho_0 \, c \;=\; \rho_2 \, u_2 \tag{4.2}$$

[8] See Appendix B for the exit pressure derived from theory.

$$P_0 + \rho_0 c^2 = P_2 + \rho_2 u_2^2 \tag{4.3}$$

Here, ρ_0 and ρ_2 are the densities of the flow entering and leaving the control volume respectively. The following equation which combines (4.2) and (4.3) expresses the velocity of the multiphase flow leaving the control volume.

$$u_2 = \frac{1}{\rho_0 c} (P_0 - P_2 + \rho_0 c^2) \tag{4.4}$$

The bulk density of the multiphase flow determined using (4.2) is as follows:

$$\rho_2 = \frac{\rho_0 c}{u_2} \tag{4.5}$$

Table 4.3 shows the properties of State (2) calculated from these equations using measured properties of State (0) for Type 1 particle transport choked at the exit.

Table 4.3 Speed and bulk density of Type 1 process with choking.

Fluid/Particle	Speed (u_2)	Density (ρ_2)
R12/ 0.5 mm Dragonite	3250 cm/s	0.268 g/cc
R114/ 0.5 mm Dragonite	1370 cm/s	0.343 g/cc

Table 4.3 shows u_2 to be much greater than the *terminal velocity for the particles,*[9] calculated to be between 100 and 200 cm/s (Appendix C). Therefore, the difference in speed between the particles and the vapor is small compared to u_2, which means that the flow is essentially homogeneous at the exit in 1g experiments. When the experiment is conducted in the centrifuge at 100g, the terminal velocity is approximately 1900 cm/s (See Table C.4 in Appendix C). In this case, since the terminal velocity is significant compared to u_2 the flow at the exit can not be treated as being homogeneous, thus the 100g case cannot be analyzed by *Control Volume Analysis #1.*

[9] The relative vapor speed where the drag on the particle equals the particle weight (Appendix C).

The terminal velocity analysis in Appendix C can be used to calculate the particle-vapor velocity differential necessary to obtain the particle accelerations observed in the motion pictures. This velocity differential is the terminal velocity calculated with the particle acceleration replacing the gravitational or centrifugal acceleration. Table 4.4 shows the approximate velocity differential necessary to produce the acceleration observed in the experiments.

Table 4.4 Velocity differential necessary to achieve the particle acceleration observed in the motion pictures of Type 1 particle transport.

Test Fluid	Acceleration	$C_D Re^2$	C_D	Δu	$M = \Delta u / a$
R12	500g	2.03×10^8	0.4	4293 cm/s	0.28
R114	80g	5.04×10^7	0.4	1537 cm/s	0.13

The Mach number of the flow accelerating the particles, M, is based on the approximate frozen vapor sound speed.

In the laboratory frame, the speed of the multiphase flow at the exit is $(u_2 - c)$. The disruption front speed, c, is nominally 380 cm/s for experiments with R12. Therefore, the particle speed of 3870 cm/s given by the data in Figure 3.5 at the beginning of the particle expulsion is equal to u_2 of 4250 cm/s. If P_0 is equal to 4.7 bars (Table 4.2), then P_2 *during the expulsion of the first particles* determined using (4.4) for u_2 equal to 4250 cm/s. The result, P_2 equal to 1.33 bars, is consistent with the exit pressure at a point during the *start-up phase,* 'C' in Figure 3.3, just prior to the impacts by the first particles expelled in the experiment. As choking develops at the exit during the next few milliseconds, the exit pressure increases to 2.2 bars and u_2 will decrease to 3250 cm/s. Such change in the exit pressure during the start-up phase may be responsible for the most energetic activity by a volcano being observed during the initial stages of an eruption.

4.2.3 Volumetric fraction of the vapor. The fraction of the liquid vaporized to achieve State (2) can be determined from the conservation of particle flux and liquid-vapor flux expressed by the following equations.

Particle Flux: $$\beta_0 \rho_{B0} c = \beta_2 \rho_{B2} u_2 \quad (4.6)$$

Liquid-Vapor Flux: $$(1 - \beta_0) \rho_{L0} c = (1 - \beta_2)(1 - \alpha_2) \rho_{L2} u_2 + (1 - \beta_2) \alpha_2 \rho_{V2} u_2 \quad (4.7)$$

In the (4.6) and (4.7), α is the volumetric fraction of vapor in the two-phase liquid-vapor system and β is the volumetric fraction of particles in the three-phase flow. From the property of packed glass spheres, β_0 is known to equal 0.6 when α is zero.[10] Equation (4.6) is used to solve for the particle volumetric fraction under the condition that the intrinsic particle density does not change; i.e, $\rho_{B0} = \rho_{B2}$.

The volumetric fraction of particles, β_2, is calculated from u_2 obtained by the earlier analysis of the bulk flow using an equation derived from (4.6):

$$\beta_2 = \frac{\beta_0 c}{u_2} \quad (4.8)$$

Since β_2 is a measure of the space occupied by a typical particle, it can be used to calculate the mean distance between the particles. A 0.5 mm diameter particle has a volume equal to 6.54×10^{-5} cc. Therefore, the mean volume of the multiphase flow containing a single particle, V_B, is expressed by the following equation:

$$V_B = \frac{6.54 \times 10^{-5} \text{ cc}}{\beta_2} \quad (4.9)$$

The mean distance between the particle centers is the cube root of this volume; the values calculated for the experiments are given in Table 4.5. It should be noted that the characteristic distance between particles in the experiments, the distance between centers minus the particle diameter ($V_B^{1/3}$ - d), are less than the particle diameter, d.

---

[10] See discussion on the glass particles in Chapter 2, section *2.2.2*.

Table 4.5 Particle volumetric fraction derived for choked Type 1 processes.

Fluid/Particle	β_2	$(V_B)^{1/3}$
R12/ 0.5 mm Dragonite	0.070	0.098 cm
R114/ 0.5 mm Dragonite	0.088	0.091 cm

With β_2 in Table 4.5, α_2 can be evaluated using the following equation which is derived algebraically from (4.7):

$$\alpha_2 = \frac{(1-\beta_0)\,\rho_{L0}\,c - (1-\beta_2)\,\rho_{L2}\,u_2}{(1-\beta_2)\,(\rho_{V2}-\rho_{L2})\,u_2} \tag{4.10}$$

If the liquid-vapor system is assumed to be saturated,[11] then the densities, ρ_{L2} and ρ_{V2}, are the properties of saturated fluid which is determined by P_2 alone. Published data for the test fluid (Reynolds, 1979) has been used to compute the values in Table 4.6.

Table 4.6 Test fluid vapor fraction for a choked Type 1 process.

Fluid/Particle	ρ_{L2}	ρ_{V2}	T_2	α_2
R12/ 0.5 mm Dragonite	1.43 g/cc	13 mg/cc	263 K	0.963
R114/ 0.5 mm Dragonite	1.52 g/cc	6.9 mg/cc	274 K	0.943

The mass fraction of the test fluid vaporized in the control volume is expressed by the following expression, a ratio between the vapor mass flux and the total mass flux for a homogeneous flow with speed u_2:

$$x_2 = \frac{\alpha_2\,\rho_{V2}\,u_2}{\alpha_2\,\rho_{V2}\,u_2 + (1-\alpha_2)\,\rho_{L2}\,u_2} \tag{4.11}$$

In (4.11), x_2 is the mass fraction of the vaporized test fluid, and ρ_L and ρ_V are liquid and vapor densities, respectively. As before, saturated test fluid properties interpolated from Reynolds' data have been used to calculate x_2 in Table 4.7.

[11] This does not imply thermal equilibrium with the particles.

Table 4.7 Mass fraction of the test fluid vaporized by choked Type 1 process.

Fluid/Particle	x_2
R12/ 0.5 mm Dragonite	0.19
R114/ 0.5 mm Dragonite	0.07

4.2.4 Analysis based on energy conservation. In the preceding analysis, the bulk density for State (2) has been calculated from experimental data. The calculations show the velocity change between States (0) and (2) is much larger than the particle-vapor velocity difference, thus the velocity difference has been neglected for obtaining first-order results. The calculations have assumed a saturated liquid-vapor system at the test cell exit since the liquid at State (2) is believed to exist as small droplets, resulting in large surface area per volume of liquid.

The maximum fraction of liquid which can be vaporized by depressurization depends on the amount of available energy. This energy, called the total enthalpy (h_t), is the sum of enthalpy or heat (h) and the kinetic energy ($u^2/2$). The adiabatic control volume requires the flux of the total enthalpy to be conserved. The total enthalpy flux based for State (0) is given by the following equation.

$$\rho_{mixture}\, u\, h_t = \rho_{mixture}\, u\, (h + u^2/2)$$
$$= \beta_0\, \rho_B\, c\, (h_{B0} + c^2/2) + (1 - \beta_0)\, \rho_{L0}\, c\, (h_{L0} + c^2/2) \qquad (4.12a)$$

The fluid flux, $\rho_{L0}\, c$, in (4.12a) can be replaced by the right side of (4.7) to obtain the following equation:

$$\rho_{mixture}\, u\, h_t = \beta_0\, \rho_B\, c\, (h_{B0} + c^2/2) + (1 - \beta_2)\, (1 - \alpha_2')\, \rho_{L2}\, u_2\, (h_{L0} + c^2/2)$$
$$+ (1 - \beta_2)\, \alpha_2'\, \rho_{V2}\, u_2\, (h_{L0} + c^2/2) \qquad (4.12b)$$

Equation (4.12b), now has terms similar to those in the following equation for the total enthalpy flux at State (2):

$$\rho_{mixture}\, u\, h_t = \beta_2\, \rho_B\, u_2\, (h_{B2} + u_2^2/2) + (1 - \beta_2)\, (1 - \alpha_2')\, \rho_{L2}\, u_2\, (h_{L2} + u_2^2/2)$$
$$+ (1 - \beta_2)\, \alpha_2'\, \rho_{V2}\, u_2\, (h_{V2} + u_2^2/2) \qquad (4.13)$$

In equations (4.12b) and (4.13a), α_2' is the volumetric fraction of vapor in State (2) which is determined by conserving total enthalpy between State (0) and State (2). To find α_2', thermal equilibrium will be assumed between the liquid and vapor at State (2). Therefore, if the actual conditions at the exit are the same as that postulated here for State (2), then α_2' will equal α_2 based on experimental data calculated in the earlier analysis.

Since the flow is essentially adiabatic for the characteristic particle transport time in the experiment, the total enthalpy of the flow is constant. Therefore, (4.12b) and (4.13) can be combined into the following equation:

$$\beta_2 \rho_B \; u_2 \; (h_{B2} + u_2^2/2) - \beta_0 \rho_B c \; (h_{B0} + c^2/2)$$
$$= (1 - \beta_2)(1 - \alpha_2')\rho_{L2} u_2 \; (h_{L0} - h_{L2} + c^2/2 - u_2^2/2)$$
$$+ \; (1 - \beta_2)\alpha_2' \rho_{V2} u_2 \; (h_{L0} - h_{V2} + c^2/2 - u_2^2/2) \qquad (4.14a)$$

The relative importance of various terms in (4.14) is given by the quantities calculated from the results of *Control Volume Analysis #1* shown in Table 4.8.

Table 4.8 Quantities of terms in the total enthalpy equation (4.14) estimated from the results of *Control Volume Analysis #1*. h_B is not given because particle-liquid heat transfer is undefined. (All values in cgsK units.)

Terms	R12	R114
ρ_B	2.95	2.95
β_0	0.6	0.6
β_2 (Table 4.5)	0.07	0.088
c	380	200
u_2 (Table 4.3)	3250	1370
T_0	300	300
$c^2 / 2$	7.22×10^4	2.00×10^4
$u_2^2 / 2$	5.28×10^6	9.38×10^5
$\Delta KE = (u_2^2 - c^2)/2$	5.21×10^6	9.18×10^5
α_2' (Table 4.6)	0.963	0.943

ρ_{L2} (Table 4.6)	1.43	1.52
ρ_{V2} (Table 4.6)	13×10^{-3}	6.9×10^{-3}
h_{L0} (300K)	9.03×10^{8}	8.98×10^{8}
h_{L2}	5.58×10^{8}	6.36×10^{8}
h_{V2}	2.12×10^{9}	2.01×10^{9}
$\Delta h_1 = h_{L0} - h_{L2}$	3.45×10^{8}	2.62×10^{8}
$\Delta h_2 = h_{V2} - h_{L0}$	1.22×10^{9}	1.11×10^{9}
$(1-\beta_2)\ (1-\alpha_2')\ \rho_{L2}\ u_2\ \Delta h_1$	5.97×10^{10}	2.90×10^{10}
$(1-\beta_2)\ \alpha_2'\ \rho_{V2}\ u_2\ \Delta h_2$	4.61×10^{10}	9.04×10^{9}
$\beta_2\ \rho_B\ u_2\ \Delta KE$	3.49×10^{9}	3.27×10^{8}

As shown in Table 4.8, the change in kinetic energy, ΔKE, is two orders of magnitude lower than the change in test fluid enthalpy, Δh_1 and Δh_2. Therefore, the change in kinetic energy can be neglected from the right side of (4.14a) as follows:

$$\beta_2\ \rho_B\ u_2\ (h_{B2} + u_2^2/2) - \beta_0\ \rho_B\ c\ (h_{B0} + c^2/2)$$
$$= (1 - \beta_2)\ (1 - \alpha_2')\ \rho_{L2}\ u_2\ (h_{L0} - h_{L2}) + (1 - \beta_2)\ \alpha_2'\ \rho_{V2}\ u_2\ (h_{L0} - h_{V2}) \qquad (4.14b)$$

The change in particle enthalpy can be determined from the particle specific heat, $c_B = 0.84 \times 10^7$ ergs/g/K. Therefore, a moderate temperature change on the order of 10K will render the ΔKE negligible on the left side of the equation and allow the following simplification:

$$\beta_2\ \rho_B\ u_2\ h_{B2} - \beta_0\ \rho_B\ c\ h_{B0}$$
$$= (1 - \beta_2)\ (1 - \alpha_2')\ \rho_{L2}\ u_2\ (h_{L0} - h_{L2}) + (1 - \beta_2)\ \alpha_2'\ \rho_{V2}\ u_2\ (h_{L0} - h_{V2}) \qquad (4.14c)$$

As shown by the order of magnitude difference between the enthalpy fluxes and the particle kinetic energy flux (last three rows in Table 4.8), about 10% error is expected from (4.14c) which neglects the particle kinetic energy terms in (4.14b).

4.2.5 Hypothetical final state #1. In the first analysis, α_2' will be determined for a hypothetical State (2) which assumes that no heat transfer has occurred between the particles and the liquid. The case where the particles and the liquid-vapor system are in thermal equilibrium is analyzed as *Hypothetical final state #2*. Since particle-liquid heat

transfer inevitably occurs in an experiment, α_2' derived for the present hypothetical case can be compared with α_2 in Table 4.6 to estimate the heat transfer that actually takes place.

The characteristic heat transfer time, τ, for a particle is determined by the thermal diffusivity, α_T, and the radius, r. The characteristic heat transfer time for a Dragonite particle used in the experiments is calculated below:

Conduction Time:	$\tau = \frac{r^2}{\alpha_T}$
For Dragonite glass used,	$\alpha_T = 0.00315$ cm^2/s
	$r = 0.025$ cm
therefore	$\tau = 0.199$ seconds

The heat transfer time, τ, must be compared to the time available in the experiment for heat transfer. Motion pictures of the experiments show particles accelerating at 80g to speeds exceeding 500 cm/s even in experiments involving the less volatile superheated liquid (R114). This means that particles will be expelled from the test cell after traveling 20 cm about in about 55 milliseconds, a small fraction of the time necessary to transfer heat out from the particle interior. Therefore, the heat from the particles available for vaporization will be limited. The heat transferred to the liquid is further limited by the low heat diffusivity in the vapor (< 0.001 cm^{2}s^{-1}) once particles and liquid droplets are dispersed. It will be impossible to calculate the heat transfer between the particle and the liquid without knowing the heat transfer characteristics of the particle-liquid-vapor interfaces.

If no heat transfer is assumed to occur between the particles and liquid-vapor, the particle enthalpy remains constant as follows:

$$h_B = h_{B0} = h_{B2}$$

Therefore, the equation for a_2' can be simplified by eliminating h_B from (4.14c) to obtain

the following equation:

$$(1 - \alpha_2')\,\rho_{L2}\,h_{L0} + \alpha_2'\,\rho_{V2}\,h_{L0} = (1 - \alpha_2')\,\rho_{L2}\,h_{L2} + \alpha_2'\,\rho_{V2}\,h_{V2} \qquad (4.15a)$$

This equation can be solved for α_2' as follows:

$$\alpha_2' = \frac{\rho_{L2}\,(h_{L0} - h_{L2})}{\rho_{L2}\,(h_{L0} - h_{L2}) + \rho_{V2}\,(h_{V2} - h_{L0})} \qquad (4.15b)$$

Using the properties of saturated liquid and vapor at P_2, the volumetric fractions of the vapor in State (2) can be computed using Equation (4.15b) for a superheated liquid with enthalpy, h_{L0}. The quantities in Table 4.9 are values calculated for the experiments where the flow is choked at the exit (Table 4.2).

Table 4.9 Volumetric vapor fractions expected from the excess energy of the superheated liquid.

Fluid/Particle	α_2'
R12/0.5 mm Dragonite	0.969
R114/0.5 mm Dragonite	0.981

The mass fraction of vapor in State (2), x_2' (Table 4.10), is obtained using (4.12).

Table 4.10 Maximum mass fraction of vapor in State (2).

Fluid/Particle	x_2'
R12/ 0.5 mm Dragonite	0.226
R114/ 0.5 mm Dragonite	0.192

The x_2' (Table 4.10) is based on the conservation of total enthalpy during the transformation from a superheated liquid to a liquid-vapor mixture in thermal equilibrium. In contrast, the x_2 (Table 4.7) is obtained by conserving mass and momentum using experimental data where State (2) is not likely to be in thermal equilibrium. The fact that x_2 is less than x_2' indicates that the total enthalpy of superheated liquid is sufficient for vaporizing ($x_2' - x_2$) more liquid; i.e., the vaporization occurring inside the test cell is

incomplete. Since particle enthalpy, which inevitably increases the vaporization occurring in the experiments, is not included in calculating x_2', the actual potential for vaporization should be greater than that indicated by x_2' in Table 4.7. Therefore, unvaporized superheated liquid is expelled from the test cell in the experiments.

The vaporization in a superheated liquid droplet will be retarded if the droplet has a cool outer layer which is in thermal equilibrium with surrounding vapor.[12] The superheated liquid in the droplet will not affect the accuracy of the results in Table 4.7 since liquid density does not vary greatly over the relevant pressure range and vapor is still saturated with the liquid at P_2. However, the analysis used to derive the results in Table 4.10 is entirely based on the assumption that no superheated liquid exists in State (2); this assumption is apparently inconsistent with what actually occurs in the experiments.

4.2.6 Hypothetical final state #2. If the test cell is extremely long and gravitational effects can be neglected, the multiphase flow produced by the disruption front will achieve equilibrium in both velocity and temperature. The sonic condition at the exit in this case is somewhat different from that observed in the experiments because the energy added to the flow by the particles is significant. This is analogous to one-dimensional, compressible flow with heat addition in which choking occurs at the conduit exit.[13] The pressure for a sonic flow with particles and vapor having the same velocity and temperature is given by the following equation derived in Appendix B:

$$P^* = \frac{1}{\frac{Y}{Z} + 1} (P_0 + \rho_0 c^2) \qquad \text{(B.21)}$$

Y and Z are terms related to vapor property with values close to unity. Although thermal equilibrium is not achieved in the experiments, State (0) from experiments with choked flow (Table 4.2) will be used as a first-order approximation for the new hypothetical case.

[12] This condition is similar to that responsible for *breadcrusting* in volcanic bombs where cold and stiff outer layer of a magmatic fragment is fractured by the vapor expanding in the hot, fluid inner material.

[13] This is a flow process represented by the Rayleigh Curve on state diagrams (Anderson 1983).

Table 4.11 gives the equilibrium sonic pressure (P*) calculated in Appendix B for use in the subsequent analysis.

Table 4.11 Choked exit pressure calculated for particle-vapor flows in thermal equilibrium.

Vapor / Particles	Exit Press. (P*)
R12 / Dragonite	2.42 bars
R114 / Dragonite	0.76 bars

The density (ρ^*), velocity (u^*), and particle fraction (β^*) for the sonic flow at P* can be calculated by conserving the fluxes of mass, momentum, and particles as follows:

$$\rho^* u^* = \rho_0 c \tag{4.16}$$

$$P^* + \rho^* u^{*2} = P_0 + \rho_0 c^2 \tag{4.17}$$

$$\beta^* \rho_B^* u^* = \beta_0 \rho_{B0} c \tag{4.18}$$

These equations are combined to express ρ^*, u^*, and β^* as follows:

$$u^* = \frac{1}{\rho_0 c}(P_0 + \rho_0 c - P_2) \tag{4.19}$$

$$\rho^* = \frac{\rho_0 c}{u^*} \tag{4.20}$$

$$\beta^* = \frac{\beta_0 c}{u^*} \tag{4.21}$$

In (4.21), the particle density has been assumed to remain constant. Table 4.12 gives flow properties evaluated using these equations.

Table 4.12 Properties of the sonic particle-vapor flow in thermal equilibrium with upstream condition found in Tables 4.1 and 4.2.

Fluid/Particle	P* (bars)	u* (cm/s)	ρ^* (g/cc)	β^*
R12/Dragonite	2.42	3000	0.290	0.076
R114/Dragonite	0.76	1668	0.282	0.072

The fraction of liquid, α^*, which must be vaporized to achieve the final state (*) is evaluated by a method similar to that used in *4.2.5*. As before, the total enthalpy available to the system is given by (4.12a). The total enthalpy for the final state is expressed by the following equation:

$$\rho_{mixture}\, u\, h_t = \beta^*\, \rho_B\, u^*\, (h_B^* + u^{*2}/2) + (1 - \beta^*)(1 - \alpha^*)\, \rho_L^*\, u^*\, (h_L^* + u^{*2}/2) + (1 - \beta^*)\, \alpha^*\, \rho_V^*\, u^*\, (h_V^* + u^{*2}/2) \qquad (4.22)$$

Since the total enthalpy is conserved, (4.12a) and (4.22) can be equated to obtain the following equation:

$$\alpha^* = \frac{\rho_L\,(h_{L0} - h_L^*) + \frac{\rho_B}{(1-\beta^*)\,u^*}\,(\beta_0\, h_{B0}\, c - \beta^*\, h_B^*\, u^*)}{\rho_L^*\,(h_{L0} - h_L^*) + \rho_v^*\,(h_v^* - h_{L0})} \qquad (4.23)$$

In (4.23), the change in kinetic energy has been neglected because it is insignificant compared to the changes in particle and test fluid enthalpies.

Following the procedure used in *Hypothetical final state #1*, the enthalpy levels for liquid and vapor saturated at P* are used for h_L^* and h_V^*, respectively. Unlike the earlier case, the particle enthalpy, h_B, changes due to heat transfer. Therefore, the change in particle enthalpy is expressed by the following equation:

$$h_{B0} - h_B^* = c_B\,(T_0 - T^*) \qquad (4.24)$$

$$c_B = 0.84 \times 10^7 \text{ ergs/g/K for glass.}^{14}$$

In the presence of both liquid and vapor, the final temperature, T*, is determined by the saturation condition at P*, so h_B^* depends on P*. The initial enthalpy, h_{B0}, on the other hand is known from the initial temperature, T_0 = 300K. However α^* is found to be greater than unity, whether the test fluid is R12 or R114, which indicates that more than 100% of the liquid can be vaporized by the energy available in the system. Since the value is meaningless, the analysis must be corrected to account for the lack of liquid in the equilibrium state.

---

[14] Ref. Holman (1981).

If no liquid exists in the final state ($\alpha^* = 1$), the final vapor density is no longer determined by liquid-vapor saturation and a state equation for the vapor must be used. The Principle of Corresponding States (Reynolds, 1979) is used in the following state equation:

$$P^* = Z\ \rho_V^*\ R\ T^* \tag{4.25}$$

Z is the compressibility factor, a function of pressure and temperature (Reid et al., 1977). In this analysis, Z is estimated from known properties at nearby states (Appendix B).

In the absence of liquid, the total enthalpy equation (4.22) can be rewritten as follows:

$$\rho_{mixture}\ u\ h_t = \beta^*\ \rho_B\ u^*\ (h_B^* + u^{*2}/2) + (1 - \beta^*)\ \rho_V^*\ u^*\ (h_V^* + u^{*2}/2) \tag{4.26}$$

Equation (4.24) is used for the particle enthalpy and the final vapor enthalpy is approximated by the following equation:

$$h_V^* = h_{V,SAT}(P^*) + c_P\ (T^* - T_{SAT}) \tag{4.27}$$

In (4.27), $h_{V,SAT}$ is the enthalpy of saturated vapor at pressure P* and temperature T_{SAT}. The expression shows the vapor temperature rising from T_{SAT} to T* as heat is transferred out of the particles in the absence of liquid. This expression is accurate if the pressure remains nearly constant after the liquid is completely vaporized.

A quadratic equation for T* is obtained by combining (4.12a), (4.24), (4.25), (4.26), and (4.27). The values for T*, evaluated for quantities in Tables 4.1, 4.2, are 4.12, are shown in Table 4.13.

Table 4.13 The equilibrium temperature for sonic particle-vapor flow with upstream condition found in Tables 4.1 and 4.2.

Fluid/Particle	c_P (erg/g/K)	Z	R (erg/g/K)	T* (K)
R12/Dragonite	0.607×10^7	0.924	687480	270.1
R114/Dragonite	0.712×10^7	0.968	486567	279.1

The results can be verified by comparing the sound speed at T* with the exit velocity (u* in Table 4.12) since the flow is choked. The following expression derived in Appendix B gives an approximate equilibrium sound speed for homogeneous particle-vapor flow.

$$a^* \approx \frac{\rho_v \, a_v^2}{\gamma \, \rho_0 \, c} \tag{4.27}$$

ρ_v, a_v, and γ are the density, the sound speed, and the ratio of specific heats for pure vapor; these are determined using (4.25) at P* and T*. The mass flux, ρ_0 c, is evaluated using data in Tables 4.1 and 4.2. Table 4.14 compares the computed a* with u* from Table 4.10 to check the analysis.

Table 4.14 Sound speed, a*, and the exit speed, u*, calculated for the hypothetical flow in thermal equilibrium.

Fluid/Particle	a* (cm/s)	u* (cm/s)	"Error"
R12/Dragonite	3010	3000	0.33%
R114/Dragonite	1671	1668	0.18%

4.3 Control Volume Analysis #2

A control volume analysis is used to analyze the discontinuity in particle acceleration at the disruption front. Unfortunately, the data obtained from the experiments are insufficient for a comprehensive analysis. In particular, the fraction of superheated liquid vaporized by the disruption front (α_1) is not known. This quantity is approximated in an *ad hoc* manner in the following analysis. Therefore, the following analysis is the first step in understanding the physical phenomena responsible for the Type 1 particle transport.

4.3.1 Control volume. The motion picture data such as Figures 3.11c and 3.18c show the particles begin accelerating at the disruption front during the Type 1 particle transport process.[15] When transformed into a steady flow (Figure 4.1), the disruption

[15] Particle acceleration jumps to 500g in experiments involving the vaporization of R12. The particle acceleration is 80g in experiments involving R114.

front will be a discontinuity in particle acceleration caused by the explosive vaporization of superheated liquid. In order to model the disruption front as an adiabatic discontinuity in steady flow, only the region of explosive vaporization will be analyzed using a control volume enclosing only the disruption front (Figure 4.3). Although the vapor speed will be significant, the change in particle speed within the limited streamwise dimension of the control volume will be negligible. Since there will be a significant difference in speeds between the vapor and particles leaving the control volume, this flow must be treated as a *separated flow* (Wallis 1969).

4.3.2 Energy available for vaporization. The material entering the control volume, State (0), is composed of superheated liquid and glass particles. In the control volume, the liquid flashes into vapor, but some liquid will remain unvaporized if the available energy is insufficient for complete vaporization. Thus, the volumetric fraction of the test fluid in vapor form, α_1, depends on the energy available in the superheated liquid. In this case, the energy is the total enthalpy for the superheated liquid entering the control volume. The potential energy due to gravity is neglected since the vertical scale of the control volume is assumed to be small.

4.3.3 Discontinuity as an adiabatic vaporization process. The glass particles can supplement the energy in the liquid during vaporization but this will be limited by the time available to transfer energy to the liquid. If the streamwise dimension of the control volume is small and the front speed is high, the residence time for a particle will be very short. Since a particle is assumed to leave the control volume before vaporization imparts additional momentum to the particle, the streamwise dimension is defined to equal one particle diameter. Therefore, the residence time for a particle is equal to the diameter divided by the front speed (Table 4.15).

Table 4.15 Control volume residence times for experiments described in Table 4.2.

Fluid/Bead	Front Speed (c)	Time (t)
R12 /0.5 mm Dragonite	380 cm/s	0.13 ms
R114/0.5 mm Dragonite	200 cm/s	0.25 ms

The ratio between the residence time and the characteristic time for heat transfer within a particle gives an indication of the internal energy transferred out of the particle during its passage through the control volume. Table 4.16 shows the ratio calculated using the characteristic heat transfer time (τ) derived in *4.2.5*.

Table 4.16 The ratio of residence time to heat transfer time.

Fluid/Bead	Time ratio (t/τ)
R12 / 0.5 mm Dragonite	0.0006
R114/0.5 mm Dragonite	0.0013

Since t is much smaller than τ, the heat transferred from within the glass to the surrounding liquid is negligible. Similarly, the glass walls are also considered adiabatic over this control volume. As a result, the vaporization occurring in the control volume will be determined from the energy available in the superheated liquid only.

4.3.4 Equations of motion. The conservation of mass, momentum, and energy for a one-dimensional multiphase flow is expressed by conservation equations for separated flow in Wallis (1969). These equations are integrated across the control volume to obtain the following equations relating State (0) to State (1):

Conservation of mass:

(Particle) $$\beta_0 \rho_{B0} c = \beta_1 \rho_{B1} c \tag{4.28}$$

(Liquid-Vapor) $$(1 - \beta_0) \rho_{L0} c = (1 - \beta_1)(1 - \alpha_1) \rho_{L1} c + (1 - \beta_1) \alpha_1 \rho_{V1} u_1 \tag{4.29}$$

Conservation of momentum:

$$\text{(Flux in)} \quad P_0 + \rho_0 c^2 = P_0 + \beta_0 \rho_{B0} c^2 + (1 - \beta_0) \rho_{L0} c^2 \tag{4.30}$$

$$\text{(Flux out)} \quad = P_1 + \beta_1 \rho_{B1} c^2 + (1 - \beta_1)(1 - \alpha_1) \rho_{L1} c^2 + (1 - \beta_1) \alpha_1 \rho_{V1} u_1^2 + D \tag{4.31}$$

(D is the pressure drop caused by the acceleration of particles.)

Conservation of total enthalpy:

$$\rho_{mixture}\ c\ h_t = \rho_{mixture}\ u\ (h + {}^1/_2\, u^2)$$

$$\text{(Flux in)} \quad = \beta_0 \rho_{B0} c\ (h_{B0} + {}^1/_2\, c^2) + (1 - \beta_0) \rho_{L0} c\ (h_{L0} + {}^1/_2\, c^2) \tag{4.32}$$

$$\text{(Flux out)} \quad = \beta_1 \rho_{B1} c\ (h_{B0} + {}^1/_2\, c^2) + (1 - \beta_1)(1 - \alpha_1) \rho_{L1} c\ (h_{L1} + {}^1/_2\, c^2) + (1 - \beta_1) \alpha_1 \rho_{V1} u_1 (h_{V1} + {}^1/_2\, u_1^2) \tag{4.33}$$

Since the effect of temperature and pressure on the particle density is negligible:

$$\rho_{B0} = \rho_{B1} \tag{4.34}$$

Therefore, the assumption that particles pass through the control volume with no change in velocity, expressed by (4.28), can be reduced to the following expression:

$$\beta_1 = \beta_0 = 0.6 \tag{4.35}$$

The numerical value is determined by the packing property of the glass spheres.

Since the change in liquid density is negligible compared to the density change due to vaporization, the following assumption will be applied:

$$\rho_{L0} = \rho_{L1} = \rho_L \tag{4.36}$$

Then, (4.29) can be rewritten as follows:

$$\rho_L c = \rho_{V1} u_1 \tag{4.37}$$

This equation expresses the mass flux of the test fluid vaporized in the control volume.

Equating the right side of the momentum equations, (4.30) and (4.31), the pressure drop across the control volume can be rewritten in the following form using (4.35), (4.36), and (4.37).

$$P_0 - P_1 = (1 - \beta_0)\, \alpha_1\, \rho_L\, c\, (u_1 - c) + D \tag{4.38}$$

This equation relates the pressure, velocity and the volume fraction of the vapor in State (1) to properties of State (0). The amount of vapor produced within the control volume depends on the amount of total enthalpy for State (0). As shown by the time ratio (t/τ) in Table 4.16 being much less than unity, the residence time is insufficient to transfer significant heat from within the particles. Therefore, the particle enthalpy is assumed to remain unchanged.

$$h_{B0} = h_{B1} \tag{4.39}$$

This allows the particle enthalpy to be cancelled when equating the right sides of (4.32) and (4.33). After dividing by the common factor, the total enthalpy equation has the following form:

$$\rho_{L0}\, c\, (h_{L0} + {}^1/_2\, c^2) = (1 - \alpha_1)\, \rho_{L,1}\, c\, (h_{L1} + {}^1/_2\, c^2) + \alpha_1\, \rho_{V1}\, u_1\, (h_{V1} + {}^1/_2\, u_1^2) \tag{4.40a}$$

This can be rewritten using (4.22) and (4.23) to obtain the following equation:

$$\rho_L\, c\, (h_{L0} + {}^1/_2\, c^2) = (1 - \alpha_1)\, \rho_L\, c\, (h_{L1} + {}^1/_2\, c^2) + \alpha_1\, \rho_L\, c\, (h_{V1} + {}^1/_2\, u_1^2) \tag{4.40b}$$

This equation can then be simplified by dividing out a common factor:

$$h_{L0} + {}^1/_2\, c^2 = (1 - \alpha_1)\, (h_{L1} + {}^1/_2\, c^2) + \alpha_1\, (h_{V1} + {}^1/_2\, u_1^2) \tag{4.40c}$$

Finally the equation can be solved for α_1.[16]

$$\alpha_1 = \frac{h_{L0} - h_{L1}}{h_{V1} - h_{L1} + u_1^2/2 - c^2/2} \tag{4.41}$$

As before, by assuming that the explosive vaporization of superheated liquid saturates the liquid-vapor system, the local pressure (P_1) will determine the thermodynamic state of the

[16] The equation expresses α_1 as a modified form of the Jakob Number, a dimensionless number which expresses the relative amount of excess heat contained by a metastable, superheated liquid.

liquid-vapor mixture. Therefore, the enthalpy for the liquid and the vapor can be expressed in the following form:

$$h_{L1} = h_{L\text{-}sat}(P_1) \tag{4.42a}$$

$$h_{V1} = h_{V\text{-}sat}(P_1) \tag{4.42b}$$

The quantities used in the analysis are interpolated from data by Reynolds (1979). The enthalpy of the superheated liquid is known from the initial temperature of the liquid, which is nominally 300K in the experiments.

Equations (4.38), (4.41), and (4.42) together express the relationship between u_1 and P_1 as a function of β_0, ρ_L, c, and D. The pressure drop, D, caused by the force induced on the stationary particles can be estimated from the particle acceleration, *a*, measured in the experiments. Whether D is significant compared to other terms in (4.38) will be determined after evaluating u_1 and P_1 with D equal to zero. The following section uses concepts from theories on gasdynamic discontinuities to obtain an additional relationship between u_1 and P_1 which is necessary for determining State (1).

4.3.5 Adiabatic discontinuity model. The disruption front is modeled as an adiabatic process because the residence time is short compared to the heat transfer time. The thermodynamic change is described by plotting the pressure against the specific volume of the initial and final states; this type of plot is called the P-v diagram (Figure 4.4). For a given *initial state* (0), the locus of possible *final states* (1) is a curve called the *Hugoniot.* A discontinuous change, or a *jump*, from the State (0) to State (1) is shown by the *Rayleigh line.* Since the jump must conserve mass and momentum, the slope of the Rayleigh line will be restricted by the following conservation relationships:

Mass flux:
$$\rho_0 u_0 = \rho_1 u_1 = J \tag{4.43}$$

Momentum flux:
$$P_0 + \rho_0 u_0^2 = P_1 + \rho_1 u_1^2 \tag{4.44}$$

Equations (4.43) and (4.44) can be combined:

$$\begin{aligned} P_1 - P_0 &= \rho_0 u_0^2 - \rho_1 u_1^2 \\ &= \frac{(\rho_0 u_0)^2}{\rho_0} - \frac{(\rho_1 u_1)^2}{\rho_1} \\ &= (\rho_0 u_0)^2 \left(\frac{1}{\rho_0} - \frac{1}{\rho_1}\right) \\ &= -(\rho_0 u_0)^2 \left(\frac{1}{\rho_1} - \frac{1}{\rho_0}\right) \\ &= -J^2 (\rho_1^{-1} - \rho_0^{-1}) \end{aligned} \tag{4.45a}$$

Specific volume is the inverse of density; i.e., $v = \rho^{-1}$. Therefore, (4.45a) can be rewritten as:

$$P_1 - P_0 = -J^2 (v_1 - v_0) \tag{4.45b}$$

Equation (4.45b) gives the slope of the Rayleigh line connecting (v_0, P_0) and (v_1, P_1) on the P-v diagram

$$\begin{aligned} \frac{\Delta P}{\Delta v} &= \frac{P_1 - P_0}{v_1 - v_0} \\ &= -J^2 \end{aligned}$$

$$\therefore \text{ (Slope of the Rayleigh Line) } = -\text{ (Mass Flux)}^2 \tag{4.46}$$

Since the right side of the (4.46) is negative definite, the locus of possible states must lie in the second and the fourth quadrants relative to State (0).

If the superheated liquid at State (0) is allowed to vaporize adiabatically at constant pressure, the final state will be at P_0 but v_1 will be greater than v_0. Therefore, the Hugoniot for the vaporization by superheated liquid must pass to the right of the State (0) on a P-v diagram. It should be noted that the Hugoniot for an exothermic process such as combustion also passes to the right of the the initial state. Although the temperature decreases in a vaporization process, it is similar to combustion in that the kinetic energy of the flow increases. In vaporization, the temperature decreases because enthalpy is converted into kinetic energy. In combustion, exothermic chemical reaction increases both

enthalpy and kinetic energy. For this reason, the present analysis follows the analysis of detonation and deflagration wave by Thompson (1988), Hill (1990), and others.

Base pressure data show changes in pressure much before the disruption front reaches the pressure transducer. Since the disruption front is subsonic, State (1) is in the *fourth quadrant* relative to State (0) on a P-v diagram (Hayes 1960).[17] The location of State (1) with respect to State (0) represents the decrease in pressure and the increase in volume associated with the disruption front. This makes the disruption front analogous to a deflagration wave which also has this property on a P-v diagram.

4.3.6 Chapman-Jouguet process. The Hugoniot for a particle-vapor flow asymptotes to the horizontal axis (v) as pressure decreases (Appendix D), therefore the Hugoniot is concave-up in the fourth quadrant. Since the Hugoniot also passes to the right of State (0), there is a Rayleigh line extending from State (0) which is tangent to the Hugoniot, and the point of tangency is called the Chapman-Jouguet point (Hayes, 1960; Thompson, 1988; Hill, 1990).[18] The Rayleigh line for State (1) coinciding with the Chapman-Jouguet point has the *maximum possible slope* which is equivalent to the maximum mass flux as shown by (4.46). Since entropy production is proportional to the mass flux squared (Thompson 1988), State (1) at the Chapman-Jouguet point also has the highest entropy,[19] thus making it a stationary entropy point on the Hugoniot. As a result, the Hugoniot and the isentrope have the same slope at the Chapman-Jouguet point. Since the Rayleigh line is tangent to the Hugoniot at the Chapman-Jouguet point, the Rayleigh line also has the same slope and the following relationship can be obtained:

---

[17] In the subsequent discussion, *fourth quadrant* will always mean the region to the lower-right of State (0) on a P-v diagram.

[18] The term is often used for tangency in the second quadrant; it is important in detonation processes. However, general definition of the Chapman-Jouguet point includes any tangency point. The point in the fourth quadrant is sometimes called the lower Chapman-Jouguet point.

[19] This is true only for deflagration-type processes where the final state is in the fourth quadrant. It should not be confused with similar analysis on a detonation process; the Rayleigh line to the Chapman-Jouguet point in the second quadrant has the *minimum* slope, thus a Chapman-Jouguet detonation *minimizes* the mass flux and entropy.

$$\text{Slope of the Isentrope: } \left(\frac{\partial P}{\partial v}\right)_s = \left(\frac{\partial P}{\partial \rho^{-1}}\right)_s$$
$$= -\rho^2 \left(\frac{\partial P}{\partial \rho}\right)_s$$
$$= -\rho^2 a^2 \qquad (4.47)$$

where a is the sound speed.

At the Chapman–Jouguet Point (ρ_1^{-1}, P_1),

$$\left(\frac{\partial P}{\partial v}\right)_{\text{Hugoniot}} = \left(\frac{\partial P}{\partial v}\right)_s = -\rho_1^2 a^2$$
$$= \left(\frac{\Delta P}{\Delta v}\right)_{\text{Rayleigh}} = -\rho_1^2 u_1^2$$

$$\therefore u_1 = a \qquad (4.48a)$$

Therefore, the mass flux and entropy is maximized when state (1) is a sonic flow.

4.3.7 Hypothetical condition for State (1). The adiabatic discontinuity in the liquid-vapor system used to derive the condition which maximizes mass flux and entropy disregards the presence of particles in State (1) in *Control Volume Analysis #2*. However, particles have an important consequence in defining the sound speed of the medium. The sound speed for the liquid-vapor is equal to the frozen sound speed in a particle-liquid-vapor system which is greater than the equilibrium sound speed due to the additional mass of the particles.[20] Therefore, with respect to the equilibrium sound speed at State (1), the vapor is supersonic and the particles are subsonic. If we consider the unlikely case in which the liquid remains affixed to the particles, then the local sound speed is that for pure vapor determined by the temperature alone. In addition, if the liquid-vapor system is saturated, the temperature is a function of local pressure and the condition for maximum mass flux can expressed in the following manner:

$$u_1 = a(T_1) = a(P_1) \qquad \text{since } T_1 = T_{sat}(P_1) \qquad (4.48b)$$

[20] This is based on the fact that the vapor sound speed exceeds the sound speed for a particle-vapor, two-phase medium. (Marble 1970).

However, the frozen sound speed will be lower than the vapor sound speed if liquid droplets are suspended in the vapor released by explosive vaporization.

With the additional condition on State (1) given by (4.48b), there are sufficient equations to solve for velocity (u_1) and pressure (P_1). In (4.38), u_1 is expressed as a function of P_1 and the liquid vaporized by the disruption front, α_1. Since α_1 is expressed as a function of u_1 and P_1 by (4.41), (4.38) and (4.41) can be combined into a single relationship between u_1 and P_1 which complements (4.48b). The curves for these equations are plotted in Figures 4.5 and 4.6. The two curves intersect at State (1), where the pressure and velocity satisfy conditions necessary to release pure vapor at the frozen sound speed. For Table 4.17, State (1) has been determined for State (0) in Table 4.2.

Table 4.17 The pressures and speeds associated with State (1) where the vapor is assumed to be flowing at sonic speed upon vaporization.

	State (0)		State (1)	
Test Fluid	Front Speed (c)	Upstream Press. (P_0)	Downstream Press. (P_1)	Vapor Speed (u_1)
R12	380 cm/s	4.7 bar	4.43 bar	14900 cm/s
R114	200 cm/s	1.45 bar	0.8 bar	11500 cm/s

The *volumetric fraction* of the test fluid vapor, α_1, is obtained from (4.41). Since we have assumed that the high-speed flow does not contain any liquid, α_1 is also equal to *the mass fraction of the superheated liquid* vaporized in the control volume. This curious fact is implied by (4.37). Table 4.18 gives the values of α_1.

Table 4.18 The fraction of the test fluid vaporized in the processes presented in Table 4.16.

Volatile Fluid	α_1
R12	0.092
R114	0.195

4.3.8 Pressure drop due to particle acceleration. Motion pictures of the Type 1 particle transport process (Figure 3.11, 3.18) shows a relatively constant particle acceleration being initiated at the disruption front. The force imparted by the vapor to accelerate the particles results in a pressure drop within the control volume. If unvaporized liquid is assumed to accelerate with the particles, then the pressure drop is approximately equal to the mean force per unit volume (F/V) shown in the following equation:

$$D = \int_{(0)}^{(1)} \frac{F}{V}\, dx \approx [\rho_L (1-\beta_0)(1-\alpha_1) + \rho_B \beta_0]\, a\, d \qquad (4.50)$$

Particle diameter is d and its acceleration is *a*. Data used to estimate the pressure drop across the disruption front, along with the results, are given in Table 4.19.

Table 4.19 Estimated pressure drop due to drag on particles and liquid in the disruption front. (ρ_B = 2.95 g/cc, β_0 = 0.6, d = 0.05 cm)

Fluid	ρ_L (g/cc)	α_1	*a*	D (bars)	$P_0 - P_1$ (bars)
R12	1.31	0.092	500g	0.055	0.27
R114	1.46	0.195	80g	0.009	0.65

The results indicate that D is not negligible but small compared to the pressure drop necessary to produce a sonic flow of vapor, $P_0 - P_1$. Therefore, the particle drag is expected to have a minor effect on the high-speed release of vapor predicted by this model.

4.4 Results Based on the Theoretical Model

4.4.1 Pressure distribution. The P_0 and P_2 measured in the experiments and P_1 from the *Control Volume Analysis #2* are shown in Table 4.20.

Table 4.20 Pressure at three points for the Type 1 particle transport model.

Test Fluid	R12	R114
Pressure Upstream of the Front (P_0)	4.7 bar	1.45 bar
Pressure Downstream of the Front (P_1)	4.43 bar	0.8 bar
Pressure at the Exit of the Test Cell (P_2)	2.2 bar	0.9 bar

The pressure distribution in the test cell based on the Chapman-Jouguet model of Type 1 particle transport is shown in Figure 4.7. The drop in pressure at the disruption front is caused by the production of high-speed vapor. In the acceleration region, a constant pressure gradient has been assumed from P_1 to P_2 since the motion pictures show relatively constant particle acceleration. The length of the acceleration region (l) is based on the particle acceleration as follows:

$$l = \frac{u_2 - c}{a} \tag{4.51}$$

The initial particle velocity (c) and the final velocity (u_2) are taken from Table 4.2 and 4.3, respectively. The particle acceleration (a) is known from motion picture data, such as Figures 3.11c and 3.18c.

4.4.2 Acceleration region. The vapor produced explosively at the disruption front transfers momentum to the particles and unvaporized liquid in the multiphase flow which constitute more than 75% of the mass. The static pressure will decrease as the bulk of the multiphase flow accelerates, so there will be a negative pressure gradient in the acceleration region. The negative pressure gradient in the acceleration region is evident in the pressure distribution based on P_1 calculated by *Control Volume Analysis #2* and data from experiments with R12 (Figure 4.7). However, the pressure drop (P_0 - P_1) calculated for R114 exceeds the overall pressure change (P_0 - P_2), which implies a positive pressure gradient which is wrong for an accelerating flow. Therefore, there is an inconsistency between (P_0 - P_1) obtained by the *Control Volume Analysis #2* and the experimental data for P_0 and P_2.

The pressure drop at the disruption front (P_0 - P_1) predicted by *Control Volume Analysis #2* for R114 is wrong because it implies a positive pressure gradient in the acceleration region where a negative gradient is expected. The approximations used in *Control Volume Analysis #2* are probably responsible for the error in the quantitative result. A large error is expected from the *ad hoc* assumption that the sound speed at State

(1) is equal to the frozen vapor sound speed; i.e., the lack of liquid droplets within the flow generated by explosive vaporization has been postulated. In reality, due to the abundance of unvaporized liquid, significant amount of liquid droplets are likely to be lofted into the flow at State (1) by the explosive vaporization. Since sound speed in a vapor-liquid mixture is lower than the vapor sound speed, $u_1 = a_1$ will be lower than that used in *Control Volume Analysis #2*. The approximate sound speed in a droplet-vapor mixture can be estimated from the equations for the sound speed given by Marble (1971) discussed in Appendix B. The following equation shows the approximate relationship between the vapor properties and the droplet-vapor mixture density, ρ_{mix}.

$$a_{mix}^2 = \frac{\rho_v}{\rho_{mix}} a_v^2$$

The mixture density is likely to be somewhere between ρ_{L0} and the value for State (2); the relevant values are given in Table 4.21.

Table 4.21 Droplet-vapor mixture density at State (0) and State (2). Mixture density for State (2) calculated from component densities and volumetric fraction in Table 4.6.

Test Fluid	ρ_{L0}	ρ_{L2}	ρ_{V2}	α_2	$\rho_{mix,2}$
R12	1.31 g/cc	1.43 g/cc	13 mg/cc	0.963	65 mg/cc
R114	1.46 g/cc	1.52 g/cc	6.9 mg/cc	0.943	93 mg/cc

As shown by ρ_{L0} and $\rho_{mix,2}$, the mixture density is likely to be on the order of 10^{-1} g/cc at State (1). Since the vapor density, ρ_v, is on the order of 10^{-2} g/cc, the sound speed in the droplet-vapor mixture, thus $u_1 = a_{mix}$ should be approximately 30% of a_v.

Since $(P_0 - P_1)$ is roughly proportional to u_1 as shown by (4.38), the sound speed in droplet-vapor mixture being 30% of the frozen value results in a 70% lower pressure drop across the disruption front. As a result, P_1 resulting from the explosive vaporization of R114 will be 1.26 bars based on P_0 in Table 4.17. Thus, by approximately accounting for

the liquid droplets at State (1) for the *Control Volume Analysis #2*, a negative pressure gradient in the acceleration region is implied by its result for R114. However, without further knowledge concerning State (1), such as the actual volumetric fraction of droplets, it is impossible to improve the analytical accuracy.

4.4.3 Base pressure. The pressure at the bottom of the test cell, the base pressure (P_0), is elevated in reaction to the acceleration process. Since the bottom is stationary, momentum conservation in the laboratory frame is expressed by the following equation:

$$P_0 A = \int_A (P + \rho u^2)\, dA \tag{4.52}$$

In this equation, P is the static pressure and ρ is the density of the fluid moving at velocity u in a test cell of constant cross section A. In experiments conducted under high centrifugal acceleration or in large scale geological events, the hydrostatic pressure due to overlying material will be included in the static pressure.

Equation (4.52) shows that P_0 is determined by the momentum flux of multiphase flow produced by the disruption front. However, since P_0 affects the explosive vaporization at the disruption front determining the momentum flux, the overall process is self-governing. The upstream condition P_0 is especially important once the multiphase flow is choked because pressure waves can no longer propagate to the disruption front. Then the explosive vaporization occurring at the disruption front completely determines the momentum flux since the acceleration region is a passive relaxation process. Although the ultimate particle velocity is determined by the downstream condition as shown in *Control Volume Analysis #1*, the acceleration rate is determined by the vapor flux at the disruption front. This is probably why darkened particles in the high-speed motion pictures accelerate at nearly identical rates as the disruption front propagates away from the test cell exit.

4.4.4 Base pressure plateau. During the propagation of the disruption front in Type 1 particle transport process, the base pressure decrease is slow compared to the decay

occurring after the front reaches the test cell bottom. Although changes in the base pressure have been neglected in the control volume analyses, the base pressure decreases from the maximum level achieved soon after vaporization is initiated. In R12 experiments, the base pressure is consistently about 90% of the maximum level when the front reaches the bottom and the base pressure begins the faster decrease to the reservoir level. The base pressure data such as Figures 3.24 and 3.32 show that the base pressure at the beginning and the end of the front propagation is the same regardless of the distance traveled by the front. Therefore, the overall change in base pressure during the front propagation does not appear to be determined by process duration. This is interpreted to mean that the pressure does not decrease as a result of the flow decaying with time.

The slow decrease in the base pressure can be caused by a portion of the initial rarefaction wave being *captured by the acceleration region*. During the start-up period, the rarefaction wave propagates upstream from the exit until a sonic flow is established; the process is illustrated in the x-t diagram of the start-up process (Figure 4.8). Since the multiphase flow is subsonic as it accelerates to the sound speed, a rarefaction wave in the acceleration region can travel upstream against the flow. However, since the wave propagates against a flow which is accelerating to sonic speed, it will have a gradual effect on State (0).

Alternatively, it can be hypothesized that the base pressure decreasing in time reflects a steady change in the upstream condition. The control volume analyses in this chapter has assumed only liquid and particles in State (0), but high-speed photographs show vapor bubbles which appear as white specks below the disruption front in the wide-angle photographs. Such bubbles will invariably form unless the momentum flux is sufficient to raise P_0 above the vapor pressure. These bubbles grow continuously as surrounding material conducts latent heat needed for vaporization (Prosperetti and Plesset, 1978). The

bubbles in the liquid-particle mixture reduces the bulk density of the mixture (ρ_0) and the pressure drop across the test cell ($P_0 - P_2$) is reduced as shown in the following equation:

$$P_0 - P_2 = \rho_0 c \ (u_2 - c) \tag{4.53}$$

Experimental data does not indicate a significant change in the speed (c) of the disruption front with time. Therefore, the pressure drop over the entire test cell ($P_0 - P_2$) is roughly proportional to ρ_0. If the exit pressure, P_2, is not affected significantly by ρ_0, then P_0 decreases as ρ_0 is decreased by the growing vapor bubbles.

4.4.5 Transition from Type 1 to Type 2 process. The decrease in P_0 during disruption front propagation is believed to be responsible for the transition from Type 1 process to Type 2 process in experiments such as FEB20-2 (Figure 3.27). The effect caused by decreasing P_0 on the *Control Volume Analysis #2* is shown by Figures 4.9 and 4.10; the series of curves for Equation (4.38) show State (1), which is represented by the intersection with the sonic curve, shifting to the left as P_0 decreases. In Figure 4.10, an intersection between the two curves does not exist if P_0 falls below about 1.3 bar in results calculated for R114. On the other hand, Figure 4.9 shows that the solutions for experiments with R12 are nowhere near the limit where there is no solution for State (1). The existence of a critical P_0 within the range of base pressures occurring in the R114 experiments may be the reason for the disruption front breaking down only in experiments involving R114.[21]

The lack of solution for *Control Volume Analysis #2* shown by Figure 4.10 indicates that R114 liquid at 1.3 bar is unable to generate the momentum flux necessary to release vapor at the frozen sound speed. This means that the superheated liquid by itself lacks the energy necessary to release the vapor in a manner that maximizes the entropy. Since additional energy must be conducted from the surrounding material to sustain the process,

---

[21] The fluctuating base pressure (Figure 3.27) and the apparent transition in the particle transport process (Figure 3.27) are attributed to the disruption front breaking down before reaching the test cell bottom.

the vaporization rate can be no greater than that for bubbles. As a result, the disruption front can no longer dominate the vaporization process since the mean mass flux will be comparable to that responsible for the growth of bubbles.

4.5 Effect of Particles on Vaporization

In the preceding discussions, the particles are assumed to be inert except as a possible source of energy. Although the disruption front has been postulated to control the transport process, no attempt has been made to explain the vapor production in detail. Comparison with explosive vaporization by superheated liquid in the absence of particles can be used to provide some indication of the role played by the particles in the vapor production. In Table 4.22, the effect of particles on the wave-like vaporization is shown by differences in quantities derived from experiments conducted with the same superheated liquid in the absence of particles (Hill, 1990).

Table 4.22 Effect of particles on wave-like vaporization phenomena with choking at the test cell exit.

Superheated Liquid	R12		R114	
Particles	No	Yes	No	Yes
Vapor Press.[22] (bars)	5.69	6.7	1.83	2.6
Max. P_0 (bars)	0.97	4.7	0.45	1.45
Momentum Flux (bars)	0.51	2.5	0.22	0.55
"Wave" Speed (cm s^{-1})	63	380	32	200
Mass Flux (g cm^{-2} s^{-1})	83.7	870	47.1	470

Although there is a discrepancy in the initial vapor pressure due to a small difference in the temperature at which the experiments were conducted, this cannot account for the gross differences in the transport properties. Although the transport process is more energetic, the superheated liquid comprises only 40% of the volume and about 25% of the mass at

[22] The initial vapor pressure of the liquid given to indicate the difference in the initial condition.

State (0) with particles. Therefore, nearly an order of magnitude increase in transport is being achieved while less liquid is vaporized overall when particles are present.

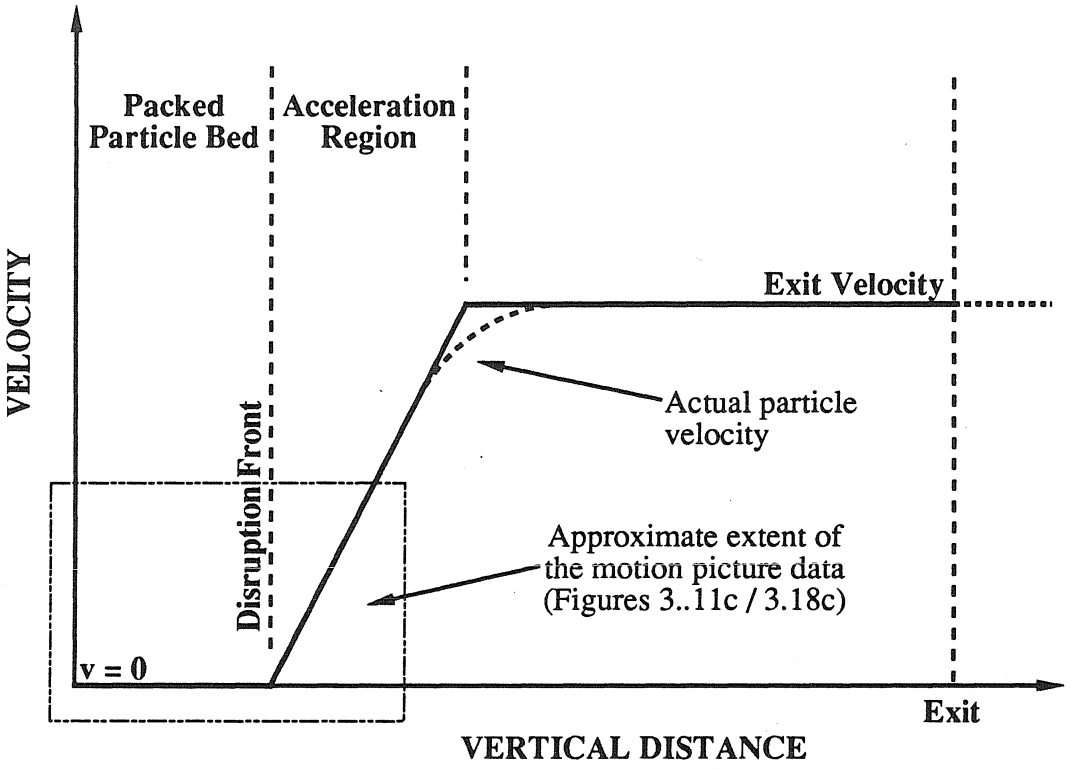

Figure 4.1 (a) Particle velocity within the test cell during the Type 1 particle transport process extrapolated from the motion picture and the data for the first particles in Figure 3.5. Particle acceleration is 500g with R12 and 80g with R114; the acceleration distance is approximately 10 cm in each case.

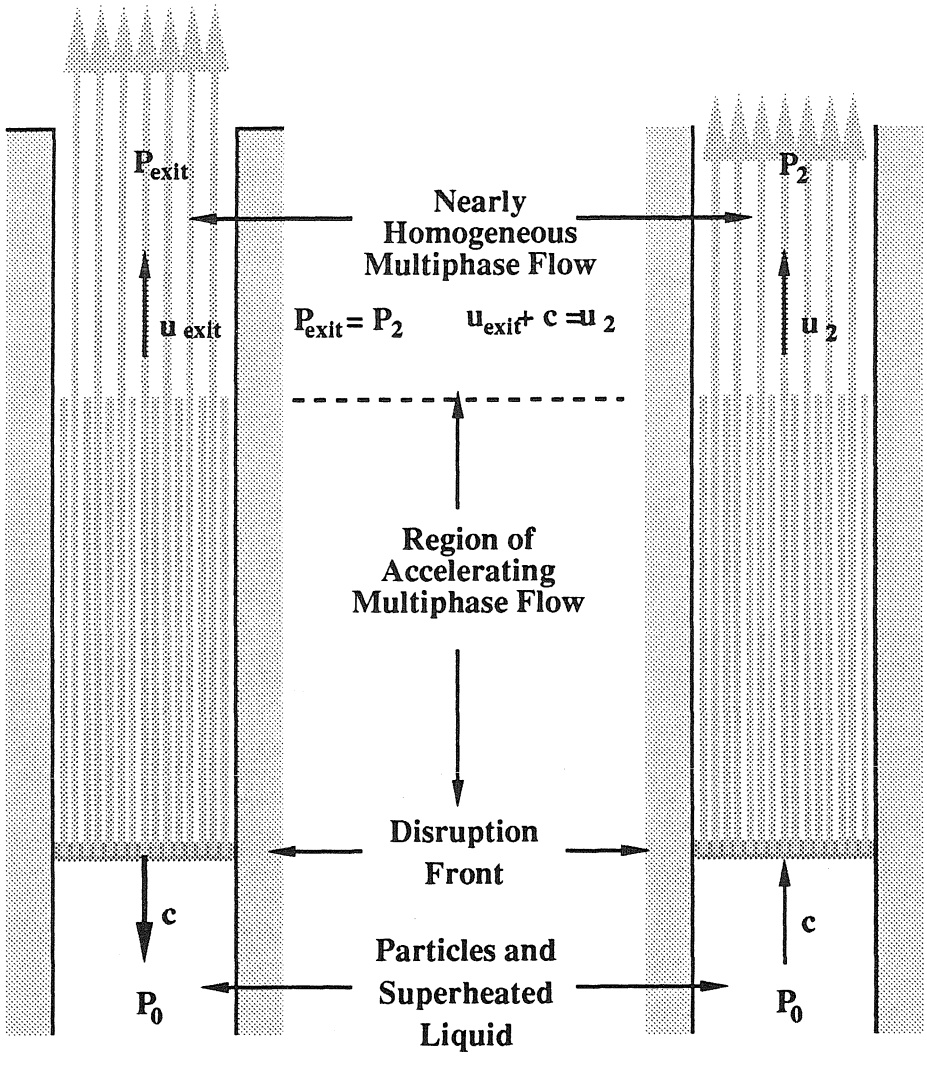

Figure 4.1 (b) Schematic drawings of Type 1 particle transport process. The drawing on the right shows the physical system modeled by the steady flow anaysis.

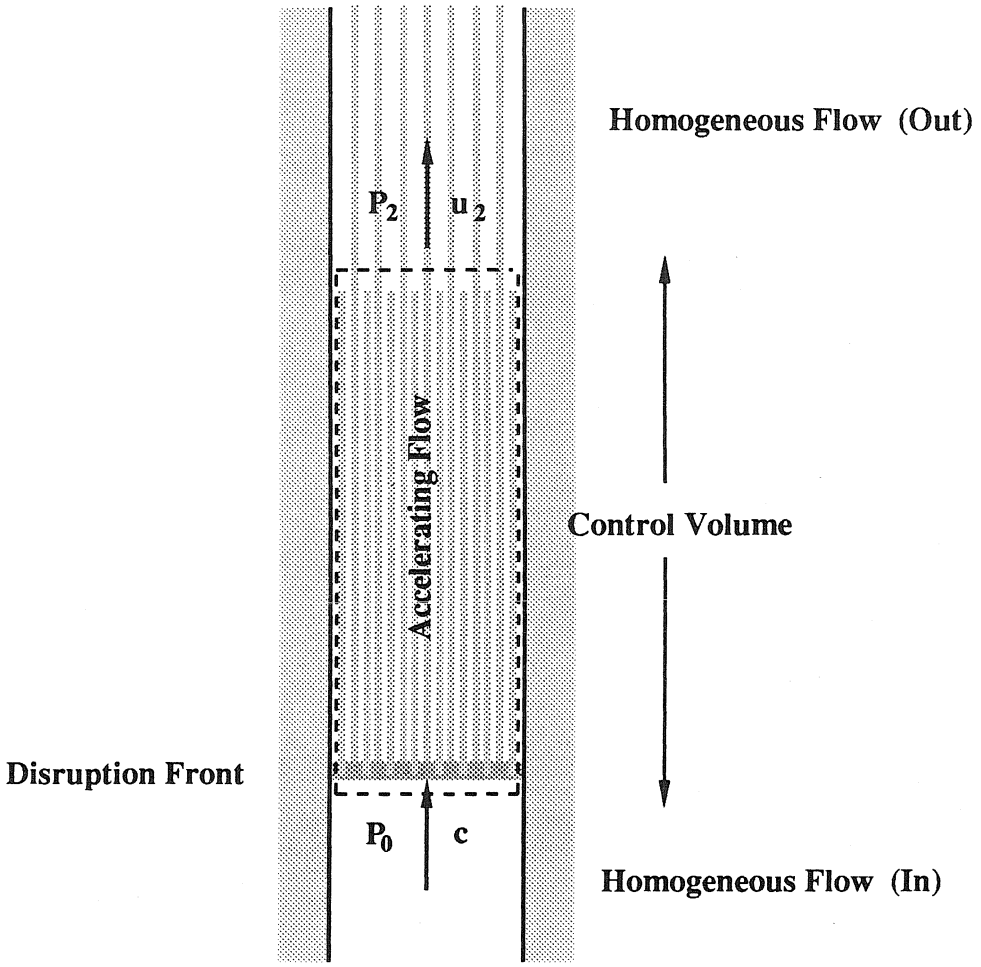

Figure 4.2 The control volume (dashed line) used in the steady state analysis of Type 1 particle transport (see discussion 4.2). The flow leaving the control volume is treated as a homogeneous flow since the slip velocity (terminal velocity) of the particle is small compared to the bulk velocity of the flow.

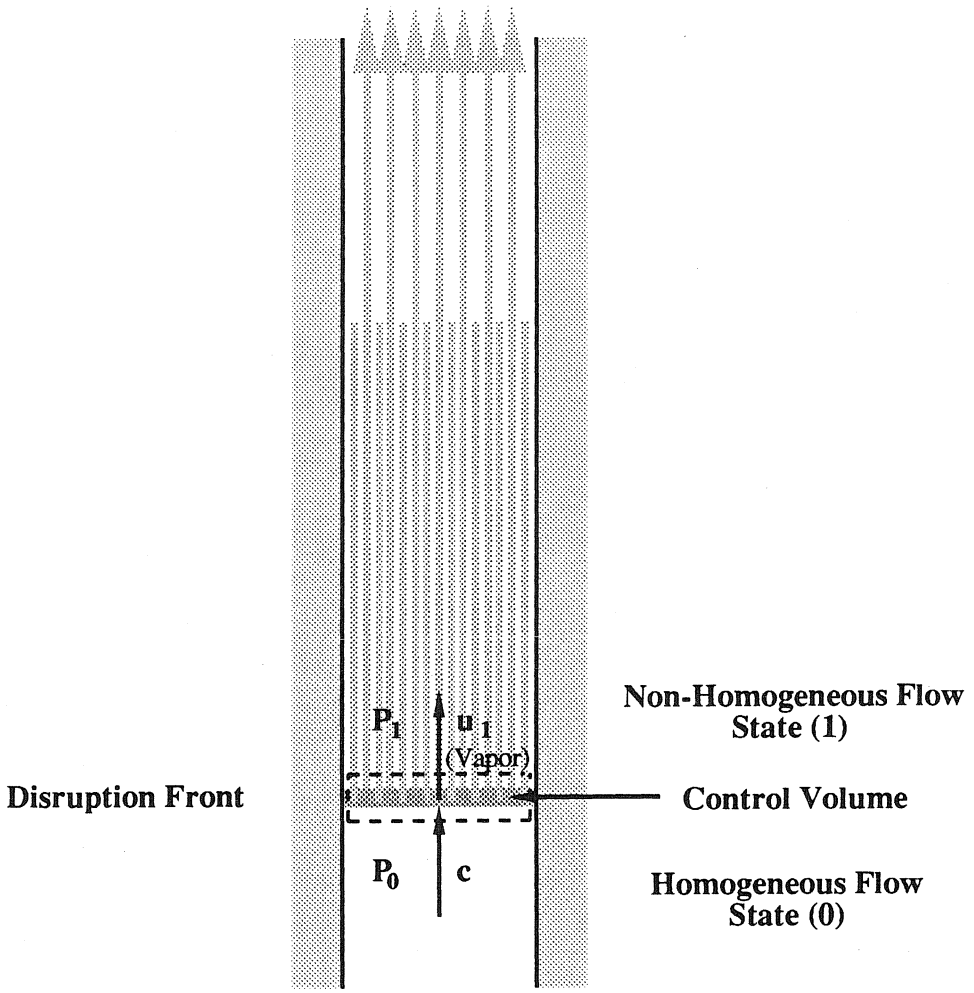

Figure 4.3 The control volume (dashed line) used in the analysis of the disruption front (see discussion 4.3). The components of the multiphase flow immediately behind the front are moving at different speeds. Particles and unvaporized liquid are assumed to pass through the narrow control volume at constant velocity, c. Explosive vaporization of superheated liquid produces vapor with velocity u_1.

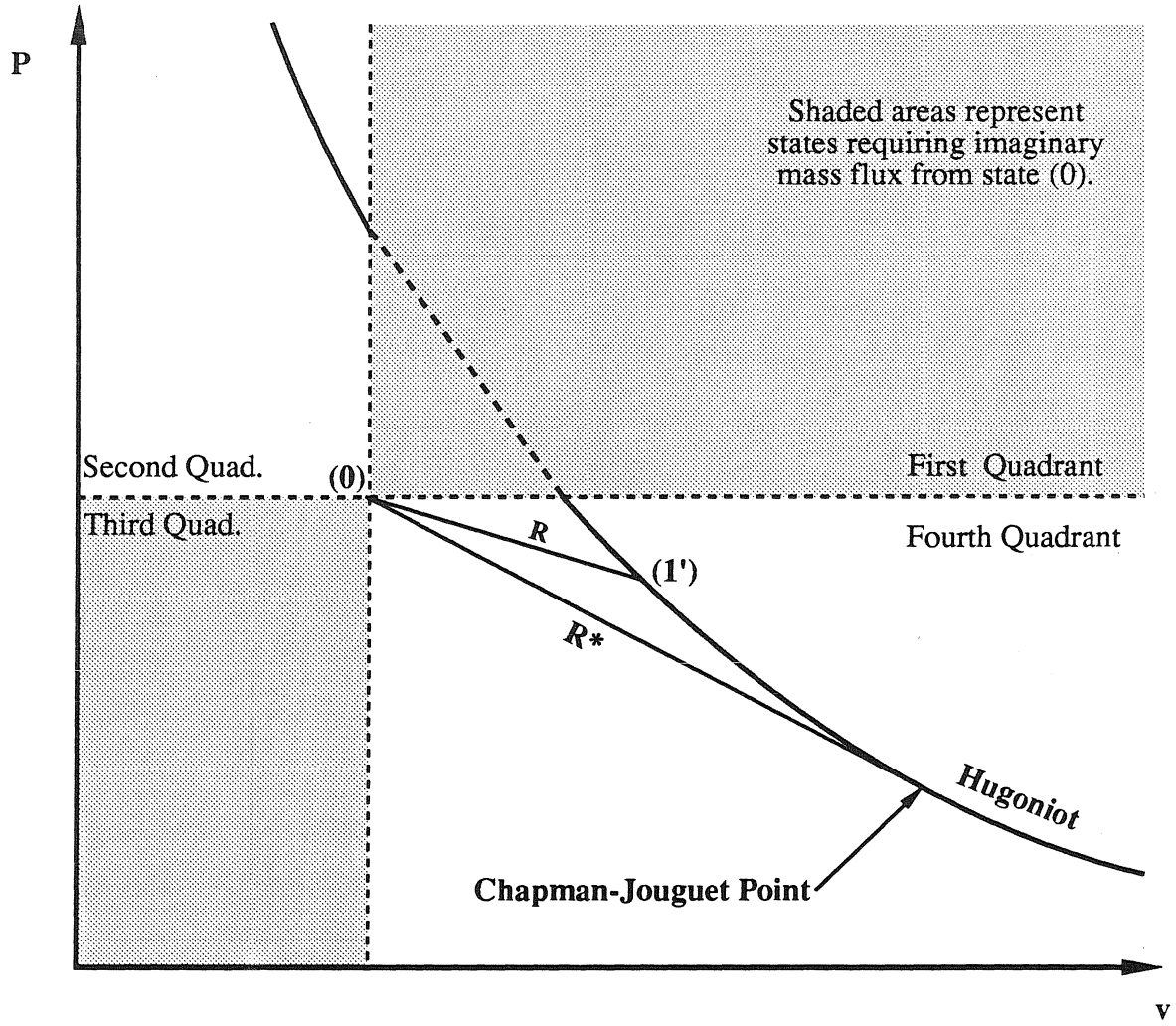

Figure 4.4 A generalized P-v Diagram for a deflagration-type process. Note the Rayleigh line (R) connecting the initial point (0) and an arbitrary final state (1') has a shallower slope than the Rayleigh line (R*) ending at the Chapman-Jouguet Point (C); the steeper slope of R* indicates higher mass flux for the Chapman-Jouguet process.

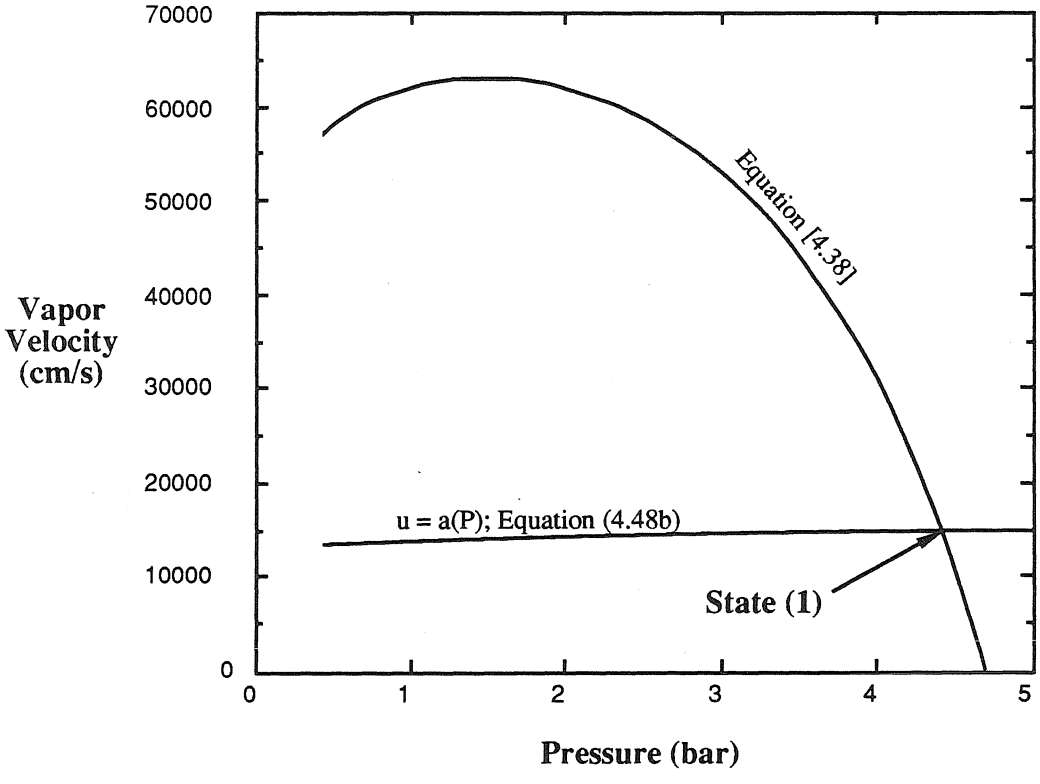

Figure 4.5 Graphical solution of State (1) which satisfies equations (4.38) and (4.48b). The parameters are based on the vaporization of superheated R12 liquid: Front Speed (c) is 380 cm/s and the pressure of the volatile mixture (P_0) is 4.7 bar. Note that the speeds of the unvaporized liquid and particles in State (1) are the same as those in State (0).

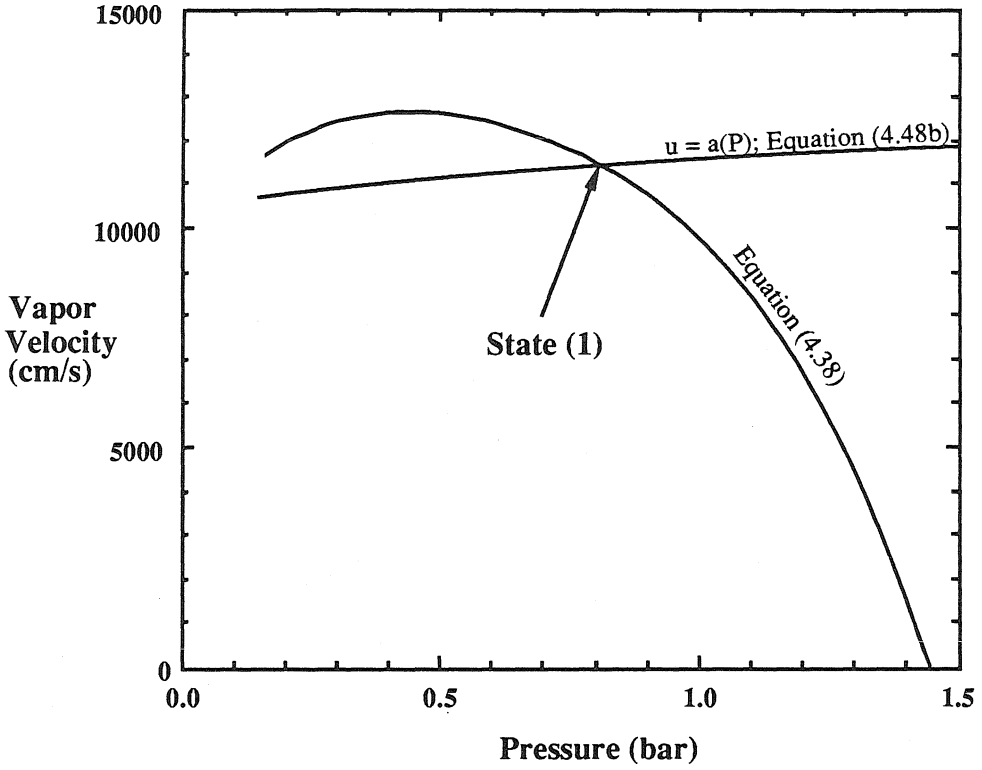

Figure 4.6 Graphical solution of State (1) which satisfies equations (4.38) and (4.48b). The parameters are based on the vaporization of superheated R114 liquid: Front Speed (c) is 200 cm/s and the pressure of the volatile mixture (P_0) is 1.45 bar.

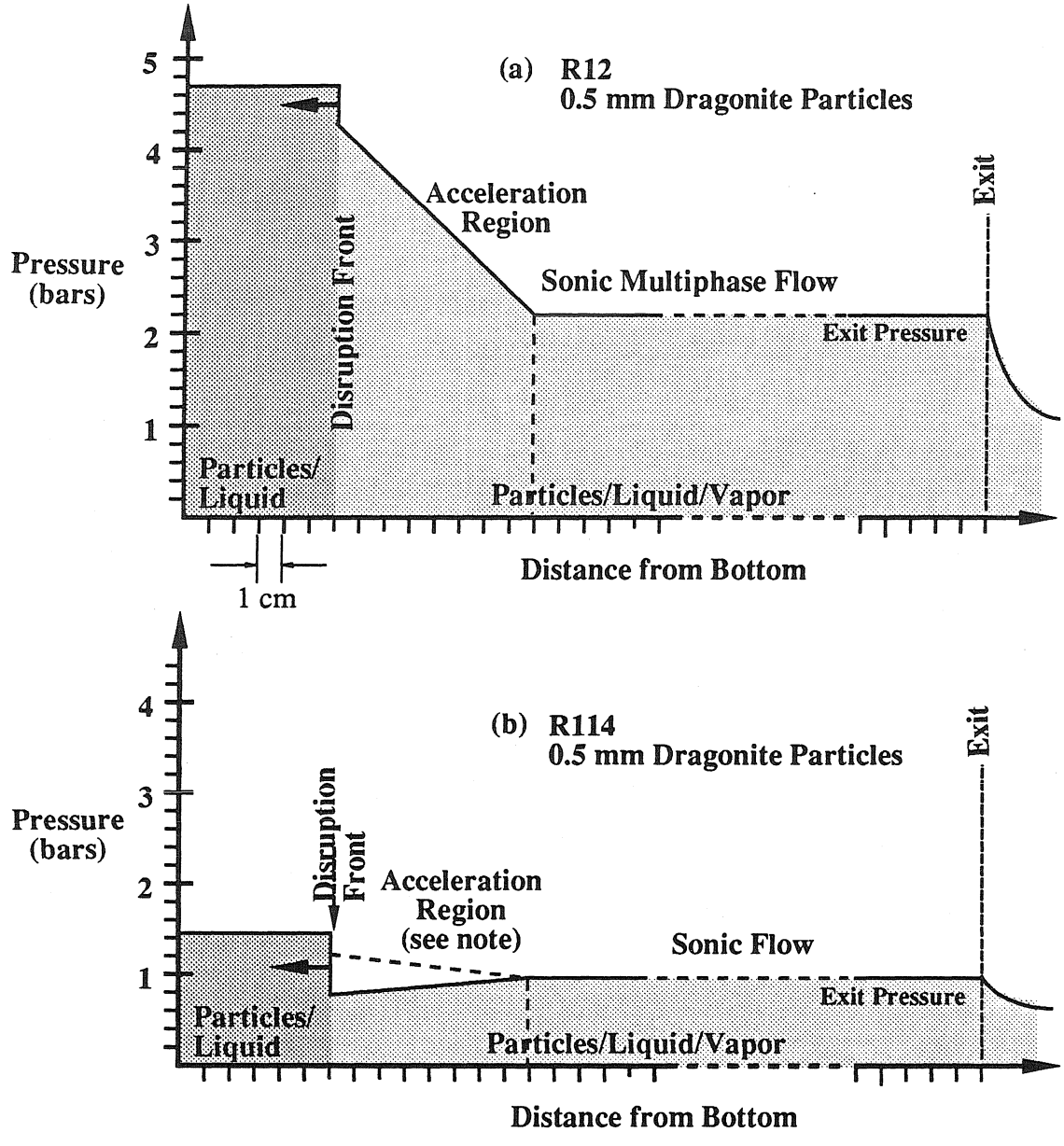

Figure 4.7 The pressure distribution during Type 1 particle transport. In each case, the pressure selected for the reservoir (right of the exit) is sufficiently low to produce choking of the multiphase flow at the exit; this is indicated by exit pressure higher than the reservoir pressure. The length of the acceleration zone is calculated from the measured particle acceleration in the motion pictures and the derived particle speed at the exit. Note: The positive pressure gradient in the acceleration region predicted by Control Volume Analysius #2 for R114 (solid line) is wrong but the correction discussed in 4.4.2 gives the negative pressure gradient (dashed line) expected in accelerating flow.

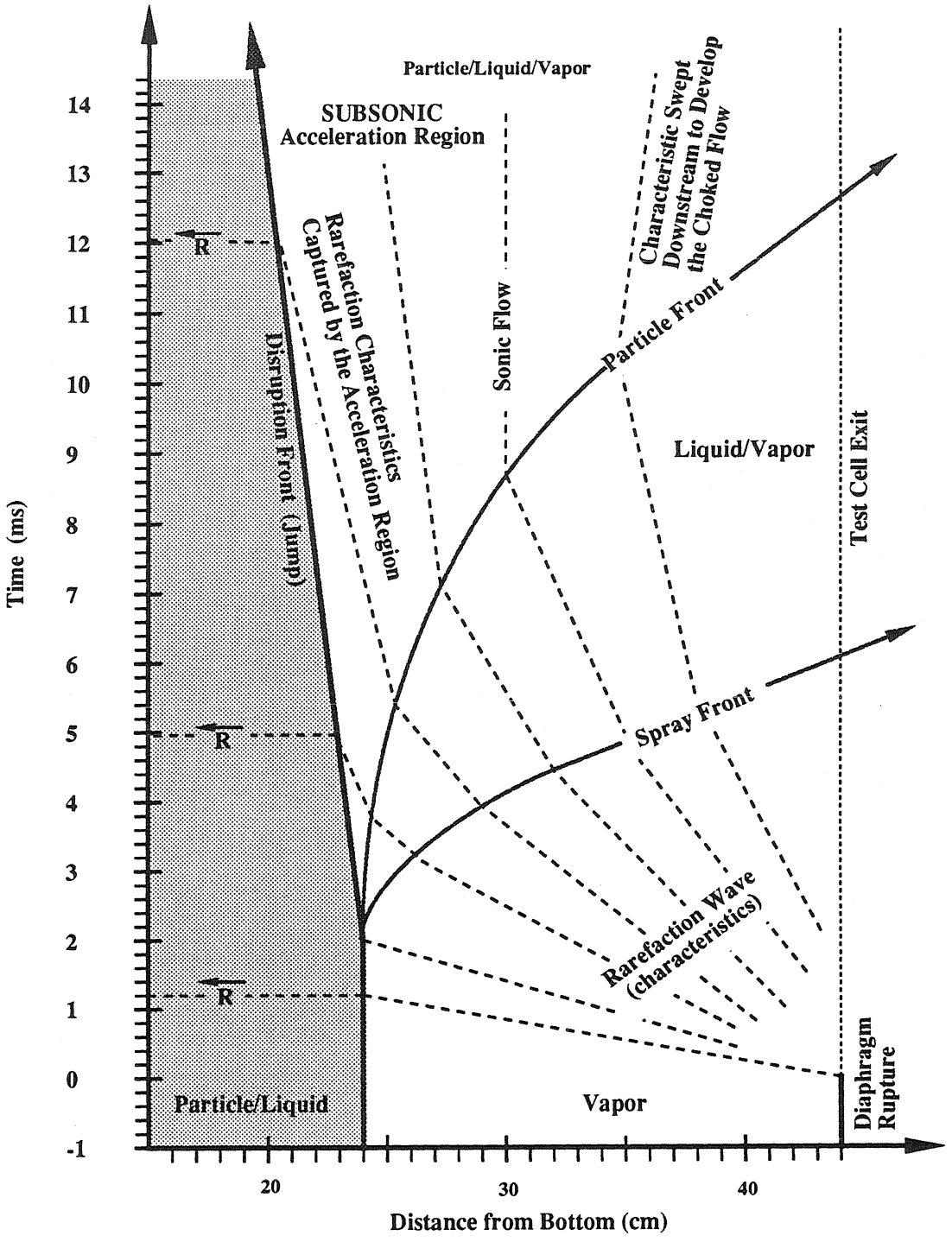

Figure 4.8 The trajectories of pressure waves inside the test cell during the startup phase of a choked Type 1 event (FEB22-3) with emphasis on the rarefaction wave. (This figure is equivalent to Figure 3.4.)

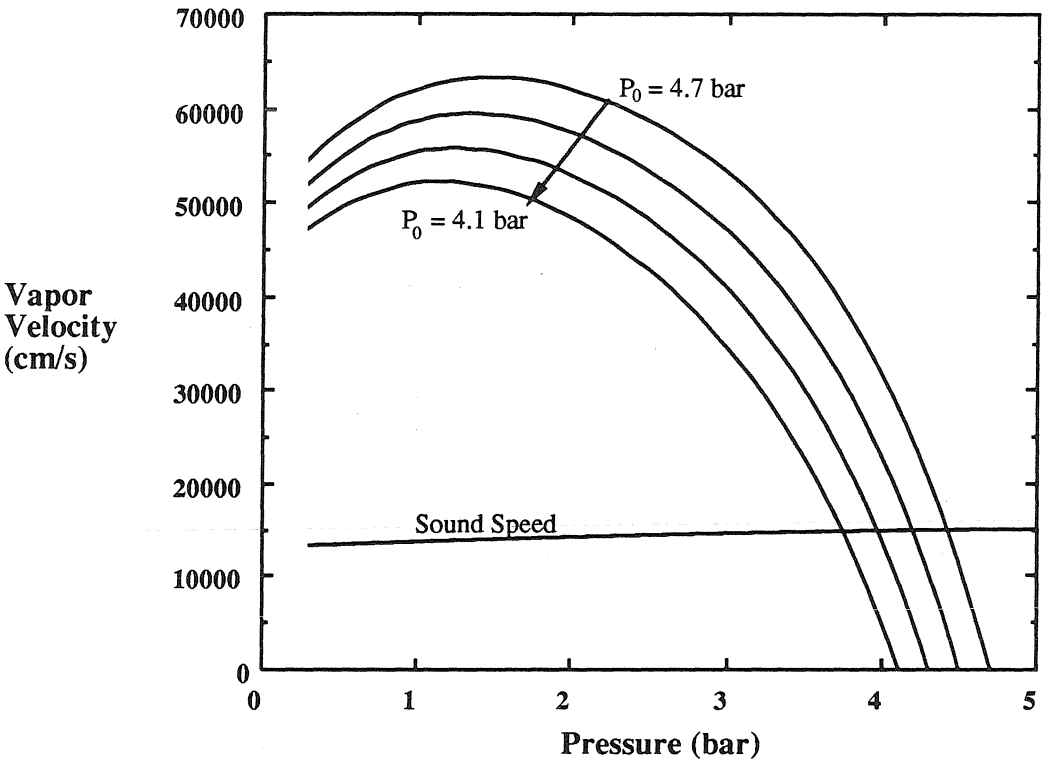

Figure 4.9 The effect of decreasing base pressure (P_0) on the graphical solution of State (1) in Type 1 particle transport by the vaporization of R12. The front speed (c) is assumed to be 380 cm/s for the cases shown. Note that the intersection of two curves shifts to the left as the base pressure decreases. (This figure is an extension of Figure 4.5.)

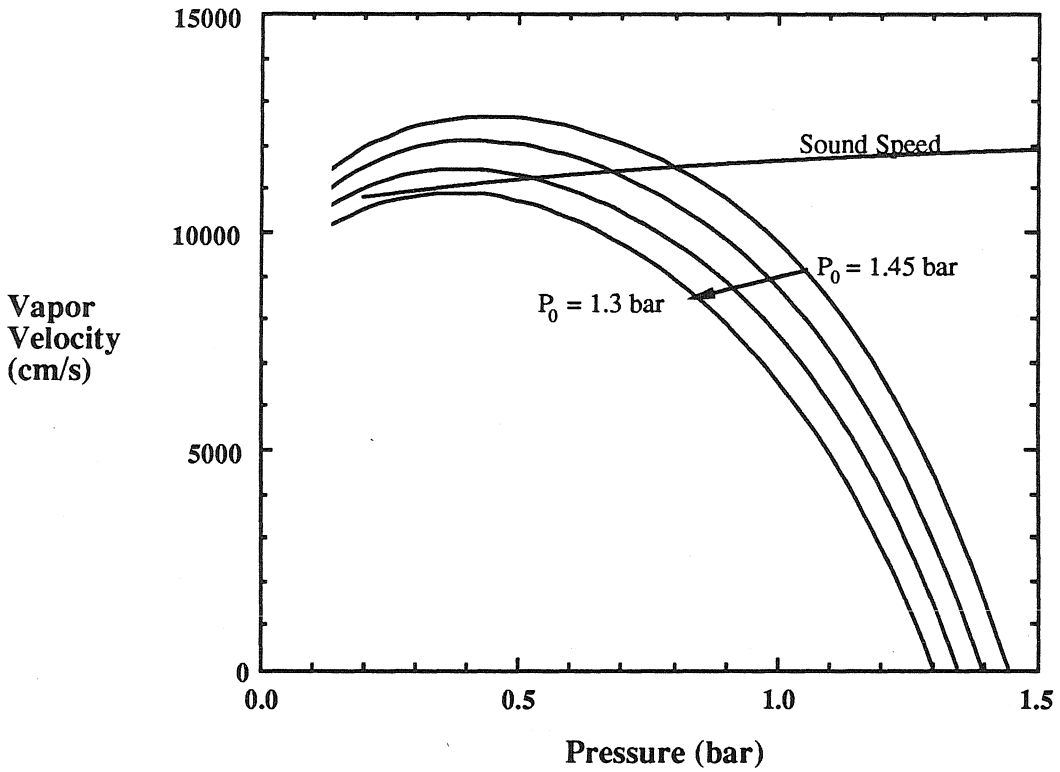

Figure 4.10 The effect of decreasing base pressure (P_0) on the graphical solutions of State (1) in Type 1 particle transport by the vaporization of R114. The front speed (c) is assumed to be 200 cm/s for the cases shown. There is no solution for State (1) in cases where the base pressure is below 1.3 bars. (This figure is an extension of Figure 4.6.)

Chapter 5

Summary and Conclusions

The experimental and analytical work on particle transport processes associated with the explosive vaporization of liquid existing in a particle matrix have been performed. Explosive vaporization occurs in a liquid which is superheated by depressurization. This investigation extends the earlier works on particle transport and rapid vaporization by Anilkumar (1989) and Hill (1990). As in the earlier works, high-speed motion pictures and fast response pressure measurements have been used to study the transient phenomena produced by the experiments. The experimental results indicate (i) that the particle bed is disrupted by one of two processes, Type 1 or Type 2, as determined by the degree of depressurization; (ii) that Type 1 particle transport is initiated by a wave-like disruption process similar to the *evaporation wave* in nucleate-free liquid; and (iii) that Type 2 particle transport is similar to the disruption of a particle bed by the expansion of interstitial gas. Depressurizing the liquid below the vapor pressure inevitably causes vapor bubbles to form in the particle bed. In Type 2 process, the coalescence and expansion by these bubbles lead to the displacement of overlying particles. When the liquid-particle mixture is depressurized to a pressure which is less than 0.55 times the vapor pressure, the Type 1 behavior is observed instead; Type 2 behavior is observed at higher pressures. In Type 1 process, a *disruption front* disperses the particles before bubble growth produces a significant effect on the bed. The disruption front travels through the liquid-particle mixture at 200 cm/s if the liquid is R114 at 300K and 380 cm/s if the liquid is R12 at 300K. Significantly more particles are transported by the Type 1 process at 0.52 times the vapor pressure than by a Type 2 process at 0.57 times the vapor pressure.

In Type 1 particle transport, during the disruption front's propagation, a quasi-steady flow of dispersed particles is observed. In high-speed motion pictures, the disruption front is observed to accelerate successively lower particles in the bed. Experiments conducted at

various centrifugal accelerations have shown a direct relationship between the particle acceleration and the centrifugal acceleration; a change in the centrifugal acceleration produces an approximately equal but opposite change in the particle acceleration. Therefore, the vapor drag minus the particle weight equals the force accelerating the particle, and the vapor drag must exceed the particle weight for the particles to be accelerated. Vapor drag produced by the R12 vaporization is capable of accelerating the particles at about 500g while the maximum particle acceleration with R114 is about 80g. Experimental data suggest that the forces on dispersed particles are characterized by the following expression, a modified Galileo number for a particle supported by an upward flow:

$$G^* = \left(\frac{\rho_B}{\rho_v} d\right)^3 \frac{Ng}{\nu^2}$$

Vapor viscosity (ν), centrifugal acceleration (Ng), and vapor density (ρ_v) have been varied in the experiments to establish an empirical relationship between G* and the particle dynamics in Type 1 transport. However, the particle density (ρ_B) can not be varied easily without varying the particle composition. Since the surface property and the heat transfer characteristics are also determined by the particle composition, no attempt has been made to vary ρ_B in the experiments. Isolating the various effects associated with a change in the particle composition is left as a challenge for future work.

The physical explanation for the two distinct transport processes occurring at different downstream conditions is investigated by analyzing the conditions under which Type 1 transport process occurs. Type 2 transport process is postulated to occur whenever the conditions are not favorable for the Type 1 transport process. This approach is used because the disruption front can be modeled as a discontinuity in a steady flow, thus simplifying its analysis. Using experimental data, the mass and momentum flux can be calculated in the region between the disruption front and the test cell exit (*Control Volume Analysis #1*). These results, when compared to results expected from the degree to which

the liquid is initially superheated, indicate that liquid is expelled from the test cell in a mildly superheated state. Further analysis indicates that conditions are far from thermal equilibrium at the exit. When the results from the experiments are compared to those found by Hill (1990), it is shown that the presence of particles increase the mass flux and momentum flux generated by vaporization by about an order of magnitude

The disruption front, a discontinuity in particle acceleration, is modeled as a narrow region in which explosive vaporization occurs; the particles are accelerated by the sudden release of vapor. In *Control Volume Analysis #2*, the disruption front is treated as an adiabatic discontinuity since heat transfer in the narrow region is limited by the short residence time. Since the mass flux and the entropy are maximized if such a discontinuity produces a sonic flow, the disruption front is assumed to have this property. This assumption is necessary because no data is available for the state immediately downstream of the disruption front. Fluid mechanical analysis shows that the superheated liquid has sufficient energy to generate a flow at the frozen sound speed under conditions observed in the experiments during Type 1 particle transport. Therefore, the theory suggests Type 1 behavior occurs when sufficient energy is readily available (i.e., in the liquid being vaporized) for the disruption front to maximize the vaporization rate.

While the Type 1 process is modeled as having a constant flux, the base pressure during the process decreases gradually from an early maximum level. It can be shown from theory that the base pressure must be above a certain level to achieve the vaporization rate which is believed necessary for Type 1 particle transport. Breakdown of Type 1 particle transport is observed in experiments with R114 where the base pressure approaches the critical level predicted by theory. This behavior adds credence to the disruption front model proposed in this work.

Appendix A
Particle Acceleration Model

The time of flight data for the first particles expelled, such as those in Figure 3.5, can be used to calculate the mean acceleration rate on the particle induced by rapid vaporization. The particle transport is modeled into two phases: (i) the acceleration region where the particles accelerate at a constant rate, a; (ii) steady flow region where the particles maintain a constant velocity, v. The data in Figure 3.5 is fitted to a trajectory based on this model shown in Figure A.1.

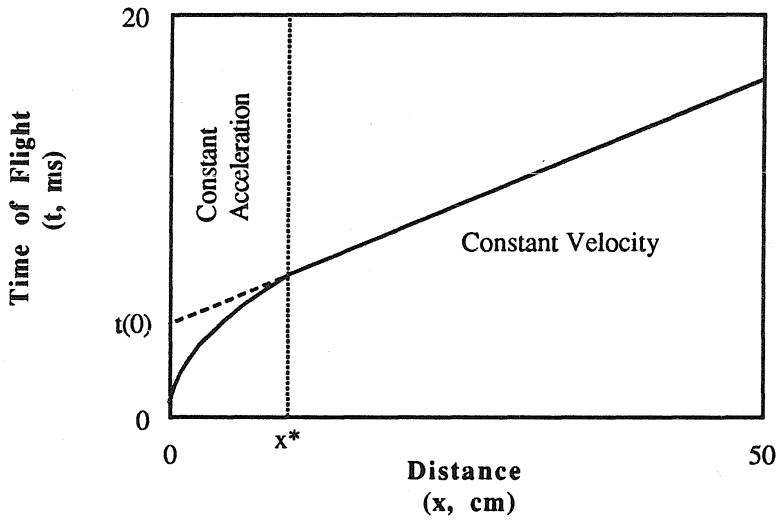

Figure A.1 Particle position versus time for the particle acceleration model. Scales are only representative of the data in Figure 3.5.

The steady flow region in Figure A.1 has a constant slope which is equal to v^{-1}. The characteristic time and distance, t* and x* respectively, of a particle achieving the steady flow after a period of constant acceleration, a, is shown in Figure A.2.

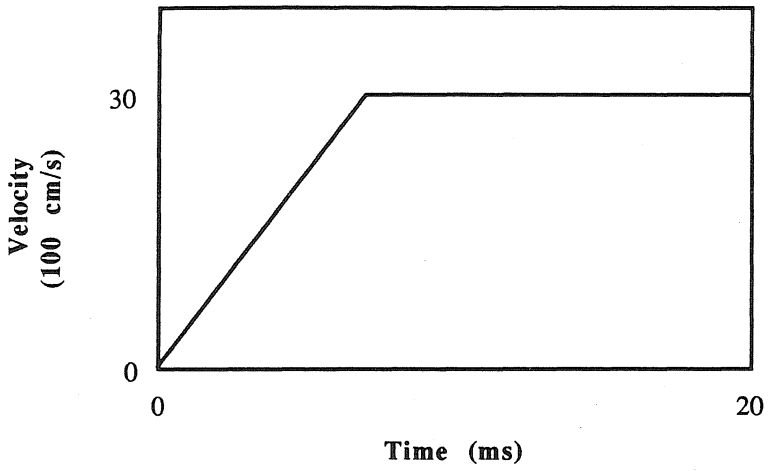

Figure A.2 Velocity profile for the particle acceleration model where v = 3000 cm/s.

In the acceleration region, the particle position (x) based on constant acceleration (a) is

$$x(t) = \frac{1}{2} a\ t^2 \tag{A.1}$$

The extent of the acceleration region is defined to be

$$0 < x < x^*$$

The data in Figure A.1 gives the following relationship

$$t(x) = t(0) + \frac{x}{v} \tag{A.2}$$

for the particles beyond the acceleration region, $x^* < x$.

The particle velocity described by (A.1) and (A.2) must match at (x^*, t^*):

$$\frac{dx}{dt}(x^*) = a\ t^* = v \tag{A.3}$$

Combining (A.1) and (A.3) at (x^*, t^*) gives

$$x^* = \frac{1}{2} a\ t^{*2} = \frac{1}{2} v\ t^* \tag{A.4}$$

Combining (A.2) and (A.3) at (x*,t*) gives

$$t^* = t(0) + \frac{x^*}{v} = t(0) + \frac{1}{2} t^*$$

$$\therefore \quad t^* = 2\, t(0) \tag{A.5}$$

Substituting the results for t* into (A.3) gives the acceleration which fits the data:

$$a = \frac{v}{2\, t(0)} \tag{A.6}$$

and the dimension of the model acceleration region is as follows:

$$x^* = v\, t(0) \tag{A.7}$$

Thus, a and x* can be determined from v and t(0) obtained from the data in Figure 3.5.

Appendix B
Equilibrium Sound Speeds in Particle-Vapor System

The sound speed in the particle-vapor mixture can be found by formulating the acoustic problem with linearized equations expressing conservation of mass, momentum, and energy for a particle-vapor system. The sound speeds for different equilibrium states are derived in Marble (1970). One equilibrium state is where the particles and vapor travel with the same velocity, equivalent to the *homogeneous flow* defined by Wallis (1969). The sound speed for this case is referred to as a_2. If the particles and vapor are also in thermal equilibrium, its sound speed will be a*. In each case, the sound speed in particle-vapor mixture is lower than that for pure vapor (a_v), which Marble (1970) calls the *frozen sound speed.*

$$a_2^2 = \frac{\rho_v}{\rho_2}\, a_v^2 \tag{B.1}$$

$$a^{*2} = \frac{\rho_v}{\rho^*}\left[\frac{\frac{c_P}{c_B} + \frac{\rho^*}{\rho_v} - 1}{\frac{c_P}{c_B} + \gamma\left(\frac{\rho^*}{\rho_v} - 1\right)}\right] a_v^2 \tag{B.2}$$

In these formulas, the vapor density is ρ_v and specific heat at constant pressure is c_p; specific heat of the particle is c_B. The integrated mixture densities are ρ_2 and ρ^*.

B.1 Approximate Vapor Properties

To express the vapor properties using pressure and temperature, the Principle of Corresponding States (Reynolds, 1979) is invoked in the following manner:

$$\rho_v = \frac{P_2}{Z R T_2} \tag{B.3}$$

$$a_v^2 = Y\ \gamma R T \tag{B.4}$$

In these equations, R is the gas constant for the vapor, γ is the ratio of specific heats, and Z is the *compressibility* shown by Reid et al. (1977) to have the following form:

$$Z = Z\left(\frac{P}{P_{critical}}, \frac{T}{T_{critical}}\right) \tag{B.5}$$

The compressibility for conditions occurring in the experiments are calculated from data by Reynolds (1979) and shown in Tables B.1 and B.2

Table B.1 Compressibility (Z) for saturated R12 vapor.
Gas constant: R = 687480 ergs/gram/°K

P (bar)	T (°K)	ρ_v (g/cc)	Z
6.85	300.0	0.0391	0.849
3.0	272.3	0.0176	0.912
2.4	265.7	0.0142	0.924
2.2	263.3	0.0131	0.928
2.0	260.6	0.0120	0.934
1.0	243.4	0.0063	0.944

Table B.2 Compressibility (Z) for saturated R114 vapor.
Gas constant: R = 486567 ergs/gram/°K

P (bar)	T (°K)	ρ_v (g/cc)	Z
2.2	300.0	0.0167	0.915
1.6	290.0	0.0122	0.943
1.1	280.0	0.0087	0.957
1.0	276.9	0.0078	0.960
0.8	270.0	0.0061	0.968
0.5	260.0	0.0041	0.976

The correlation factor for the sound speed, Y, is obtained by comparing empirical sound speed data (a_{emp}) to values calculated for a perfect gas (a_{pg}). The perfect gas model is

relatively accurate when the temperature is low compared to the critical temperature, which are 385.2K for R12 and 418.9K for R114. The values of Y for R12 vapor are shown in Table B.3.

Table B.3 Correlation factor (Y) for sound speed in R12 vapor.
Perfect gas sound speed (a_{pg}) based on
$\gamma = 1.139$, R = 687480 ergs/gram/°K
Empirical sound speed (a_{emp}) from Schaffs (1967)

T (°K)	a_{pg} (m/s)	a_{emp} (m/s)	Y
300.0	153.240	153.010	0.997
373.2	170.953	168.716	0.974
473.4	192.579	189.961	0.973

Since the temperature at State (0) is 300K, the temperature of the vapor produced by vaporization will be less than 300K by evaporative cooling; therefore, Y will equal unity in the subsequent analysis of the experiments. Since the author has been unable to locate published data for sound speed in R114 vapor, its Y is assumed to equal unity as well.

B.2 Sonic Flow for Homogeneous Particle-Vapor Flow

If the particles and vapor have nearly the same constant velocity at the exit, choking at the exit implies that the flow is locally sonic, thus defining State (2).

$$u_2 = a_2 \tag{B.6}$$

The particle-vapor sound speed, given by (B.1), can be used obtain the following equation:

$$\rho_2 a_2^2 = \rho_v a_v^2 \tag{B.7}$$

The mass flux at State (2) is known from the speed, c, and the density, ρ_0, of State (0):

$$\rho_2 u_2 = \rho_0 c \tag{B.8}$$

Thus, substituting (B.6) and (B.8) into (B.7) gives the following equations:

$$\rho_0 c u_2 = \rho_v a_v^2 \tag{B.9}$$

$$u_2 = \frac{\rho_v a_v^2}{\rho_0 c} \tag{B.10}$$

By substituting (B.3) and (B.4) into (B.10), the following result is obtained:

$$u_2 = \frac{1}{\rho_0 c} \frac{P_2}{Z R T_2} Y \gamma R T_2$$

$$= \frac{\frac{Y}{Z} \gamma P_2}{\rho_0 c} \tag{B.11}$$

Exit velocity, u_2, is also expressed by the conservation of momentum (4.4):

$$u_2 = \frac{P_0 + \rho_0 c^2 - P_2}{\rho_0 c^2} \tag{4.4}$$

Therefore, (B.11) and (4.4) can be equated to derive the following relationship:

$$\frac{Y}{Z} \gamma P_2 = P_0 + \rho_0 c^2 - P_2 \tag{B.12}$$

This can be solved for the pressure, P_2, of the sonic flow.

$$P_2 = \frac{1}{\frac{Y}{Z}\gamma + 1} (P_0 + \rho_0 c^2) \tag{B.13}$$

As a comparison, the equation for the exit pressure if the particles and liquid at State (0) is replaced by a perfect gas:

$$P^*_{pg} = \left(\frac{2}{\gamma + 1}\right)^{\frac{\gamma}{\gamma+1}} (P_0 + \rho_0 c^2) \tag{B.14}$$

In Table B.4, P_2 calculated using (B.13) and quantities in Tables 4.1 is shown with the exit pressure in the experiments. In this analysis, Z based on the data in Tables B.1 and B.2 have been used.

Table B.4 Comparison of theoretical and experimental exit pressures for experiments in which choking occurs at the exit.

Test Fluid	Y	Z	P_2 (B.13)	P_2 (exp)
R12	1	0.928	2.26 bars	2.2 bars
R114	1	0.97	0.73 bars	0.9 bars

The homogeneous flow is used to model the flow occurring in the experiments because the particle-vapor velocity difference is small relative to the bulk velocity. This model is more accurate in experiments with R12 than those with R114 as shown by the u_2 in Table 4.3 and the terminal velocity calculated in Appendix C. The high P_2 measured in R114 experiments indicates that the exit velocity is significantly lower than the sound speed for a homogeneous flow which will occur if gravitational effects are negligible.

B.3 Sonic Homogeneous Flow in Thermal Equilibrium

In the case where the particles and vapor are in thermal equilibrium as well as dynamic equilibrium, the sound speed is expressed by (B.2). Therefore, if the experiment is conducted with an extremely long test cell and gravitational effects are negligible, the exit velocity, u*, will equal a*. The continuity equation in this case is as follows:

$$\rho^* u^* = \rho_0 c \tag{B.15}$$

Following the analysis used to obtain (B.10), the following expression can be derived for the velocity at the exit:

$$u^* = \frac{\frac{c_P}{c} + \frac{\rho^*}{\rho_v} - 1}{\frac{c_P}{c} + \gamma\frac{\rho^*}{\rho_V} - \gamma} \frac{\rho_v a_v^2}{\rho_0 c} \tag{B.16}$$

The expression (B.16) can be simplified by comparing the terms and neglecting small terms. Table B.5 lists parameters which are relevant to this analysis.

Table B.5 Quantities of the parameters in (B.16).

Substance	c_p (erg/g/K)	γ	$\rho_2 \approx \rho^*$ (g/cc)[1]
R12	6.07×10^6	1.14	0.268
R114	7.12×10^6	1.09	0.343
Dragonite	$c = 8.4 \times 10^6$ erg/g/K		

Therefore, based on typical ρ_v shown in Tables B.1 and B.2, the following relationships are obtained:

$$\frac{\rho_v}{\rho_0} > 20$$

$$\frac{c_p}{c} < 1$$

$$\gamma < 1.2$$

$$\frac{\rho^*}{\rho_v} >> \gamma > \frac{c_p}{c} > 0 \qquad \text{(B.17)}$$

Based on (B.17) certain terms in (B.16) can be neglected to obtain the following approximation for the equilibrium sonic speed:

$$u^* \approx \frac{1}{\gamma} \frac{\rho_v a_v^2}{\rho_0 c} \qquad \text{(B.18)}$$

Using (B.3) and (B.4), the expression can be simplified into the following form:

$$u^* \approx \frac{Y P^*}{Z \rho_0 c} \qquad \text{(B.19)}$$

Conservation of mass and momentum in this flow gives another equation for u* which is equivalent to (4.4).

$$u^* = \frac{P_0 + \rho_0 c^2 - P^*}{\rho_0 c} \qquad \text{(B.20)}$$

[1] From Table 4.3.

Combining (B.19) and (B.20), the pressure, P*, for dynamic and thermal equilibrium sonic flow is obtained.

$$P^* = \frac{1}{\frac{Y}{Z} + 1} (P_0 + \rho_0 c^2) \qquad (B.21)$$

In Table B.6, P* for particle-vapor flow in dynamic and thermal equilibrium have been calculated using (B.21) with upstream conditions given in Tables 4.1/4.2. Z has been calculated iteratively using data in Tables B.1/B.2 to achieve consistency with P* .

Table B.6 Theoretical exit pressure for choked particle-vapor flows which have achieved dynamic and thermal equilibrium.

Test Fluid	Y	Z	P*
R12	1	0.924	2.42 bars
R114	1	0.968	0.76 bars

The differences between the results in Table B.4 and B.5 can be attributed to the heat transfer from the particles to the vapor necessary to achieve thermal equilibrium. However, the results in Table B.5 are approximate not only due to (B.18), but because the upstream conditions used in the analysis are measured in experiments where thermal equilibrium is not achieved at the exit. If the flow speed is approximately 2800 cm/s (Table 4.3), a 560 cm test cell will be needed to provide the characteristic heat transfer time of 0.199 seconds derived in *4.2.5*.

Appendix C
Particle Speed Relative to the Vapor

The velocity of vaporized test fluid necessary to suspend a particle against gravity is computed below using similarity arguments. The lofting ability for a test fluid vapor at State (2) in a choked Type 1 process is evaluated by analysis; Table C.1 summarizes the properties for the two test fluids.

Table C.1 Vapor properties at State (2) in a choked Type 1 process.

Test Fluid	P_2 (bar)	ρ (g/cc)	μ (cp)	ν (cm^2/s)
R12	2.2	0.0131	0.0123	0.00939
R114	0.9	0.0164	0.0112	0.00683

A particle is defined to be suspended against gravity when its weight (W) equals fluid dynamic drag (D),

$$W = D \tag{C.1}$$

and the particle translates at a constant speed (u) relative to the fluid.

The drag for a particular geometry is determined by the dynamic pressure, $^1/_2\ \rho\ u^2$, the frontal area, and the Reynolds number, Re. The drag coefficient, C_D, is a function of the Reynolds number which is defined as follows:

$$C_D(Re) = \frac{D}{\frac{1}{2}\rho\, u^2 A} \tag{C.2}$$

For the drag of a sphere, the Reynolds number is based on the diameter (d):

$$Re = \frac{u\, d}{\nu} \tag{C.3}$$

Therefore, (C.2) and (C.3) can be combined to form a new dimensionless parameter which is a function of Reynolds number, but one in which u does not appear explicitly.

$$C_D Re^2 = \frac{W d^2}{\frac{1}{2} \rho v^2 A} \qquad (C.4)$$

Where W has been substituted for D to obtain the relationship between fluid dynamic and gravitational forces a body; the parameter is the Galileo number discussed in Chapter 4.

The weight and the frontal area for a sphere of density ρ_s are given as follows:

$$W = {}^1/_6 \pi d^3 \rho_s Ng \qquad (C.5)$$

$$A = {}^1/_4 \pi d^2 \qquad (C.6)$$

In (C.5), the acceleration by gravity is expressed as Ng; N is equal to unity for normal gravitational conditions, and N equals 100 for highest centrifugal force studied.

By substituting (C.5) and (C.6) into (C.4), the Galileo number of a sphere in the test fluid can be found as follows:

$$C_D Re^2 = \frac{4 \rho_s d^3 Ng}{3 \rho v^2} \qquad (C.7)$$

Table C.2 gives the values evaluated for spheres used in the experiments.

Table C.2 $C_D Re^2$ for particles used in the experiments.
(ρ_s = 2.95 g/cc and d = 0.05 cm.)

Test Fluid	N = 1	N = 100
R12	4.17×10^5	4.17×10^7
R114	6.30×10^5	6.30×10^7

The values in Table C.2 are used to determine the drag coefficient using data from dynamically similar experiments (Figure C.1). The drag coefficient (C_D) for values of $C_D Re^2$ in Table C.2 are given in Table C.3.

Table C.3 Drag coefficients (C_D) for C_DRe^2 in Table C.2.

Test Fluid	N = 1	N = 100
R12	0.50±0.05	0.40±0.05
R114	0.45±0.05	0.35±0.05

The velocity, u, for the experiments can be calculated using C_D with the following equation:

$$u = \sqrt{\frac{4\,\rho_s\,d\,Ng}{3\,\rho\,C_D}} \qquad (C.8)$$

Equation (C.8) gives the velocity differential for a particle and the test fluid at State (2) in a choked Type 1 process. The values are given in Table C.4.

Table C.4 Relative vapor velocity necessary to suspend a particle against gravity.

Test Fluid	N = 1 (cm/s)	N = 100 (cm/s)
R12	171±8	1920±112
R114	162±9	1830±149

It should be noted here that the velocities given in Table C.4 are valid only for single particles. The effect on the velocity due to the presence of other particles can be approximated from the data for C_DRe^2 equal to 2.3×10^5 (Figure C.2). The velocity necessary to suspend the particles against gravity decreases with increasing particle concentration only in cases where the particles are dispersed; the opposite effect occurs when bubbles of fluid forms. Therefore, values in Table C.4 should be the upper limit for velocity differential between particles and vapor in a Type 1 process. However, it is not clear if a dispersed particulate flow is possible at C_DRe^2 greater than 10^6 for this conclusion to hold for the 100g results.

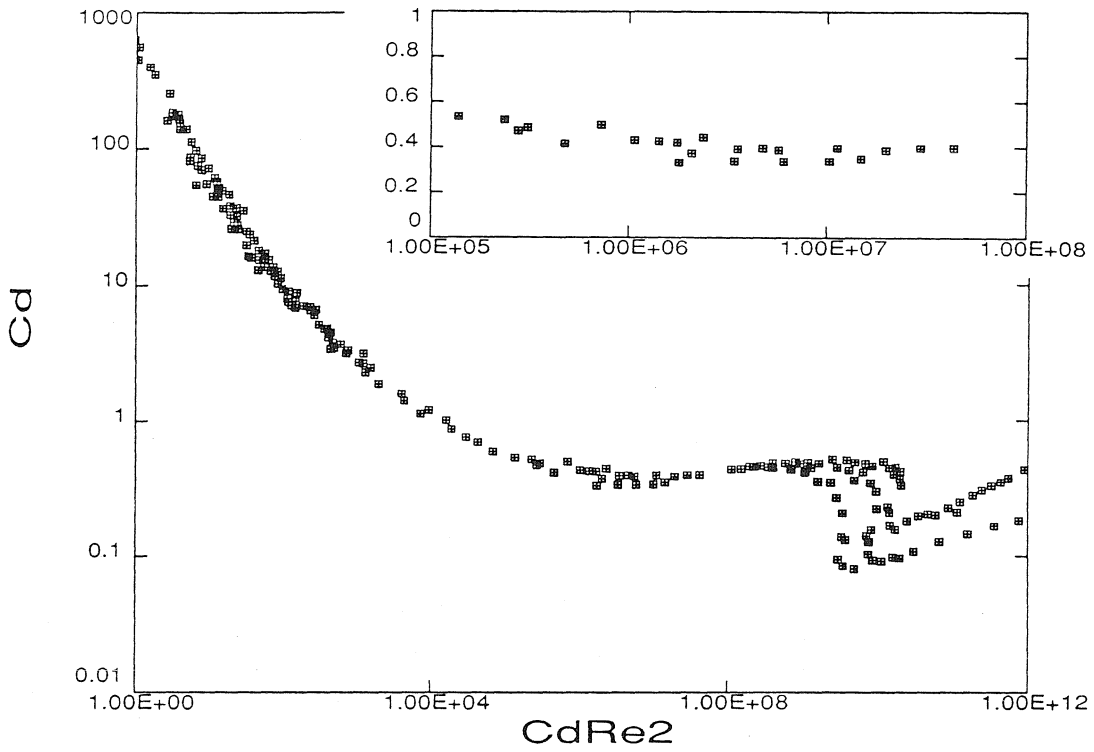

Figure C.1 Relationship between the drag coefficient C_D and $C_D\,Re^2$ for a sphere. The data is based on experimental data for the relationship between C_D and Re (Zahm, 1927). The inset is and enlargement for $C_D\,Re^2$ between 10^5 and 10^8, the range found in the experiments.

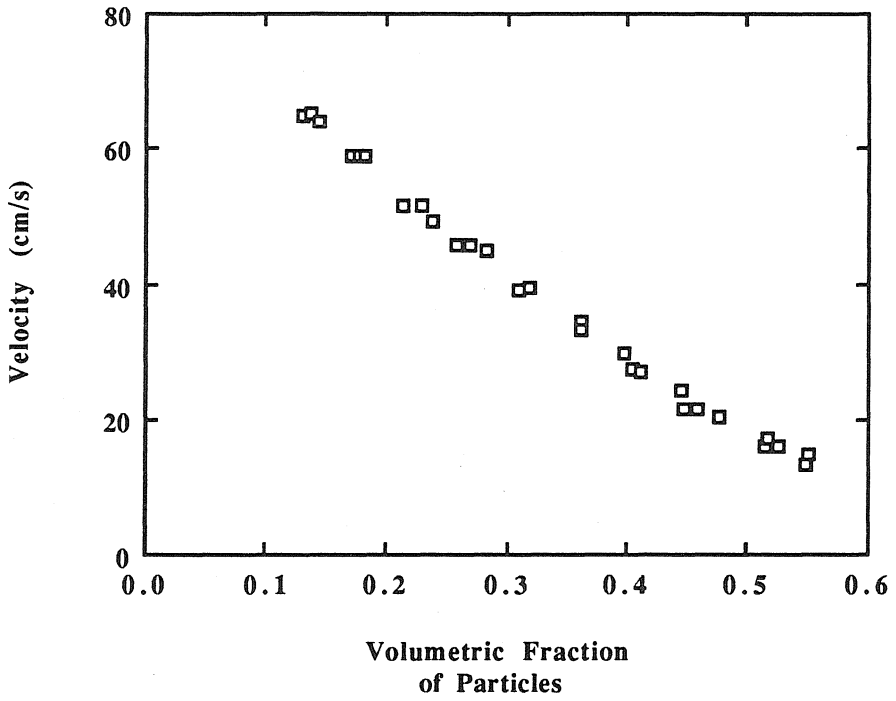

Figure C.2 Upward velocity necessary to suspend 0.63 cm ball bearings against gravity in water. The tube diameter for this fluidization experiment is 6.2 cm. The velocity necessary to suspend the particles increases as particles are more widely dispersed and the volumetric fraction is decreased. (Data: Richardson 1971.)

Appendix D

Adiabatic Expansion of a Multiphase Medium

The relationship between states (0) and (1) on either side of an adiabatic discontinuity is given by the following equation (Landau & Lifshitz, 1959):

$$\frac{v_2}{v_1} = \frac{(\gamma+1)\,P_1 + (\gamma-1)\,P_2}{(\gamma-1)\,P_1 + (\gamma+1)\,P_2} \tag{D.1}$$

This equation can be rewritten as follows:

$$\frac{P_2}{P_1} = \frac{(\gamma-1)\,\frac{v_2}{v_1} - (\gamma+1)}{(\gamma-1) - (\gamma+1)\,\frac{v_2}{v_1}} \tag{D.2}$$

At the limit for the expansion,

$$\frac{v_2}{v_1} \rightarrow \infty$$

Equation (D.2) asymptotes to a finite quantity:

$$\frac{P_2}{P_1} \rightarrow -\frac{\gamma-1}{\gamma+1} \tag{D.3}$$

This result can be applied to a homogeneous multiphase flow by representing the medium as a pseudo gas with the following ratio of specific heats (Wallis, 1969):

$$\gamma = \frac{c_p + m\,c_B}{c_v + m\,c_B} \tag{D.4}$$

This equation, where m is the particle-liquid mass per vapor mass, shows that γ will be very close to unity if the particle-liquid specific heat, m c_B, is much greater than the vapor specific heats, c_p and c_B. Therefore the limiting case for the adiabatic expansion is achieved at the limit expressed by (D.3):

$$\frac{P_2}{P_1} \rightarrow 0 \tag{D.5}$$

This means that the Hugoniot, the locus of P_2, asymptotes to the positive v-axis.

References

Anderson, J.D. (1982) *Modern Compressible Flow,* McGraw Hill.

Anilkumar, A.V. (1989) "Experimental studies of high-speed dense dusty gas," Ph.D. thesis, California Institute of Technology, Pasadena.

Barnea, E. and Mizrahi, A. (1973) "A generalized approach to the fluid dynamics of particulate systems. Part 1: Generalized correlation for fluidization and sedimentation," *Chem. Eng. J.*, **5**, 171-189.

Blevins, R.D. (1984) *Applied Fluid Dynamics Handbook*, Van Nostrand, New York.

Chaves, H. (1981) "Verdampfungswellen in retrograden flussigkeiten," Diplomarbeit, Geog-August-Universitat, Gottingen.

Chaves, H. (1984) "Phasenubergange und wellen bei der entspannung von fluiden hoher spezifischer warme," Dissertation, Georg-August-Universitat, Gottingen.

Darton, R.C. (1985) "The physical behavior of three-phase fluidized beds," *Fluidization*, second edition, Academic Press, New York, 495-528.

Grolmes, M.A. and Fauske, H.K. (1974) "Axial propagation of free surface boiling into superheated liquids in vertical tubes," *Proc. 5th Int. Heat Trans. Conf.*, **4**,B1.7, 30-34.

Hayes, W.D. (1960) *Gasdynamic Discontinuities*, Princeton University Press.

Hill, L. (1990) "An experimental study of evaporation waves in a superheated liquid," Ph.D. thesis, California Institute of Technology, Pasadena.

Holman, J.P. (1981) *Heat Transfer*, McGraw Hill.

Kieffer, S.W. (1977) "Sound speed in liquid-gas mixtures: water-air and water-steam," *J. Geophys. Research*, **82**, 2895-2904.

Kieffer, S.W. (1981) "Fluid dynamics of the May 18 blast at Mount St. Helens," U.S. Geological Survey Professional Paper 1250, 379-400.

Kieffer, S.W. and Sturtevant, B.(1984) "Laboratory studies of volcanic jets," *J. Geophys. Research*, **89**, 8253-8268.

Lacerda, N.L. (1986) "On the start up of supersonic underexpanded jets," Ph.D. thesis, California Institute of Technology, Pasadena.

McTaggart, K.C. (1960) "The mobility of nuees ardentes," *Am. J. Sci.*, **258**, 369-382.

Marble, F.E. (1963) "Dynamics of a gas containing small solid particles," *Combustion and Propulsion*, 5th AGARDograph Colloquium, Pergamon Press, 175-213.

Marble, F.E. (1970) "Dynamics of dusty gas," *Ann. Rev. Fluid Mechanics*, **2**, 397-446.

Marshall, W.R. Jr. (1954) "Atomization and spray drying," *Chem. Eng. Prog. Monograph Series*, **50** (2).

Nairn, I.A. and Wiradiradja, S. (1980) "Late quaternary hydrothermal explosion breccias at Kawerau geothermal field, New Zealand," *Bull. Volcanol.*, **43**, 1-13.

Ortiz, L.A., Scott, R., and Lee, J. (1983) "Dynamic centrifuge testing of a cantilever retaining wall," *Earthquake Eng. and Structural Dynamics*, **11**, 251-268.

Ostergaad, K. (1971) "Three-phase fluidization," *Fluidization*, Academic Press, New York, 751-780.

Prosperetti, A. and Plesset, M.S. (1978) "Vopour-bubble growth in a superheated liquid," *J. Fluid Mechanics*, **85** (2), 349-368.

Reid, R.C. (1983) "Rapid phase transitions from liquid to vapor," *Adv. Chem. Eng.*, **12**, 105-208.

Reid, R.C., Prausnitz, J.M., and Sherwood, T.K. (1977) *Properties of Gases and Liquids* Third Edition, McGraw Hill.

Reinhart, J.S. (1980) *Geysers and Geothermal Energy*, Springer-Verlag, New York.

Reynolds, D. (1954) "Fluidization as a geological process, and its bearing on the problem of intrusive granites," *Am. J. Sci.*, **252**, 577-613.

Reynolds, W.C. (1979) *Thermodynamic Properties in SI*, Stanford University.

Richardson, J.F. (1971) "Incipient fluidization and particulate systems," *Fluidization*, Academic Press, New York.

Schaffs, W. (1967) "Molecular Acoustics," in *Landolt-Bornstein, Numerical Data and Functional Relationships in Science and Technology,* New Series, II, Vol. **5**, 140.

Scott, R. (1983) "Centrifuge model testing at Caltech," *Soil Dyn. Earthquake Eng.*, **2** (4), 188-198.

Sellens, R.W. and Brzustowski, T.A. (1985) "A prediction of the drop size distribution in a sray from first principles," *Atomization and Spray Technology,* **1**, 89-102.

Sheriden, M.F. (1979) "Emplacement of pyroclastic flows: a review," *Ash Flow Tuffs*, Geol. Soc. Am. Spec. Paper 180, 125-136.

Sheriden, M.F. and Wohletz, K.H. (1983) "Hydrovolcanism," *J. Volcanol. Geotherm. Res.*, **17**, 1-29.

Sparks, R.S.J. (1976) "Grain size variations in ignimbrite and implications for the transport of pyroclastic flows," *Sedimentology*, **23**, 147-188.

Sparks, R.S.J. (1978a) "The dynamics of bubble formation and growth in magmas: a review and analysis," *J. Volcanol. Geotherm. Res.*, **3**, 1-37.

Sparks, R.S.J. (1978b) "Gas release rates from pyroclastic flows: an assesment of the role of fluidization in their emplacement," *Bull. Volcanol.*, **41**, 1-9.

Sturtevant, B. and Kieffer, S.W. (1982) "The fluid mechanics of volcanic eruptions: A proposal to stucy transient jets of multiphase fluids," unpublished.

Thompson, P.A. (1988) *Compressible-Fluid Dynamics*, Advanced Engineering Series.

Thompson, P.A., Carofano, G.C., and Kim, Y.G. (1986) "Shock waves and phase changes in a large-heat-capacity fluid emerging from a tube," *J. Fluid Mechanics*, **166**, 57-92.

Thompson, P.A., Chaves, H., Meier, G.E.A., Kim, Y.G., and Speckmann, H.D. (1987) "Wave splitting in a fluid of large-heat-capacity," *J. Fluid Mechanics*, **185**, 385-414.

Vergniolle, S. and Jaupart, C. (1986) "Separated two -phase flow and basaltic eruptions," *J. Geophys. Research*, **91**, 12842-12860.

Wallis, G.B. (1969) *One-dimensional Two-phase Flow*, McGraw Hill, New York.

Wilson, L. (1976) "Explosive volcanic eruptions-III. Plinian eruption columns," *Geophys. J. Roy. Astr. Soc.*, **45**, 543-556.

Wilson, C.J.N. (1984) "The role of fluidization in the emplacement of pyroclastic flows, 2: Experimental results and their interpretation," *J. Volcanol. Geotherm. Res.*, **20**, 55-84

Wilson, C.J.N. (1985) "The Taupo eruption, New Zealand. II. The Taupo ignimbrite," *Phil. Trans. Roy. Soc. London*, **A 314**, 229-310.

Winters, W.S. and Merte, H., Jr. (1979) "Experiments and nonequilibrium analysis of pipe blowdown," *Nuclear Sci. Eng.*, **69**, 411-429.

Wolfe, J.A. (1980) "Fluidization versus phreatomagmatic explosions in breccia pipes," *Economic Geology*, **75**, 1105-1111.

Woods, A.W. and Bursik, M.I. (1990) "Particle fallout and volcanic plumes," to be published.

Zahm, A.F. (1927) "Flow and drag formulas for simple quadratics," NACA R-253.